Optical properties of nanoscale silver structures fabricated by nanosphere lithography

Submitted by

William Andrew Murray

to the University of Exeter
as a thesis for the degree of
Doctor of Philosophy in Physics

August 2005

I certify that all material in this thesis which is not my own work has been identified and that no material has previously been submitted and approved for the award of a degree by this or any other University.

Abstract

A technique known as nanosphere lithography (NSL) has been extensively used to fabricate arrays of nanoparticles upon solid surfaces. This thesis describes NSL applied to the fabrication of periodic arrays of silver nanoparticles, and also an extension to the technique that allows the fabrication of periodic arrays of holes in an otherwise continuous silver film. This is followed by a description of experiments that probe the optical response of the structures. Of particular interest are surface electromagnetic modes known as localised surface plasmon resonances (LSPRs) and surface plasmon-polaritons (SPPs).

The LSPR associated with metallic particles are excited when light of a certain frequency is incident upon the particle. The frequency depends on the geometry of the particle and the dielectric environment; results are presented that probe these dependences. By varying the diameter of nanospheres used to create the lithographic mask it is possible to increase the width of the particles. Also, by increasing the amount of silver deposited onto the mask the height may be varied. Results indicate that a red-shift of the LSPR occurs with increasing width and reducing height. To investigate the response of the LSPR to changes to the external environment, monomolecular layers of 22-tricosenoic acid were deposited onto the particle arrays. A red-shift occurs with increasing thickness. It is found that an oscillation in the frequency-shift occurs even beyond saturation. It is suggested that this is due in part to the interaction of the LSPR field and the retarded field reflected from the dielectric-dielectric interfaces.

By etching the nanosphere array prior to deposition of silver it is possible to increase the size of the particles until eventually they merge to form a continuous array. It is shown that there is an abrupt transition in the optical behaviour correlating with the point at which full connectivity occurs between adjacent particles. The effect of varying the thickness of the silver film and diameter of the holes on the optical transmittance is also described. In particular, attention is paid to how the dispersion of the SPP modes that exist on the structures is altered.

Contents

Abstract 2

Contents 3

List of figures 7

Acknowledgements 15

1. Introduction 16

2. Optical response of metallic nanoparticles

- 2.1 Introduction 22
- 2.2 Scattering, absorption, extinction 24
- 2.3 Small spherical particles: the quasi-static approximation 28
- 2.4 Spherical particles: Mie theory 34
- 2.5 Size Effects 39
- 2.6 Non-spherical particles - shape effects 42
- 2.7 Periodic arrays of particles and particle interactions 48
- 2.8 Dielectric overlayers and substrate effects 51
- 2.9 Summary 54

3. Optical response of extended metallic surfaces

- 3.1 Introduction 55
- 3.2 Surface plasmon polariton 56
- 3.3 Dispersion relation 57
- 3.4 Propagation length of the SPP 60
- 3.5 Penetration depth of the SPP 61
- 3.6 Dispersion curve of the SPP 62
- 3.7 Effect of a dielectric overlayer on SPP dispersion 64
- 3.8 SPPs on thin metal films 66
  - 3.8.1 Symmetric thin metal films 66
  - 3.8.2 Asymmetric thin metal films 68
- 3.9 Coupling of light to SPP modes 70
  - 3.9.1 Prism coupling to SPP modes 70
  - 3.9.2 Grating coupling to SPP modes 73

3.10 Coupling strength to SPP modes 78
  3.10.1 Prism-coupling 79
  3.10.2 Grating-coupling 81
3.11 Two dimensional grating structures 86
3.12 SPP photonic bandgaps 89
3.13 Summary 91

4. Fabrication of patterned nanoscale structures using nanosphere lithography

4.1 Introduction 93
4.2 Nanosphere lithography 94
4.3 Assembly of nanospheres into ordered arrays 98
  4.3.1 Arrays formed at gas-liquid interfaces 99
  4.3.2 Physical confinement 100
  4.3.3 Evaporation 101
4.4 Dynamics of evaporative self-assembly 102
4.5 Fabrication of metallic arrays of particles and holes 106
  4.5.1 Substrate preparation 106
  4.5.2 Nanosphere ordering 109
  4.5.3 Thermal evaporation of metals 118
  4.5.4 Reactive-ion etching 120
4.6 Summary 123

5. Optical properties of silver nanoparticles formed by nanosphere lithography

5.1 Introduction 124
5.2 Experiment 125
  5.2.1 Fabrication 125
  5.2.2 Langmuir-Blodgett deposition 126
    5.2.2.1 Langmuir monolayers 127
    5.2.2.2 Film transfer 130
    5.2.2.3 Langmuir-Blodgett apparatus 131
    5.2.2.4 Procedure 132
  5.2.3 Optical measurements 133

5.3 Polarisation dependence 136
5.4 Size dependence 138
5.5 Dependence on optical environment 141
  5.5.1 Optical response 145
  5.5.2 Theory and further discussion 147
5.6 Summary 151

6. Transition from localised surface plasmon resonance to extended surface plasmon-polariton as metallic nanoparticles merge to form a periodic hole array

6.1 Introduction 153
6.2 Experimental 155
  6.2.1 Sample fabrication 155
  6.2.2 Optical characterisation 156
6.3 Dispersion scans and sample orientation 158
6.4 Scattered light-line and SPP schematics for hex array 160
6.5 Results and discussion 163
  6.5.1 SEM images 163
  6.5.2 Optical measurements 166
6.6 Summary 174

7. Optical properties of hole-arrays formed by nanosphere lithography

7.1 Introduction 175
7.2 Experimental 178
  7.2.1 Fabrication 178
  7.2.2 Optical measurements 180
7.3 Results and discussion 181
  7.3.1 Polarisation and orientation 181
  7.3.2 Thickness of silver film 191
  7.3.3 Hole diameter 195
7.4 Summary 200

8. Conclusions and future work

8.1 Summary of thesis 202

8.2 Future work 204
8.2.1 Particles 204
8.2.2 Particle-hole transition 205
8.2.3 Holes 205

Publications 207

References 208

List of figures

Figure 1.1 Real and imaginary components of the relative permittivity of silver taken from *Palik (1985)* (solid lines) and theoretical values calculated using the Drude approximation with plasma frequency ω_p = 8.57 eV and Γ = 0.0145 eV (dotted lines). 19

Figure 2.1 Schematic showing scattered field ($\mathbf{E}_s$,$\mathbf{H}_s$) and incident field ($\mathbf{E}_i$,$\mathbf{H}_i$) that together give the total external field ($\mathbf{E}_2$,$\mathbf{H}_2$). The internal field of the particle is ($\mathbf{E}_1$,$\mathbf{H}_1$) 25

Figure 2.2 Diagram illustrating particle surrounded by reference sphere of radius R with surface A. The incident field is directed parallel to the z-axis. 26

Figure 2.3 Dipolar charge distribution set up within a nanoparticle due to incident electromagnetic wave. 30

Figure 2.4 Spherical polar coordinate system centred on a spherical particle with diameter *a*. 35

Figure 2.5 Non-retarded incident field (upper diagram) and retarded incident field (lower diagram. 40

Figure 2.6 Mie theory calculations of the extinction cross-section (a) and extinction efficiency (b) of spherical silver particles with radii ranging from 10 nm to 90 nm (code adapted from *Bohren and Huffman (1983)*). The refractive index of the external medium n_2 = 1.55. 41

Figure 2.7 (a) Ratio of LSPR frequency associated with ellipsoidal particles ω_{LSP} to the plasma frequency ω_P as a function of shape factor *L* for relative permittivities of the external medium increasing from ε_2 = 1 to 5 (calculated using equation (84). (b) Shape factors L_a and L_c associated with oblate ($L_a = L_b$) and prolate spheroids ($L_b = L_c$) as a function of eccentricity *e* (calculated using equations (86)-(89)). The dotted line is at L_i = 1/3, the shape factor of a sphere. 47

Figure 2.8 (a) Extinction efficiency as a function of wavelength for silver particles with a 20 nm radius embedded in media with refractive index *n* = 1.0 to *n* = 2.0 (code adapted from BHMIE (*Bohren and Huffman (1983)*)). (b) Maximum extinction as a function of refractive index; the line is a linear fit with gradient 200 nm/RIU. 52

Figure 3.1 A schematic diagram of light with incident wavevector $\mathbf{k}_1$ incident on an interface bounded by two media described by complex permittivities indices ε_1 and ε_2. 58

Figure 3.2 A representation of the polarisation surface charge density and associated normal electric field component for the SPP mode. The 62 electric field decays exponentially into both the metal (ε_1) and dielectric (ε_2).

Figure 3.3 Schematic diagram showing the dispersion of the SPP mode (solid line) and light line (closely-spaced dotted line). The shaded region represents the range of frequencies accessible to light propagating in the dielectric bounding the metal. The light-line k_{LL} is the limit of the region for a given frequency. 63

Figure 3.4 Structure consisting of a dielectric overlayer with permittivity ε_3 and thickness d sandwiched between a semi-infinite metallic layer with permittivity ε_2 and semi-infinite dielectric layer with permittivity ε_1. 65

Figure 3.5 Schematic diagram showing the effect of adding a dielectric overlayer to the dispersion of the SPP mode (solid lines) and light lines (dotted lines). The lightly shaded area indicates the radiative region for the material with permittivity ε_1 and the darker shaded region the additional area accessible to light with the addition of a thick overlayer of permittivity ε_3. 65

Figure 3.6 Diagram showing (a) metal slab bounded by identical dielectrics (symmetric structure) and (b) metal slab bounded by different dielectrics (asymmetric structure). 67

Figure 3.7 Schematic diagrams showing field distributions and charge distributions for (a) the short-range SPP and (b) the long-range SPP. 67

Figure 3.8 Dispersion curve showing region of reciprocal space where coupling between light incident at the silica prism-metal interface and the SPP mode propagating at the air-metal interface. 71

Figure 3.9 Prism-coupling of light to SPP modes; the Otto configuration (a) and the Kretschmann-Raether configuration (b). 72

Figure 3.10 Diagram of a corrugated grating structure illustrating the coordinate system defined relative to the azimuthal orientation φ and plane of incidence. 74

Figure 3.11 Diagram illustrating the dispersion of scattered light-lines (dotted) and SPP modes (solid) from a mono-grating oriented $\varphi = 0°$ (a) and $\varphi = 90°$ (b). The shaded area is the radiative region. 76

Figure 3.12 A plane in reciprocal space for a constant value of ω. The dotted lines represent the dispersion of the scattered light lines for constant ω as a function of the wave vector components in the x and y directions. The solid lines represent the scattered SPP modes. The shaded region is the area of reciprocal space accessible to radiation and is bounded by the zero order light line and SPP. The mechanism for grating coupling of light into the SPP mode is shown. 77

Figure 3.13 Zero-order TM reflectivity as a function of frequency for a 1μm pitch 83

30nm amplitude sinusoidal silver grating for normal incidence and $\phi = 0°$. Three features are evident; at f = 0.36×10^{15}Hz a SPP minimum due to the first order SPP, at f = 0.37×10^{15}Hz a pseudo critical edge due to the 1st diffracted order becoming evanescent, and at f = 0.735×10^{15}Hz a small reflectivity maximum due to the second order SPP (courtesy of I. R. Hooper).

Figure 3.14 Zero-order TM reflectivity as a function of grating amplitude a_1. Other grating parameters as for figure 14 (courtesy of I. R. Hooper). 84

Figure 3.15 Representation of a square lattice in real-space. Shown are the primitive real-space lattice vectors a_1 and a_2 and the orientation of the corresponding primitive reciprocal lattice vectors b_1 and b_2. The dotted outlines show the unit cells of the structures. 86

Figure 3.16 Reciprocal space diagrams illustrating the scattering centres associated with the first- and second-order grating vectors. Each diagram (a)-(d) represents sections taken through reciprocal space in the k_x-k_y plane for increasing values of frequency ω. The shaded region is the radiative zone. 88

Figure 3.17 Schematic diagram illustrating the scattered light-lines (dotted) and SPP modes (solid) for a two-dimensional square grating (negative values of m and n are represented by $\overline{m}$ and $\overline{n}$. The $(n,1)$ modes are degenerate with the $(n,\overline{1})$ 89

Figure 4.1 Schematic representation of a hexagonally close-packed nanosphere array and the resulting nanoparticle array formed from a monolayer (a) and a bilayer (b). 95

Figure 4.2 Diagrams showing two spheres partially immersed in a liquid layer on a solid substrate (a) and the convective flow of spheres from bulk solution towards the ordered phase (b). The convective flow arises from an increased evaporation rate from ordered regions resulting in a capillary flow between the spheres that draws fluid from the bulk solution. 104

Figure 4.3 Schematic of fabrication process. (1) Drop pipette colloidal solution, (2) Ordering of nanospheres as fluid evaporates, (3) Silver evaporation onto non-etched (left) and etched (right) nanosphere arrays, (4) Plan view of arrays prior to sphere removal, (5) Particle array (left) and hole array (right) after nanosphere removal. 107

Figure 4.4 Diagram of apparatus used in the nanosphere ordering process, side-view (left), plan-view (right). 111

Figure 4.5 Digital photo of a nanosphere array formed from 390 nm diameter polystyrene spheres with (A) monolayer region, (B) multilayer regions, (C) nanosphere wall and (D) single monolayer domain 112

indicated.
Figure 4.6 Diffraction patterns from single monolayer domains (a), (b) and from multiple domains (c). 114
Figure 4.7 Illustrations showing undistorted and distorted sphere arrays with the associated ruled diffraction grating and diffraction pattern for orientations of $\varphi = 0°$ (a), (c), (e) and $\varphi = 30°$ (b), (d), (f). Figures (a) and (b) are for the undistorted array. Figures (c) and (d) show the effect of introducing a small gap between the spheres on the diffraction pattern. Figures (e) and (f) show the effect of introducing a shape distortion of the spheres on the diffraction pattern. Also indicated is the direction of convective flow that would produce the type of distortion and associated diffraction patterns. 116
Figure 4.8 Mechanism for defect propagation through ordered array to produce structure in figure 4.7(c). 118
Figure 4.9 Schematic diagram of vacuum thermal evaporation system used to deposit silver. 119
Figure 4.10 Nanoparticle array formed from nanospheres with a mean diameter of 390 nm. Bow-tie and line defects are clearly seen. 120
Figure 4.11 Schematic diagram of reactive ion etcher. 121
Figure 4.12 SEM image of an array of holes in a 50 nm thick silver film formed by etched nanosphere lithography. Inset shows a magnified region of the sample. 122
Figure 5.1 The molecular structure of 22-tricosenoic acid. 128
Figure 5.2 Structural phase transitions of a long chain fatty acid Langmuir film on a water surface showing the gas phase (a), liquid phase (b) and solid phase (c). Each molecule comprises of an aliphatic chain represented by a zig-zag line and carboxylic acid headgroup represented by a circle. 129
Figure 5.3 Diagram showing Langmuir-Blodgett film transfer on the downstroke (a) and upstroke (b). 130
Figure 5.4 Diagram of Langmuir-Blodgett apparatus. 131
Figure 5.5 Schematic diagram of the experimental setup for obtaining transmittance data as a function of wavelength. 134
Figure 5.6 A typical example of the spectral transmittance of an array of nanoparticles formed using nanosphere lithography. The diameter of the spheres used to form the lithographic mask was 390 nm and the height of the particles was 50 nm. The scale bar represents a distance of 500 nm. 135
Figure 5.7 Diagram illustrating azimuthal angle φ as defined relative to the 136

distorted–hexagonal diffraction pattern (a) and to a nanoparticle array (b).

Figure 5.8 Normal incidence transmittance spectra of silver nanoparticles formed from 390 nm diameter spheres as a function of the azimuthal angle. The incident light was linearly polarised with the azimuthal angle defined as the angle between the polarisation direction and the Bragg vector associated with the short pitch of the distorted grating. 137

Figure 5.9 Transmittance spectra of silver nanoparticle arrays formed from nanospheres with mean diameters of 220 nm (solid line), 390 nm (dashed line) and 630 nm (dotted line). The height of the particles was 50 nm as measured by a quartz crystal thickness monitor during evaporation. 140

Figure 5.10 Transmittance spectra of silver nanoparticle arrays formed from arrays of 390 nm diameter nanospheres. The height of the particles was varied from 20 nm to 50 nm in 10 nm steps as measured by a quartz crystal thickness monitor during evaporation. 140

Figure 5.11 Schematic diagram of a coated nanoparticle array. By varying the dip length a stepped overlayer geometry is fabricated allowing a single sample to be used to collect the data. 144

Figure 5.12 (a) Transmittance (upper) and dark-field scattering spectra (lower) from Sample 1. (b) Relative shift of the LSPR minimum as a function of overlayer thickness. 145

Figure 5.13 (a) Transmittance (upper) and dark-field scattering spectra (lower) from Sample 2. (b) Relative shift of the LSPR minimum as a function of overlayer thickness. 146

Figure 5.14 Schematic diagram of the system modelled using Maxwell-Garnett theory incorporated into CPS theory. The thickness of the LB and composite layers are denoted by t_{LB} and t_{MG} respectively and the separation of the dipole from the LB/composite interface is denoted by *s*. 147

Figure 5.15 Theoretical plot of the wavelength shift (arbitrary units) of a dipole oscillator as a function of overlayer thickness. 150

Figure 6.1 Experimental apparatus used to collect transmittance and reflectance as a function of frequency ω and in-plane wave vector $k_{//}$. The kit bounded with the dotted line is used in lining up the sample; the mirror in the beam is removed during data acquisition. The inset illustrates the incident, perpendicular component and parallel (in-plane) component of the wave vector and the angle of incidence θ. 157

Figure 6.2 Schematic diagrams illustrating orientation of hole array relative to coordinate axes for a sample in the classical mount (φ = 0°) (a) and 159 in the conical mount ($\varphi \neq 0°$) (b). Shown are the primitive reciprocal lattice vectors $\mathbf{b}_1$ and $\mathbf{b}_2$ where θ is the angle of incidence, incident wave vector $\mathbf{k}_0$ and in-plane wave vector $\mathbf{k}_{//}$. The azimuthal angle φ is defined as the angle the plane of incidence (represented by the long dotted line) makes with the (1,0,0) axis. Shown also is the orientation of the polarisation states – *p*-polarised light is in the plane of incidence and *s*-polarised light is perpendicular to the plane of incidence. The second dotted line in (b) represents the axis of rotation used to vary $\mathbf{k}_{//}$.

Figure 6.3 A two-dimensional reciprocal space diagram illustrates the orientation of the in-plane wave vector relative to the reciprocal lattice points for the two azimuthal angles. 162

Figure 6.4 Dispersion plots of the scattered light-lines and grating-coupled silica SPP modes for azimuthal angles of $\varphi = 0°$ (a) and $\varphi = 30°$ (b). The SPP dispersion is calculated using the Drude approximation for silver and a periodicity of 335 nm. Included are the (0,0) silica light-lines for comparison; no account is taken of mode interactions. 162

Figure 6.5 SEM images of (a) nanoparticle array formed without etching nanosphere array, (b) intermediate structure formed after etching nanosphere array for 70 s and (c) hole array formed after etching nanosphere array for 120 s. 165

Figure 6.6 Transmittance spectra for *p*-polarised light with $k_{//} = 0$ from samples etched for 0 s, 50 s, 70 s, 100 s and 120 s. Arrows indicate position of the localised surface plasmon resonance. 166

Figure 6.7 Measured transmittance as a function of in-plane wavevector and frequency in the form of a greyscale diagram for p-polarised light incident upon the (a) nanoparticle array, (b) intermediate structure and (c) hole array imaged in figure 3. 168

Figure 6.8 Superimposed upon the data from figure 5c (A) the diffracted (±1,0) silica light lines (dotted lines) and (B, C) modelled dispersion of grating coupled (±1,0) SPP modes associated with a planar silver-silica interface. The dashed lines (B) correspond to the SPP dispersion on a semi-infinite slab whereas the solid lines (C) correspond to the SPP dispersion on a 15 nm thick slab with the second silver interface bounded by air. 169

Figure 6.9 Power dissipated by a dipole as a function of frequency and in-plane wave vector. The dipole is embedded in a semi-infinite silica layer located 50 nm from a silver slab of thickness *d* = 15.0 nm. A semi-infinite air layer bounds the opposite surface of the silver. 171

Figure 6.10 Transmittance, reflectance and inferred absorbance spectra at $k_{//}$ = 172

0.5 μm^{-1} for *p*-polarised light incident upon a hole-array formed with a 120 s etch (detected light was un-polarised).

Figure 7.1 SEM image of a hole array in a silver film with a thickness of 50 nm formed from nanospheres with an initial mean diameter of 390 nm. The approximate diameter of the holes is 300 nm. The light regions within the holes are from a charging of the substrate during image capture. 182

Figure 7.2 Transmittance dispersion scans obtained from sample shown in figure 6.3 with (a) *p*-polarised light and azimuthal angle φ = 0°, (b) *s*-polarised light and φ = 0°, (c) *p*-polarised light and φ = 90°, and (d) *s*-polarised light and φ = 90°. 183

Figure 7.3 Dispersion of silica light lines (dotted) and SPP modes (solid) for grating orientations of φ = 0° (a) and φ = 90° (b). Parameters used in the calculations were pitch λ_G = 335 nm, silica refractive index n = 1.46 and silver thickness t = 14.5 nm. 185

Figure 7.4 Transmittance *T* (dashed), reflectance *R* (solid) and inferred absorbance *A* (dotted) spectra for a constant in-plane wave vector $k_{//}$ = 0.5 μm^{-1} and with *p*-polarised light ((a) and *s*-polarised light (b) incident. The vertical line represents the wavelength (frequency) above (below) which the structure is zero-ordered. An absorbance maximum is indicative of a SPP mode in this region. 187

Figure 7.5 Transmittance as a function of frequency and azimuthal angle for an in-plane wave vector of $k_{//}$ = 0.5 μm^{-1}. The dark regions of low transmittance are due to the excitation of the grating-coupled SPP modes. 189

Figure 7.6 Dispersion of single interface SPP modes calculated using a pitch of 330 nm for the (1,0) and (-1,0) modes (dotted) and 340 nm for the (0,1) and (0,-1) modes (dashed). 190

Figure 7.7 Transmittance dispersion scans from hole arrays with Ag thickness 15 nm (a), 25 nm (b), 30 nm (c), 40 nm (d), 50 nm (e) and 70 nm (f). 193

Figure 7.8 Plot of actual thickness of the Ag film evaporated against the effective thickness calculated by modelling the dispersion of an SPP mode on a planar film and fitting to the data in figure 6.7. The solid line is a fit generated by an inverse exponential function. 194

Figure 7.9 SEM image of a hole-array with mean hole diameter *d* ~ 260 nm and silver thickness *t* = 50 nm. 195

Figure 7.10 Transmittance dispersion scan of the sample in figure 6.9 taken with *p*-polarised light incident at an azimuthal angle φ = 0°. The dark region at low frequency, high wave vector is an experimental artefact. 196

Figure 7.11 SEM images of hole arrays with mean hole diameters of ~ 200 nm (a), 150 nm (b) and 100 nm (c). 197

Figure 7.12 Normal incidence transmittance scans of a series of hole arrays formed with decreasing hole diameter (as indicated) in silver films with a thickness of 15 nm. The solid lines in figures (b) and (c) correspond to the short dashed lines shown in figures (a) and (b) respectively. 197

Figure 7.13 Transmittance dispersion scans and associated normal incidence line-scans from three samples with *d* ~ 320 nm (a), 280 nm (b) and 220 nm (c). Incident light was *p*-polarised and the sample was oriented with φ = 0°. 199

Acknowledgements

Without the help of many people much of what has passed over the last three-and-a-bit years would have left me gibbering into my pint of Guinness. It is therefore only right and proper to take this opportunity to acknowledge the people who have had a direct hand in assisting me with this work. The first of these is Bill Barnes, my supervisor, who has provided inspiration, encouragement and limitless enthusiasm. Thanks for everything. The second of these is Roy Sambles whose insight, commitment and support are extended towards all the members of G13 and G20 without exception. Thanks also to my mentor Rob Hicken.

A mention now of those departed to alternative employment, Piers Andrew who was always willing and particularly able with any help, Pete ‘Hobbit’ Hobson and Simion Astilean. Full recognition too to those still knocking around, Tim T, Tim A, Sharon Jewell, Lucy Steve Smith Wedge, Joe Noyes, Jimmy K, John the Bear, Simon ‘Fret-gazer’ Garrett and Ian Hooper whose golfing prowess is matched only by his golfing gullability… Further thanks to my fellow 110ers, R. Kelly, Ben Evans, Jimmy Head and Gemma Winter, who has a penchant for dressing like a witch and poisoning people with cheap gin... you’ve been warned. Much gratitude to Pete Cann and the rest of the workshop, an overdue bottle or two are on the way.

A special thank you next to the people I lunch with. Pete ‘Media muncher’ Vukusic, just a good man all round with an unnatural ability for extreme jamminess. Alastair Hibbins, a terminally happy chap always willing to bore us with the finer details of nappy-changing. And Matt Lockyear whose prowess at hitting a golf ball is matched only by his prowess at throwing a golf ball…

Thanks to Jules for being a top notch housemate and Stew and Bernie for the music.

Finally, thanks to Mum, Dad, Thomas and Alice for being all anyone could want in a family.

Chapter 1

Introduction

The interaction of light with surface electromagnetic (EM) modes bound to a dielectric-metallic interface has provided a rich and varied area of research to exploit and develop. Confinement of the modes leads to locally intense EM fields that decay exponentially with distance away from the interface. The nature of the EM fields lends their use as probes of the materials that define the interface. Both the effect of the mode on the surroundings and the surroundings on the mode permits their use in a number of diverse applications. Experiments designed to sense chemical and biological moieties, even down to the single molecule limit [*Kneipp (1997), Nie and Emory (1997)*] have utilised the specific properties of surface EM modes. The characterisation of thin organic overlayers deposited on metals is also possible [*Barnes (1986)*], as is modifying the fluorescence of molecules located near metallic structures [*Lakowicz (2001)*]. A second consequence of the localisation of EM fields due to the excitation of surface modes is the enhancement of transmittance through thin metallic films. An effect of particular relevance in the context of this thesis is the enhanced transmission of light through regular arrays of sub-wavelength apertures perforating a metallic film [*Ebbesen (1998)*]. The increased penetration of the locally intense electromagnetic fields associated with surface modes allow more light to be transmitted than would be the case in the absence of the mode. The ability of the modes to allow the channelling of light through certain types of structure implies that these structures may be used as components in photonic circuitry. Moreover, these components are often sub-wavelength leading to circuits with length scales much smaller than those currently achieved [*Hecht (1996), Pendry (1999)*].

All of the phenomena described above owe their existence to the nature of the interaction of electromagnetic radiation with the metal, mainly dominated by the response of the conduction electrons at optical frequencies. In general, the response of a material to an incident electromagnetic field is governed by the complex permittivity ε, complex permeability μ, and complex refractive index

n of the material. The three quantities are co-dependent and together may be used to describe the optical properties of a material. They are related by

$$n = \sqrt{\frac{\varepsilon\mu}{\varepsilon_0\mu_0}}, \tag{1}$$

where ε_0 and μ_0 are the permittivity of free space and permeability of free space respectively with

$$n = n' + in'', \tag{2}$$

$$\varepsilon_\mathrm{r} = \frac{\varepsilon}{\varepsilon_0} = \varepsilon' + i\varepsilon'', \tag{3}$$

$$\mu_\mathrm{r} = \frac{\mu}{\mu_0} = \mu' + i\mu'', \tag{4}$$

where ε_r and μ_r are the relative permittivity and relative permeability with the single prime denoting the real part and the double prime denoting the imaginary part. The materials used in the work described within this thesis are all treated as being non-magnetic and as such a value of $\mu_\mathrm{r} = 1$ is assigned for the relative permeability leading to the following relations between the refractive index and relative permittivity:

$$\begin{aligned} \varepsilon' &= n'^2 - n''^2, \\ \varepsilon'' &= 2n'n''. \end{aligned} \tag{5}$$

For non-conducting materials (dielectrics) the refractive index is assumed to have no imaginary part yielding *Maxwell's Relation* $n' = \sqrt{\varepsilon'}$.

The refractive index and permittivity of materials are not independent of frequency and for some materials can vary substantially within the visible frequency range of the EM spectrum. In one of his well-known experiments Isaac Newton used prisms to disperse white light into its constituent colours and thus the variation of the optical parameters as a function of frequency became known as *dispersion*. To understand dispersion it is necessary to account for the influence of the electromagnetic field at an atomic scale. The *Lorentz Model* developed towards the end of the 19th century by *H. A. Lorentz* described the optical properties of materials by considering the atoms or molecules as identical, independent simple harmonic oscillators. When exposed to an electromagnetic field the electrons are displaced relative to the positive ion core and a polarisation charge is induced. A restoring force in the form of the Coulombic attraction between the positive ion core and the electrons acts to return the electrons to their equilibrium position resulting in an oscillatory motion. Upon solving the equation of motion for this system the following expression is derived for the relative permittivity,

$$\varepsilon_{\mathrm{r}} = 1 + \frac{\omega_{\mathrm{p}}^2}{\omega_0^2 - \omega^2 - i\Gamma\omega} \tag{6}$$

where ω_0 is the natural frequency of the oscillating electron bound to the ion core. The relaxation frequency Γ and the *plasma frequency* ω_{p} are defined by

$$\Gamma = \frac{e^2 N\rho}{m_e}, \tag{7}$$

$$\omega_{\mathrm{p}} = \sqrt{\frac{e^2 N}{\varepsilon_0 m_e}}, \tag{8}$$

where e is the electronic charge, m_{e} is the effective mass, N is the number density of the electrons and ρ is the resistivity.

For metals this equation may be simplified if one assumes that the conduction electrons dominate the optical response. In this case the electrons that undergo an oscillation due to the incident electromagnetic field do not see the positive ion cores and therefore respond purely to the changing electric field of the incident wave. This means it is possible to set ω_0 to zero resulting in a modified expression for the permittivity,

$$\varepsilon = 1 - \frac{\omega_{\mathrm{p}}^2}{\omega^2 + i\Gamma\omega}, \tag{9}$$

with real and imaginary parts

$$\varepsilon' = 1 - \frac{\omega_{\mathrm{p}}^2}{\omega^2 + \Gamma^2}, \tag{10}$$

$$\varepsilon'' = \frac{\omega_{\mathrm{p}}^2 \Gamma}{\omega\left(\omega^2 + \Gamma^2\right)}. \tag{11}$$

This is the *Drude Model* for the complex permittivity and serves as a good approximation for many metals at visible wavelengths. In the limit of small damping, $\omega \gg \Gamma$, the expressions for the real and imaginary components of the relative permittivity reduce to

$$\varepsilon' = 1 - \frac{\omega_{\mathrm{p}}^2}{\omega^2}, \tag{12}$$

$$\varepsilon'' = \frac{\omega_p^2 \Gamma}{\omega^3}. \qquad (13)$$

and it is seen that at the plasma frequency the real part of the relative permittivity is zero. Substituting a value of $\varepsilon' = 0$ into Maxwell's equations yields the interesting result that a longitudinal charge density fluctuation is set up within the material known as the *bulk* or *volume* plasmon. This has a characteristic energy of $\hbar\omega_p$ and has been observed in electron energy loss experiments [*Powell (1959)*].

The bulk plasmon propagates through the metal with the plasma frequency defining the onset of transparency. At frequencies $\omega < \omega_p$ the real part of the relative permittivity is negative ($\varepsilon' < 0$) and non-propagating (evanescent) solutions of the wave equation exist. At frequencies $\omega > \omega_p$, $\varepsilon' > 0$ and propagating solutions of the wave equation exist. For many metals, such as silver, account must be taken of the contribution of bound electrons to the optical response, particularly when the frequency of the incident EM radiation is in the *ultra-violet* region of the spectrum. This introduces transparency into metals at frequencies lower than that expected. Taking the example of silver,

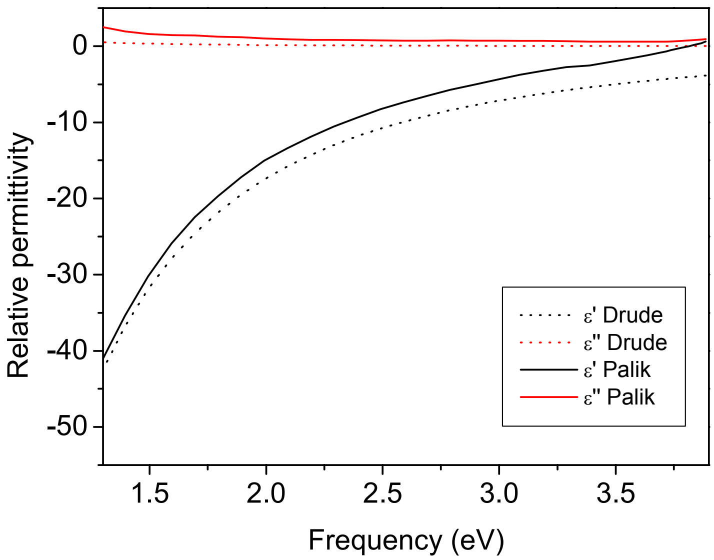

Figure 1.1. Real and imaginary components of the relative permittivity of silver taken from *Palik (1985)* (solid lines) and theoretical values calculated using the Drude approximation with plasma frequency ω_p = 8.57 eV and Γ = 0.0145 eV (dotted lines).

the plasma frequency is predicted by equation (8) to occur at 8.57 eV where values of N and m_e are obtained from *Weast (1972)*. Experimental observations estimate the actual value of ω_p to be ~3.8 eV.

Figure 1.1 shows a comparison between the real and imaginary parts of the relative permittivity of silver calculated using the Drude approximation (equations (8)-(11), Γ = 0.0145 eV, ω_p = 8.57 eV) and obtained experimentally [*Palik (1985)*] in the visible spectral region. An offset is observed between the two curves. This is mainly due to surface effects that result in a reduced ε' and increased ε'' of the experimentally derived values relative to the calculated values. Data collected from silver surfaces carefully prepared and isolated from contaminants provide values for the relative permittivity that agree reasonably well with the Drude model [*Nash (1996)* and references therein].

Upon introducing a metal-dielectric interface, plasmon modes with an altered eigenfrequency compared to the bulk plasmon may be excited. These are the surface EM modes referred to earlier. Two separate regimes are identified relating to plasmon modes that are excited upon particles small compared to the wavelength of light and plasmon modes excited upon extended metallic surfaces. The former of these is known as the localised surface plasmon resonance (LSPR), sometimes referred to as the particle plasmon mode, and is described in Chapter 2. Effects such as changing the size, shape and external environment on the LSPR are detailed. Chapter 3 describes the second type of plasmon mode, the surface plasmon polariton (SPP). The dispersion relation of the SPP is derived from which it is shown that the mode is non-radiative. To couple light with the SPP mode requires a means of matching the wave vectors for a given frequency. Methods by which this is achieved are explained. Chapter 4 introduces the nanoscale fabrication technique of nanosphere lithography. This is an inexpensive technique that utilises the self assembly of polystyrene nanospheres on solid substrates. Regular arrays are produced that can be used as a lithographic mask to produce particle and hole arrays. Optical experiments performed on these arrays are described in Chapters 5-7. Chapter 5 investigates the effect of changing the size and dielectric environment of silver particles. Chapter 6 explores how merging regular arrays of particles to form a continuous, perforated film leads to a transition in the optical response dominated by the LSPR to that dominated by the SPP. Chapter 7 investigates how changing the diameter of the holes and thickness of the silver perforated film alters the dispersion of the SPP mode. Finally Chapter 8 concludes and discusses future work.

Chapter 2

Optical response of metallic nanoparticles

2.1 Introduction

The manner in which metallic nanoparticles (commonly referred to as clusters for dimensions approaching the atomic scale) respond when electromagnetic radiation is incident upon them has proved to be a fascination to artisans and scientists for many years. Many of us have unknowingly appreciated their optical effects since certain types of stained glass owe their vivid colouring to the presence of gold nanoparticles of a particular size and composition. The first qualitative observation that dramatic colours could be generated by the presence of dispersed metallic particles is attributed to *Faraday (1857)*. He formed ruby, green, violet and blue aqueous colloidal gold by reducing gold chloride solution with phosphorous. A quantitative analysis of Faraday's observations followed some fifty years later when in 1908 *Gustav Mie* developed a theory based on the solution of Maxwell's equations for scattering and absorption by spherical particles. Provided the relative permittivity of the material was known and the particle was embedded in a non-absorbing medium *Mie* theory could be applied to generate extinction, scattering and absorption spectra. In particular, much effort was devoted to discerning the physical origin of the *Mie resonances* predicted by the theory, wavelengths at which the scattering and absorption was seen to increase significantly. This was the key to understanding the striking appearance of Faraday's colloidal solutions as the resonant processes occurred in the visible region of the electromagnetic spectrum for gold particles. The ruby coloured solutions had a strong extinction peak towards the blue end of the spectrum whilst the blue solutions had a strong extinction peak towards the red end of the spectrum. Since the development of the free electron theory, as described in chapter 1, the optical behaviour of noble and alkali metals is now understood to be dominated by the response of the conduction electrons. From this the *Mie* resonances were identified as arising from a coherent oscillation of the conduction electrons in the particles now known as *localised surface plasmon resonances* (LSPR) [*Kreibig and Völlmer (1995), Bohren and Huffman (1983)*]. Large enhancements of the electromagnetic field close to the particle occur on resonance. These enhancements are exploited in various applications and have in recent years lead to significant research efforts in many areas. Raman scattering, a process that occurs when a molecule inelastically scatters light due to the partial absorption of energy into a vibrational or rotational state of the molecule, can be enhanced by adsorbing the analyte molecule onto the surface of metallic nanostructures. This is known as surface enhanced Raman scattering (SERS) [review by *Moskovits (1985)*] and has been demonstrated on colloidal silver nanoparticles allowing the detection of single molecules [*Nie and Emory (1997), Kneipp (1997)*]. The modification of the emissive properties of dye molecules as a result of interactions with the LSPR of metal nanoparticles has lead to surface enhanced fluorescence (SEF) [*Glass (1981), Eagen (1981), Lakowicz JR (2001)*]. *Ditlbacher et al. (2001)* illustrated enhanced fluorescence from dye molecules deposited onto ellipsoidal particles for which there are two LSPRs associated with the orthogonal major and minor axes. The frequency of one of these resonances overlapped with the absorption of the dye molecule. When light was polarised in such a way so as to excite this resonance a higher quantum yield was observed from the molecules than when the orthogonal mode was excited. Increasing the fluorescence quantum yield is one method of improving molecular sensing; a different approach utilises the dependence of the LSPR position on the external environment. Molecules adsorbed onto a conjugated particle change the local refractive index and can therefore be detected with a high degree of sensitivity by monitoring the frequency shift of the LSPR [see review by *Schultz (2003)*].

The sensitivity to changes in the medium surrounding the particle illustrates one of several parameters that affect the position and form of the LSPR. The different colours observed by Faraday were due to the size-dependence of the resonance position; the extinction maximum for small gold particles is towards the blue end of the spectrum and for larger particles moves towards the red end of the spectrum. An increase in radiation damping and retardation with increasing size induces the red-shift and results in significant broadening of the LSPR. For very small particles a consequence of decreasing particle size is the onset of a size-dependent relative permittivity, leading to a blue-shift of the resonance position. These size effects are described in more detail in Section 2.5. The shape of the particle also has a significant effect on the LSPR with the extinction spectra of triangular and rod-like particles displaying very different features compared to spherical particles. This is described in more detail in Section 2.6. Further changes can occur from interactions between particles separated by distances small compared to the wavelength. The coupling between pairs of particles and regular arrays of particles are described in Section 2.7. Section 2.8 considers the effect of changes to the dielectric medium surrounding the particle on the LSPR including a discussion of the effect of substrate interactions. The chapter proceeds with a general description of the extinction, absorption and scattering of electromagnetic radiation incident on an arbitrary particle. This is followed by an introduction to the classical theoretical approaches of the quasi-static approximation (Section 2.3) and *Mie* theory (Section 2.4).

2.2 Scattering, Absorption, Extinction

Energy may be removed from a beam of light incident on a particle embedded within a homogeneous, non-absorbing medium by two processes. Firstly light may be scattered whereby a photon is redirected along a path that is no longer parallel to the incident beam. Secondly light may be absorbed by the particle whereby energy is converted into another form, for instance heat. In almost all cases both scattering and absorption are present and the combined effect is referred to as extinction,

EXTINCTION = SCATTERING + ABSORPTION.

Extinction is a measure of the attenuation of a beam of light traversing a medium from which the energy is removed by scattering and absorption. The amount of light absorbed and the amount of light scattered depends on the nature of the particle, its composition, size and shape. Common themes between very different particles that interact with light in very different ways do exist and these will be identified in this section before focusing on the specific properties of individual particles.

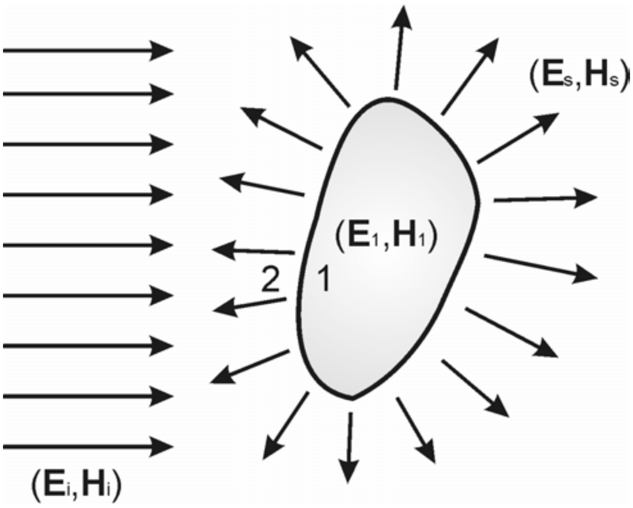

Figure 2.1. Schematic showing scattered field ($\mathbf{E}_s$,$\mathbf{H}_s$) and incident field ($\mathbf{E}_i$,$\mathbf{H}_i$) that together give the total external field ($\mathbf{E}_2$,$\mathbf{H}_2$). The internal field of the particle is ($\mathbf{E}_1$,$\mathbf{H}_1$)

To determine the response of a particle to an incident electromagnetic field the fundamental problem is to determine the electromagnetic fields inside and outside an arbitrary particle illuminated by a plane wave of a given frequency. The electromagnetic field inside the particle is ($\mathbf{E}_1$, $\mathbf{H}_1$) and outside the particle is ($\mathbf{E}_2$, $\mathbf{H}_2$). At any point outside the particle the total field is a superposition of the scattered fields ($\mathbf{E}_s$, $\mathbf{H}_s$) and the incident fields ($\mathbf{E}_i$, $\mathbf{H}_i$) (figure 2.1):

$$\mathbf{E}_2 = \mathbf{E}_\mathrm{i} + \mathbf{E}_\mathrm{s}, \quad \mathbf{H}_2 = \mathbf{H}_\mathrm{i} + \mathbf{H}_\mathrm{s}. \tag{1}$$

To calculate the energy flow at any point outside of the particle surface the time-averaged Poynting vector **S** is used, given by

$$\mathbf{S} = \frac{1}{2}\mathrm{Re}\{\mathbf{E}_2 \times \mathbf{H}_2^*\} = \frac{1}{2}\mathrm{Re}\{(\mathbf{E}_\mathrm{i} + \mathbf{E}_\mathrm{s}) \times (\mathbf{H}_\mathrm{i}^* + \mathbf{H}_\mathrm{s}^*)\}. \tag{2}$$

where $\mathbf{H}^*$ is the complex conjugate of **H**. Expanding the cross-product yields the three expressions

$$\mathbf{S}_\mathrm{i} = \frac{1}{2}\mathrm{Re}\{\mathbf{E}_\mathrm{i} \times \mathbf{H}_\mathrm{i}^*\} \tag{3}$$

$$\mathbf{S}_\mathrm{s} = \frac{1}{2}\mathrm{Re}\{\mathbf{E}_\mathrm{s} \times \mathbf{H}_\mathrm{s}^*\} \tag{4}$$

$$\mathbf{S}_\mathrm{ext} = \frac{1}{2}\mathrm{Re}\{\mathbf{E}_\mathrm{i} \times \mathbf{H}_\mathrm{s}^* + \mathbf{E}_\mathrm{s} \times \mathbf{H}_\mathrm{i}^*\} \tag{5}$$

where $\mathbf{S}_i$ is the Poynting vector of the incident wave, $\mathbf{S}_s$ is the pointing vector of the scattered wave, $\mathbf{S}_{ext}$ is the Poynting vector associated with some interaction between the incident and scattered waves, and

$$\mathbf{S} = \mathbf{S}_{\text{inc}} + \mathbf{S}_{\text{sca}} + \mathbf{S}_{\text{ext}}\,. \tag{6}$$

If a spherical reference surface of radius R and surface area A is constructed about the particle (figure 2.2) then the net flow of energy across this surface may be calculated by integrating the time-averaged Poynting vector **S** over the surface area of the sphere:

$$W_{\text{abs}} = -\int_A \mathbf{S} \cdot \hat{\mathbf{e}}_{\text{r}} dA\,. \tag{7}$$

Here W_{abs} denotes the net energy flow into the spherical surface due to absorption and $\hat{\mathbf{e}}_{\text{r}}$ is the radial unit vector directed outward from the origin. The medium surrounding the sphere is non-absorbing; therefore all of the energy absorbed within the reference sphere is due to absorption within the particle. Substituting equations (3)-(5) into equation (7) according to the relation in equation (6) it is possible to obtain expressions for the rate at which energy is incident on and scattered by the object and the energy associated with the interaction between the scattered and incident radiation:

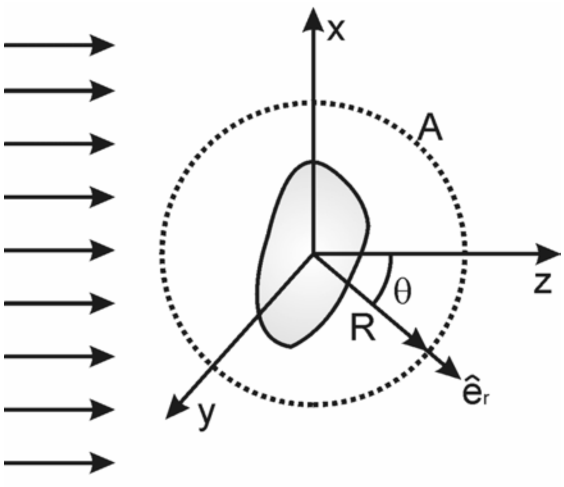

Figure 2.2. Diagram illustrating particle surrounded by reference sphere of radius R with surface A. The incident field is directed parallel to the z-axis.

$$W_{\text{inc}} = -\int_A \mathbf{S}_{\text{inc}} \cdot \hat{\mathbf{e}}_{\text{r}} dA \tag{8}$$

$$W_{\text{sca}} = \int_A \mathbf{S}_{\text{sca}} \cdot \hat{\mathbf{e}}_{\text{r}} dA \tag{9}$$

$$W_{\text{ext}} = \int_A \mathbf{S}_{\text{ext}} \cdot \hat{\mathbf{e}}_{\text{r}} dA \tag{10}$$

with

$$W_{\text{abs}} = W_{\text{inc}} - W_{\text{sca}} + W_{\text{ext}}\,. \tag{11}$$

The rate at which energy is scattered across the surface of the reference sphere is W_{sca}, and for a non-absorbing medium the energy flow of the incident beam W_{inc} vanishes when integrated over a closed surface. Therefore W_{ext} is, by conservation of energy, simply the addition of the scattering term and the absorption term

$$W_{\text{ext}} = W_{\text{abs}} + W_{\text{sca}}\,. \tag{12}$$

For convenience the extinction, scattering and absorption are often referred to by their respective cross-sections. This means that the total energy scattered in all directions is equal to the energy from the incident wave falling upon an area equal to the scattering cross-section C_{sca}. Similarly the absorption cross-section C_{abs} is defined as the equivalent area upon which energy from the incident wave is absorbed, and the extinction cross-section C_{ext} is defined as the sum of the scattering and absorption cross-sections. More formally the cross-sections are defined as the ratio of the energy evolved per second to the energy density of the wave [*Stratton (1947) pp 569*]; in terms of equation (12):

$$C_{\text{ext}} = C_{\text{sca}} + C_{\text{abs}} = \frac{W_{\text{ext}}}{I_{\text{i}}} = \frac{W_{\text{sca}}}{I_{\text{i}}} + \frac{W_{\text{abs}}}{I_{\text{i}}} \tag{13}$$

where I_{i} is the irradiance of the incident wave. Finally, the extinction, scattering and absorption efficiencies are defined as the ratio of the respective cross-sections to the geometrical cross-section of the particle G as projected onto a plane perpendicular to the propagation direction of the incident radiation,

$$Q_{\text{ext}} = \frac{C_{\text{ext}}}{G}, \quad Q_{\text{sca}} = \frac{C_{\text{sca}}}{G}, \quad Q_{\text{abs}} = \frac{C_{\text{abs}}}{G}. \tag{14}$$

Provided it is possible to generate expressions for the scattered and incident electromagnetic fields it is possible to evaluate the flow of energy scattered and absorbed by the particle and from there calculate the cross-sections and efficiency factors described above. Experimentally it is far easier to evaluate C_{ext} and C_{sca}; it is then a trivial matter given the conditions described above to calculate C_{abs}. In particular, C_{ext} is related to the intensity loss $\Delta I_{\mathrm{ext}}(z)$ of transmitted light propagating in the z-direction by the Lambert-Beer law

$$\Delta I_{\mathrm{ext}}(z) = I_{\mathrm{i}}(1 - \exp^{-NC_{\mathrm{ext}}z}), \tag{15}$$

where N is the number concentration of the particles. Expressions for C_{ext} and C_{sca} are readily derivable for simple shapes from various scattering theories allowing comparison with experiment in certain cases. However, the problem of scattering from particles without some degree of spherical symmetry is extremely complex.

2.3 Small spherical particles: the quasi-static approximation

Applying electrostatic theory to the problem of scattering and absorption of electromagnetic radiation by small metal spheres (radius $a << \lambda$) enables some understanding of the fundamental physical processes to be gained. The simplest scenario to consider consists of a non-magnetic ($\mu = \mu_0$) sphere surrounded by a homogeneous, linear and isotropic medium that is non-absorbing. It is assumed that the particle initially experiences a uniformly polarised field throughout the entire volume of the sphere. Phase shifts that would exist in a non-uniform field are neglected, thus multipolar resonances predicted by Mie theory are restricted to the dipole mode. The mode is induced by the movement of the electrons relative to the positively charged ion cores of the atomic nuclei under the influence of the externally applied electric field. Provided the permittivities of the sphere and the external medium are different a charge is developed at the surface resulting in a polarisation field within the particle. The external field is, by virtue of equation (1), modified by the electromagnetic field generated by the polarisation charge.

Standard methods in electrostatics can be applied to derive expressions for the electric fields inside ($\mathbf{E}_1$) and outside ($\mathbf{E}_2$) the sphere from the scalar potentials $\varphi_1(r,\theta)$ and $\varphi_2(r,\theta)$ using

$$\mathbf{E}_{\mathrm{i}} = -\nabla\varphi_{\mathrm{i}}, \qquad \mathrm{i} = 1,2 \tag{16}$$

and the Laplace equation

$$\nabla^2\varphi = 0\,. \tag{17}$$

The boundary conditions at the interface ($r = a$) between the sphere and the medium necessitate that the potential is continuous,

$$\varphi_1 = \varphi_2, \tag{18}$$

and that their radial derivatives satisfy

$$\varepsilon_1 \frac{\partial \varphi_1}{\partial r} = \varepsilon_2 \frac{\partial \varphi_2}{\partial r}\,. \tag{19}$$

where ε_1 is the complex permittivity of the particle and ε_2 is the permittivity of the external medium. A further condition is that far from the particle the field is unperturbed by the particle,

$$\begin{aligned} \mathbf{E}_2 &= \mathbf{E}_0 \qquad (r \to \infty) \\ \varphi_2 &= -E_0 z = -E_0 r\cos\theta \end{aligned}, \tag{20}$$

and is equal to the incident field now defined as $\mathbf{E}_0 = E_0\mathbf{z}$. Solving equation (17) and applying the boundary conditions yields the following expressions for the potential inside (φ_1) and outside (φ_2) the sphere,

$$\varphi_1 = -\frac{3\varepsilon_2}{\varepsilon_1 + 2\varepsilon_2} E_0 r\cos\theta, \tag{21}$$

$$\varphi_2 = -E_0 r\cos\theta + a^3 E_0 \frac{\varepsilon_1 - \varepsilon_2}{\varepsilon_1 + 2\varepsilon_2}\frac{\cos\theta}{r^2}. \tag{22}$$

Instantly one can see by comparison with equation (20) that the field outside of the sphere is a superposition of the incident field and the field generated by the particle. By comparison with the equation for the potential due to an ideal dipole,

$$\varphi = \frac{\mathbf{p}\cdot\mathbf{r}}{4\pi\varepsilon_2 r^3} = \frac{p}{4\pi\varepsilon_2}\frac{\cos\theta}{r^2} \tag{23}$$

where **p** is the dipole moment, the second term in equation (22) is identified as being that of an ideal dipole with moment,

$$\mathbf{p} = 4\pi a^3 \frac{\varepsilon_1 - \varepsilon_2}{\varepsilon_1 + 2\varepsilon_2}\varepsilon_2 \mathbf{E}_0, \tag{24}$$

and polarisability α,

$$\alpha = 4\pi a^3 \frac{\varepsilon_1 - \varepsilon_2}{\varepsilon_1 + 2\varepsilon_2}\,. \tag{25}$$

The derivation above has required a spatially constant electric field and has neglected the application of a time-varying electric field. An electromagnetic wave incident on a sphere as defined above naturally has a time-varying electric field and therefore when applying electrostatic theory to these situations is often referred to as the *quasi-static approximation*. This acknowledges that although spatially invariant at an instant in time, the particle experiences a field with a time dependent phase.

The polarisability is related to the absorption and scattering cross-sections by

$$C_{sca} = \frac{k^4}{6\pi}\left|\alpha^2\right|, \tag{26}$$

$$C_{\mathrm{abs}} = k\,\mathrm{Im}\{\alpha\}, \tag{27}$$

yielding, upon substitution of the polarisability in equation (25),

$$C_{\mathrm{abs}} = \pi a^2 4x\,\mathrm{Im}\left\{\frac{\varepsilon_1 - \varepsilon_2}{\varepsilon_1 + 2\varepsilon_2}\right\} \tag{28}$$

$$C_{\mathrm{sca}} = \pi a^2 \frac{8}{3} x^4 \left|\frac{\varepsilon_1 - \varepsilon_2}{\varepsilon_1 + 2\varepsilon_2}\right|^2 \tag{29}$$

where $x = ka = 2\pi a n_2/\lambda$ is the *size parameter*. From these relations it is clear how the absorption, scattering and extinction from a particle small compared to the wavelength λ depend on the size, wavelength and relative permittivities of the particle and the external medium.

For a small particle consisting of a material with a dielectric function only weakly dependent on the frequency of the incident radiation and satisfying the conditions above the absorption is proportional to $1/\lambda$ and the scattering intensity proportional to $1/\lambda^4$. This is known as *Rayleigh scattering* after Lord Rayleigh who used the relationship to explain the colour of a clear blue sky [*Rayleigh*

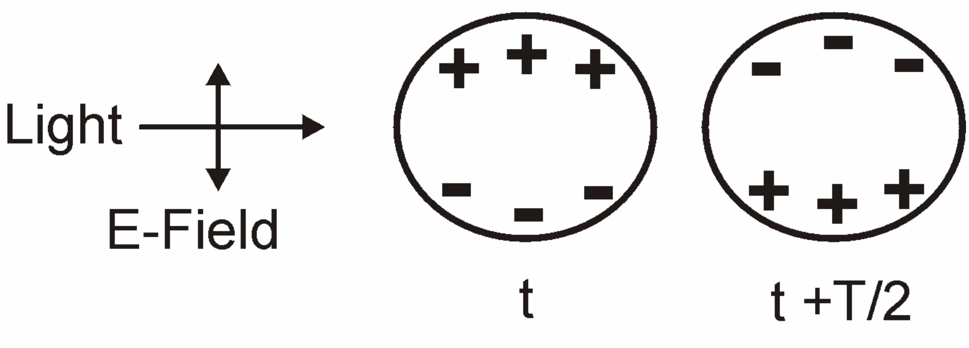

Figure 2.3. Dipolar charge distribution set up within a nanoparticle due to incident electromagnetic wave.

(1871)]. Particles in the atmosphere much smaller than the wavelength of visible light scatter blue light more efficiently than red light hence the blue colour of a clear sky. *Metallic* particles on the other hand behave differently and do not necessarily scatter blue light more efficiently than red. The reason for this is that the dielectric function of metals, in particular the noble and alkali metals, vary significantly as a function of the frequency of the incident light in the visible part of the electromagnetic spectrum (as was shown in the previous chapter, the real part of the complex relative permittivity of silver varies from -4 to -30 across the visible spectral region). When the complex permittivity of the particle has a value such that the denominator in equation (25) is minimised the polarisability becomes very large,

$$\begin{aligned} &\left|\varepsilon_1 + 2\varepsilon_2\right| = \min \\ &\left(\varepsilon_1' + 2\varepsilon_{r2}\right)^2 + \left(\varepsilon_1''\right)^2 = \min \end{aligned} \quad . \qquad (30)$$

where ε_{r2} is the relative permittivity of the external medium. This results in large scattering, absorption and extinction cross-sections and is interpreted as a forced, damped dipole oscillation of the conduction electrons in the particle, shown schematically in figure 2.3. As mentioned previously, the oscillation is commonly called the *localised surface plasmon resonance* (LSPR) following the terminology developed in Chapter 1 for the electron plasma oscillations at dielectric-metal interfaces.

If a small particle formed from a metal with a negligible imaginary part of the complex permittivity is embedded in a medium with ε_{r2} = 1 the resonance condition is satisfied when $\varepsilon_1' = -2$. Recalling from chapter 1 the Drude model for the relative permittivity of metals with negligible damping, inserting this into equation (30) and equating to zero, the resonance frequency ω_{LSP} in terms of the bulk plasma frequency ω_p is

$$\omega_{LSP} = \frac{\omega_P}{\sqrt{1+2\varepsilon_{r2}}} = \frac{\omega_P}{\sqrt{3}} \qquad (31)$$

For an external medium with a permittivity $\varepsilon_{r2} \sim 1$ there is very little or no charge present outside of the particle to compensate for the charge generated within the particle. The polarisation of the external medium is negligible and therefore the resonant frequency of the mode is entirely determined by the motion of the conduction electrons within the particle. If the permittivity of the external medium is no longer unity then there is some contribution from an induced polarisation of the external atoms or molecules. This will act to depolarise the field produced by the plasma oscillation therefore reducing the restoring force and resonant frequency.

The amplitude and width of a resonance feature are as important in fully characterising the behaviour of an oscillatory system as the spectral position. Damping mechanisms experienced by a harmonic oscillator reduce the amplitude and increase the linewidth with the latter defined as the full width at half maximum (FWHM). In the frequency domain the FWHM ($\Delta\omega$) is sometimes referred to as the relaxation frequency or relaxation rate and for a Lorentzian oscillator is related to the *total dephasing time* T_2 by

$$\Delta\omega = \frac{2}{T_2}. \tag{32}$$

The value of T_2 indicates the time taken for the oscillation amplitude to decay to 1/e of the initial amplitude. An electron in a metal undergoes both elastic and inelastic dephasing. Elastic dephasing ('*pure*' dephasing) encompasses scattering from impurities, lattice defects, phonons and electrons that involve no loss of energy. However, any directional information is lost by the electron resulting in a loss of coherency within a collective oscillation. Inelastic dephasing involves some energy loss of the electron principally by electronic transitions, phonon excitation or photon emission. In a collective oscillation this may be referred to as *population* dephasing as the population of a particular energy eigenstate is reduced. The total dephasing time T_2 is determined by the relative contributions of population (T_1) and pure (T_2^*) dephasing, linked by $\frac{2}{T_2} = \frac{1}{T_1} + \frac{1}{T_2^*}$. Typically the contribution from T_2^* is neglected resulting in the population dephasing time T_1 associated with the *energy* of the oscillation decays at twice the rate of the total dephasing time associated with the *amplitude* of the oscillation. Values of T_2 are in the femtosecond regime for silver and gold particles [*Heilwell (1985)*].

For a plasmon mode, to completely describe the damping requires contributions from collective and singular energy loss mechanisms. However, to a good approximation the plasmon oscillation can be described using an independent electron approximation, as with the Drude model. The imaginary part of the dielectric function ε'' defines the frequency dependent damping experienced by individual electrons in bulk matter. Therefore the shape of the LSPR is significantly affected by the value of ε'' in the region of the resonant frequency. For an ideal free-electron metal it is only these processes that are present and dephasing of the LSPR oscillation is due entirely to elastic collisions. In realistic metals inelastic scattering of the electrons is possible and is manifested by intraband (within the conduction band) and interband (from valence bands to the conduction band) transitions of electrons between energy eigenstates. In free-electron metals such as the alkali metals the LSPR is below the frequency threshold of interband transitions. In nearly-free electron metals such as gold and copper the influence of inelastic dephasing of the LSPR is significant since the plasmon resonance may overlap the frequency range in which interband transitions occur. Silver is also significantly influenced by the core electrons resulting in a reduced plasma frequency relative to that predicted by simple Drude theory. However, the resonant frequency of the dipole LSPR is also reduced to a value beyond the interband transition threshold thus reducing inelastic dephasing. Consequently the lifetime T_2 of the LSPR in silver nanoparticles is larger than that in gold and copper and therefore is a sharper, more pronounced feature in optical spectra.

To simplify matters energy loss channels are separated into two types of mechanism, radiative damping and non-radiative damping. Radiative damping is the coupling of energy from the LSPR into a propagating mode associated with the external medium. For particles in the quasi-static approximation these effects are negligible when compared to the absorptive processes and only the magnitude of the polarisability is a function of the particle size. As the particle size is increased radiative damping substantially increases with scattering processes dominating over non-radiative damping for particles with diameters approaching the wavelength of the driving field. For particles too large to be considered in the quasi-static limit the frequency position of the LSPR will depart substantially from the condition in equation (30). To describe completely the interaction of a spherical particle of any size with an electromagnetic field requires the implementation of more complex theories such as Mie theory.

2.4 Spherical particles: Mie theory

To date the most widely implemented rigorous scattering theory for particles has been *Mie theory (Mie 1908)*, providing a general framework enabling exact solutions to the problem of light scattering by an arbitrary sphere. In his original work Mie solved Maxwell's equations using appropriate boundary conditions with the system expressed in spherical polar coordinates. The incoming electromagnetic field was represented as multipole expansions of a transverse electric (magnetic) wave and transverse magnetic (electric) wave. Magnetic and electric *scalar* potentials were introduced to describe the components of the incident, scattered and internal fields each being a solution to the scalar wave equation. A more general approach is to expand the incident, scattered and internal fields in terms of *spherical vector wave harmonics* as detailed by *Bohren and Huffman (1983)* and *Stratton (1947)*. A reduced description follows detailing the main points.

To begin Maxwell's equations are expressed in the complex representation,

$$\nabla \cdot \mathbf{E} = 0 \tag{33}$$

$$\nabla \cdot \mathbf{H} = 0 \tag{34}$$

$$\nabla \times \mathbf{E} = \mathrm{i}\omega\mu\mathbf{H} \tag{35}$$

$$\nabla \times \mathbf{H} = -\mathrm{i}\omega\varepsilon\mathbf{E} \tag{36}$$

From these equations it is possible to show that the time-harmonic vector fields **E** and **H** in a linear, isotropic, homogeneous medium are solutions of the vector wave equations

$$\nabla^2\mathbf{E} + k^2\mathbf{E} = \mathbf{0} \tag{37}$$

$$\nabla^2\mathbf{H} + k^2\mathbf{H} = \mathbf{0} \tag{38}$$

where $k^2 = \omega^2\varepsilon\mu$. The vector functions

$$\mathbf{M} = \nabla \times \mathbf{a}\psi, \quad \mathbf{N} = \frac{1}{k}\nabla \times \mathbf{M}, \tag{39}$$

where ψ is a scalar function, k is the wave vector and **a** is an arbitrary constant vector are defined in such a way that they satisfy the equation

$$\nabla^2\mathbf{C} + k^2\mathbf{C} = \nabla \times \left[\mathbf{a}\left(\nabla^2\psi + k^2\psi\right)\right], \tag{40}$$

where **C** represents either of the two vector functions. From this it is seen that subject to ψ satisfying the *scalar* wave equation

$$\nabla^2\psi + k^2\psi = 0\,, \tag{41}$$

M and **N** are both solutions to the *vector* wave equation. Moreover, the particular solutions of equation (41) that are finite, continuous and single-valued form a discrete set with each separate solution denoted as ψ_n. Associated with the ψ_n are the discrete vector functions $\mathbf{M}_n$ and $\mathbf{N}_n$ that linearly combined can be used to represent any arbitrary wave function. These are the spherical vector wave harmonics. It is seen from equation (39) that the divergence of the vectors **M** and **N** vanish and furthermore that **M** can be expressed as a function of **N**. Therefore the following three conditions supplement the definitions of **M** and **N** in equation (39):

$$\nabla\cdot\mathbf{M} = 0, \qquad \nabla\cdot\mathbf{N} = 0,, \qquad \mathbf{M} = \frac{1}{k}\nabla\times\mathbf{N}\,. \tag{42}$$

The vectors **M** and **N** have all the properties of an electromagnetic field in that they are each proportional to the curl of the other and are divergence-free. Therefore the fields **E** and **H** may be represented by a linear combination of the vectors **M** and **N**

$$\mathbf{E} = -\sum_{n} A_n\mathbf{M}_n + B_n\mathbf{N}_n\,, \qquad \mathbf{H} = \mathrm{i}\omega\varepsilon k\sum_{n} A_n\mathbf{N}_n + B_n\mathbf{M}_n \tag{43}$$

Using this approach finding solutions to the electromagnetic field equations has been reduced to finding solutions to the scalar wave equation.

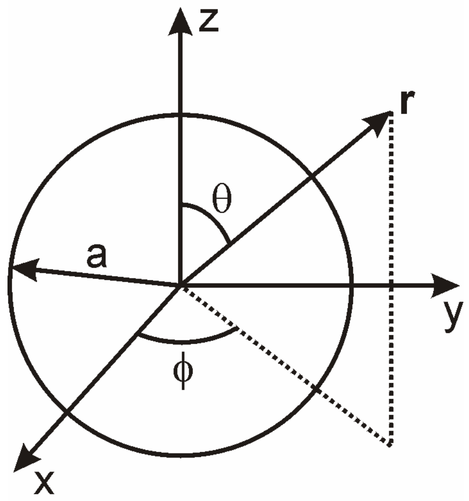

Figure 2.4. Spherical polar coordinate system centred on a spherical particle with diameter *a*.

Until this point the choice of the scalar function ψ (called the generating function) and vector **a** (called the pilot vector) has been arbitrary. The pilot vector is chosen to be the radius vector **r** as this ensures **M** is a solution to the vector wave equation in spherical polar coordinates. The form of ψ is governed by the symmetry of the problem and is in this case most suitably expressed in terms of a spherical coordinate system (figure 2.4) with even and odd separable solutions to the scalar wave equation given by

$$\psi_{\mathrm{emn}}(r,\theta,\varphi)=R(r)\Theta(\theta)\Phi(\varphi)=\cos(m\varphi)P_{\mathrm{n}}^{\mathrm{m}}(\cos\theta)z_{\mathrm{n}}(kr) \tag{44a}$$

$$\psi_{\mathrm{omn}}=\sin(m\varphi)P_{\mathrm{n}}^{\mathrm{m}}(\cos\theta)z_{\mathrm{n}}(kr) \tag{44b}$$

where $z_{\mathrm{n}}(kr)$ represents spherical Bessel functions of the first, second and third kind and the $P_{\mathrm{n}}^{\mathrm{m}}(\cos\theta)$ are associated Legendre polynomials. By substituting equations (44a) and (44b) into the equations for **M** and **N** the vector spherical harmonics appropriate for the representation of the electromagnetic fields **E** and **H** are derived.

In terms of the spherical harmonics the expansion of the plane wave is given for an arbitrary polarisation by

$$\mathbf{E}_{\mathrm{i}}=\sum_{\mathrm{m}=0}^{\infty}\sum_{\mathrm{n}=\mathrm{m}}^{\infty}\left(B_{\mathrm{emn}}\mathbf{M}_{\mathrm{emn}}+A_{\mathrm{emn}}\mathbf{N}_{\mathrm{emn}}+B_{\mathrm{omn}}\mathbf{M}_{\mathrm{omn}}+A_{\mathrm{omn}}\mathbf{N}_{\mathrm{omn}}\right). \tag{45}$$

The coefficients A and B are determined by considering the orthogonality of the spherical harmonics and applying the restriction that the wave is polarised in the x-direction. The coefficients $A_{\mathrm{omn}} = B_{\mathrm{emn}} = 0$ for all m and n and all coefficients vanish for $\mathrm{m} \neq 1$ leading to

$$\mathbf{E}_{\mathrm{i}}=E_0\sum_{\mathrm{n}=1}^{\infty}\mathrm{i}^{\mathrm{n}}\frac{2n+1}{n(n+1)}\left(\mathbf{M}_{\mathrm{o1n}}^{(1)}-\mathrm{i}\mathbf{N}_{\mathrm{e1n}}^{(1)}\right), \tag{46}$$

where the superscript (1) denotes the incorporation of the Bessel function of the first kind, $j_{\mathrm{n}}(kr)$ into the generating functions ψ_{o1n}. This choice is based on the requirement that the field is finite at the origin. Taking the curl of equation (46) provides the corresponding incident magnetic field,

$$\mathbf{H}_{\mathrm{i}}=-\frac{k_2}{\omega\mu_2}E_0\sum_{\mathrm{n}=1}^{\infty}\mathrm{i}^{\mathrm{n}}\frac{2n+1}{n(n+1)}\left(\mathbf{M}_{\mathrm{e1n}}^{(1)}+\mathrm{i}\mathbf{N}_{\mathrm{o1n}}^{(1)}\right). \tag{47}$$

The incident field expansions used in conjunction with the boundary conditions for **E** and **H** at the boundary of the particle,

$$\left(\mathbf{E}_{\mathrm{i}}+\mathbf{E}_{\mathrm{s}}-\mathbf{E}_1\right)\times\hat{\mathbf{e}}_{\mathrm{r}}=0\,, \tag{48a}$$

$$(\mathbf{H}_{\mathrm{i}} + \mathbf{H}_{\mathrm{s}} - \mathbf{H}_1) \times \hat{\mathbf{e}}_{\mathrm{r}} = 0\,, \tag{48b}$$

generate the following expressions for the scattered fields ($\mathbf{E}_{\mathrm{s}}$,$\mathbf{H}_{\mathrm{s}}$) and the internal fields ($\mathbf{E}_1$,$\mathbf{H}_1$):

$$\mathbf{E}_1 = \sum_{\mathrm{n}=1}^{\infty} E_{\mathrm{n}} \left(c_{\mathrm{n}} \mathbf{M}^{(1)}_{\mathrm{o1n}} - \mathrm{i} d_{\mathrm{n}} \mathbf{N}^{(1)}_{\mathrm{e1n}} \right) \tag{49a}$$

$$\mathbf{H}_1 = -\frac{k_1}{\omega \mu_1} \sum_{\mathrm{n}=1}^{\infty} E_{\mathrm{n}} \left(d_{\mathrm{n}} \mathbf{M}^{(1)}_{\mathrm{e1n}} + \mathrm{i} c_{\mathrm{n}} \mathbf{N}^{(1)}_{\mathrm{o1n}} \right) \tag{49b}$$

$$\mathbf{E}_{\mathrm{s}} = \sum_{\mathrm{n}=1}^{\infty} E_{\mathrm{n}} \left(\mathrm{i} a_{\mathrm{n}} \mathbf{N}^{(3)}_{\mathrm{e1n}} - b_{\mathrm{n}} \mathbf{M}^{(3)}_{\mathrm{o1n}} \right) \tag{50a}$$

$$\mathbf{H}_{\mathrm{s}} = -\frac{k_2}{\omega \mu_2} \sum_{\mathrm{n}=1}^{\infty} E_{\mathrm{n}} \left(\mathrm{i} b_{\mathrm{n}} \mathbf{N}^{(3)}_{\mathrm{o1n}} + a_{\mathrm{n}} \mathbf{M}^{(3)}_{\mathrm{e1n}} \right) \tag{50b}$$

where

$$E_{\mathrm{n}} = \mathrm{i}^{\mathrm{n}} E_0 \frac{2n+1}{n(n+1)}\,, \tag{51}$$

a_{n} and b_{n} are the scattered field coefficients and c_{n} and d_{n} are the internal field coefficients. The superscript (3) in the scattered field equations represents the incorporation of Bessel functions of the third kind. These are linear combinations of the first and second order Bessel functions and are often referred to as *Hankel* functions. The coefficients a_{n} and b_{n} are derived from these functions and are given by

$$a_{\mathrm{n}} = \frac{m\psi_{\mathrm{n}}(mx)\,\psi'_{\mathrm{n}}(x) - \psi_{\mathrm{n}}(x)\,\psi'_{\mathrm{n}}(\mathrm{mx})}{m\psi_{\mathrm{n}}(mx)\,\xi'_{\mathrm{n}}(x) - \xi_{\mathrm{n}}(x)\,\psi'_{\mathrm{n}}(\mathrm{mx})} \tag{52}$$

$$b_{\mathrm{n}} = \frac{\psi_{\mathrm{n}}(mx)\,\psi'_{\mathrm{n}}(x) - m\psi_{\mathrm{n}}(x)\,\psi'_{\mathrm{n}}(\mathrm{mx})}{\psi_{\mathrm{n}}(mx)\,\xi'_{\mathrm{n}}(x) - m\xi_{\mathrm{n}}(x)\,\psi'_{\mathrm{n}}(\mathrm{mx})} \tag{53}$$

where $m = n_1/n_2$ is the relative refractive index (n_1 is the complex refractive index of the particle, n_2 is the refractive index of the surrounding medium), $x = 2\pi n_2 a/\lambda$ (a is the radius of the sphere and λ is the wavelength in vacuo), ψ_{n} and ξ_{n} are the Riccati-Bessel functions and the permeabilities $\mu_1 = \mu_2 = 1$.

With the scattering coefficients a_{n} and b_{n} the extinction and scattering cross-sections for a spherical particle are derived by appealing to the expressions defined in section 2.2. Expanding equations (4) and (5) and incorporating the results into equations (9) and (10) yields the following expressions for the net energy scattered through an arbitrary spherical surface centred at the origin and the net extinction,

$$W_{\mathrm{sca}} = \frac{1}{2}\int_0^{2\pi}\int_0^{\pi}\left(E_{\mathrm{s\theta}}H_{\mathrm{s\varphi}}^{*} - E_{\mathrm{s\varphi}}H_{\mathrm{s\theta}}^{*}\right)r^2 \sin\theta d\theta d\varphi \tag{54}$$

$$W_{\mathrm{ext}} = \frac{1}{2}\int_0^{2\pi}\int_0^{\pi}\left(E_{\mathrm{i\varphi}}H_{\mathrm{s\theta}}^{*} - E_{\mathrm{i\theta}}H_{\mathrm{s\varphi}}^{*} - E_{\mathrm{s\theta}}H_{\mathrm{i\varphi}}^{*} + E_{\mathrm{s\varphi}}H_{\mathrm{i\theta}}^{*}\right)r^2 \sin\theta d\theta d\varphi\,. \tag{55}$$

The next step is to use the calculated electric and magnetic fields to find explicit expressions for the scattering and extinction cross-sections. Substituting these into equations (54) and (55) and evaluating the integrals yields

$$C_{\mathrm{sca}} = \frac{2\pi}{k^2}\sum_{\mathrm{n}=1}^{\infty}(2n+1)(|a_{\mathrm{n}}|^2 + |b_{\mathrm{n}}|^2) \tag{56}$$

$$C_{\mathrm{ext}} = \frac{2\pi}{k^2}\sum_{\mathrm{n}=1}^{\infty}(2n+1)\mathrm{Re}\{a_{\mathrm{n}} + b_{\mathrm{n}}\} \tag{57}$$

where k is the wave vector of the incident plane wave. These expressions can be solved computationally or in certain limiting cases simplified to produce approximate solutions that may provide some insight into the physical behaviour of the particles. One such case is when the particle is small compared to the wavelength of the incident light, x<<1. Expanding the spherical Bessel functions as a power series and considering only those terms of the order x^6 and below results in the following approximations for the scattering and absorption efficiencies,

$$Q_{sca} = \frac{8}{3}x^4\left|\frac{m^2-1}{m^2+2}\right|^2, \tag{58}$$

$$Q_{abs} = 4x\,\mathrm{Im}\left\{\frac{m^2-1}{m^2+2}\right\}. \tag{59}$$

The coefficients a_1, a_2 and b_1 all contain terms up to the order x^6, however equations 58 and 59 stem from the coefficient a_1, the other terms neglected as they become negligible as $x \rightarrow 0$. These results are directly comparable with those derived for the absorption and scattering cross-sections using the quasi-static approximation. This illustrates that in the limit of $a \rightarrow 0$ the scattering problem of Mie theory reduces to that of electrostatic theory.

At this point it is worth emphasizing the limitations imposed given that the particles studied in this thesis are different to those to which the theory applies. Non-spherical particles exhibit very different optical spectra compared to those modelled in Mie theory. In addition the interactions between particles that are often present in samples are completely neglected. However, by using Mie theory it is possible to gain insight into many features in the optical spectra obtained from arbitrarily shaped particles.

2.5 Size Effects

For particles large enough so that there is no significant dependence of the relative permittivity on the size of the particle electrostatic theory predicts that the position of the resonant frequency is independent of size. From equation (25) it is seen that whilst the magnitude of the polarisability is a function of the size of the particle, the resonant frequency is not and is governed only by the condition (30). However, as the dimensions of a particle become comparable with the wavelength of light the position of the LSPR shifts with respect to that predicted by electrostatic theory. A number of factors may contribute to a shift in the resonance position with increasing dimensions. Firstly the particle experiences a retarded field as the incident field is no longer continuous across the particle length (figure 2.5). The inhomogeneous polarisation of the nanoparticle allows the excitation of higher order resonant modes (quadrupole, octupole, etc.) that superpose to produce broad features in optical spectra. Furthermore, the spatial variation leads to an overall depolarisation of the internal fields and a reduction of the associated restoring force. Secondly, electronic screening effects become more important as described by the skin or penetration depth of the electric field within the particle material. An electromagnetic wave impinging on a metal surface will suffer attenuation characterised by the skin depth δ,

$$\delta = \frac{c}{\omega n''} = \frac{\lambda}{2\pi n''} \qquad (60)$$

where c is the speed of light and n'' is the imaginary part of the refractive index. This is the distance into the metal where the field amplitude has decayed to $1/e$ of the value at the surface and for silver has a value of a few tens of nanometres at visible wavelengths. A reduced amplitude of the incident field within the particle results in a reduced polarisation. Thirdly increased radiation damping induces shifts to the resonance position as well as broadening of the resonance peak. The decay time in the absence of radiation is purely determined by

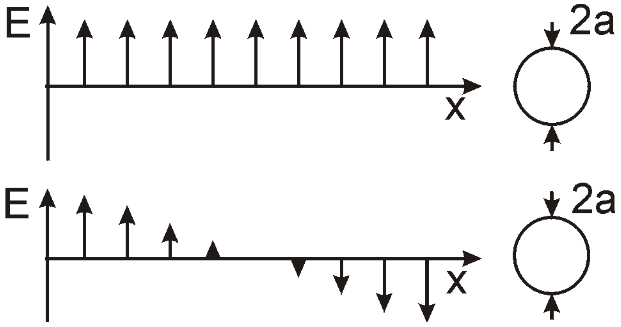

Figure 2.5. Non-retarded incident field (upper diagram) and retarded incident field (lower diagram).

collisional damping. The additional energy loss process of radiation damping leads to an increase in the overall damping and a reduction of the dephasing time of the electron oscillations. Electromagnetic fields produced by the emission of radiation act to depolarise the field induced by the incident wave resulting in a reduction of the eigenfrequency of the system.

The quasi-static approximation can be modified to account for the influence of size effects on the polarisation of the particles. The correction is referred to as the *modified long wavelength approximation* (MLWA) (*Meier (1983))* and results in an altered expression for the dipole moment

$$\mathbf{p} = \alpha\left(\mathbf{E}_0 + \mathbf{E}_{\text{rad}}\right) \qquad (61)$$

where $\mathbf{E}_0$ is the incident field and $\mathbf{E}_{\text{rad}}$ is the radiative correction field given by

$$\mathbf{E}_{\text{rad}} = \frac{2}{3}\mathrm{i}k_0^{\,3}\mathbf{p} + \frac{k_0^{\,2}}{a}\mathbf{p} \qquad (62)$$

with the free-space wave vector $k_0 = \omega/c$. The first term arises from the radiative damping of the free-electron oscillations and the second term from the retardation of the radiated electric field. The approximation completely neglects multipole contributions but accurately describes dipolar resonances on particles with radii ranging from 10 nm to 100 nm (*Gunnarsson (2003)*).

Figure 2.6 displays results from calculations using Mie theory of the extinction cross-sections (a) and efficiencies (b) of silver spherical particles with radii ranging from 10 nm to 90 nm using the Drude model. The code used was adapted from the BHMIE code, as published in *Bohren and Huffman (1983)*, with input parameters of n_1 and n_2, the refractive indices of the particle material and external material, wavelength λ and radius a. For small particles a single

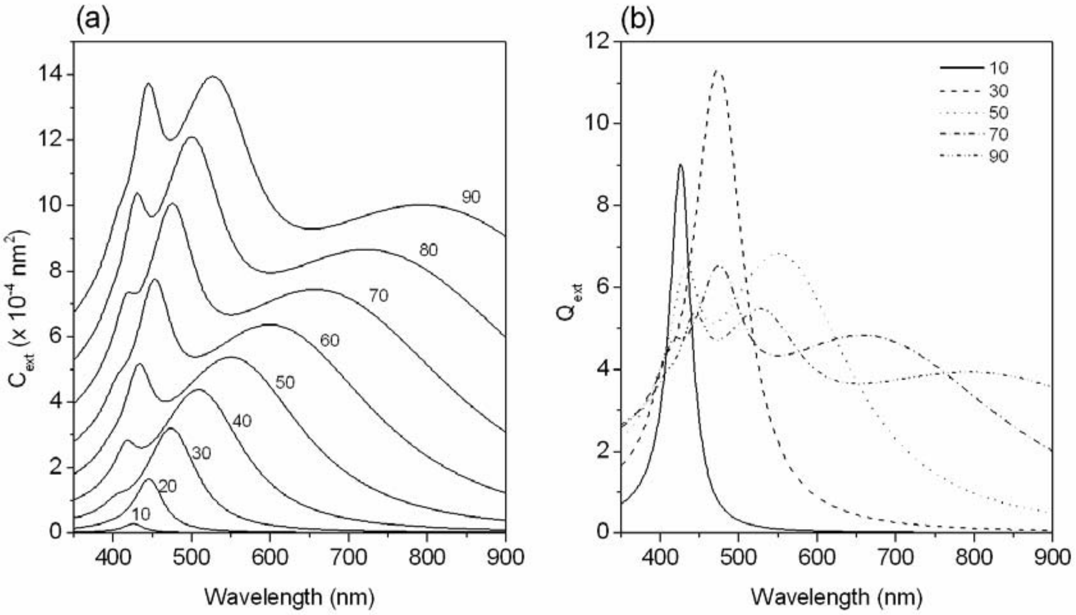

Figure 2.6. Mie theory calculations of the extinction cross-section (a) and extinction efficiency (b) of spherical silver particles with radii ranging from 10 nm to 90 nm (code adapted from *Bohren and Huffman (1983)*). The refractive index of the external medium n_2 = 1.55.

resonance is observed at a frequency approaching that of the LSPR predicted by the quasi-static approximation. As the particle size is increased the resonance position is red-shifted and the band- width increased with respect to the small particles. Higher-order modes become significant in the spectra beginning with the onset of the quadrupole mode observed as a shoulder at ~400 nm in the spectra from the 30 nm radius particle. Further size increases result in an increased prominence of the quadrupole mode and a substantial broadening and reduction in relative amplitude of the dipole resonance. The data for a 90 nm radius particle indicate four resonances with the dipole resonance almost completely smeared out and the quadrupole and octupole resonances similar in amplitude.

The results shown for spherical particles show many of the effects present in particles of arbitrary shape. The limitation is in the fact that isolating the separate size-dependent processes introduced earlier in this section is not possible since an increase in radius of a sphere leads to identical size increases in all directions. For a plane wave incident on a thin disk and propagating parallel to the axis of symmetry of the particle retardation effects due to the incident field may be neglected. However, a shift in the position of the resonance may still be expected due to increased radiation damping since this is dominated by the size of the particle parallel to the transverse incident fields and perpendicular to the direction of propagation.

For large particles the relative permittivity of the metal does not deviate significantly from that of the bulk material. However, for small particles with a radius R of a few nanometres the relative permittivity is not only a function of frequency but also of size; $\varepsilon(\omega)$ becomes $\varepsilon(\omega,R)$. The dominant mechanism that induces the deviation from bulk properties is from the limitation of the mean free path of the conduction electrons [*Kreibig (1974)*]. This equates to an increase in the Drude model damping coefficient Γ given by

$$\Gamma(R) = \Gamma_{\infty} + \Delta\Gamma(R) = \Gamma_{\infty} + A\frac{v_{\mathrm{F}}}{R} \tag{63}$$

where Γ_{∞} is the collision frequency of the bulk material and $\Delta\Gamma(R)$ is the additional surface scattering term. The parameter A is of the order of 1 and is dependent upon theoretical considerations. The Fermi velocity v_{F} is included via the assumption that it is only electrons near to the Fermi energy that contribute. The effect this has on the relative permittivity is to increase both the real imaginary parts relative to the bulk values as size is decreased. A less negative real part leads to a small red-shift with decreasing size; however the more obvious effect is an increased bandwidth and reduced amplitude of the resonance from the increased imaginary part. As $R \to 0$ the surface term becomes the dominant factor in determining the collisional damping; additional contributions from a quantisation of the energy eigenstates become influential as the size approaches the atomic scale.

2.6 Non-spherical particles - shape effects

Mie theory gives an exact solution to the problem of scattering, absorption and extinction of homogeneous spherical particles of arbitrary size and composition. Extending the original formulation to tackle non-spherical particle geometries is limited and in general may only be applied to particles with a shape described in coordinate systems that allow separable solutions to the wave equation. Alternative theories and modelling techniques exist for particles of arbitrary shape. The discrete dipole approximation (*Purcell and Pennypacker (1973)*) divides the particle into an array of elements small enough to be described as dipole oscillators. Each is assigned with a dipole moment calculated by accounting for the combined effect of the incident field and the fields generated by all other elements in the array. Summing all of the individual contributions gives the total scattered field and from this the various cross-sections and efficiencies. Other discretisation methods use either finite difference or finite element computational techniques. The finite difference time domain (FDTD) method is applied widely to electrodynamic scattering problems involving complex geometrical systems (see review by *Taflove (2000)*). *Köttmann and Martin (2000)* have modelled the response from metallic two-dimensional shapes using a finite element method. The scattering spectra from triangular nanowires showed multiple resonance features and high local field enhancements in particular when the symmetry of the section is reduced.

As with spherical particles, simplifications are possible when a non-spherical particle is much smaller than the wavelength of the incident radiation. In the quasi-static limit electrostatic theory may be applied in much the same manner as for a spherical particle. Solutions are found to the Laplace equation by applying boundary conditions provided the particle shape can be described in an appropriate coordinate system. Solutions exist for an ellipsoidal particle with semi-axes a, b, c where $a > b > c$, aligned along orthogonal x, y and z-axes respectively [see for example *Bohren and Huffman (1983)*]. With the centre of the ellipsoid at the origin the surface of the ellipsoid is then defined by

$$\frac{x^2}{a^2} + \frac{y^2}{b^2} + \frac{z^2}{c^2} = 1. \tag{64}$$

Ellipsoidal coordinates (ξ, η, ζ) are used in approaching the specific problem of determining the dipole moment of an ellipsoidal particle in the quasi-static field approximation and are defined by

$$\frac{x^2}{a^2+\xi} + \frac{y^2}{b^2+\xi} + \frac{z^2}{c^2+\xi} = 1, \qquad -c^2 < \xi < \infty \tag{65}$$

$$\frac{x^2}{a^2+\eta} + \frac{y^2}{b^2+\eta} + \frac{z^2}{c^2+\eta} = 1, \qquad -b^2 < \eta < -c^2 \tag{66}$$

$$\frac{x^2}{a^2+\zeta} + \frac{y^2}{b^2+\zeta} + \frac{z^2}{c^2+\zeta} = 1, \qquad -a^2 < \zeta < -b^2. \tag{67}$$

Any point (x, y, z) corresponds to a specific set of ellipsoidal coordinates (ξ, η, ζ); however the coordinates (ξ, η, ζ) do not specify a single point (x, y, z), rather eight points corresponding to symmetric points in each of the eight octants of the x, y and z-axes. Rearranging equations (65)-(67) results in the following expressions for x, y and z in terms of the semi-axes and the ellipsoidal coordinates,

$$x^2 = \frac{\left(a^2+\xi\right)\left(a^2+\eta\right)\left(a^2+\zeta\right)}{\left(b^2-a^2\right)\left(c^2-a^2\right)}, \tag{68}$$

$$y^2 = \frac{\left(b^2+\xi\right)\left(b^2+\eta\right)\left(b^2+\zeta\right)}{\left(a^2-b^2\right)\left(c^2-b^2\right)}, \tag{69}$$

$$z^2 = \frac{\left(c^2+\xi\right)\left(c^2+\eta\right)\left(c^2+\zeta\right)}{\left(a^2-c^2\right)\left(b^2-c^2\right)}. \tag{70}$$

For a homogeneous ellipsoid in a uniform electrostatic field aligned along the z-axis it is possible to apply symmetry conditions to reduce the number of non-degenerate values a given set of ellipsoidal coordinates defines in Cartesian space. In this case the potential has the symmetry properties

$$\varphi(x,\ y,\ z)=\varphi(-x,\ y,\ z)=\varphi(x,\ -y,\ z)=\varphi(-x,\ -y,\ z), \tag{71}$$

$$\varphi(x,\ y,\ -z)=\varphi(-x,\ y,\ -z)=\varphi(x,\ -y,\ -z)=\varphi(-x,\ -y,\ -z), \tag{72}$$

where x, y, and z are positive. Therefore it is only necessary to calculate the potential in two octants, one with positive z, one with negative z.

The aim is to develop an expression for the polarisability of the particle in much the same way as for the sphere. There are three separate potentials to consider in the system as a whole, that within the ellipsoid φ_1, that due to the incident field φ_0 and that due to presence of the particle φ_p. Outside of the sphere the total potential φ_2 is the sum of φ_0 and φ_p. The incident electric field is again defined as being parallel to the z-axis resulting in the following expression for the incident potential

$$\varphi_0 = -E_0 z = -E_0\left[\frac{\left(c^2+\xi\right)\left(c^2+\eta\right)\left(c^2+\zeta\right)}{\left(a^2-c^2\right)\left(b^2-c^2\right)}\right]^{1/2}. \tag{73}$$

At large distances from the particle φ_p is negligible compared to φ_0 requiring that

$$\lim_{\xi\to\infty}\varphi_\mathrm{p} = 0. \tag{74}$$

Further conditions are that the potential is continuous across the surface of the particle,

$$\varphi_1(0,\eta,\zeta) = \varphi_0(0,\eta,\zeta) + \varphi_p(0,\eta,\zeta) \tag{75}$$

and that the normal component of **D** is also continuous across the surface of the particle,

$$\varepsilon_1 \frac{\partial \varphi_1}{\partial \xi} = \varepsilon_2 \frac{\partial \varphi_0}{\partial \xi} + \varepsilon_2 \frac{\partial \varphi_p}{\partial \xi}. \tag{76}$$

It is then a case of solving the Laplace equation $\nabla^2 \varphi = 0$ in elliptical coordinates inside and outside the particle by assuming separable solutions for φ_1 and φ_p of the same form as φ_0. Applying the boundary conditions stated above leads to the following expressions:

$$\varphi_1 = \frac{\varphi_0}{1 + \frac{L_c(\varepsilon_1 - \varepsilon_2)}{\varepsilon_2}},$$

$$\varphi_p = \varphi_0 \frac{\frac{abc}{2}\frac{\varepsilon_1 - \varepsilon_2}{\varepsilon_2}\int_\xi^\infty \frac{dq}{(c^2+q)f(q)}}{1 + \frac{L_c(\varepsilon_1 - \varepsilon_2)}{\varepsilon_2}}, \tag{77}$$

where L_c, the geometrical or shape factor is given as

$$L_c = \frac{abc}{2}\int_0^\infty \frac{dq}{(c^2+q)f(q)} \tag{78}$$

and $f(q) = \{(q + a^2)(q + b^{2)} (q + c^2)\}^{1/2}$. At large distances from the origin the integral in equation (77) may be solved approximately yielding the potential φ_p:

$$\varphi_p \sim \frac{E_0 \cos\theta}{r^2} \frac{\frac{abc}{2}\frac{(\varepsilon_1 - \varepsilon_2)}{\varepsilon_2}}{1 + \frac{L_c(\varepsilon_1 - \varepsilon_2)}{\varepsilon_2}}, \quad (r >> a,b,c), \tag{79}$$

which is similar to equation (24) and is the potential of a dipole with moment

$$\mathbf{p} = \frac{4}{3}\pi abc \frac{\varepsilon_1 - \varepsilon_2}{\varepsilon_2 + L_c(\varepsilon_1 - \varepsilon_2)} \varepsilon_2 \mathbf{E}_0. \tag{80}$$

It is now possible to define the polarisability α_c of the particle along the z-axis as for a spherical particle,

$$\alpha_c = V \frac{\varepsilon_1 - \varepsilon_2}{\varepsilon_2 + L_c(\varepsilon_1 - \varepsilon_2)}, \tag{81}$$

where $V = 4\pi abc/3$ is the volume of the particle. Similar expressions exist for the polarisablity and geometrical factors associated with the other principal axes when the incident electric field is so aligned. For a sphere $a = b = c$, $L_a = L_b = L_c$ and

$$L = \frac{a^3}{2}\int_0^\infty \frac{dq}{\left(a^2 + q\right)^{5/2}} = \frac{1}{3}, \tag{82}$$

leading to the polarisability for a sphere as derived in equation (25). In terms of the shape factor the resonance condition and resonant frequency of an ellipsoidal particle are defined as

$$\varepsilon_1'(\omega) = -\varepsilon_2 \frac{1 - L_\mathrm{i}}{L_\mathrm{i}}, \quad i = a,b,c \quad \text{and} \tag{83}$$

$$\omega_\mathrm{LSP} = \frac{\omega_\mathrm{P}}{\sqrt{1 + \varepsilon_2\left(\frac{1 - L_\mathrm{i}}{\mathrm{L_i}}\right)}} \tag{84}$$

reducing in air/vacuum to

$$\omega_\mathrm{LSP} = \omega_\mathrm{P}\sqrt{L_i}\,. \tag{85}$$

In the quasi-static limit ellipsoidal particles have three distinct plasmon resonances. Whether these are excited or not depends on the polarisation of the incident light and the orientation of the particle relative to the incident radiation. Only one resonance will be observed in extinction spectra if the light is polarised in such a way that it is parallel to one of the principal axes and perpendicular to the other two. Figure 2.7(a) shows how ω_LSP (plotted as the ratio to ω_P and calculated using equation (84)) varies as a function of the shape factor L for ε_2 = 1 to 5. This illustrates the wide range of resonant frequencies possible for non-spherical particles, from $\omega = 0$ up to the plasma frequency $\omega = \omega_\mathrm{p}$

Ellipsoidal particles with two principal axes of the same length are known as spheroids. Rotation of the ellipse about the major axis generates a *prolate* spheroid and rotation about the minor axis generates an *oblate* spheroid. If the axis of rotation is defined as a then for $a > b = c$ the spheroid is cigar-shaped (*prolate* – a is the major axis) and for $a = b > c$ the spheroid is disk-shaped (*oblate* – a and b are the major axes). The functional forms of the shape factors associated with the principal axes are then given by

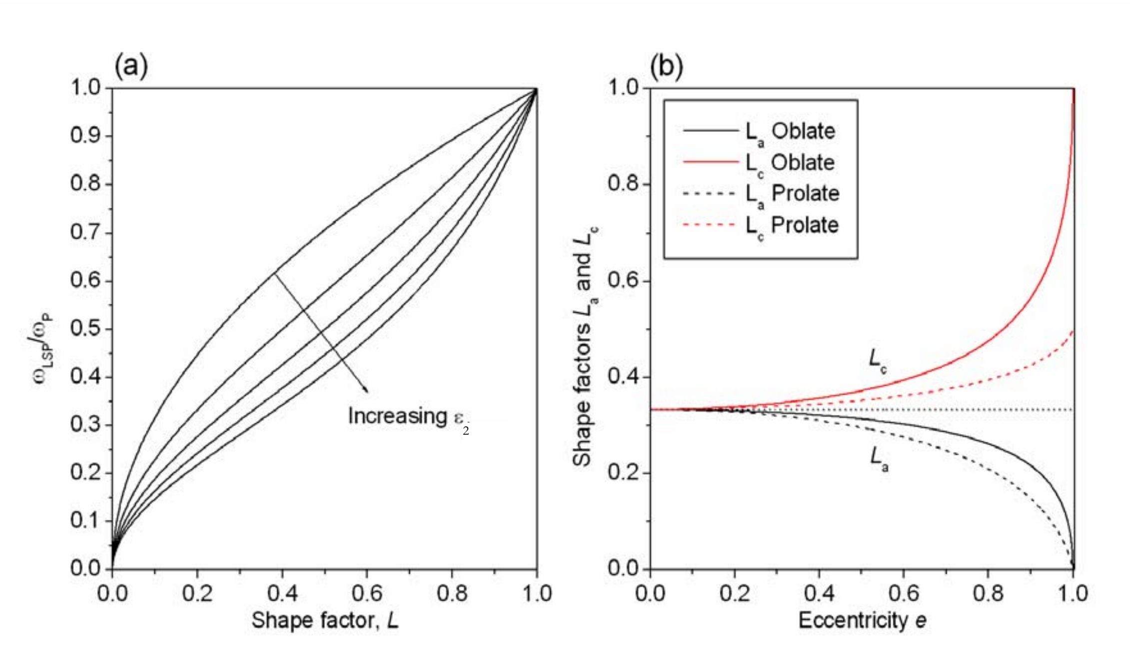

Figure 2.7. (a) Ratio of LSPR frequency associated with ellipsoidal particles ω_{LSP} to the plasma frequency ω_P as a function of shape factor L for relative permittivities of the external medium increasing from ε_2 = 1 to 5 (calculated using equation (84). (b) Shape factors L_a and L_c associated with oblate ($L_a = L_b$) and prolate spheroids ($L_b = L_c$) as a function of eccentricity e (calculated using equations (86)-(89)). The dotted line is at L_i = 1/3, the shape factor of a sphere.

$$L_a = \frac{1-e^2}{e^2}\left(-1+\frac{1}{2e}\ln\left(\frac{1+e}{1-e}\right)\right), \tag{86}$$

for prolate spheroids where the *eccentricity* e is a measure of the distortion relative to a sphere,

$$e = \sqrt{\left(1-{}^{c^2}\!\!/_{a^2}\right)} \tag{87}$$

and

$$L_a = \frac{g(e)}{2e^2}\left(\frac{\pi}{2}-\tan^{-1}g(e)\right)-\frac{g^2(e)}{2} \tag{88}$$

for oblate spheroids where

$$g(e) = \left(\frac{1-e^2}{e^2}\right)^{1/2}. \tag{89}$$

The minor axes then follow from the sum-rule $L_a + L_b + L_c = 1$. The shape factors L_a and L_c associated with oblate ($L_a = L_b$) and prolate spheroids ($L_b = L_c$) are illustrated in figure 2.7(b) as a function of the eccentricity. The intersection at e =

0, L_i = 1/3 is the point that represents a sphere and a dotted line is projected across the figure to illustrate the deviation in the L_i as eccentricity (and therefore aspect ratio (= a/c)) is increased. A reduction in the shape factor relative to the sphere equates to a *red*-shift of the associated LSPR and an increase in the shape factor equates to a *blue*-shift of the associated LSPR.

Particles formed on solid supports are often approximated as oblate spheroids and have been studied extensively due to the relative ease with which samples are fabricated. *Warmack (1986)* observed two surface plasmon resonances on gold particles formed in this way, one associated with the axis perpendicular to the surface and one associated with the axis parallel to the substrate. Angular deposition onto roughened surfaces and subsequent annealing has also been used to form arrays of particles approximated as prolate spheroids (*Bloemer (1988)*). Again two plasmon resonances were observed on gold particles associated with the major and minor axes. More recently, *Link (1999)* observed the absorbance spectra of rod-shaped particles formed in colloidal solutions with similar, but more pronounced and sharper features due to a narrower size and shape distribution.

Recent advances in fabrication technology have enabled the study of more exotic particle shapes. *Mock et al. (2002)* synthesized colloidal silver particles with a variety of shapes and sizes. They were able to locate and measure the extinction spectra of individual triangular, pentagonal and spherical particles and correlate the extinction maximum with the size and shape. Spherical particles exhibit peak extinction towards the blue, similarly sized pentagonal particles in the mid-visible range and triangular particles towards the red end of the spectrum. The red-shift of triangular particles relative to those with spherical symmetry was also observed by *Jin (2001)* during a photo-induced shape transition of spherical colloidal silver particles. *Krenn et al. (2000)* have fabricated elongated silver particles by electron beam lithography and excited multipolar plasmon modes along their long axes.

2.7 Periodic arrays of particles and particle interactions

Already the effects of size and shape on the resonance features obtained from metallic particles have been discussed; also of importance are the influence inter-particle interactions have on the properties of extinction, scattering and absorption. The reaction of individual nanoparticles to an electromagnetic field when in close proximity to other nanoparticles is markedly different to that of isolated individual nanoparticles. In the near-field Coulombic forces exist between adjacent nanoparticles inducing shifts in the position and changes in the width of the LSPR of metallic nanoparticles. In addition, far-field radiative coupling between particles may also influence the LSPR. A problem in the interpretation of optical spectra is that often samples consist of many particles randomly distributed with a variety of shapes and sizes. A solution is to produce regularly spaced arrays of particles with a consistent size and shape as these will respond in self-similar ways to an incident electromagnetic field. Early experiments by *Craighead and Niklasson (1984)* utilised electron beam lithography (EBL) to fabricate gold nanoparticle arrays with narrow size distributions across areas sufficient to allow investigation of the optical properties using conventional characterisation techniques. Recent advances in spectroscopic methods have allowed the investigation of single particles and particle pairs. *Tamaru (2002)* recently demonstrated distinct differences in the optical spectra obtained from pairs of almost touching colloidal spherical silver nanoparticles compared with single spherical particles of a comparable size. Further, anisotropy in the optical spectra was obtained from the nanoparticle pair when light was polarised parallel and perpendicular to the inter-particle axis. A more comprehensive analysis was conducted by *Rechberger (2003)* who investigated the near-field interactions between particle pairs of varying separation, this time fabricated by EBL. They found that the LSPR red-shifted with decreasing particle separation when the incident light was polarised parallel to the inter-particle axis, where as a blue-shift was measured with decreasing particle separation for incident light polarised in the orthogonal direction. These observations were qualitatively explained by considering the LSPRs of each particle as coupled dipole oscillators. With the incident electric field directed parallel to the inter-particle axis an attractive force exists between the particle pair that acts in the opposite direction to the restoring force within the particle. This results in a weakening of the resultant force acting to restore the neutral state of the particle and corresponds to a decrease in the resonant frequency of the particles. Conversely, with the incident electric field directed perpendicular to the inter-particle axis the electric fields generated by the individual nanoparticles act cooperatively. The restoring force within the nanoparticles is increased accompanied by an increase in the resonant frequency of the particles. Similar work has been carried out by *Gunnarsson (2003)* who collected dark-field scattering spectra from individual particles and particle pairs. The polarisation dependence of the spectra described above was observed and modelled using both the coupled dipole approximation (CDA) [*Zhao (2003)*] and discrete dipole approximation (DDA). Good agreement was found using both methods for surface separations down to 20 nm. Below this value the CDA no longer agreed with the data and it was surmised that this was due to the contribution of short-range multipolar fields and the onset of finite size effects (the CDA models the particle as a point dipole). In addition overlapped particles were examined and found to exhibit very large shifts in the resonance compared to a single particle. Comparing the position of the resonance to that measured experimentally for an ellipsoid with similar dimensions [*Krenn (2000)*] yielded good agreement. A further feature is the appearance of a quadrupole mode towards the blue end of the spectrum that red-shifts with increasing size again in agreement with the results of *Krenn (2000)*. In a theoretical study *Kottmann (2001)* calculated the scattering cross-sections of pairs of cylinders with a diameter d varied from 20 nm to 100 nm and separation a scaled as $d/a = 5$ with light polarised as above. As the particle size was increased an additional mode appeared in the scattering cross-section spectra attributed by the authors to coupled LSPRs driven out of phase with one another. This also red-shifted with increasing diameter and separation scaled appropriately. The interaction between the LSPRs of neighbouring particles has also been observed in experiments by *Maier (2001, 2002)* in which a linear chain of closely spaced nanoparticles are illuminated with light polarised parallel and perpendicular to the chain. The spectra from light incident with a parallel polarisation indicate a red-shift in the position of the LSPR relative to the resonance of an isolated nanoparticle where as for the perpendicular polarisation a blue-shift is observed. The interactions are sufficient to allow the propagation of a surface plasmon wave along the chain at a maximum velocity of 0.1c. Unfortunately the large damping associated with the wave (24 dB/μm) imposes limitations upon the applicability of particle chains in photonic devices.

Describing the optical response from large two-dimensional periodic arrays is complicated by the need to account for the coherency in the phase relationship between the light scattered from individual particles. *Meier (1985)* studied theoretically the collective behaviour of nanoparticles arranged in a square grating. They found particularly strong dipolar interactions to occur when the LSPR coincided in frequency with a grazing diffracted order. At this frequency the optical fields generated at and by each particle in the array were in-phase yielding strong interactions between the particles. A further effect is that with the onset of propagating diffracted orders the radiative damping is increased and therefore the dephasing time will decrease substantially. This behaviour was observed by *Lamprecht (2000)* in experiments designed to investigate the influence of the grating period on the LSPR of disk-shaped gold particles. Maximum dephasing time was observed when the LSPR was excited by radiation that produced no propagating diffracted orders. Moreover, this maximum was just below the critical edge, the frequency at which a diffracted order becomes grazing with the plane of the substrate. A red-shift in the frequency of the resonance was observed when the LSPR coincided with a grazing diffracted order. A similar dependency of the LSPR frequency on grating period was observed by *Haynes (2003a)* for particles of a variety of shapes.

2.8 Dielectric overlayers and substrate effects

The influence exerted by the external environment has a profound effect on the optical properties of metal nanoparticles. In the dipole approximation for a sphere, an increase in the relative permittivity of the dielectric medium results in a red-shift of the LSPR as dictated by the resonance condition, equation (31). This behaviour is illustrated in figure 2.8(a) where Mie theory calculations of the extinction cross-sections for a silver particle with a 30 nm radius embedded in non-absorbing media with refractive index varied from 1.0 to 2.0 are shown. Several effects can be seen the most obvious being the shift to longer wavelengths of the dipole mode, as expected. The linewidth also increases in part due to the rise in the imaginary part of the relative permittivity. Increased radiative damping and retardation due to a shorter wavelength of the incident radiation in higher index media will also result in an increased linewidth. A further observation is the development of the quadrupole mode. Its position appears to be less influenced by changes to the external environment with a smaller shift allowing the mode to become more distinct from the dipole mode. The shift to longer wavelengths of the dipole mode is linear and equates to 200 nm/RIU (refractive index unit) (figure 2.8(b)).

Other particle shapes have been shown to exhibit a similar dependence on the refractive index. *Hanarp (2003)* fabricated gold nanodisks with aspect ratios = *a*/*c* (*c* = 20 nm) of 1, 3.5 and 7 and observed the wavelength shift of the long-axis LSPR as a function of the refractive index. The sensitivity was found to increase with aspect ratio and good agreement was shown with electrostatic theory corrected for radiation damping. A similar dependence was observed by *Jensen (1999a)* from arrays of triangular particles formed by nanosphere lithography.

The sensitivity of the LSPR to changes in the external environment has encouraged research into sensing applications (*Haes (2002)*). If a thin layer of material is deposited onto a particle supported on a substrate the decaying field extending through the layer samples material with a different refractive index compared to the uncoated particle inducing a shift in the position of the

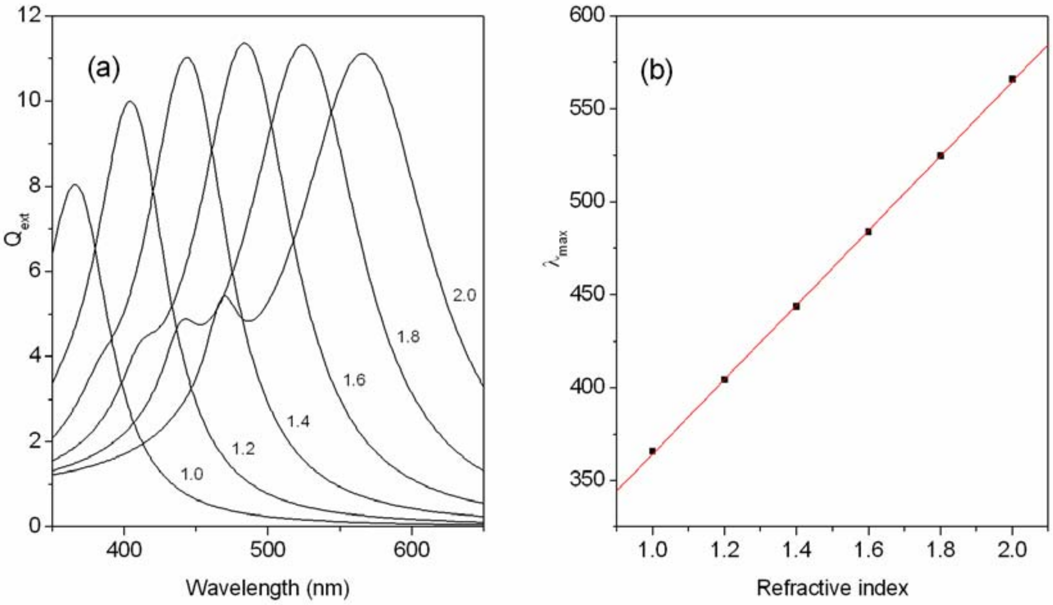

Figure 2.8. (a) Extinction efficiency as a function of wavelength for silver particles with a 20 nm radius embedded in media with refractive index *n* = 1.0 to *n* = 2.0 (code adapted from BHMIE (*Bohren and Huffman (1983)*)). (b) Maximum extinction as a function of refractive index; the line is a linear fit with gradient 200 nm/RIU.

resonance. If the thickness of the layer coating the particle is increased more of the particle's electromagnetic field samples the material and further shifts are induced. For a thickness greater than the decay length of the LSPR the field is contained entirely within the coating material and the shift in position of the resonance is expected to approach an asymptotic value. This has been observed by *Haes et al. (2004a)* who monitored the resonance position as successive layers of a self-assembled monolayer (SAM – refractive index n ~ 1.5-1.6) were attached to Ag and Au particles formed by nanosphere lithography. The average thickness of each successive layer was 1.4 nm for the Au particles and 1.6 nm for the Ag particles. Normal incidence extinction measurements were performed on single samples after each layer was added and the dipolar-type extinction peak position (λ_{LSP}) monitored. The maximum thickness was ~30 nm corresponding to upwards of 20 layers. The λ_{max} was observed to red-shift and approach saturation with a relative shift $\Delta\lambda$ ~ 120 nm. Other investigations have focussed on the LSPR response to the adsorption of single layers of SAM molecules with varying chain length [*Duval-Malinsky (2001)*], how changing particle size, shape and composition alters the near-field sensitivity of the LSPR [*Haes (2004b)*] and the effect of immersing substrate supported nanoparticles in bulk solvents *[Meriaudeau (1998)].*

For particles supported by a substrate the electromagnetic field associated with the LSPR samples regions of differing relative permittivity. *Duval-Malinsky (2001)* conducted experiments on nanosphere lithography derived triangular particles on a number of substrates with refractive indices ranging from 1.46 to 1.73. In this range a peak-shift sensitivity of 87 nm/RIU was observed. An average permittivity (effective medium) may be used to describe the external environment for similar materials [*Gotschy (1996)*]. However, more advanced descriptions are required if the underlying substrate is able to support propagating modes. *Felidj (2002)* proposed SPP mediated coupling between gold particles deposited on a planar gold substrate. The particles are arranged in a periodic array that couples incident light into the SPP mode via grating-coupling. The propagating SPP is then able to excite LSPRs in distant particles. *Linden (2001)* observed suppressed extinction of the LSPR when waveguide modes were excited in an underlying indium tin oxide layer. Stratified media with interfaces close to the particle may also complicate the response due to reflected incident and scattered fields. Chapter 5 describes experiments in which aligned fatty acid molecular monolayers with a well-prescribed thickness are deposited across arrays of triangular nanoparticles. In this case contributions from the reflected fields from the interfaces and scattered fields from the particles play an important role in altering the shape and position of the LSPR.

2.9 Summary

This chapter has described the behaviour of metallic nanoparticles when subjected to an oscillating incident electromagnetic field. The quasi-static approximation in which a spatially homogeneous but time-varying field is applied to a particle was used to identify the fundamental optical resonance associated with noble and alkali metals as a dipole oscillation of the free-electron plasma. Mie theory was introduced to illustrate the importance of retardation and radiative damping on the optical response from particles too large to be considered in the quasi-static approximation. The excitation of multipolar modes and frequency shifts and broadening of the LSPR modes was shown to occur as particle size was increased. Inter-particle interactions and the effect of coherent scattering of light from periodic arrays of particles was discussed. The extinction of particles embedded in media with different refractive indices was compared and a red-shift of the resonant wavelength calculated for 30 nm radius particles. Finally, the effect of the substrate, in particular when able to support propagating electromagnetic surface modes, was introduced.

Chapter 3

Optical response of extended metallic surfaces

3.1 Introduction

In the previous chapter the concept of a surface mode that exists on a metallic particle typically of the order of and smaller than the wavelength of the incident radiation was discussed. The *localised* surface plasmon resonance (LSPR) was introduced as a resonant oscillation of the conduction electrons with the resonant frequency determined mainly by the charge developed at the surface. A second type of surface mode may be identified if one considers a *semi-infinite* planar interface between a metal and a dielectric. The confinement of charge at the boundary between the dielectric and the metal can result in a resonant longitudinal oscillation of the conduction electrons at a different eigenfrequency to that for a three-dimensionally restricted surface. With the development of the free electron theory of metals the mode became known as the *surface plasmon* (SP) [*Ritchie (1957)*] and is excited at the surface plasmon frequency ω_{SP},

$$\omega_{\mathrm{SP}} = \frac{\omega_{\mathrm{P}}}{\sqrt{1+\varepsilon_{\mathrm{r2}}}} = \frac{\omega_{\mathrm{P}}}{\sqrt{2}} \quad \left(\varepsilon_{\mathrm{r2}} = 1\right) \tag{1}$$

where the plasma frequency ω_{P} and the relative permittivity of the dielectric $\varepsilon_{\mathrm{r2}}$ are as defined previously (Chap. 1). Evidence for the existence of the SP mode was reported from electron energy loss experiments by *Powell (1960)*. Electrons impinging from a vacuum onto magnesium and aluminium foils were found to exhibit a peak in energy loss spectra corresponding to $\hbar\omega_{\mathrm{P}}/\sqrt{2}$. Upon oxidation of the foil surfaces the associated peaks were observed to decrease in intensity with a new peak emerging at a lower energy loss. This illustrated the sensitivity of the mode to the surface chemistry thus providing conclusive proof for the existence of the SP mode.

Associated with the SP mode is a dispersion relation relating the frequency ω of the oscillation with its wave vector k_{SP}. For typical values of the wave vector of the SP mode excited with electrons the frequency is close to the surface plasmon frequency. However, for small SP wave vectors, not resolved by electron energy loss spectra and therefore excited by other means, the frequency approaches $\omega = 0$. Rather than an oscillating plasmon mode generated at the surface, a propagating plasmon wave is excited. The concept of such a wave propagating at the interface between a metal and a dielectric was first proposed by *Fano (1941)* to explain the observations by *Wood (1902)* of regions of low intensity in wavelength dependent reflectivity data on ruled metallic gratings. The wave became known as the surface plasmon-*polariton* (SPP) to emphasise the wave-like nature opposed to the purely oscillatory nature of the SP mode. It is the excitation and behaviour of the SPP propagating on thin silver films that is the focus of this chapter.

3.2 Surface plasmon-polariton

Consider the interface between two isotropic, semi-infinite, planar media. Light incident upon the interface at some angle θ_i may be broken down into components of the oscillating electric and magnetic fields that are parallel and perpendicular to the plane of incidence (defined as the plane perpendicular to the interface containing the incident and reflected wave vectors). If the light is polarised such that the electric field vector is parallel to the plane of incidence and the orthogonal magnetic field is perpendicular to the plane of incidence the light is *p*-polarised. Alternatively it may be referred to as transverse magnetic (TM) polarised as the magnetic field oscillates tangentially to the interface. The opposite case where the magnetic field vector is parallel to the plane of incidence and the electric field perpendicular to the plane of incidence is referred to as *s*-polarised light or transverse electric (TE).

If the materials are assumed to be non-magnetic (meaning that $\mu = \mu_0$) the incident magnetic field does not see a boundary as the light crosses the interface. Therefore the influence on the radiation of the abrupt discontinuity in the material properties at the interface is governed by the dielectric permittivity of the media. It may be shown from Maxwell's equations that to satisfy the boundary conditions at the interface the normal component of the displacement field **D** must be continuous across the interface. With this in mind one can see from the constitutive relation

$$\mathbf{D} = \varepsilon \mathbf{E}, \tag{2}$$

where **E** is the electric field and ε is the permittivity of the medium, that if the sign of the real part of ε changes across the interface then the normal component of the electric field must change direction across the interface. This may be satisfied in the visible regime for a metal-dielectric interface where the dielectric has a positive valued ε' and the metal has a negative valued ε'. The discontinuity in the normal component of the electric field traps charge at the interface. If the electric field is directed away from the interface into the bounding media then negative charge (electrons) will collect at the interface. If the electric field is directed towards the interface in the bounding media then positive charge (nuclei) will be created at the interface as the more mobile electrons will be forced away. If the incident field is time varying then the induced charge distribution is also time varying. An electromagnetic wave incident on a planar surface can therefore induce polarisation charge oscillations provided there is a component of the electric field normal to the interface. Such a condition is satisfied for light that is TM polarised. Light that is TE polarised has the electric field vector oriented perpendicularly to the plane of incidence (parallel to the interface) and the magnetic field vector parallel to the plane of incidence and as such does not couple to the SPP mode on a planar surface.

3.3 Dispersion relation

Consider now the TM wave illustrated in figure 3.1 incident from a dielectric with relative permittivity ε_{r2} onto a metal with dielectric permittivity ε_{r1}[1]. The incident field $\left(\mathbf{E}_2^-, \mathbf{H}_2^-\right)$ produces a reflected field $\left(\mathbf{E}_2^+, \mathbf{H}_2^+\right)$ and transmitted field $\left(\mathbf{E}_1^-, \mathbf{H}_1^-\right)$. The waves propagate in the *x*-*z* plane and are invariant in the *y*-direction. The SPP mode is non-radiative on a planar surface (this is not the case for a periodically modulated surface – more later) and therefore only a single electromagnetic wave need exist in each medium to provide a solution to Maxwell's equations. Arbitrarily this allows one of the fields in the dielectric

---

[1] The following derivation is from *Raether (1988)*.

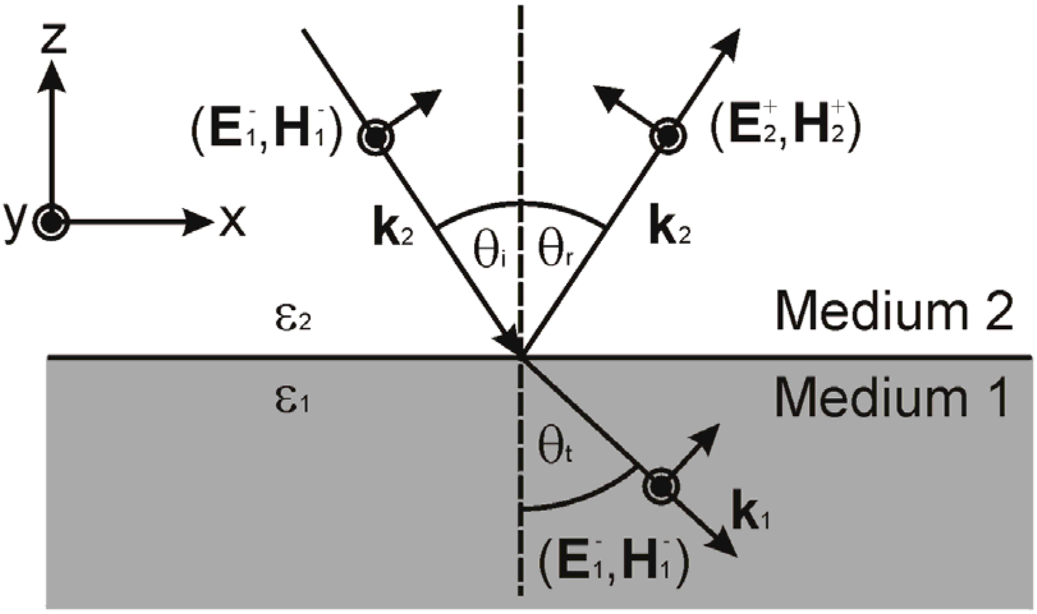

Figure 3.1. A schematic diagram of light with incident wavevector $\mathbf{k}_2$ incident on an interface bounded by two media described by complex permittivities ε_1 and ε_2.

upper half-space to be set to zero. The incident field is chosen to be zero resulting in the following field equations for the reflected and transmitted fields:

$$\mathbf{E}_1 = [E_{x1}, 0, E_{z1}]\exp[\mathrm{i}(k_x x - k_{z1} z - \omega t)] \tag{3}$$

$$\mathbf{H}_1 = [0, H_{y1}, 0]\exp[\mathrm{i}(k_x x - k_{z1} z - \omega t)] \tag{4}$$

$$\mathbf{E}_2 = [E_{x2}, 0, E_{z2}]\exp[\mathrm{i}(k_x x + k_{z2} z - \omega t)] \tag{5}$$

$$\mathbf{H}_2 = [0, H_{y2}, 0]\exp[\mathrm{i}(k_x x + k_{z2} z - \omega t)] \tag{6}$$

where k_x and k_z are the tangential and normal components of the wave vector of the radiation. By applying Maxwell's equation

$$\nabla \times \mathbf{H} = \varepsilon \frac{\partial \mathbf{E}}{\partial t} \tag{7}$$

to the equations (3)-(6) the following relationships between H_y and E_x are obtained:

$$k_{z1} H_{y1} = -\omega \varepsilon_1 E_{x1}, \tag{8}$$

$$k_{z2} H_{y2} = \omega \varepsilon_2 E_{x2}. \tag{9}$$

Finally the boundary conditions at the interface (z = 0) are applied. Here the requirement is that the tangential components of the **E** and **H** fields are continuous, hence

$$H_{\mathrm{y1}} = H_{\mathrm{y2}}, \tag{10}$$

$$E_{\mathrm{x1}} = E_{\mathrm{x2}}. \tag{11}$$

These equalities can then be used in conjunction with equations (8) and (9) to obtain the following relationship between the relative permittivities and the normal components of the wave vectors in the two media:

$$\frac{k_{\mathrm{z1}}}{\varepsilon_{\mathrm{r1}}} + \frac{k_{\mathrm{z2}}}{\varepsilon_{\mathrm{r2}}} = 0. \tag{12}$$

The wave vector of an electromagnetic wave propagating in a medium of dielectric constant ε is related to the angular frequency ω and speed of light c by

$$k^2 = \varepsilon_{\mathrm{r}}\left(\frac{\omega}{c}\right)^2 \tag{13}$$

where $k = 2\pi / \lambda$ and λ is the wavelength. Splitting k into the normal and tangential components of the wave vector results in

$$k_{\mathrm{x}}^2 + k_{\mathrm{zi}}^2 = \varepsilon_{\mathrm{ri}}\left(\frac{\omega}{c}\right)^2, \tag{14}$$

with i = 1,2 indicating the medium. Combining equations (12) and (14) then yields the dispersion relation for the SPP mode given by

$$k_{\mathrm{x}} = \frac{\omega}{c}\sqrt{\frac{\varepsilon_{\mathrm{r1}}\varepsilon_{\mathrm{r2}}}{\varepsilon_{\mathrm{r1}} + \varepsilon_{\mathrm{r2}}}} = k_{\mathrm{SPP}}. \tag{15}$$

As described in chapter 1, for real metals the relative permittivity $\varepsilon_{\mathrm{r1}}$ is a complex quantity where as for dielectrics the relative permittivity $\varepsilon_{\mathrm{r2}}$ is assumed to be real and positive. The wave vector of the SPP is therefore also a complex quantity,

$$k_{\mathrm{SPP}} = k'_{\mathrm{SPP}} + \mathrm{i}k''_{\mathrm{SPP}}, \tag{16}$$

where the first term describes the propagation of the SPP and the second term describes the damping due to absorption in the metal. For a propagating mode to exist k_{SPP} must have a real component placing the condition on the permittivities that $|\varepsilon_{\mathrm{r1}}| > \varepsilon_{\mathrm{r2}}$. If for the metal $\varepsilon'_{\mathrm{r1}} < 0$ and $|\varepsilon'_{\mathrm{r1}}| >> \varepsilon''_{\mathrm{r1}}$ and $\varepsilon_{\mathrm{r2}}$, equation (15) may be used to derive the following expressions for the real and imaginary parts of the SPP wave vector,

$$k'_{\mathrm{SPP}} = \frac{\omega}{c}\sqrt{\frac{\varepsilon'_{\mathrm{r1}}\varepsilon_{\mathrm{r2}}}{\varepsilon'_{\mathrm{r1}} + \varepsilon_{\mathrm{r2}}}}\,, \tag{17}$$

$$k''_{\mathrm{SPP}} = \frac{\omega}{c}\left(\frac{\varepsilon'_{\mathrm{r1}}\varepsilon_{\mathrm{r2}}}{\varepsilon'_{\mathrm{r1}} + \varepsilon_{\mathrm{r2}}}\right)^{3/2} \frac{\varepsilon''_{\mathrm{r1}}}{2(\varepsilon'_{\mathrm{r2}})^2}\,. \tag{18}$$

By considering equation (17) with the above conditions it is seen that the SPP wave vector is *always* larger than that of an incident photon, $k'_{\mathrm{SPP}} > \sqrt{\varepsilon_{\mathrm{r2}}}(\omega / c)$, even at grazing incidence (corresponding to the maximum wave vector the photon may possess parallel to the propagation direction of the SPP). The implication is that the SPP mode cannot be excited by an incident photon as to do so requires the wave vectors (momentum $\hbar k$) to be matched. The mode on a planar surface is therefore non-radiative. In order to excite the SPP mode some means of matching the wave vectors of the photon and SPP in the plane of the interface is required. Several methods exist and will be treated in a later section. A further implication is evident from equation (14) indicating that k_{zi} is always imaginary. This is consistent with the SPP being a trapped surface mode with exponentially decaying electromagnetic fields into the surrounding media. Prior to discussing the dispersion relation further it is of worth to discuss the spatial extent of the fields associated with the SPP mode.

3.4 Propagation length of the SPP

The imaginary component of the complex wave vector of the SPP suggests that as the mode propagates the amplitude decays exponentially as $\exp(-k''_{\mathrm{SPP}}x)$ and therefore the intensity as $\exp(-2k''_{\mathrm{SPP}}x)$. The propagation length is defined as the distance the SPP mode has travelled when the intensity has decayed to 1/e of its initial value and is given by

$$L_{\mathrm{SPP}} = \frac{1}{2k''_{\mathrm{SPP}}} = \frac{\lambda_0}{2\pi}\left(\frac{\varepsilon_2 + \varepsilon'_{\mathrm{r1}}}{\varepsilon_2\varepsilon'_{\mathrm{r1}}}\right)\frac{\varepsilon'^2_{\mathrm{r1}}}{\varepsilon''_{\mathrm{r1}}}\,. \tag{19}$$

As an example the relative permittivity of silver at λ = 632.8 nm is $\varepsilon_{\mathrm{r1}}$ = -17.6 + i0.7. These values substituted into equation (19) result in a propagation length of 42.6 μm. An important consideration is if the SPP mode is propagating along a corrugated surface. If the propagation length is greater than the periodicity of the grating it is possible for the SPP mode to Bragg scatter from the structure and radiate. The wave vector of the mode is altered enabling it to couple to radiation, a process described in detail later.

3.5 Penetration depth of the SPP

The penetration depth is a measure of the spatial extent of the electromagnetic field of the SPP in the media bounding the interface. The amplitude of the fields decay exponentially into the bounding media as the wave vector perpendicular to the plane of the interface k_{zi} is purely imaginary. The penetration depth is defined as the distance normal to the interface where the field strength has decayed to 1/e of the maximum value. Since the fields decay as $\exp(-k_{\mathrm{zi}}z)$ the penetration depth is given by $L_{\mathrm{zi}} = 1/|k_{\mathrm{zi}}|$. To obtain a value for L_{zi} equation (14) is rearranged for k_{zi} and combined with equation (14) to yield the following expression:

$$k_{\mathrm{zi}} = \pm k_0 \left[\varepsilon_{\mathrm{ri}} - \left(\frac{\varepsilon_{\mathrm{r1}}\varepsilon_{\mathrm{r2}}}{\varepsilon_{\mathrm{r1}} + \varepsilon_{\mathrm{r2}}} \right) \right]^{1/2} = \pm k_0 \left(\frac{\varepsilon_{\mathrm{ri}}^2}{\varepsilon_{\mathrm{r1}} + \varepsilon_{\mathrm{r2}}} \right)^{1/2}, \tag{20}$$

where the subscript i = 1,2 denotes the medium in which k_{z} is being determined. Assuming the same conditions as previously, namely $\varepsilon'_{\mathrm{r1}} < 0$ and $|\varepsilon'_{\mathrm{r1}}| >> \varepsilon''_{\mathrm{r1}}$ and $\varepsilon_{\mathrm{r2}}$, the equation for k_{zi} simplifies to

$$k_{\mathrm{zi}} = \pm k_0 \left(\frac{(\varepsilon'_{\mathrm{ri}})^2}{\varepsilon'_{\mathrm{r1}} + \varepsilon_{\mathrm{r2}}} \right)^{1/2}. \tag{21}$$

This can now be substituted into the expression for L_{zi} above to give

$$L_{\mathrm{z1}} = \frac{\lambda_0}{2\pi} \left| \frac{\varepsilon'_{\mathrm{r1}} + \varepsilon_{\mathrm{r2}}}{\varepsilon_{\mathrm{r2}}^2} \right|^{1/2}, \tag{22}$$

$$L_{\mathrm{z2}} = \frac{\lambda_0}{2\pi} \left| \frac{\varepsilon'_{\mathrm{r1}} + \varepsilon_{\mathrm{r2}}}{\varepsilon'^2_{\mathrm{r1}}} \right|^{1/2}. \tag{23}$$

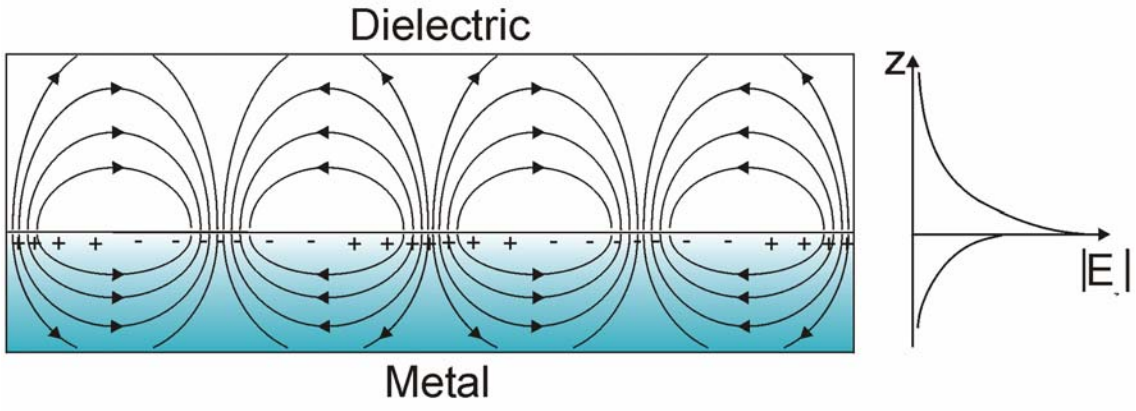

Figure 3.2. A representation of the polarisation surface charge density and associated normal electric field component for the SPP mode. The electric field decays exponentially into both the metal (ε_1) and dielectric (ε_2).

Considering a silver-air interface with the same values for the relative permittivity used in calculating the propagation length it is found that the penetration depths into the air and silver are L_{z2} = 434 nm and L_{z1} = 25 nm respectively. The electromagnetic field from the SPP extends much farther into the dielectric than the metal, shown schematically in figure 3.2 along with a representation of the charge distribution. The penetration of the SPP field into the metal becomes of interest when the metallic film is very thin, of the order of the penetration depth into the metal. Here the field extends through the metal film into the dielectric bounding the opposite surface and is therefore not contained entirely within the metal. This modifies the dispersion of the SPP mode and can lead to mode splitting if the dielectrics bounding each surface are identical. Further discussion of the properties of SPPs on such structures is given in section 3.8.

3.6 Dispersion curve of the SPP

The dispersion relation of the SPP may be used in conjunction with the frequency-dependent relative permittivity $\varepsilon'_{r2}(\omega)$ of the metal to produce the dispersion curve illustrated in figure 3.3 for a planar air-silver interface. Also included in the diagram is the light line defined as the maximum wave vector a photon of a given frequency propagating in the dielectric may possess in the plane of the interface. The shaded area represents the region of frequencies

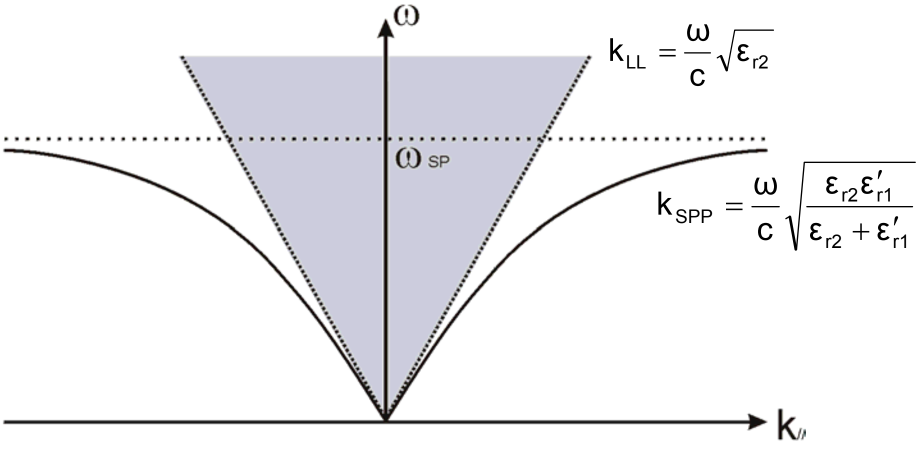

Figure 3.3. Schematic diagram showing the dispersion of the SPP mode (solid line) and light line (closely-spaced dotted line). The shaded region represents the range of frequencies accessible to light propagating in the dielectric bounding the metal. The light-line k_{LL} is the limit of the region for a given frequency.

and wave vectors possible for a photon propagating in the dielectric. The SPP dispersion curve remains outside of this region indicating that the SPP is always at a higher wave vector for a given frequency than an incident photon (as discussed above).

The SPP dispersion curve is shown to approach two asymptotic limits. Firstly, as the frequency tends to zero the SPP dispersion curve approaches the light-line; in effect the SPP mode becomes more ‘photon-like’. At low frequencies the metal responds instantaneously to the incident electromagnetic field to cancel it and is deemed to be loss-free. The relative permittivity is therefore of the form $\varepsilon_{r1} = -\infty + 0.0i$ and upon substitution into equation (19) results in an infinite propagation length for the SPP. Substitution into equations (22) and (23) indicates that the field is completely excluded from the metal whilst infinite in extent in the dielectric medium. With reference to equation (15) it is seen that the dispersion relation reduces to the form

$$k'_{SPP} = \frac{\omega}{c}\sqrt{\varepsilon_{r2}} \qquad (24)$$

which is identical to that of a photon propagating at grazing incidence; hence the description of the SPP as photon-like. Secondly the dispersion of the SPP becomes flat as the frequency tends to the surface plasmon frequency ω_{SP}, first encountered in section 3.1. At the surface plasma frequency the real part of the relative permittivity of the metal is equal in magnitude, but opposite in sign to the relative permittivity of the dielectric. In the absence of damping it is seen from equation (21) that the perpendicular components of the wave vector associated with the SPP in each medium are equal. Furthermore, from the constitutive relation equation (2) in conjunction with the boundary conditions that the normal component of **D** and tangential component of **E** are conserved we see that the electric fields in the two media are equal in magnitude and mirrored about the interface. Noting that in the limit of large $k_{//}$ the wavelength of the SPP $\lambda_{SPP} \rightarrow 0$ the mode becomes a purely longitudinal oscillation and is therefore more plasmon-like; the mode is no longer the surface plasmon polariton and is referred to as the surface plasmon.

3.7 Effect of a dielectric overlayer on SPP dispersion

As can be seen from equation (14) the SPP dispersion relation is a function of the relative permittivities of both the metal and the dielectric. It has been shown how the frequency-dependent relative permittivity of the metal defines the form of the dispersion curve of the SPP; now the effect of changing the relative permittivity of the dielectric on the dispersion curve is discussed.

Consider the structure illustrated in figure 3.4 consisting of a dielectric slab of thickness d and relative permittivity ε_{r3} sandwiched between semi-infinite dielectric and metal layers with relative permittivities ε_{r2} and ε_{r1} respectively with $\varepsilon_{r3} > \varepsilon_{r2}$. In the limit of $d \rightarrow 0$ the dispersion relation is of the form derived earlier for a single interface (equation (14)). If the thickness is in the range $0 < d < \lambda$ the electromagnetic field associated with the surface mode exists in both dielectric media and the resulting SPP wave vector is given by a double-interface solution [*Pockrand (1978)*].

For a given frequency the SPP wave vector associated with the double-interface will be greater than that for the single-interface due to the contribution from ε_{r3}. As the thickness is increased so that $d > \lambda$ the electromagnetic field associated with the SPP is almost entirely within the dielectric slab. The dispersion relation is once more given by a single-interface solution with ε_{r2} replaced by ε_{r3}. The effect this has on the dispersion curve is shown in figure

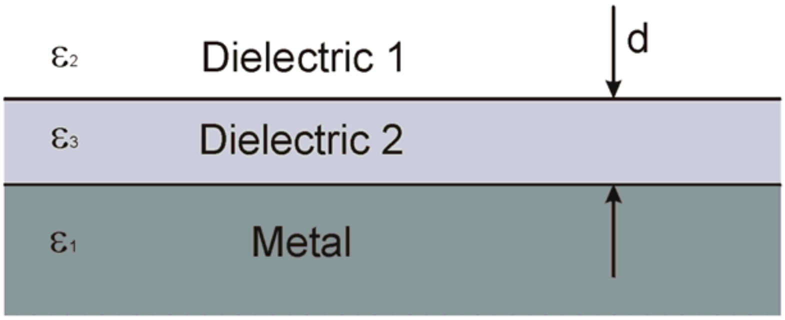

Figure 3.4. Structure consisting of a dielectric overlayer with permittivity ε_{r3} and thickness d sandwiched between a semi-infinite metallic layer with permittivity ε_{r1} and semi-infinite dielectric layer with permittivity ε_{r2}.

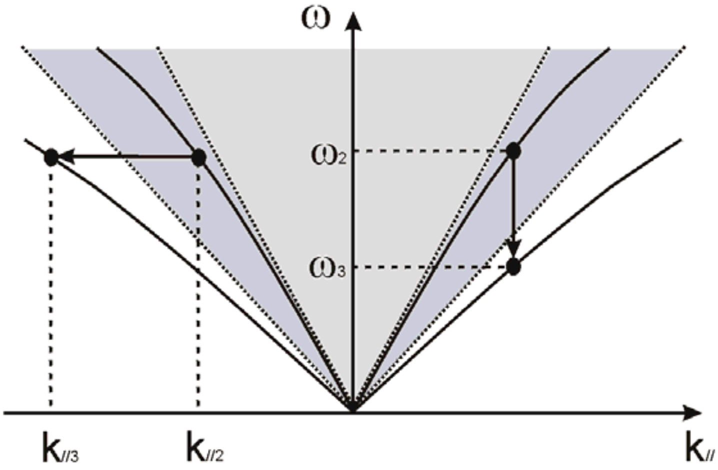

Figure 3.5. Schematic diagram showing the effect of adding a dielectric overlayer to the dispersion of the SPP mode (solid lines) and light lines (dotted lines). The lightly shaded area indicates the radiative region for the material with permittivity ε_{r2} and the darker shaded region the additional area accessible to light with the addition of a thick overlayer of permittivity ε_{r3}.

3.5 and where it is seen that for a given frequency the magnitude of the wave vector of the SPP has shifted to higher values ($k_{//2} \rightarrow k_{//3}$). For a given wave vector the frequency of the mode has shifted to a lower value ($\omega_{//2} \rightarrow \omega_{//3}$), an effect observed in the behaviour of the localised surface plasmon modes on metallic particles (chapter 2, section 8). There it was noted that the frequency change is due to a depolarisation of the charge distribution within the metal by the electromagnetic fields from the induced polarisation of the dielectric. A similar effect is the cause of the reduced dispersion of the SPP.

3.8 SPPs on thin metal films

The dispersion of a SPP propagating on an optically thin metal film is influenced by the extension of the SPP's electromagnetic field through the metal into the dielectric bounding the opposite interface. Initially two types of planar structure are considered, one with the metal slab bounded by dielectric media with identical relative permittivities (the *symmetric* case, figure 3.6(a)), the other with the metal slab bounded by dielectric media with different relative permittivities (the *asymmetric* case, (figure 3.6(b)). The symmetric structures support SPPs with the same dispersion on each side of the film and are thus able to couple together. The asymmetric structures support SPPs that have a different dispersion and as such cannot couple together if excited on a planar film.

The situation becomes more complex if one or both of the surfaces are patterned periodically. This leads to the possibility of coupling between scattered SPP modes in both symmetric and asymmetric structures at frequencies defined by the periodicity of the grating and thickness of the film. If the periodic patterning is due to an array of apertures the electromagnetic field of the SPP is less attenuated through the apertures than it would be in a continuous film, and may give rise to enhanced transmission. In view of the relevance of these effects to later chapters the following sections describe the properties of asymmetric and symmetric metal films in more detail.

3.8.1 Symmetric thin metal films

For an optically thick metal film bounded by identical or very similar dielectric media the SPPs on each surface are isolated from one another. The evanescent fields from the two modes decaying into the metal do not overlap significantly and the modes have the same characteristics as those of a mode propagating on a single interface. Now consider an *optically thin* ($d \leq 100$ nm) planar metal film bounded by identical dielectric media (figure 3.6(a). The exponentially decaying fields penetrate a sufficient distance through the metal to overlap and coupling occurs between the SPPs. This results in a splitting of the degenerate mode into a mode with a symmetric charge distribution and a mode with an antisymmetric charge distribution. These are respectively known

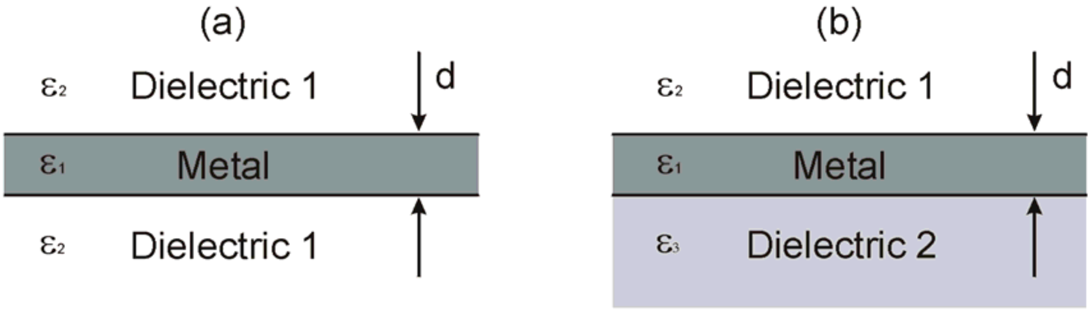

Figure 3.6. Diagram showing (a) metal slab bounded by identical dielectrics (symmetric structure) and (b) metal slab bounded by different dielectrics (asymmetric structure).

as the short-range surface plasmon polariton (SRSPP – figure 3.7(a)) and the long-range surface plasmon polariton (LRSPP – figure 3.7(b)) in reference to their propagation lengths relative to the single interface mode. The difference in the propagation lengths is a consequence of the different field distributions of the two modes, shown in figure 3.7, that produce differing power distributions within the structures. There is more power distributed within the metal for the

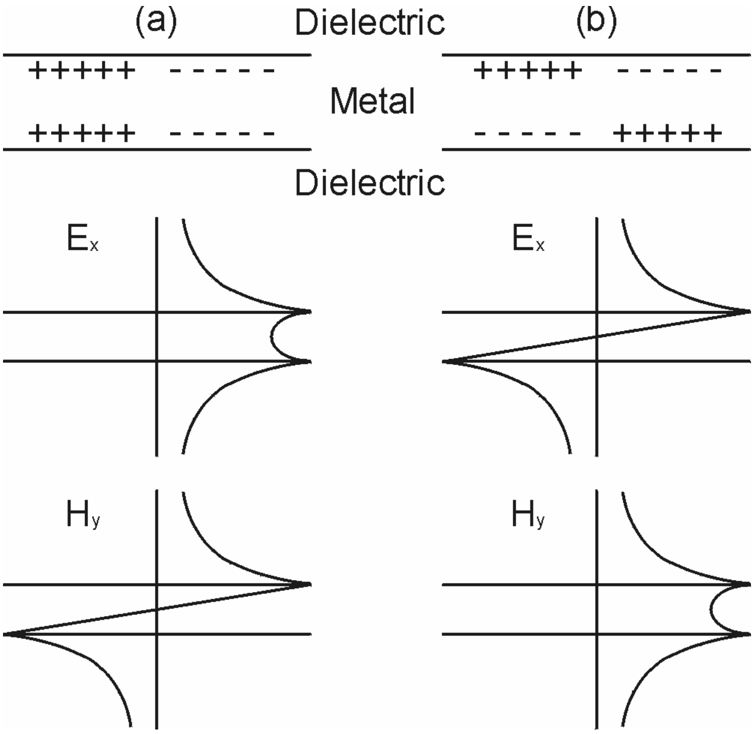

Figure 3.7. Schematic diagrams showing field distributions and charge distributions for (a) the short-range SPP and (b) the long-range SPP.

SRSPP compared to the LRSPP and hence an increased loss and shorter propagation length. The LRSPP has less power distributed within the metal, more in the dielectric resulting in a reduced loss and longer propagation length.

The same coupling conditions apply for the coupled SPP modes on thin films as for the uncoupled SPP modes on thick films; an enhancement of the wave vector of light incident on the surface is required to excite the modes. Prism-coupled modes have been shown to enhance the transmittance of light through otherwise opaque metallic thin films [*Dragila (1985)*]. Alternatively, grating-induced coupled SPP modes may also be excited if one or both of the surfaces are patterned periodically. *Hooper (2004)* investigated theoretically the optical response (transmittance, reflectance and absorbance) of thin silver films with a periodic modulation on both surfaces. The structures were both in-phase with one another (conformal) and out-of-phase (non-conformal) and were studied with the gratings oriented in the classical mount. They showed for a non-conformal geometry (the gratings are out of phase by 180°) a large enhancement in the transmittance of light through the sample over a range of frequencies and for all incident angles. By analysing the field magnitudes the field strength maxima were deduced to occur at the troughs where the silver is thinnest resulting in significant penetration of the fields through to the opposite interface.

3.8.2 Asymmetric thin metal films

For an optically thick metal film bounded by dielectric media with significantly different relative permittivities the SPP modes at each interface will have a different dispersion according to equation (14). As the thickness is decreased the field from the SPP extends through the metal film and into the dielectric bounding the opposite interface altering the dispersion of the mode. This is similar to the situation described in section 3.7 where the electromagnetic field associated with the SPP samples two different relative permittivities associated with the two bounding dielectrics. Note the field must penetrate significantly into the opposite medium, a constraint not applicable with the SPP field interactions in the symmetric structure where the fields simply had to overlap. This means the film thickness needs to be lower than in the symmetric structure to observe a perturbation of the dispersion of the SPP in the asymmetric structure.

As with the symmetric slab geometry, some interesting effects are observed when one or both of the surfaces are modulated periodically to allow the excitation of grating coupled SPPs. *Schröter and Heitmann (1999)* investigated the optical response of thin metal films ~80 nm thick corrugated on one or both surfaces supported on a silica substrate with air bounding the opposite interface. It was found that the first order modes associated with the two interfaces were both excited if only one surface was modulated. When both surfaces were modulated with identical grating profiles with the gratings in-phase with one another (conformal geometry) it was suggested that only one of the modes (that on the incident side) could be excited. It has subsequently been shown by *Hooper (2003)* that the second mode *is* excited, however only very weakly for the conformal geometry. The evanescent diffracted field that couples light with the SPP is strongly suppressed resulting in a small coupling efficiency into the SPP mode. As the relative phase of the gratings is altered the coupling efficiency is increased.

It is also possible to enhance the transmission of light through a metallic film in corrugated asymmetric structures. First observed by *Pockrand (1975)*, the process is known as cross-coupling and occurs when the scattered SPP modes associated with each interface cross one another in reciprocal space. At a certain frequency and wave vector the SPP modes are excited on both surfaces enabling an enhancement in the transmittance over that expected from a simple addition of the contributions from each mode. This process was recently shown by *Gifford (2002)* to allow the recovery of energy that would otherwise be lost within surface-emitting organic light emitting diode (OLED) structures. A more comprehensive analysis was performed by *Wedge et al. (2004)* on similar structures. They investigated the photoluminescence of dye molecules through corrugated Ag films as a function of film thickness and also found that the transmission enhancement was consistent with a SPP cross-coupling process. A similar mechanism leads to the enhanced transmission through hole arrays observed by *Ebbesen (1998)*. A silver film was deposited onto a silica substrate and then perforated with a square array of holes. The periodic arrangement allowed the optical excitation of SPPs associated with the air-metal interface and silica-metal interface. Where the two modes became degenerate a maximum in the transmittance enhancement occurred. In light of the importance SPP excitation in optical devices some methods by which light can be used to excite the mode are now discussed.

3.9 Coupling of light to SPP modes

The SPP mode on a single planar interface cannot be coupled with light as a consequence of the increased wave vector of the SPP relative to that of an incident photon. This means that in order to couple light with the SPP mode some way of matching the wave vectors is required, either by reducing the wave vector of the SPP or by enhancing the *tangential* (or *in-plane*) wave vector of the photon. For radiation incident from a source in the far-field this is typically achieved by one of two techniques. The first is known as *prism coupling* and exploits the enhancement of the photon wave vector by the phenomenon of attenuated total reflection (ATR). The second method requires the surface to be roughened at the scale of the wavelength of the incident radiation. This is known as *grating coupling* provided the roughening is in the form of a periodic surface modulation. The following sections describe these techniques in more detail paying special attention to the use of prism coupling in characterising thin metallic films and the importance of grating coupling in enhancing transmission through metallic films.

3.9.1 Prism coupling to SPP modes

Light that is incident on an interface comprising of media with differing refractive index will undergo total internal reflection if the light is incident from the high index medium onto the low index medium beyond the critical angle θ_c,

$$\sin\theta_c = \frac{n_1}{n_2}, \quad n_2 > n_1. \tag{25}$$

The tangential component of the wave vector in the high index medium given by $k_{//} = n_2 k_0 \sin\theta_c$ is too large to allow a propagating wave in the low index medium. However, an evanescent wave is generated at the interface that decays into the low index medium. The tangential wave vector of the evanescent wave is equal to that of the incident wave and provides a means of coupling to an SPP mode provided a metal surface is within the range of the evanescent field. A further constraint is that for coupling to occur the dispersion of the SPP mode must lie within the region of reciprocal space bounded by the light lines associated with the prism and the external medium. This is shown as the light-shaded region of figure 3.8. The dark-shaded region is that accessible to light in both the air and the silica. Typically three features are observed as the wave vector (angle of incidence) is increased for a given frequency. The reflectivity from a planar film rises as the critical angle (point (a)) is approached. At the critical angle the reflectivity reaches a maximum of 1 and in angle-dependent reflectivity scans is referred to as a ‘critical edge’. Beyond this point it is possible to satisfy equation (14) and light can couple to the SPP associated with the air-metal interface. When this occurs (point (b)) the reflectivity reduces and for perfect coupling falls to zero. At point (c) the angle of incidence of light within the prism is grazing. For wave vectors of the air SPP greater than that of the maximum wave vector for light in the prism coupling is no longer possible. Because the evanescent field is generated by what would otherwise be total reflection at an interface, these coupling techniques are known as attenuated total reflection (ATR) methods to account for the energy transferred into the surface mode.

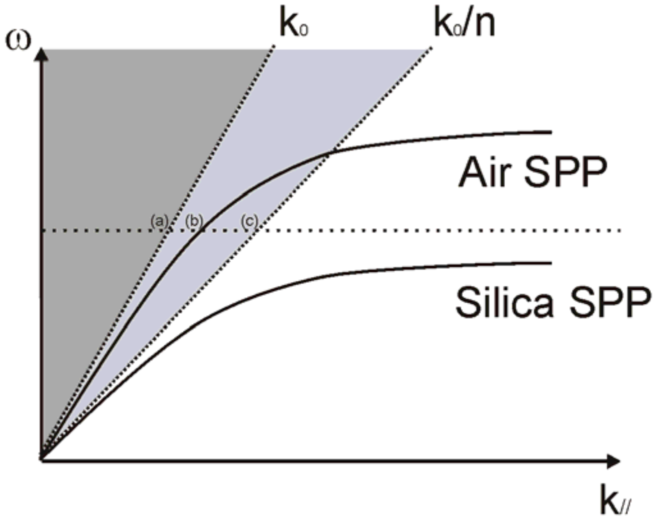

Figure 3.8. Dispersion curve showing region of reciprocal space where coupling between light incident at the silica prism-metal interface and the SPP mode propagating at the air-metal interface.

There are two methods of using a prism to couple light to an SPP mode at a planar interface. In the *Otto* configuration [*Otto (1968)*] the prism is separated from the silver film by a thin spacer layer with a refractive index n_S less than the refractive index of the prism n_P (figure 3.9(a)). Light incident on the prism-spacer interface beyond the critical angle sets up an evanescent field within the spacer layer extending to the metal surface. The evanescent field couples to the SPP at the spacer-metal interface and energy is transferred into the mode. The strength of the coupling is dependent on the thickness of the spacer layer, a reduction of the thickness leading to an increase in the magnitude of the evanescent field. However, the field generated by the SPP mode will be perturbed by the presence of the prism for a small spacer layer thickness. The optimum for coupling to the SPP is therefore achieved when the thickness of the spacer is of the order of the wavelength of the incident radiation. This presents practical problems, particularly if visible radiation is used, as the thickness required may be less than the dimensions of surface contaminants such as dust particles. At visible wavelengths great care must be taken to ensure a clean sample, however at longer wavelengths, for instance in the infra-red regime the correct thickness of spacer layer is more easily accomplished. The major use of the Otto configuration is in the characterisation and study of the surface modes on optically thick bulk films. The second technique, first demonstrated by *Kretschmann and Raether (1968)*, requires an

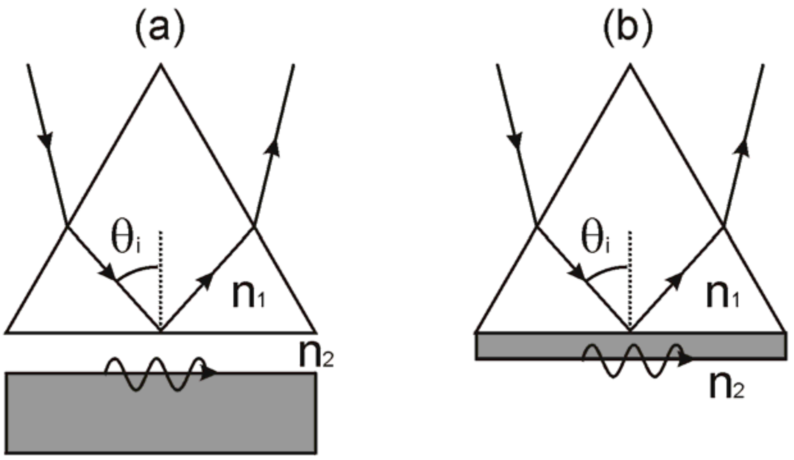

Figure 3.9. Prism-coupling of light to SPP modes; the Otto configuration (a) and the Kretschmann-Raether configuration (b).

optically thin metal film either in direct contact with the prism or index-matched to the prism should the film be deposited on a substrate (figure 3.9(b)). In this configuration the evanescent field generated by total reflection at the metal-prism interface decays through the metal film and excites the SPP mode at the metal-air interface. The obvious advantage over the Otto configuration is that experiments are more easily carried out in the visible spectral region since a sub-wavelength spacer layer is no longer required. In the Kretschmann-Raether configuration optimum coupling is achieved with a film thickness of around 45 nm for silver at visible wavelengths.

3.9.2 Grating coupling to SPP modes

In a series of early experiments by *Wood (1902)* light from incandescent lamps was shone onto ruled metallic gratings and the reflectance observed. Rather than a set of continuous spectra there were anomalous features present consisting of cusps and sharp dips in the reflectance. The features could not be explained by the nature of the light source and a full understanding of their origin had to wait for the best part of 40 years. Quite soon after *Wood* published his observations *Rayleigh (1907)* was able to explain that the cusps in the reflectivity intensity were created by a particular diffracted order becoming evanescent. The energy associated with the evanescent order is redistributed into the propagating orders, including the zero-order or specular direction, leading to an increase in reflected intensity. In 1941 *Fano* indicated that the sharp dips were due to the excitation of the TM-polarised surface waves that are now known to be grating coupled SPPs.

For a planar surface the SPP is non-radiative – coupling between light and the SPP is not possible. Surfaces with some roughness on the scale of the wavelength of the incident radiation change this situation by providing a means of enhancing the in-plane wave vector of an incident photon. As with prism coupling the process requires an evanescent field in order to couple radiation into the SPP mode. In contrast to prism-coupling, the evanescent field is not generated through evanescent tunnelling of the photon, but through scattering of the incident radiation into an evanescent diffracted order. Since a rough surface may be considered as a superposition of a number of gratings with varying amplitude, pitch and orientation the physics underlying the coupling is simplified if just a single grating is considered.

A grating structure on an optically thick metallic film modulated periodically along one dimension only with an upper half-space of refractive index n_1 is shown in figure 3.10. The polar angle θ defines the angle of incidence measured from the normal to the average plane of the grating and the azimuthal angle φ defines the rotation of the plane of incidence with respect to the positive x-axis. The separation between successive modulations is known as the period of the grating λ_G and defines the magnitude of the *primitive* reciprocal lattice vector $|\mathbf{b}| = 2\pi / \lambda_G$. There are in principle an infinite number of reciprocal lattice vectors **G** corresponding to integer multiples of **b**,

$$\mathbf{G} = n\mathbf{b} \tag{26}$$

where $n = \pm 0,1,2\ldots$ is known as the order of the diffracted wave. When a wave is incident from the upper half-space onto the grating at an angle θ_i it may be diffracted (scattered) back into the upper half-space at certain angles θ_s according to the Bragg relation,

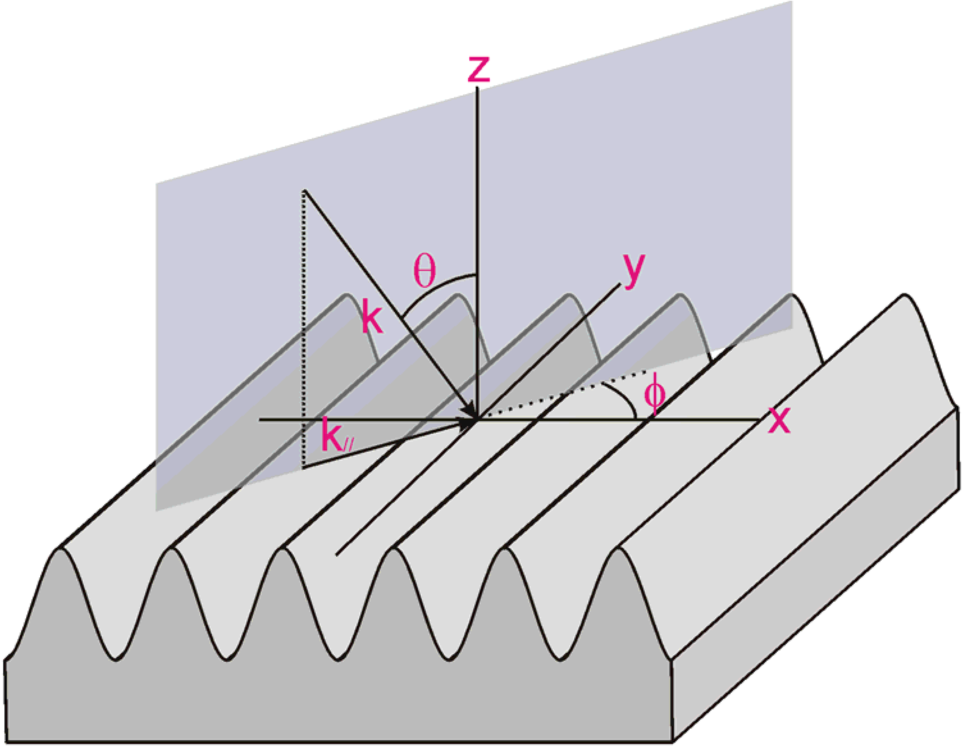

Figure 3.10. Diagram of a corrugated grating structure illustrating the coordinate system defined relative to the azimuthal orientation φ and plane of incidence.

$$\mathbf{k}_0 \sin\theta_\mathrm{i} + \mathbf{G} = \mathbf{k}_0 \sin\theta_\mathrm{s} \tag{27}$$

where $\mathbf{k}_0$ is the wave vector of the incident photon ($k_0 = (\omega / c)\sqrt{\varepsilon_1}$), $\mathbf{k}_0\sin\theta_\mathrm{i} = \mathbf{k}_{//}$ is the parallel component of the incident wave vector and $\mathbf{k}_0\sin\theta_\mathrm{s}$ is the parallel component of the diffracted wave vector. Equation (27) allows for the parallel component of the wave vector of the diffracted wave to be greater than that of a grazing photon. This gives rise to a non-propagating evanescent diffracted wave with an imaginary perpendicular wave vector component. It is the enhancement of the incident in-plane wave vector that enables the grating coupling of radiation to the SPP mode according to the relation

$$\mathbf{k}_{//} + \mathbf{G} = \mathbf{k}_\mathrm{SPP}\,. \tag{28}$$

The inverse process is also possible whereby a SPP mode is scattered by the grating into a radiative mode,

$$\mathbf{k}_\mathrm{SPP} + \mathbf{G} = \mathbf{k}_{//}\,. \tag{29}$$

Furthermore, SPP modes may scatter into other SPP modes if the Bragg coupling condition is satisfied,

$$\mathbf{k}_\mathrm{SPP} + \mathbf{G} = \mathbf{k}'_\mathrm{SPP}\,. \tag{30}$$

Here, $\mathbf{k}'_\mathrm{SPP}$ is the wave vector of an SPP mode that could otherwise be coupled into from an incident photon scattered by a different value of **G**.

In the above discussion no constraint was placed on the orientation of the grating with respect to the incident wave vector. If the plane of incidence is parallel to the grating vectors then the direction of propagation of the grating coupled SPP modes will also be in this direction. The grating vector, parallel component of the incident wave vector and SPP wave vector are collinear and the grating is said to be in the *classical* mount. This corresponds to an azimuthal angle of $\varphi = 0$ and in such a case the dispersion curves of the scattered SPPs and the scattered light lines have the form of those plotted in figure 3.11(a). The shaded region represents the area of reciprocal space accessible to radiative modes and is bounded by the light lines associated with the incident unscattered light. It is conventional to label the grating-coupled SPP modes and associated light lines in terms of the diffracted order that provides the coupling mechanism. At frequencies below the (-1), (+1) diffracted light lines the structure is *zero-ordered* meaning that no diffraction into the far-

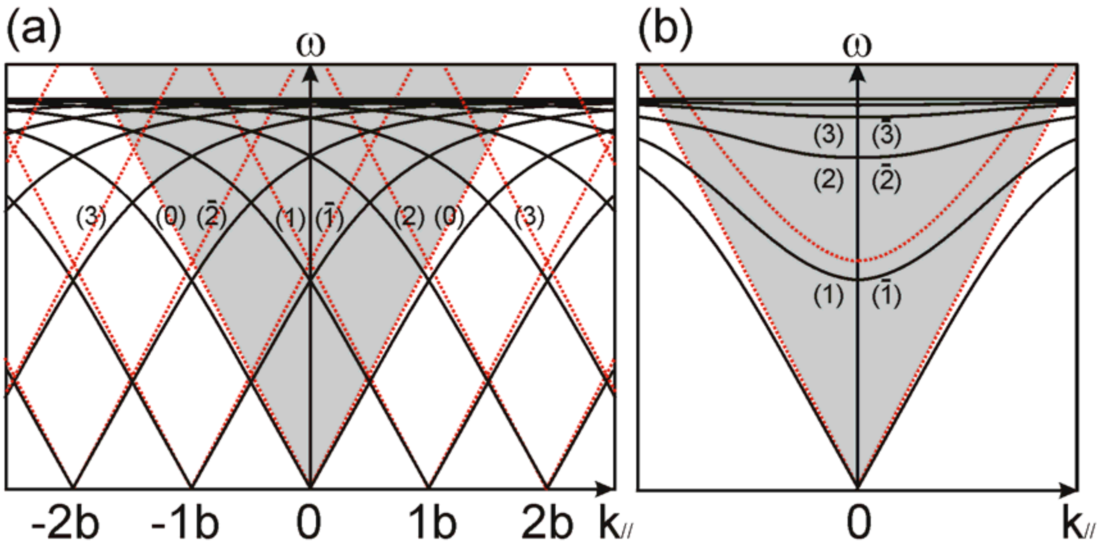

Figure 3.11. Diagram illustrating the dispersion of scattered light-lines (dotted) and SPP modes (solid) from a mono-grating oriented $\varphi = 0°$ (a) and $\varphi = 90°$ (b). The shaded area is the radiative region.

field is permitted. This illustrates that it is the *evanescent* diffracted field that couples light into the SPP mode as the SPPs associated with the (–1), (+1) diffracted orders are at frequencies below the associated light lines. For the one-dimensional grating of figure 3.10 the scattering centres in reciprocal space occur only along the *x*-axis, not necessarily in line with the $k_{//}$-axis (plane of incidence). Indeed, this only occurs if the grating is oriented in the classical mount. If light is incident with the grating oriented at a non-zero azimuthal angle (the *conical* mount) the dispersion curves as plotted in figure 3.11(a) take on a different form. If each of the scattering centres is considered as a 'source' at $\omega = 0$ of SPP dispersion curves then as the frequency is increased eventually the SPP dispersion curves will intersect with the ω-$k_{//}$ plane. When the incident light wave vector, grating vectors and SPP wave vector are collinear the initial intersection as frequency is increased occurs at $\omega = 0$ because the scattering centres lie along the $k_{//}$ axis. As the azimuthal angle is increased from 0˚ to 90˚ the intersection occurs at increasing values of frequency defined by the shape of the dispersion curve and periodicity of the grating (magnitude of the grating vector). The dispersion curve of the scattered SPP for a grating oriented at an azimuthal angle of $\varphi = 90°$ is shown in figure 3.11(b). The minimum frequency at which coupling can occur is at $k_{//} = 0$ (normal incidence) and rises towards the surface plasma frequency ω_{SP} as the magnitude of the in-plane wave vector is increased. In this orientation the [(+1),(-1)], [(+2),(-2)], etc. pairs of scattered SPP modes each become degenerate for all (ω, $k_{//}$) values.

Now consider the diagram in figure 3.12 showing a slice through ω-k space for a constant value of ω. The dashed circle about the origin represents the maximum wave vector of an incident photon and the shaded area within the circle indicates where coupling between radiative and non-radiative modes is permitted. The solid circle about the origin corresponds to the wave vector of the zero-order (unscattered) SPP and is always greater in magnitude than the incident photon, as expected. The circles originating from the scattering centres to either side of the origin correspond to the scattered light lines (dashed) and SPPs (solid). When the dispersion of a scattered SPP is within the shaded region coupling can occur by the mechanism illustrated. The in-plane component of the incident wave vector $\mathbf{k}_{//}$ incident at an azimuthal angle φ is scattered by the grating vector $\mathbf{G}$ to couple to the SPP with wave vector $\mathbf{k}_{SPP}$ propagating at an angle Ψ relative to the positive k_x-axis.

In prism coupling to a planar surface there had to be a component of the

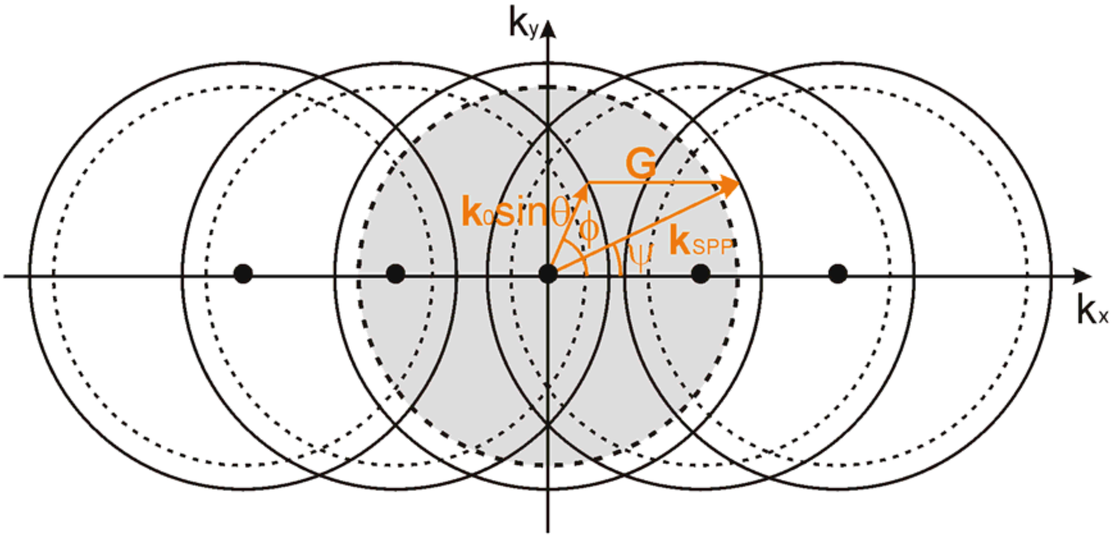

Figure 3.12. A plane in reciprocal space for a constant value of ω. The dotted lines represent the dispersion of the scattered light lines for constant ω as a function of the wave vector components in the *x* and *y* directions. The solid lines represent the scattered SPP modes. The shaded region is the area of reciprocal space accessible to radiation and is bounded by the zero order light line and SPP. The mechanism for grating coupling of light into the SPP mode is shown.

incident electric field perpendicular to the interface, a requirement satisfied for TM polarised light but not satisfied for TE polarised light. In grating-coupling the polarisation state of the incident light is defined in the usual manner where for TE polarised light the electric field is perpendicular to the plane of incidence and for TM polarised light the electric field is parallel to the plane of incidence. However, it is now possible to couple to the SPP using both TE and TM polarised light. The incident light may have components of the incident electric field perpendicular to the surface for TE light as well as TM light depending on the orientation of the grating with respect to the incident light. For instance, in the classical mount (φ = 0˚) the grooves of the grating are perpendicular to the plane of incidence and TE polarised light will not excite the SPP since the electric field is parallel to the surface for all incident polar angles. However, for an azimuthal angle φ = 90˚ TE polarised light can excite the SPP as the electric field does have a perpendicular component of electric field to the surface at all points apart from the peaks and troughs of the grating. For azimuthal angles between 0˚ and 90˚ both TE and TM polarisations may couple to the SPP. The relative coupling strengths of each polarisation is dependent on the orientation of the grating and for TM polarised light is a maximum at φ = 0˚ generally falling to zero at φ = 90˚, the opposite being true for TE polarised light. *Bryan-Brown (1990)* demonstrated this behaviour for TM polarised light incident on small amplitude, non-blazed gratings, observing also a TE polarised component in the reflected field. This arises from the conversion of TM polarised light to TE polarised light and is a maximum when the grating grooves are at 45˚ to the plane of incidence. For light incident on gratings with a large amplitude relative to the pitch it is possible to couple to a SPP mode with p-polarised light and orientation φ = 90˚ [*Watts (1997)*]. In this case circulating electromagnetic fields are excited within the grating grooves and leads to some polarisation conversion of the re-radiated light.

3.10 Coupling strength to SPP modes

The shape and position of the SPP mode is extremely sensitive to the properties of the surface and its environment. As described for prism coupling to a planar interface, typically the resonance is observed as a reflectivity minimum in optical data and is dependent upon the thickness of the silver film, the wavelength of the incident light and the relative permittivities of the dielectric and metal that constitute the interface. The appearance of a reflectivity minimum is due to the absorption of electromagnetic energy into the metal through inelastic scattering of the electrons (Joule heating). However, to consider only the absorption neglects the important role of re-radiation (light that is coupled into the SPP mode and is then coupled back out into a radiative mode) in defining the form of the reflectance and transmittance features observed in optical measurements. Furthermore it is emphasised that the spectral width of the resonance is determined by both inelastic *and* elastic scattering processes that result in the damping or, more descriptively, *dephasing* of the SPP. The electrons lose directional information upon scattering from defects, impurities, etc. that results in a reduced coherency between the many electrons contributing to the plasmon mode. Absorption as stated above refers to *direct* inelastic scattering that contributes to the overall dephasing of the SPP and *indirect* inelastic scattering (involving the de-excitation of an electron that has previously undergone elastic scattering) that does not contribute to the overall dephasing of the SPP.

3.10.1 Prism-coupling

Since light may be coupled into the SPP mode, light may also be coupled out of the SPP mode; the SPP mode is radiative and as such experiences some radiative damping as well as internal damping. The direction in which the light is emitted is given by the equation

$$k_{\mathrm{SPP}} = n_1 k_0 \sin\theta_{\mathrm{r}} \tag{31}$$

and for a planar interface propagates in the same direction as the specularly reflected beam [*Pockrand (1980), Weber (1979)*]. The relative phase of the reflected and re-radiated light determines whether excitation of the SPP leads to a maximum or minimum in reflectance. For a planar metallic interface the re-radiated light is not in phase with the reflected light resulting in destructive interference and a reflectance minimum. For optimum coupling to occur the intensity of light re-radiated by the SPP is identical to and in anti-phase with that reflected from the surface. The energy that would otherwise be lost by the SPP mode to radiative damping is redistributed and eventually lost to Joule heating within the metal. For a given frequency optimum coupling occurs for a specific thickness of metal film when using the *Kretschmann-Raether* geometry to couple to the SPP. If the metal thickness is less than this value the SPP is under-coupled and the intensity of the re-radiated light is less than that of the reflected light. If the metal thickness is greater than this value the SPP is over-coupled and the re-radiated intensity is greater than the reflected intensity. Also, the depth of the resonance is influenced by the relative contributions of the radiative and non-radiative damping to the dephasing of the SPP. When the spectral broadening due to radiative damping $\Delta\omega_{\mathrm{rad}}$ is equal to that due to internal damping $\Delta\omega_{\mathrm{int}}$ the resonance has a minimum in reflectivity (R = 0). Essentially this is stating that the radiative decay rate is equal to the non-radiative decay rate. Therefore two conditions for optimum coupling are identified:

- $I_{\mathrm{rad}} = I_{\mathrm{ref}}$
- $\Delta\omega_{\mathrm{rad}} = \Delta\omega_{\mathrm{int}}$.

The dependence of the reflectance on the physical structure and material properties of the metallic film and external environment provide a means of characterising these parameters by applying a suitable theoretical model. For planar interfaces this is relatively straightforward and is tackled by solving Maxwell's equations within each medium and applying the relevant boundary conditions. These are:

1. The continuity of the tangential **E** and **H** fields across the interface.
2. All fields remain finite as $z \rightarrow \pm \infty$, known as the *outgoing wave condition*.

The Fresnel coefficients defining the transmittance and reflectance can then be generated and the resulting theoretical curves compared to experimental data. This approach may be applied to multilayer structures allowing the calculation of the material parameters and thickness of each separate layer [*Berreman (1972, 1973)*]. The parameters that influence the form of the SPP mode described above are equally important when SPPs are generated on grating structures, but with additional effects due to the form of surface profile.

3.10.2 Grating-coupling

To gain an understanding of the effect of the surface profile of a metallic grating on the coupling strength between electromagnetic radiation and an SPP it is most instructive to describe results from a number of theoretical studies. To model the behaviour of an SPP propagating on a grating it is possible to adopt a similar approach to that briefly outlined for prism-coupling. However, it is no longer a trivial undertaking to match the boundary conditions at the interface. To deal with non-planar interfaces a number of theories have been developed that allow modelling of the reflectance from grating surfaces. A widely used technique is known as the Chandezon method [*Chandezon (1982)*] approaching the problem of matching the boundary conditions across a non-planar interface by employing a co-ordinate transformation to effectively flatten the surface. The translation used is

$$\begin{aligned} v &= x, \\ u &= z - A(x), \\ w &= y, \end{aligned}$$

where $A(x)$ is a function describing the profile of the surface. The consequence of this is that Maxwell's equations and the incident, reflected and transmitted fields must now be expressed in terms of the new co-ordinate system. This is achieved by expanding the fields and Maxwell's equations as a Fourier series in terms of the wave vector in the u-direction.

The original theory of Chandezon was only capable of modelling the optical response from multilayer structures, each layer with the same single sinusoidal modulation in the classical mount ($\varphi = 0$, plane of incidence parallel to grating vector). The theory has since been extended to allow for gratings in the conical mount ($\varphi \neq 0$, plane of incidence *not* parallel to grating vector) [*Elston (1991a,b)*] and to model bi-grating structures where an interface is corrugated in two different directions [*Granet (1995), Harris (1996)*]. By implementing these improvements it is possible to acquire a detailed understanding of the influence subtle changes in the grating profile have on the form of the surface plasmon resonance feature observed in reflectance spectra and angle dependent reflectivity.

In the simplest scenario a grating consists of a purely sinusoidal modulation. However, experimentally it is unlikely that the profile will consist of just a single harmonic component. To cope with a non-sinusoidal grating the profile may be described by a Fourier series expanded in terms of the primitive reciprocal lattice vector **b**,

$$\begin{aligned} A(x) = a_1 \sin(|\mathbf{b}|x + \varphi_1) + a_2 \sin(2|\mathbf{b}|x + \varphi_2) + a_3 \sin(3|\mathbf{b}|x + \varphi_3) + \ldots \\ + a_\mathrm{n} \sin(n|\mathbf{b}|x + \varphi_\mathrm{n}), \end{aligned} \tag{32}$$

where a_n and φ_n are respectively the amplitude and phase of the n^th harmonic component. The number of terms required is dependent on the complexity of the profile with relatively few needed for gratings fabricated by UV lithography. This increases quite dramatically if sharp edges are introduced, for instance with a square-grating profile. By varying the amplitude and phase it is possible to alter the coupling characteristics (shape, position and strength) of the SPP modes associated with each diffracted order. These effects may then be used to gain some insight into the behaviour of more complicated grating structures [*Watts (1999)*].

In figure 13 a theoretical plot is shown of the specular reflectance R as a function of frequency f of TM polarised light at normal incidence ($k_{//}$ = 0) from a grating with a singly sinusoidal profile. The grating is in the classical mount with a pitch of 1 μm and amplitude of 30 nm. There are three features to observe in the spectrum. Firstly there is a deep minimum in the reflectance at a frequency of f = 3.6 x 10^{14} Hz corresponding to the excitation of the grating-coupled ±1 SPP modes. Close to this mode at f = 3.7 x 10^{14} Hz there is the critical edge or Rayleigh anomaly corresponding to when the ±1 diffracted orders become evanescent. Finally there is a reflectance maximum at a frequency of 7.35 x 10^{14} Hz and corresponds to the frequency at which the grating-coupled ±2 SPP modes are excited. It is immediately obvious that the form of the SPPs coupled to by first and second order processes are very different. The former gives rise to a reflectance minimum and the latter to a reflectance maximum. To produce a reflectance minimum there must be destructive interference between the reflected and re-radiated light whilst a reflectance maximum implies constructive interference. The corollary is that a 180° difference exists in the relative phase of the re-radiated light from the two different orders of the SPP. To explain this

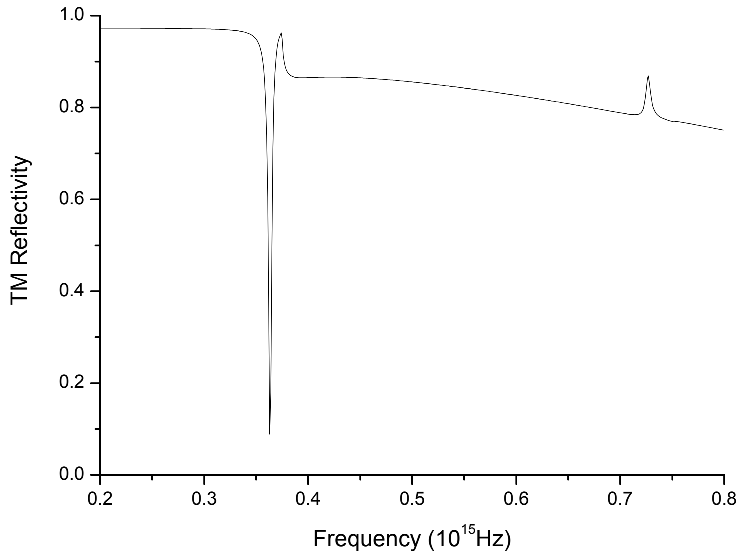

Figure 3.13. Zero-order TM reflectivity as a function of frequency for a 1μm pitch 30nm amplitude sinusoidal silver grating for normal incidence and $\phi = 0°$. Three features are evident; at f = 0.36x10^{15}Hz a SPP minimum due to the first order SPP, at f = 0.37x10^{15}Hz a pseudo critical edge due to the 1st diffracted order becoming evanescent, and at f = 0.735x10^{15}Hz a small reflectivity maximum due to the second order SPP (courtesy of I. R. Hooper).

behaviour the coupling mechanisms that result in the re-radiation of light from each SPP are considered. Incident light that is to be re-radiated by the first order SPP initially undergoes a 90° phase change when scattered into the first diffracted order. The SPP is a forced, damped oscillator and as such is driven 90° out of phase with respect to the evanescent diffracted order resulting in a 180° phase change of the SPP relative to the incident light. The reverse process resulting in light re-radiated by the SPP is accompanied by a further change in phase of 180° meaning that the re-radiated light is in-phase with the incident light. To account for destructive interference between the specularly reflected light and the re-radiated light this means that the reflected light is 180° out-of-phase with the incident light. For an optically thick film this is indeed the case and leads to the reflectance minimum of figure 3.13. The phase argument is easily extended to explain the reflectance maximum observed for the second order SPP. Light that is scattered into the second diffracted order does so via a two-scatter process; the light is scattered twice by the primitive reciprocal lattice vector. To couple into the second order SPP the light therefore experiences an extra 90° change of phase. Likewise, an extra 90° change of phase occurs in the reverse process, as the SPP re-radiates, resulting in a total phase change relative to the incident light and first order SPP of 180°. Therefore the re-radiated light from the second order SPP is *in-phase* with the directly reflected light to produce a reflectance maximum in figure 3.13. The effect is small compared to the reflectance minimum of the first order SPP as the probability of a two-scatter process is far less than that of a single-scatter process.

As described for prism-coupling, the shape of the resonance is determined by the relative amounts of radiative and non-radiative damping and the interference of the re-radiated light with the directly reflected light. In grating-coupling the amount of energy from the incident field coupled into the SPP is altered by varying the amplitude of the grating – deeper gratings result in increased diffraction and increased coupling of energy into the SPP. Figure 3.14 illustrates how varying the amplitude of the fundamental harmonic component a_1 affects the form of the –1 SPP resonance and critical edge in reflectance spectra. For shallow gratings the resonance appears as a shallow, but sharp feature increasing in depth as the amplitude is increased. Optimum coupling of energy into the SPP mode is achieved for an amplitude of ~20 nm. At this point the intensity of light re-radiated by the SPP matches exactly the

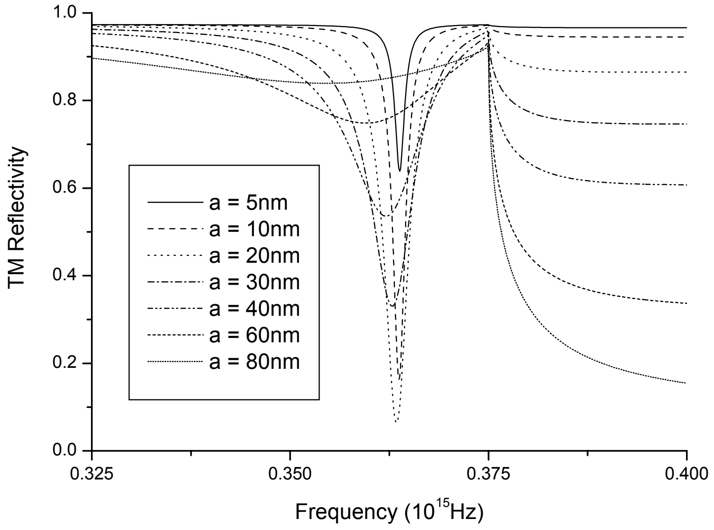

Figure 3.14. Zero-order TM reflectivity as a function of grating amplitude a_1. Other grating parameters as for figure 3.13 (courtesy of I. R. Hooper).

intensity of the light directly reflected and is in anti-phase. The reflected light and re-radiated light interfere destructively and the energy is absorbed within the metal. As the amplitude is further increased the SPP becomes over-coupled leading to a broadening of the feature with a concomitant decrease in the depth of the resonance.

The second order SPP is also influenced by the variation in amplitude of the fundamental grating component. As the amplitude is increased the reflectance maximum associated with the mode increases and is broadened. In figure 3.13 the feature is observed to be small compared to the first order SPP. This is explained by considering the relative intensities of the diffracted orders that provide the coupling mechanism between light and the SPP. The ± 1 diffracted orders are more intense than the ± 2 and higher diffracted orders since first order diffraction requires a single scattering event and second order diffraction requires a less probable double scattering event.

The introduction of a 2**b** component to the grating profile, characterised by the amplitude a_2 and phase φ_2, allows light to be diffracted directly into the second order altering the coupling of radiation into and out of the SPP mode. This can lead to features that are a) much larger since single scattering processes are more likely to occur, and b) appear as minima since the single scattering process leads to the re-radiated light being in anti-phase with the specularly reflected light. Furthermore, with the addition of a first harmonic to the profile there are now two principal routes for light to be coupled into the first diffracted order. Firstly, light can be scattered by the primitive reciprocal lattice vector **b**, a single-scatter event. Secondly light can be scattered through a combination of the 2**b** and **b** reciprocal lattice vectors, a double-scatter event. However, since the amplitude of the diffracted field associated with the latter is small any modification will also be small.

With the addition of further distortions of the surface profile in the form of higher harmonics the form of the SPP is increasingly modified. The more complex the grating profile is the greater the number of mechanisms that exist for the coupling of light into the SPP. Inclusion of only the first two harmonics of a grating is sufficient to allow the accurate modelling of grating structures fabricated, for instance, by interferometric UV lithography. However, the periodic structures described in this thesis are rather more complicated and cannot be described by a simple Fourier series expansion. Nevertheless, the points raised in the previous sections remain valid and as such provide the basis for understanding some of the features observed in reflectance and transmittance spectra. The sensitivity of the optical response of gratings to the grating profile, and the accuracy of theoretical models, allows the profile of a grating described by a Fourier series to be accurately determined [*Pockrand (1974), Pipino (1994), Wood (1995)*].

3.11 Two dimensional grating structures

Up to this stage the discussion of grating-coupled SPP modes has centred on the optical response of one-dimensional grating structures (surfaces modulated along one direction). If a second modulation is superimposed on the original surface with a different azimuthal orientation then the resulting surface has periodicity in two directions and is referred to as a two-dimensional grating. Figure 3.15 is a representative diagram of a two-dimensional grating with square symmetry. Shown are the primitive real-space lattice vectors, $\mathbf{a}_1$ and $\mathbf{a}_2$ each with grating pitch λ_G and the direction of the corresponding primitive reciprocal lattice vectors $\mathbf{b}_1$ and $\mathbf{b}_2$. The conventions that previously defined the

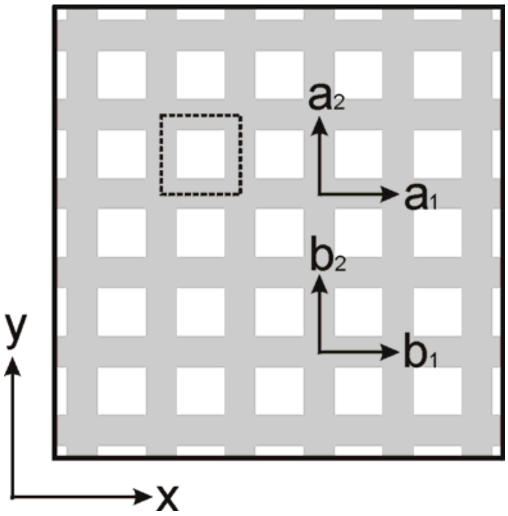

Figure 3.15. Representation of a square lattice in real-space. Shown are the primitive real-space lattice vectors a_1 and a_2 and the orientation of the corresponding primitive reciprocal lattice vectors b_1 and b_2. The dotted outline shows the unit cell of the structure.

angle of incidence θ and azimuthal angle φ are continued where it is emphasised that φ = 0° is set so that in this orientation the plane of incidence is parallel to the primitive reciprocal lattice vector denoted as $\mathbf{b}_1$. For a square lattice the reciprocal and real-space primitive lattice vectors are collinear. This is not always the case and the general relation

$$\mathbf{b}_i \cdot \mathbf{a}_j = 2\pi\delta_{ij}, \tag{33}$$

where $\delta_{ij} = 1$ if $i = j$ and $\delta_{ij} = 0$ if $i \neq j$ defines the primitive real space and reciprocal lattice vectors for any periodic structure.

The reciprocal lattice vectors **G** are now given by a slightly modified version of equation (25),

$$\mathbf{G} = n\mathbf{b}_1 + m\mathbf{b}_2, \tag{34}$$

where n and m are integers (positive or negative) and denote the order of diffraction. This equation can be used to map out the scattering centres in reciprocal space and for a square grating result in a square lattice of points, shown in figure 3.16. The (1,0) reciprocal lattice point denotes scattering by the single primitive reciprocal lattice vector $\mathbf{b}_1$, from equation (34) n = 1, m = 0, and is equivalent to equation (26). The (0,1) reciprocal lattice point denotes scattering by $\mathbf{b}_2$ (n=0, m=1) and the (1,1) reciprocal lattice point scattering by both $\mathbf{b}_1$ and $\mathbf{b}_2$ with a resultant magnitude of $\sqrt{2}|\mathbf{b}|$. All integer combinations are possible, including those with negative values.

Each of the reciprocal lattice points acts as a source for the scattered light cones and SPP modes as described in section 3.9.2. By assigning the z-axis as the frequency in reciprocal space diagrams it is possible to map the dispersion of the scattered light cones and SPP modes. Considering initially the dispersion of the light cones, if a section in the k_x-k_y plane is taken at increasing values of frequency, concentric circles of increasing diameter are produced (figures 3.16(a)-(d) where negative values of m and n are represented by $\overline{m}$ and $\overline{n}$). If the plane of incidence is taken to be parallel with the k_x axis, in figure 3.16(b) only those modes associated with (1,0) and (-1,0) diffracted orders will be observed within the radiative region (shaded). Eventually the light cones associated with the scattering centres away from this axis will intersect with the ω-$k_{//}$ plane. This is shown in figure 3.16(c) and corresponds to the lowest

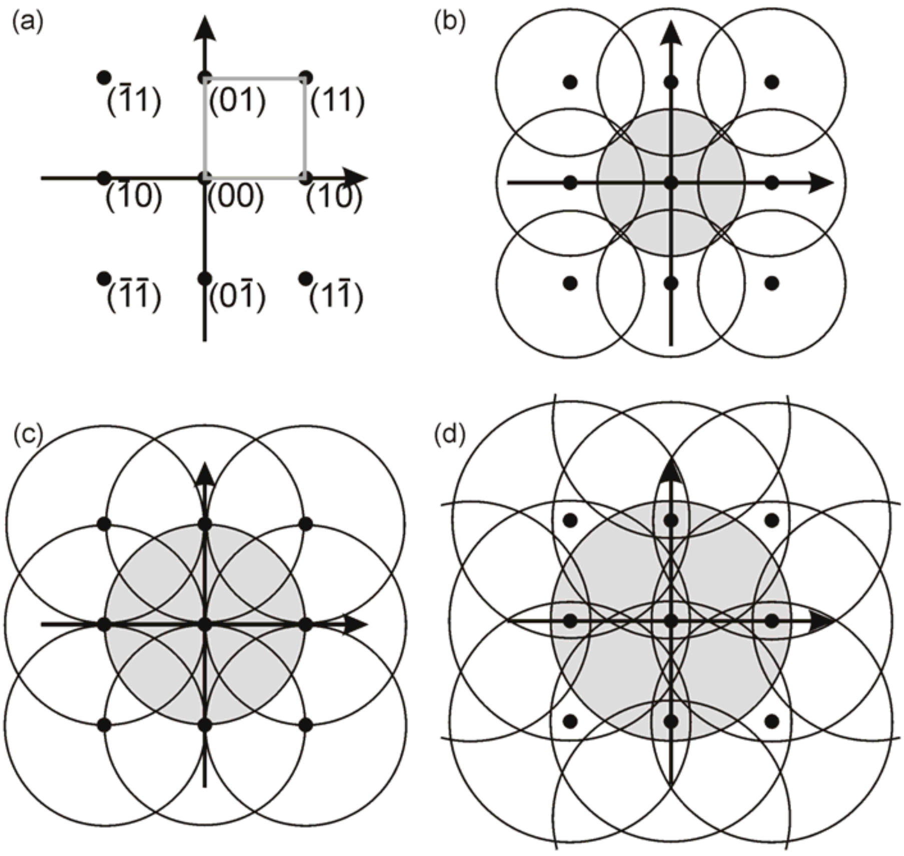

Figure 3.16. Reciprocal space diagrams illustrating the scattering centres associated with the first- and second-order grating vectors. Each diagram (a)-(d) represents sections taken through reciprocal space in the k_x-k_y plane for increasing values of frequency ω. The shaded region is the radiative zone.

frequency at which the ‘off-axis’ modes will be observed in a dispersion curve plot. In figure 3.16(d) the (2,0) and (-2,0) modes are within the radiative region and would be observed in optical measurements at frequencies higher than that for a lower order mode with an equivalent $k_{//}$. Neglecting any perturbation of the modes the photonic band structure for a square grating in the classical mount is that shown in figure 3.17. The parabolas are associated with the scattering centres located away from the $k_{//}$ axis. By symmetry the modes (n_1,m_1) and (n_2,m_2) are degenerate for all ω and $k_{//}$ values if $n_1 = n_2$ and $m_1 = -m_2$. Other degeneracy conditions exist for any orientation of the plane of incidence that is parallel to a line of symmetry of the grating in reciprocal space.

The co-ordinate system is defined with respect to the grating meaning that the reciprocal lattice vectors are independent of the azimuthal angle. This is not the case for the plane of incidence, so for gratings oriented in the conical

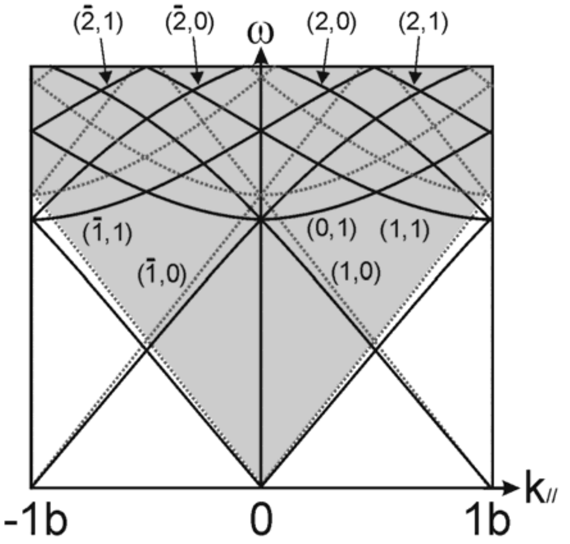

Figure 3.17. Schematic diagram illustrating the scattered light-lines (dotted) and SPP modes (solid) for a two-dimensional square grating (negative values of *m* and *n* are represented by $\overline{m}$ and $\overline{n}$. The (*n,*1) modes are degenerate with the (*n*, $\overline{1}$) modes.

mount (plane of incidence not collinear with a grating vector) the in-plane wave vector will consist of two components $k_{//x}$ in the (1,0,0) direction and $k_{//y}$ in the (0,1,0) direction with the resultant magnitude given by $k_{//} = k_0 \sin\theta$ and the component magnitudes given by

$$\begin{aligned} k_{//x} &= k_0 \sin\theta \cos\varphi, \\ k_{//y} &= k_0 \sin\theta \sin\varphi. \end{aligned} \tag{35}$$

These expressions with equation (34) can then be substituted into the condition for the grating-coupling of light into SPP modes (equation (28)) to generate the unperturbed dispersion of the SPP modes. In real structures it is likely that the mode dispersion will differ from that of this simple theory through interactions between the scattered modes and confinement within certain types of structure.

3.12 SPP photonic bandgaps

Analogous to the *electronic* energy band gaps set up in crystals, energy band gaps exist in the dispersion relation for the propagation of light through structures with some modulation of the refractive index on the scale of the wavelength of light. These *photonic* bandgaps were predicted by *Yablonovitch*

(1987) to prevent the propagation of light through such structures in the frequency range of the bandgap. To provide experimental evidence for their existence a three-dimensional *macroscopic* photonic crystal in the microwave regime was designed, thus avoiding the fabrication difficulties associated with optical structures [*Yablonovitch (1993)*]. Photonic stop-bands and bandgaps may also be set up on metallic structures with one-dimensional (single-grating) and two-dimensional (bi-grating) periodicity respectively. Grating induced stop-bands were first reported by *Ritchie (1968)* in the dispersion of SPP modes propagating on a corrugated metallic surface. Since these modes are by their nature confined to an interface it is possible to entirely prohibit their propagation on surfaces that exhibit a full two-dimensional SPP bandgap. This was first observed experimentally by *Kitson (1996)* on a silver surface patterned with a hexagonal array of bumps. *Barnes (1995, 1996)* previously explained the origin of the SPP photonic gaps by formulating an analytical theory based upon the Chandezon technique.

Consider a SPP propagating perpendicularly to the grooves of a grating (the grating is in the classical mount) with a surface profile represented by a function $A(x)$ including two terms, a fundamental and first harmonic

$$A(x) = a_1 \sin bx + a_2 \sin(2bx + \varphi_2), \tag{36}$$

where the terms are as defined in section 3.10. The reciprocal lattice vector b couples normal incidence radiation into forward and backward propagating SPPs whilst the $2b$ reciprocal lattice vector couples these modes together. The counter-propagating SPPs interfere to form two different standing waves with distinct field profiles; one with field maxima at the peaks associated with the $2b$ component and one with field maxima at the troughs associated with the $2b$ component. The field distributions of each mode are different and therefore exist at different energies (frequencies). This results in a gap in the dispersion curve of the SPPs at the point in reciprocal space where the (1) and (-1) modes cross. In the dispersion diagram, figure 3.11(a), this occurs at $k_{//} = 0$. Similar arguments hold for other pairs of grating coupled SPPs. For instance, a gap is formed at $k_{//} = 0$ when the (2) and (-2) modes are coupled together by a $4b$ scatter and at $k_{//} = b/2$ when the (-1) and (2) are coupled together by a $3b$ scatter.

The presence of the 2*b* component is not essential for the formation of a bandgap since it is possible to couple the counter-propagating SPP modes via a two-scatter process. However, the likelihood of this occurring is far less than for a single 2*b* scattering event provided the amplitude a_1 of the fundamental grating component is small. An important influence the 2*b* component has on the SPP coupling characteristic is the effect of changing its phase relative to the *b* component. *Barnes (1996)* considered three cases for the phase of the 2*b* component, $\varphi_2 = 0°$, $\varphi_2 = +90°$ and $\varphi_2 = -90°$. For $\varphi_2 = -90°$ the troughs of the 2*b* component coincide with the slope of the *b* component whilst the peaks coincide with the peaks and troughs. Now recall that a requirement of coupling to the SPP mode is a component of the incident electric field perpendicular to the surface. For normally incident radiation the low energy SPP mode has field maxima at the peaks of the 2*b* component and at the peaks and troughs of the *b* component. Therefore at these points there is no component of electric field from a normally incident beam perpendicular to the surface and the low energy mode cannot be excited. The high energy mode has field maxima at the troughs of the *b* component, coinciding with the slopes of the 2*b* component and there is now a component of the normally incident field perpendicular to the surface; coupling can occur. The opposite is true for a phase $\varphi_2 = +90°$, the low energy mode is excited and the high energy mode is not. With no phase difference between the components both modes are equally coupled. The above discussion illustrates the importance of a perpendicular field component in coupling to the SPP mode.

3.13 Summary

This chapter has described many of the properties of the surface plasmon polariton, a coherent oscillation of the electron plasma at the interface between a metal and a dielectric with a mixed longitudinal and transverse character. The dispersion relation for the SPP mode was derived from which it was shown that the electromagnetic fields associated with the SPP decay exponentially into the surrounding media. Furthermore by comparing the dispersion with that of the light line associated with an incident electromagnetic wave it was evident that the mode on a planar interface is non-radiative. To enable excitation of the

SPP by incident electromagnetic radiation required the use of prism or grating-coupling techniques with the latter described in detail.

Chapter 4

Fabrication of patterned nanoscale structures using nanosphere lithography

4.1 Introduction

A limiting factor in the study of periodic metallic nanoscale structures is the fabrication of features with a uniform size and shape. In general, extremely advanced and complex techniques are required to produce structures with the regular dimensions required to allow an investigation of the many interesting effects that can be observed. A particularly versatile system employs a focussed ion-beam (FIB) to mill features directly into surfaces by a ballistic process. Focussed ion-beam milling affords the greatest versatility of all the fabrication techniques, enabling not only controlled milling with a resolution of 5-10 nm, but also controlled material deposition on length scales of this order. The related technique of electron (e-) beam lithography writes features into an electro-sensitive mask by focussing an electron beam with comparable resolution to that of the FIB. Both techniques work on the same principle as a scanning electron microscope (SEM) and in many cases the e-beam systems are converted SEMs. The motivation behind developing these techniques lies in the impressive resolution and control that is afforded to the user enabling the fabrication of many types of structures that exhibit interesting optical effects. However, they are handicapped in particular by the high cost of the systems, serial manufacture of samples and (on a macroscopic scale) the small area of the sample that may be patterned. Photolithographic techniques such as ultra-violet (UV) lithography permit the fabrication of large areas, but with relatively low resolution, limited by diffraction. To cope with the increasing demand for nanoscale structures new methods are being investigated that provide accurate control of feature size and shape, combined with low cost and parallel sample manufacture. Techniques that offer such attributes include diffusion controlled aggregation at surfaces [*Roder (1993)*], laser focussed atom deposition

[*McClelland (1993)*] and the chemical synthesis of metal particle colloids [*Jin (2001)*]. A versatile and conceptually simple technique for the fabrication of both two-dimensional and three-dimensional structures is the assembly of ordered arrays of sub-micron colloidal spheres (nanospheres). The structures formed using this technique have found many applications including the formation of photonic band-gap crystals [*Dinsmore (1998)*], as optical microlenses in image processing [*Hayashi (1991)*] and as models for the investigation of physical phenomena such as crystallisation, melting and phase transitions [*Murray (1998)*]. In these applications the arrays are used ‘as is’, without further processing. Applying subsequent fabrication steps by using the ordered arrays as deposition templates and etch masks yields other types of structure. These extended techniques are the focus of this chapter, in particular the use of nanosphere arrays as lithographic masks to fabricate metallic nanostructures. The *van Duyne*[1] group coined the phrase nanosphere lithography [*Hulteen (1995)*] to describe the method and the first below section details the basic concept and the types of structure that have been fabricated using this technique. This is followed by a review of a variety of methods for ordering the nanospheres into hexagonal arrays, leading to a detailed description of the method used at Exeter. The subsequent processing of the arrays to form periodic arrays of metallic particles and periodic arrays of holes in metallic films is described, including thermal evaporation and reactive-ion etching techniques.

4.2 Nanosphere lithography

Most forms of lithography proceed via three basic steps. Firstly, a mask perforated with an array of apertures is fabricated usually supported by a substrate; secondly, material is deposited onto the mask and through the apertures; thirdly, the mask is removed (a process known as lift-off) leaving the deposited material on the substrate. Subsequent processing of the pattern by dry etching, wet etching or further lithographic steps may then be used to yield alternative structures. Nanosphere lithography is an easily implemented, low-

---

[1] North Western University, USA

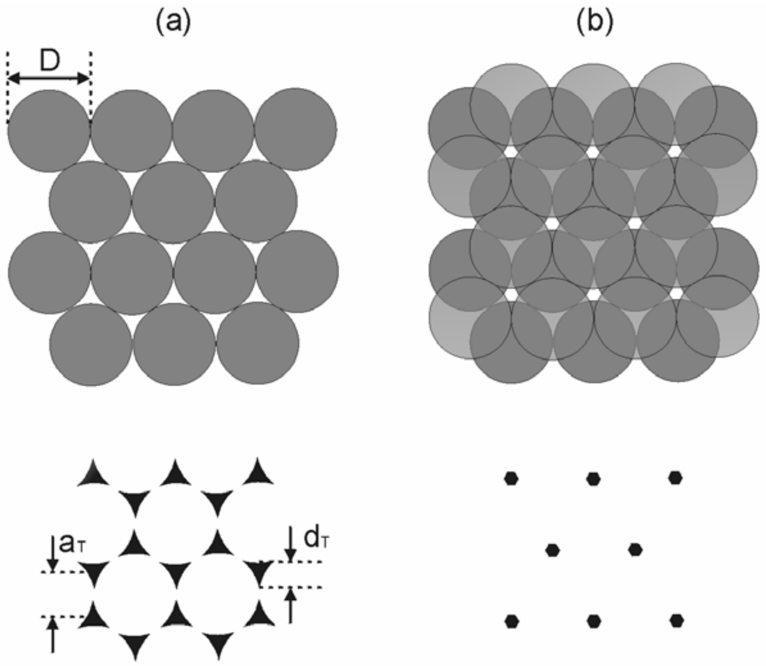

Figure 4.1. Schematic representation of a hexagonally close-packed nanosphere array and the resulting nanoparticle array formed from a monolayer (a) and a bilayer (b).

cost and versatile technique that uses a single layer (monolayer) or double layer (bilayer) array of hexagonally close-packed spheres with a diameter of less than a micron as the mask in the first step. The self-assembly of latex nanospheres into a mask was first utilised by *Fischer and Zingsheim* in 1981 for contact imaging with visible light, and further developed by *Deckman* in 1982 as a mask for patterned material deposition and reactive ion etching across macroscopic areas. Material deposited onto the array passes through the gaps between the spheres and collects on the supporting substrate. After removal of the spheres an array of particles remain of sub-micron dimensions as shown in figure 4.1. When viewed from above the monolayer of nanospheres produces an array of triangularly shaped nanoparticles with a perpendicular bisector d_T and centre-centre separation a_T given by

$$d_T = D\left(\sqrt{3} - \frac{3}{2}\right) \qquad \text{and}$$

$$a_T = \frac{D}{\sqrt{3}}$$

where D is the diameter of the nanospheres. With a bilayer of nanospheres every other interstice is covered resulting in an array of hexagonally shaped nanoparticles. The distance between opposite sides d_H and the interparticle separation a_H are given by

$$d_H = D\left(\frac{2}{\sqrt{3}} - 1\right)$$

$$a_H = D.$$

By varying the diameter of the nanospheres the lateral dimensions of the resulting particles may be controlled with an accuracy governed by the size dispersity of the nanospheres. The height of the particles is controlled by the amount of material deposited through the array with the maximum height less than the radius of the spheres. Deposition of material with a thickness greater than the radius of the spheres results in a continuous film preventing lift-off of the mask.

A direct legacy from the pioneering work of *Deckman* and co-workers, the studies of the *van Duyne* group extended their approach by fabricating periodic arrays of noble metal particles from monolayer and bilayer arrays of spheres across a sufficiently large area to enable detailed investigations of their optical and structural characteristics [*Haynes (2001) and references therein*]. Other groups have looked at alternative types of photoactive materials such as semiconducting metal oxides [*Bullen (2002)*]. Titanium oxide (TiO_2) nanoparticles were fabricated with a view to investigating their photocatalytic properties. The size dependence of the magnetic properties of materials is also of interest and this has been studied by fabricating nickel (Ni) and cobalt (Co) particle arrays using nanosphere lithography [*Rybczynski (2003), Wiesendanger (1997)*]. Further applications of sub-micron Ni dots formed by nanosphere lithography are as catalysts for the growth of carbon nanotubes [*Huang (2003), Kempa (2003)*] and carbon nanoflakes [*Wang (2004)*].

The basic technique described above is easily extended to allow the fabrication of alternative types of structure. Conventionally material is deposited at an angle that is perpendicular to the plane of the substrate. Depositing material at an angle to the sample enables the fabrication of a number of nano-gap, nano-overlap, chain and wire structures [*Haynes (2002, 2003), Kosiorek (2004)*]. Possible applications might involve utilisation of the optical properties of the high aspect ratio particles from nano-overlap structures in chemical and biological sensing. Recently angular deposition has been combined with a reactive ion etch to fabricate pores in silicon substrates with a three-fold reduction in size relative to pores fabricated with the sample directed normally [*Whitney et al. (2004)*].

The addition of a RIE step, where material is removed from a surface by chemical reactions and physical bombardment with a gaseous plasma, greatly enhances the versatility of nanosphere lithography. The nanosphere arrays may be used as an etch mask or alternatively used to produce a patterned resist that may subsequently be used as an etch mask. *Deckman and Dunsmuir (1982)* used a conventional array of nanoparticles formed by nanosphere lithography as an etch mask to produce an array of pillars in silica. *Russell et al. (1987)* used this type of structure to produce spheroidal particles by the evaporation of silver at an angle. This coated the tips of the pillars with the silver and subsequent annealing allowed investigation of the optical properties of the resultant particles and a direct comparison with *Mie* theory [*Mie (1908)*]. Alternatively, by selecting a process gas appropriate for etching the nanospheres (and not the substrate) it is possible to reduce in a controlled manner their diameter whilst maintaining the lattice parameters of the crystal. Thus it is possible to fabricate arrays of larger particles and arrays of holes by etching the nanospheres prior to evaporating the material. This extra step in the fabrication process was first incorporated by *Haginoya (1997)* who successfully fabricated arrays of holes in silicon. After etching the nanospheres a Pt-Pd alloy was thermally evaporated to form a perforated resist layer. After sphere lift-off the resist pattern was transferred into the silicon substrate by selectively etching the circular regions of silicon not covered by the Pt-Pd mask. Recently there have been several papers published that illustrate the increased versatility of nanosphere arrays in the fabrication of patterned substrates by incorporating a reactive ion etch [*Wellner (2001), Kuo (2003), Choi (2004)*]. An extension of the work of *Haginoya* was employed by *Weekes (2004)* who formed nanosphere arrays on a 200 nm layer of SiO_2 evaporated onto copper (Cu) and Titanium (Ti) films. After etching the spheres a magnesium fluoride (MgF_2) mask was evaporated onto the samples and spheres removed. Holes were then etched through the silica layer to the conductive Cu or Ti film and following electrodeposition arrays of cylindrical Co and Ni particles formed.

Some interesting architectures are generated when nanospheres are ordered upon substrates that are pre-patterned to act as a template for crystal growth. Striped, square, centred-rectangular and hexagonal arrays have been formed on one-dimensional and two-dimensional grating structures by evaporative self-assembly [*Ye (2001b)*] and entropic depletion [*Lin (2000)*]. Controlled aggregation of colloidal particles has also been demonstrated by manipulating spheres via a controlled flow of solution across a patterned surface [*Xia (2003)*]. The spheres drop into cylindrical holes etched into the surface to form aggregates of a consistent pattern defined by the geometrical parameters of the hole.

The work in this thesis requires the use of several of the fabrication methods described above beginning with the formation of arrays of silver particles using the standard nanosphere lithography technique. Investigations of the optical properties of particles with varying size contained in changing optical environments are described in chapter 5. The basic technique is extended with the incorporation of a RIE stage. The principal aim is to reduce steadily the diameter of the nanospheres and then evaporate silver onto the modified array. Arrays of silver particles of increasing size are produced until eventually they merge to form periodic arrays of holes in an otherwise continuous metallic film. This is described in more detail in section 3.7 and chapters 6 and 7. The first step in nanosphere lithography is the formation of arrays of well-ordered nanosphere arrays and this is outlined in the following section.

4.3 Assembly of nanospheres into ordered arrays

The major drawback in the use of nanospheres to form both two- and three-dimensional structures is the relatively high density of dislocation and vacancy defects. This has limited their use in industrial applications and complicated the optical response from the structures formed directly and indirectly from the nanosphere arrays. A number of strategies have been developed for the ordering of nanospheres into crystalline structures with emphasis placed on reducing the density of defects. The most popular and easily implemented ordering processes involve the controlled evaporation of the fluid in which the nanospheres are contained. This acts to produce fluid flow within the solution that forces the nanospheres towards the meniscus of the colloid where crystal growth occurs. Alternative methods physically confine the solution within a container and subsequently promote the growth of a crystalline array either by applying mechanically induced shear forces or by introducing a flow within the cell. It is also possible to form the crystalline structures at gas-liquid interfaces under certain conditions and these can be subsequently transferred to a solid substrate. More detailed descriptions of each of the methods follow.

4.3.1 Arrays formed at gas-liquid interfaces

A versatile strategy capable of producing large area (several cm^2) two-dimensional ordering of colloidal spheres on solid substrates initially forms the structure at a gas-liquid interface. A spreading agent (for example methanol) is required to disperse the colloidal solution onto the surface of a liquid sub-phase and the spheres aggregate into a two-dimensional structure [*Hurd (1985)*]. The extent to which this occurs is dependent upon the size and concentration of the spheres, surface chemistry of the spheres and composition of the sub-phase. The self-assembly of polystyrene latex spheres at an air-liquid interface was first observed by *Pieranski (1980)*. Hexagonally ordered arrays of 245 nm diameter spheres were formed at the surface of a thin layer of water. The centre-centre distance of the spheres was significantly larger than their diameter indicating the presence of a repulsive interaction. The nature of the repulsive force is electrostatic resulting from the like-charged surfaces of the spheres. To overcome the electrostatic repulsion an electrolyte solution may be used as the sub-phase, recent studies by *Rybczynski (2003)* yielding monolayer areas of several cm^2 with nanosphere diameters ranging between 400 and 1000 nm. The influence of the dissociated ions within the electrolyte is two-fold, acting to prevent the miscibility of the nanospheres with the sub-phase and to reduce the electrostatic repulsion between nanospheres by a screening effect.

In order to perform lithographic applications with arrays formed on liquid surfaces they must be transferred from the air-liquid interface onto the surface of a solid substrate. There are a number of techniques to achieve this. In the Langmuir-Blodgett technique a substrate is dipped through the array whilst it is continually compressed to maintain the packing density. As the substrate passes into the subphase the array is transferred onto the substrate. A number of groups have successfully transferred arrays to solid substrates using the Langmuir-Blodgett technique obtaining monolayer areas as large as several square centimetres [*Lenzmann (1994), Fulda (1994)*]. Alternatively transferral is achieved by contacting the spheres to a horizontal substrate lowered onto the surface yielding similar results [*Fulda (1994)*].

4.3.2 Physical confinement

Enclosing the spheres entirely within solid boundaries can produce crystalline structures with a reduced density of defects compared to other techniques. Typically ordering occurs between two planar substrates sandwiched together, their separation governing the thickness of the resulting nanosphere structure. *Xia* and co-workers [*Lu (2001), Park (1998)*] describe methods that produce large scale (several cm^2) areas of three-dimensional structures using nanospheres ranging in size from 50 nm to 1 μm. The colloidal solution is injected between two glass substrates, the top substrate having been treated in an organic vapour ($C_6F_{12}C_2H_4SiCl_3$) to make the surface non-sticky to polystyrene beads. The edge of the cell is sealed by a patterned photoresist with channels along the bottom face that are large enough to allow fluid to flow out of the cell, but narrow enough to retain the nanospheres. A positive pressure of nitrogen is applied to force the fluid through the channels and induce a flux of nanospheres within the cell. Close-packed arrays form near to the channels with crystal growth progressing across the cell as more spheres are forced towards the ordered phase. The cell is sonicated throughout and then baked after the ordering process is completed to remove any remaining solvent. Monolayers and multilayers of a well-defined thickness can be produced using this method by varying the thickness of the cell. The main limiting factor is the thickness of the photoresist, values quoted by *Park (1998)* ranging between 0.5 μm and 50 μm.

An alternative scheme uses a mechanically induced shear force to order nanospheres confined between two substrates into multilayer structures [*Amos*

(2000)]. Large area domains consisting of close-packed structures were observed with the type of lattice (hexagonal close-packed, face-centred cubic or combination of the two) dependent on the direction and amplitude of the shear force. The best quality nanosphere arrays formed by these techniques tend to consist of three-dimensional multilayer structures unsuitable for lithographic applications.

4.3.3 Evaporation

Conceptually the simplest method of assembling nanospheres into ordered structures is by evaporation of colloidal solution dropped onto a suitable substrate. The self-assembly of nanospheres into specific crystalline structures requires the careful preparation of the substrate surface and subtle regulation of the environmental conditions. By selecting an appropriate amount of solution and controlling the rate of evaporation it is possible to control the formation of monolayer and multilayer arrays of nanospheres. The main parameters to consider are the concentration of the solution, humidity and temperature of the ambient conditions, and tilt angle of the substrate. Appropriate values for each are required for spheres of a specific composition and diameter to optimise the ordering process.

Several research groups have investigated the influence of these parameters on array formation with the objective of reducing the concentration of defects and increasing domain size. *Denkov et al*. *(1992, 1993)* examined in detail the ordering of monolayer films by observing through a microscope the movement of nanospheres deposited onto a glass substrate. The nanospheres were dropped onto an area of the substrate bounded by a Teflon ring with an inner diameter of 14 mm. The resulting profile of the drop is concave when viewed from the side with a smallest depth at the centre of the drop. As water evaporated, a monolayer of spheres begins to form at the centre progressing outwardly as the edge of the meniscus retreats towards the ring. By direct observation they were able to propose a mechanism for the formation of arrays of nanospheres and this is described in detail later (section 4.4). *Micheletto (1995)* demonstrated a slightly different procedure whereby a glass substrate thermally stabilised by a Peltier cell is tilted to initiate ordering at the top edge of the meniscus. This technique was repeated in a study by *Rakers et al. (1997)* on the effect of altering the evaporation rate on the size and quality of the arrays. Mean sphere diameters of 80 nm and 220 nm were used and the temperature varied from 2-25 °C. It was found that the packing order at low temperatures was improved compared to that at higher temperatures for the 80 nm diameter spheres whereas for the 220 nm spheres there was little or no dependence on temperature in this range. *Ye et al. (2001a)* have also conducted experiments in which the temperature was varied. They used a vertical deposition technique whereby a substrate is immersed vertically in a colloidal solution and placed in an oven. As the water evaporates the level of the solution on the substrate falls whilst spheres order at the contact line between the fluid and the substrate. After the drying process is completed two-dimensional or three-dimensional crystals are left on the substrate with the thickness of the crystal dependent on the initial conditions and evaporation rate. The diameter of the spheres used were 310 nm with the best crystal quality obtained when the temperature was 55°C. A more comprehensive study by *Kuai (2004)* using the same deposition technique also investigated the effect of evaporation rate by varying the temperature and relative humidity, on this occasion using bead diameters of 300 nm and 596 nm. They found optimal conditions for ordering to be a temperature of 60 °C, relative humidity of between 80% and 90% with an initial volume fraction of spheres in the colloid ranging between 0.1-0.2%.

To obtain a crystal with highly ordered structures across a large area requires the subtle variation of a number of parameters. Temperature, humidity, concentration of the colloid and tilt angle of the substrate all influence the quality of the nanosphere crystal with the added complication that the optimal conditions depend strongly upon the diameter and composition of the nanospheres.

4.4 Dynamics of evaporative self-assembly

A mechanism for the self -assembly of colloidal spheres on solid substrates has been suggested by *Denkov et al. (1992)* for samples fabricated using the technique described in Section 3.2.3. They identified two dominant processes:

- Lateral capillary attraction between spheres due to the deformation of the meniscus in water films with a depth less than the diameter of the sphere.
- Convective flow of spheres due to the increased evaporation rate from ordered regions relative to the bulk solution.

In their system the two processes run consecutively with the capillary attraction sometimes referred to as the *nucleation* stage and the convective flow as the *growth* stage.

Nucleation occurs when the thickness of the water layer is approximately equal to the sphere diameter. Because the spheres are physically constrained in the vertical direction by the presence of the substrate a deformation of the water surface develops that gives rise to strong and long-range attractive capillary forces. These are known collectively as immersion forces arising principally from the wetting properties of the particle such as the contact angle and position of the contact line. A second group of capillary forces associated with colloidal particles are flotation forces. The particles are contained in a bulk dispersion medium and float at the liquid-gas interface; there is no physical constraint other than the liquid-gas interface. The effect of gravity on the particles operating against their buoyancy generates a deformation of the meniscus and is therefore the origin of the attractive or repulsive force between the particles. The perturbation of the wetting film by a particle floating at a surface is limited by the buoyancy and weight of the particle. Small and light particles do not cause a significant deformation of the wetting layer and therefore produce small lateral capillary forces. This is not so for a particle immersed in a thin wetting layer as it is restricted in the vertical direction. Therefore the deformation of the wetting film can be very large allowing a strong lateral force to develop even for small, light particles. Flotation forces become

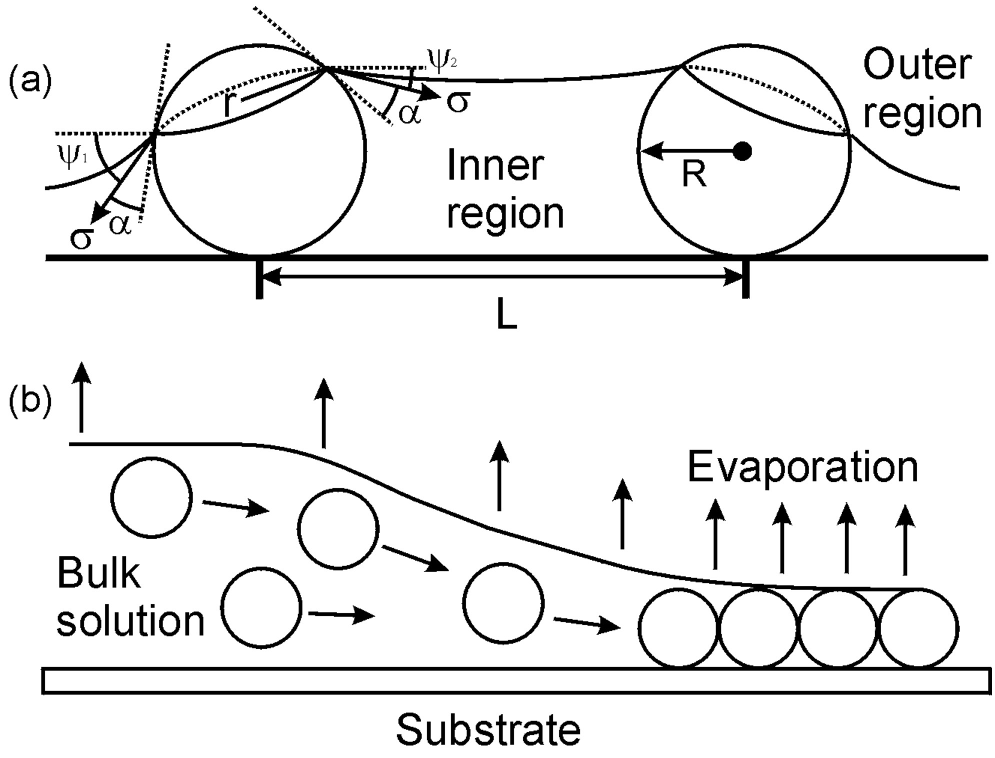

Figure 4.2. Diagrams showing two spheres partially immersed in a liquid layer on a solid substrate (a) and the convective flow of spheres from bulk solution towards the ordered phase (b). The convective flow arises from an increased evaporation rate from ordered regions resulting in a capillary flow between the spheres that draws fluid from the bulk solution.

negligible for a particle radius R ~ 10 µm where as immersion forces can remain significant compared to thermal fluctuations down to R ~ 10 nm.

The capillary forces can be either attractive or repulsive depending on whether there are similar or dissimilar interacting pairs of particles. A pair of hydrophilic particles or a pair of hydrophobic particles will attract, where as a hydrophilic and hydrophobic particle pair will repel. The main factor in determining the nature of the interaction is the meniscus slope angle ψ measured from the horizontal to a line tangential to the liquid-gas interface at the three-phase contact line (figure 4.2(a)). Hydrophilic particles have a positive value of ψ, hydrophobic particles have a negative value of ψ and for $\psi = 0$ there is no meniscus slope angle and therefore no interaction force. There are two values for identical particles, ψ_1 measured between the spheres and ψ_2 measured on the opposite side of the spheres along a line taken through the sphere centres. Differences in the magnitudes of ψ_1 and ψ_2 result in a variation of the horizontal component of the surface tension σ_x and, for the particles depicted in figure 4.2(a), a net horizontal force in a direction from the outer region to the inner region.

The formation of the ordered nucleus of spheres enables the second stage, that of the convective flow of particles towards the ordered region (figure 4.2(b). Between the closely-packed spheres in the ordered phase the profile of the meniscus has a high curvature and therefore a high evaporation rate. As the fluid between the spheres evaporates it is replaced from below by fluid contained in the bulk phase through a capillary action and spheres are observed to move towards the ordered phase. This motion occurs even when the spheres are immersed entirely within the bulk solution where the depth of the water layer is larger than the diameter of the spheres. Therefore lateral capillary forces between the particles as described above do not exist and the motion can only be explained by this convective effect. Confirmation of this premise is easily provided by direct observation of the effect of altering the local humidity on the motion of micron-sized spheres. As would be expected the ordering rate decreases as evaporation rate decreases and *vice versa*.

It should be noted that convective flow will occur towards any region that has a higher evaporation rate compared to the bulk solution. For samples, such as those fabricated in Exeter, that are prepared by dropping solution onto a substrate without a boundary the dispersion fluid will have a higher curvature at the edge of the substrate, particularly at the corners. Therefore it is likely that lateral capillary attraction and convective flow occur simultaneously.

A third force exists between adjacent spheres, that of electrostatic repulsion, and is responsible for the non-close-packed arrays of spheres observed at fluid-air interfaces in bulk solutions. The magnitudes of the forces associated with the capillary attraction and convective flow processes is much greater than the magnitude of the force associated with the electrostatic repulsion between the colloidal particles thus enabling close-packing of the spheres.

4.5 Fabrication of metallic arrays of particles and holes

The use of arrays of nanospheres as lithographic masks for the formation of metallic nanostructures fundamentally requires three fabrication steps. Firstly, fabrication of a monolayer or bilayer crystalline structure on a solid substrate; secondly, a means of depositing material across the substrate; thirdly, lift-off whereby the nanosphere mask is removed leaving the triangular and hexagonal structures of figure 4.1. In this section the methods of sample fabrication developed at Exeter are described starting with the formation of large area monolayer sphere arrays using the drop-coat method as employed by *Jensen (2000)* and *Haynes (2001)*. This is followed by a description of the thermal evaporation of metals across the arrays including a description of the lift-off technique. Finally, an extension to the basic three step process outlined above is described in which nanosphere arrays are etched in a reactive gaseous plasma to reduce the sphere diameter. This occurs prior to material evaporation and is essential to the formation of hole arrays with long-range order. The overall process is illustrated schematically in figure 4.3. An amount of colloidal solution containing the polystyrene nanospheres is drop-pippetted onto a clean substrate (1). The nanospheres order at the edge of the droplet (2) producing the types of array illustrated in figure 4.1. This is followed by deposition of the metal across the arrays illustrated for both a non-etched monolayer array (left) and etched monolayer array (right) (3). A plan view of the two types of array is shown (4) and the resulting particle array and hole array after sphere removal (5). These steps are described now in further detail beginning with the preparation of a suitable substrate surface.

4.5.1 Substrate preparation

The substrates used are fused silica (quartz) glass with an area of 25 mm x 25 mm and thickness of 1 mm. The extremely high purity of fused silica means that it has a number of advantages over traditional glass. It is non-fluorescent in the visible spectrum and near infra red; energy that would be absorbed and re-radiated by impurities in ordinary glass may instead be absorbed by lattice vibrations. It has a high degree of optical homogenity with little variation in

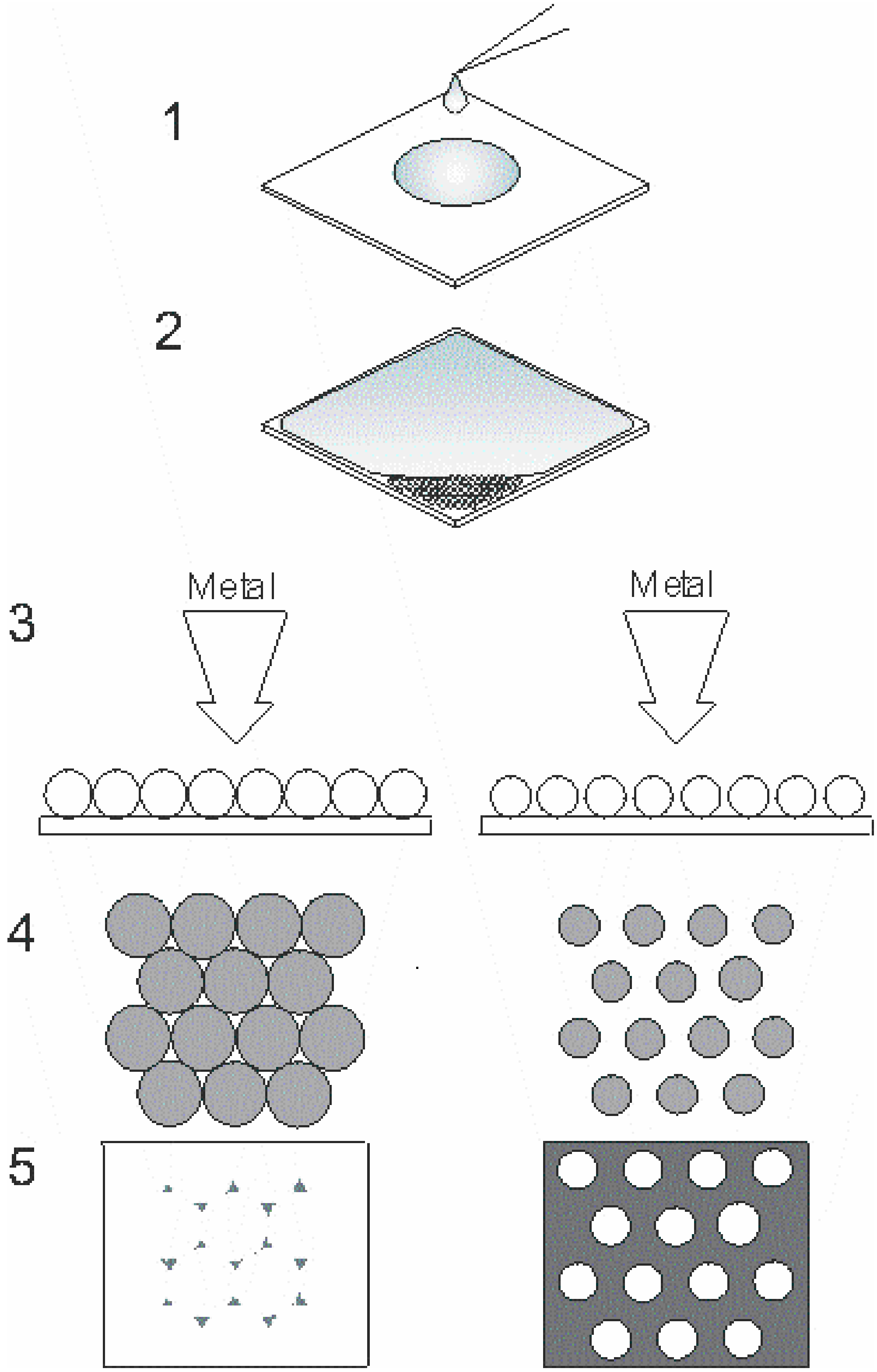

Figure 4.3. Schematic of fabrication process. (1) Drop pipette colloidal solution, (2) Ordering of nanospheres as fluid evaporates, (3) Silver evaporation onto non-etched (left) and etched (right) nanosphere arrays, (4) Plan view of arrays prior to sphere removal, (5) Particle array (left) and hole array (right) after nanosphere removal.

refractive index across a single substrate and between different substrates. It also has a higher chemical resistance with very few acids able to react with the surface (only phosphoric acid and hydrofluoric acid will react with fused silica and then to a lesser degree than traditional glass). The substrates are highly polished with a surface level variation of the order of $\lambda/10$.

The primary concern in the fabrication of arrays of spheres using the drop-coat method is the need for a clean, flat surface for the spheres to order upon. Any impurities adsorbed on the surface can affect dramatically the quality of the nanosphere crystals. Contaminants contained within the solution will also be deposited onto the surface of the substrate after evaporation of the dispersion fluid. Therefore the first stage of the surface preparation is to remove any impurities such as dust or grease by using a wet etch. The substrates, supported in a Teflon boat (Teflon container with slots cut into the sides to hold the substrates), are immersed for a minimum of two hours in a 3:1 solution of sulphuric acid (H_2SO_4) to hydrogen peroxide (H_2O_2). This is known as a 'piranha etch' and may be considered as a two-step process starting with the oxidation by the H_2O_2 of organic contaminants. The products of the reaction are then etched (broken up into soluble components) by the H_2SO_4. The time needed for this process to be effective may be reduced by maintaining the solution at temperatures in excess of 70°C. The wet etch is followed by a thorough rinse in ultrapure water obtained from an Elgastat UHQ-PS water purification system. This is a multiple filtration system supplied with mains water pre-filtered to prevent contamination by large particles. A reverse osmosis unit then removes the majority of dissolved impurities (~95%) and feeds an 80 ltr reservoir. When required, water from the reservoir is drawn into a filtration unit capable of producing water with a resistivity of > 18 MΩcm and total organic carbon content of < 20 parts per billion. The rinse is followed by a further wet chemical treatment required to render the substrate surface hydrophilic (water-loving) and to augment the piranha etch. The substrates are immersed in a 5:1:1 solution of water, ammonium hydroxide (NH_4OH) and hydrogen peroxide. The primary action of this base treatment is to create negatively charged entities at the surface of the substrate to increase the mutual attraction between the water molecules and the silica molecules. The OH^- ions in the alkaline solution bind to the surface molecules of the silica substrate, more particularly to surface Si atoms. The oxygen atom in the O-H bond is highly electronegative resulting in a polarisation charge associated with the bond and an increased probability of a hydrogen bond developing between the surface and the water molecules. Inorganic impurities tend to be hydrophobic in character and are adsorbed onto the surface when exposed to ambient atmospheric conditions. These impurities are desorbed from the surface by the combined action of the oxidising agent and alkali. The alkali promotes the negative charging of the substrate surface whilst the oxidiser promotes negative charging of the desorbed particle. The electrostatic repulsion between the negatively charged particle and substrate cause the impurities to be removed and prevents further readsorption onto the surface. The final stage of the substrate preparation is a further rinse in ultrapure water until the pH of the rinse matches that of the water. The cleaned substrates are stored in ultrapure water to preserve the hydrophilic nature of the surface as exposure to atmospheric conditions would result in the readsorption of inorganic impurities to the surface. The substrates retain their hydrophilicity for ~2 days.

4.5.2 Nanosphere ordering

There are a multitude of different types of nanospheres manufactured with a variety of diameters and surface chemistries for many research and diagnostic applications. The choice of which to use for the formation of two-dimensional arrays requires careful consideration of the size and surface properties of the spheres. The spheres are usually supplied as monodispersed colloidal solutions consisting of either silica or polymer spheres dispersed in water. The silica spheres are manufactured using controlled precipitation and the polymer spheres either by emulsion polymerisation or suspension polymerisation. The mean diameters range from 10 nm up to 100 μm for the polymer spheres and a few nm up to 1 μm for the silica spheres. The standard deviation about the mean diameter is termed the coefficient of variation (CV) and is quoted as a percentage of the diameter. The size of the CV varies according to the diameter of the spheres and chemical composition with minimum values of < 1%. A small CV indicates a low variation in diameter and therefore the potential for fewer defects in a crystalline array. The stock nanosphere solutions used were supplied from Duke Scientific and IDC latex as 4% solids by volume equating to ~4 x 10^{12} spheres per ml for 390 nm diameter spheres. The nanospheres are composed of polystyrene long chain molecules terminated with carboxyl (COOH) groupings resulting in a hydrophobic negatively charged surface of the spheres. A hydrophobic surface is essential to maintain the mobility of the spheres during the ordering process as there is a repulsive interaction with the surface of the substrate. If the surfaces of the spheres were hydrophilic the attractive force between substrate and sphere would compromise the lateral movement of the spheres across the substrate surface. The dispersion medium is ultrapure water and requires dilution by further amounts of ultrapure water to obtain the correct concentration of spheres for ordering.

To achieve large area monolayer regions with significant domain sizes the initial concentration of the nanosphere solution must be carefully controlled. Since the cleaned substrates are stored under water the first task is to dry the substrates on a glass plate placed in an oven (~15 minutes at a temperature of 55°C) prior to depositing the colloidal solution. After the substrates have dried a droplet of ultrapure water is pipetted onto the centre of the substrate with a volume of 100 µL. Provided the surface treatments were carried out correctly the droplet will disperse readily across the surface. Next, the nanosphere solution is dropped onto the film of water with the amount required dependent on the diameter of the nanospheres. The amount of solution required increases with diameter as the solution concentration is defined in terms of the percentage of a given volume consisting of the spheres, this being the same for all solutions used. For 390 nm diameter spheres the volume that produced the best results was 8.0 µL. The number of spheres in this volume of solution is of the order of 3 x 10^{10}, many more than would produce a hexagonally close-packed monolayer across the entire substrate surface. This is necessary as multilayer structures that are required to produce the best quality monolayer regions form during the initial stages of the ordering. The spheres are dispersed in the wetting film by rocking and rotating the sample until their distribution appears consistent to the eye. The samples are covered with a glass Petri dish to maintain some humidity within the chamber and reduce the contamination of the sample by airborne particles. Finally they are placed on a tilting stage held at

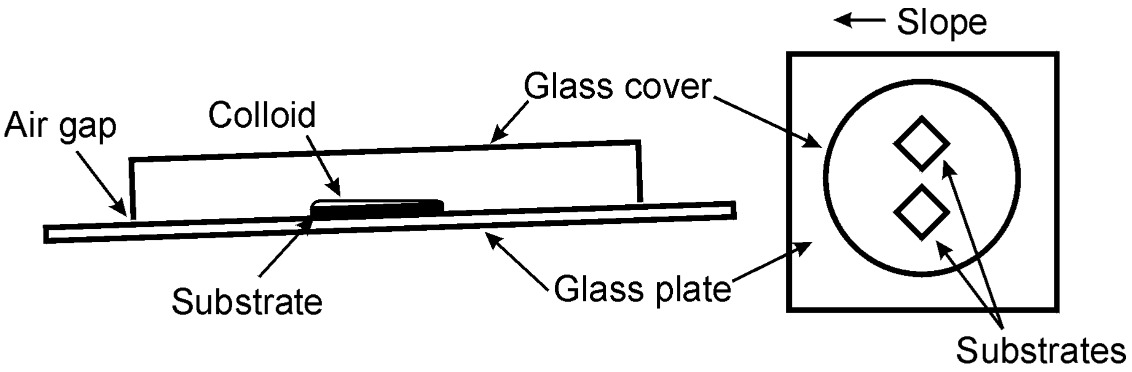

Figure 4.4. Diagram of apparatus used in the nanosphere ordering process, side-view (left), plan-view (right).

an angle of ~1° and dried at a temperature of 55°C (figure 4.4). This takes about 45 minutes during which the water evaporates inducing the assembly of spheres into the crystalline structures.

The volume of water used in pre-wetting the substrate is crucial to the overall nanosphere packing. Large monolayer areas of the order of a few square centimetres are possible with a film of water ~0.5 mm thick compared to narrow monolayer rings surrounding regions of multilayer packing formed with a somewhat shallower film of water. The large depth of the meniscus in relation to the nanosphere diameter at the edge of the substrate allows the formation of a multilayer wall. The effect of the wall is to reduce the rate of evaporation at the edge of the meniscus reducing the convective drain of solution from the centre of the substrate observed with thin wetting films. Monolayer ordering generally progresses from the corner of the substrate and consists of irregularly shaped domains up to a maximum of 15 mm^2 in area. As more water evaporates the concentration of spheres increases until a threshold is reached after which a bilayer forms. The transition between monolayer and bilayer hexagonal close packing often includes the formation of small domain intermediary square lattices. Further concentration increases result in successive multilayer formation. The depth of the water layer at the meniscus edge also plays an important role in determining whether a monolayer or multilayer structure forms. If the depth is less than the thickness of two or more spheres a multilayer cannot form thus providing a means of extending the formation of a monolayer, desirable for lithographic nanosphere applications. By maintaining a fluid depth less than the thickness of a bilayer, larger monolayer regions would be produced.

An example of a nanosphere array formed with 390 nm diameter spheres is shown in figure 4.5. The monolayer region (outlined) covers an area of ~ 3 cm^2 and consists of randomly oriented monocrystalline domains. The largest single domain indicated is ~10 mm^2 in area, adjoined by a large well-ordered bilayer region. Surrounding the monolayer region is a variety of multilayer regions with different thickness and structure. In the early stages of the ordering process the depth of the water rises very quickly at the edge of the substrate. This allows the formation of a narrow nanosphere wall up to 1 mm thick and 30 layers deep also indicated in figure 4.5. As more of the dispersion medium evaporates the depth is reduced eventually allowing the formation of monolayer arrays. The presence of the nanosphere wall appears to aid in the production of large monolayer areas with large domains perhaps due to the bottom layer of spheres acting as a template for the subsequent monolayer. Multilayers also form from the base of the wall at the edge of the substrate

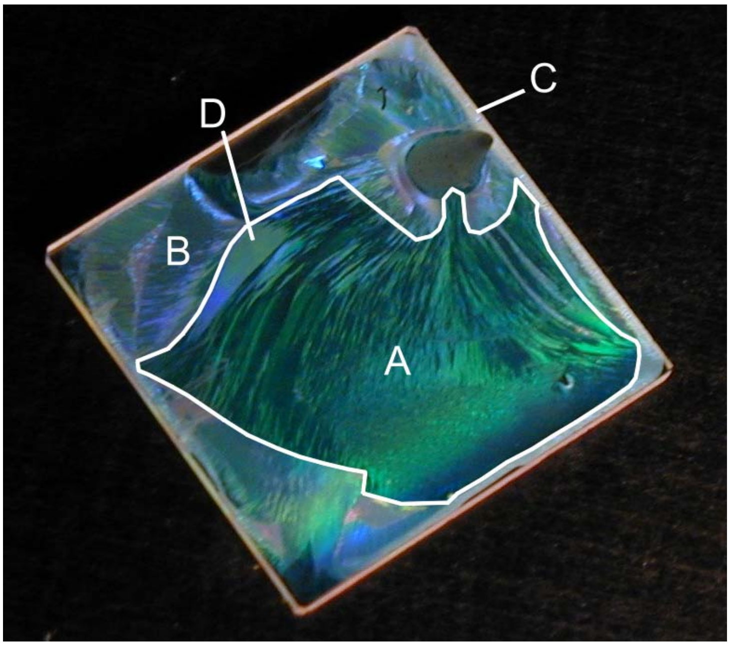

Figure 4.5. Digital photo of a nanosphere array formed from 390 nm diameter polystyrene spheres with (A) monolayer region, (B) multilayer regions, (C) nanosphere wall and (D) single monolayer domain indicated.

and there seems to be a correlation between the presence of these regions and the formation of the largest monolayer domains. The ordering progressed from the bottom corner of the substrate towards the top corner. Monolayer regions have been fabricated with monolayer areas as large as 4 cm^2 with single domains ~15 mm^2.

The separate monolayer domains are easily distinguished by observing the diffraction patterns from incident ambient and laser light. Since adjacent domains are oriented differently to one another light is scattered in different directions from each. In ambient white light the patterns display the full range of spectral colours as the viewing angle is increased away from a direction normal to the plane. This is apparent in figure 4.5 where the bright green and blue colours are due to diffraction of incident light by the hexagonal array. The dark regions in the monolayer area are not due to the absence of spheres, but instead are due to light being scattered in a direction away from the viewer. It is possible to observe scattering in six directions from a single domain as the samples are rotated azimuthally (about an axis perpendicular to the plane of the surface) through 360°. The diffraction patterns generated when a UV laser beam with an emission wavelength of 325 nm is incident upon two single monolayer domains are shown in figures 4.6(a) and 4.6(b). Rather than the six clearly defined equidistant spots expected for a sample with pure hexagonal symmetry there are six elongated regions of high intensity. In both patterns there are four spots equidistant from the centre with the remaining two first-order diffracted spots further from the centre in figure 4.6(a) and nearer to the centre in figure 4.6(b).

The periodicity of an hcp array of spheres is $D\sqrt{3}/2$ where D is the centre to centre separation of the spheres and for an array of 390 nm diameter spheres is 338 nm. The wavelength of the illuminating radiation is close to the periodicity of the array and will therefore be scattered at large angles relative to the sample normal according to the Bragg relation

$$\lambda_{\mathrm{G}} \sin\theta = \lambda$$

where λ_{G} is the periodicity θ is the scattering angle measured from the sample normal and λ is the wavelength of the illuminating radiation. The scattering angle of a diffracted beam calculated from the above values is 74° and when

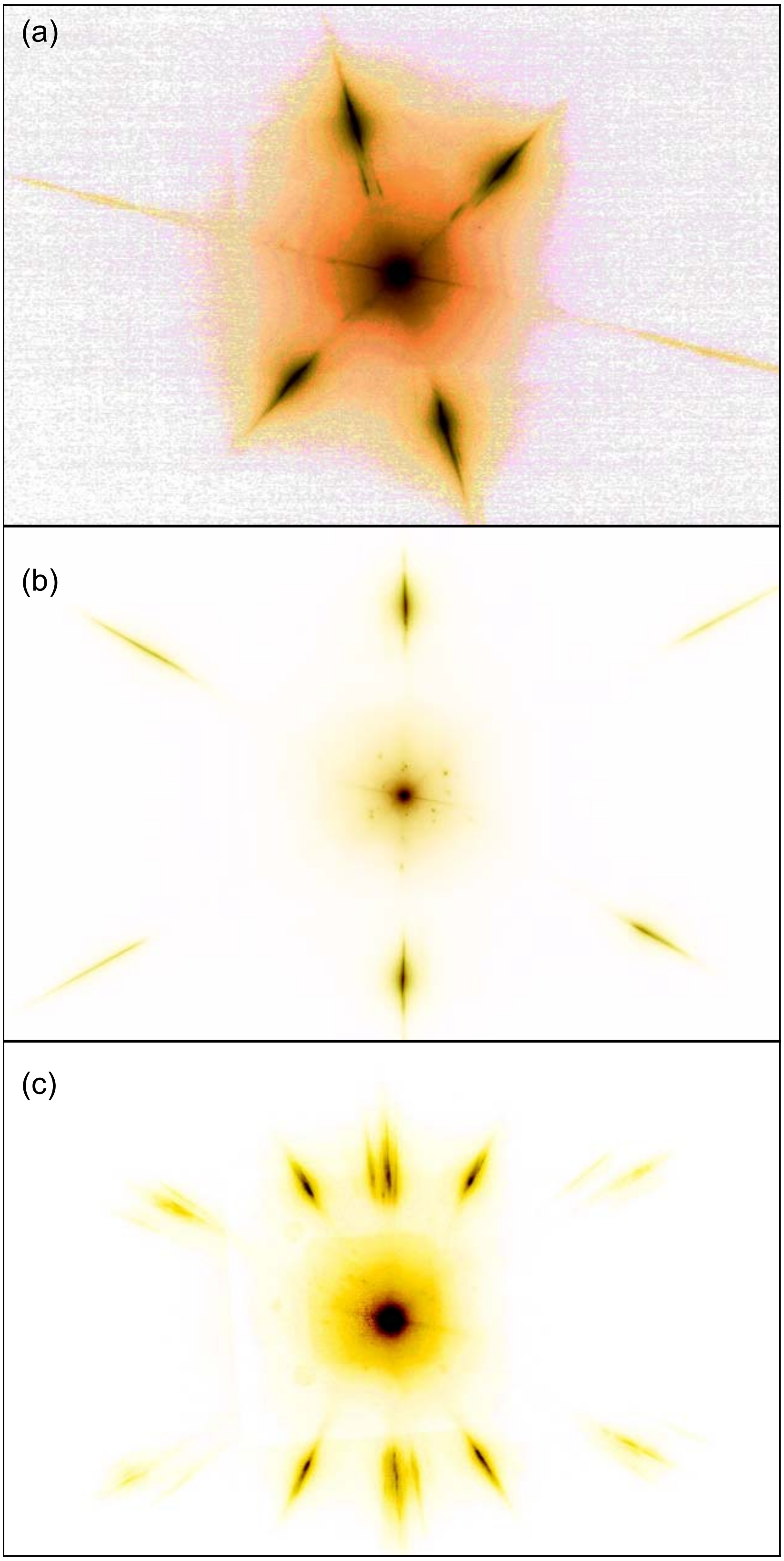

Figure 4.6. Diffraction patterns from single monolayer domains (a), (b) and from multiple domains (c).

projected onto a planar screen will produce an elongated spot. Also, the value for the diameter of the nanospheres is a mean with an associated standard deviation of 3%. Therefore the pitch may be more or less than 338 nm within the area illuminated by the incident beam (beam diameter ~1 mm) again resulting in an elongated spot. Defects within the structure also perturb the shape of the diffracted spots and produce the lines observed in the diffraction patterns. Slip dislocations, nanosphere diameter variations and, to a lesser extent, vacancies act as sources of diffuse scattered light that subsequently interfere constructively to produce the bands of high intensity connecting opposite pairs of spots in figure 4.6(a). Similar lines have been observed in X-ray diffraction where they are referred to as Kossel and Kikuchi lines, K-lines collectively [*Kikuchi (1928), Cowley (1984)*].

The increase in scattering angle of two of the six diffracted spots in figure 4.6(a) suggests a decrease in the periodicity of the array in this direction relative to the other two. Furthermore, a detailed analysis of the diffraction pattern shows that the azimuthal angles the diffracted beams are directed along are not separated by 60°. The angular separation between the upper pair and lower pair of spots is > 60° and the separation between the horizontal spots and their nearest neighbours is < 60°. Conversely, in figure 4.6(b) the upper and lower spots are diffracted by a smaller angle than the four spots equidistant from the centre to the left and right. The reduction in scattering angle can only be caused by a relative *increase* in the periodicity in this direction. The azimuthal angular separation between spots in figure 4.6(b) is < 60° for the pairs of spots on the left and right and > 60° for the upper and lower spots and their nearest neighbours. A third observation is that some domains exhibit diffraction patterns intermediate between those in figures 4.6(a) and 4.6(b). The three scattering planes produce opposite pairs of diffracted spots, with each pair a different distance from the central spot relative to the other two. Finally, 'powder' diffraction from regions where light is incident on multiple domains with many orientations is also observed and is elliptical in shape with the major axis aligned parallel to the direction of flow of spheres towards the ordered phase (*i.e.* perpendicular to the edge of the meniscus). From these observations it is clear that a distortion of the hexagonal close-packed structure occurs and depends upon the orientation of the resulting array relative to the direction of convective flow.

Two possible causes of this type of distortion are from a separation between spheres along a direction perpendicular to the flow (parallel to the meniscus edge) or the close-packing of homogeneously shaped ellipsoidal particles with the major axis aligned perpendicularly to the flow. These are shown in figure 4.7 for orientations of the array that produce the symmetrical patterns of figures 4.6(a) and 4.6(b). Figures 4.7(a) and 4.7(b) show undistorted arrays with the corresponding ruled diffraction grating and the diffraction patterns produced for the two orientations. If the spheres are separated from the neighbours along a line perpendicular to the flow direction then the structures and associated diffraction patterns of figures 4.7(c) and 4.7(d) are produced. If a shape distortion is applied whereby the spheres are compressed along the flow direction and stretched perpendicularly to the

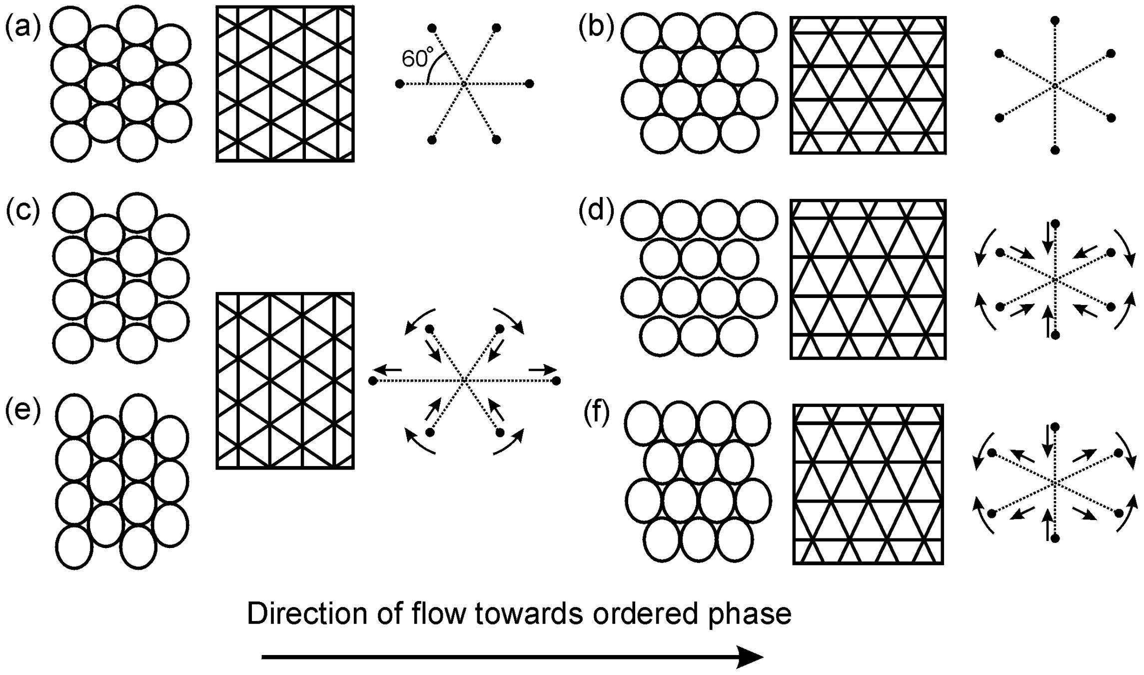

Figure 4.7. Illustrations showing undistorted and distorted sphere arrays with the associated ruled diffraction grating and diffraction pattern for orientations of $\varphi = 0°$ (a), (c), (e) and $\varphi = 30°$ (b), (d), (f). Figures (a) and (b) are for the undistorted array. Figures (c) and (d) show the effect of introducing a small gap between the spheres on the diffraction pattern. Figures (e) and (f) show the effect of introducing a shape distortion of the spheres on the diffraction pattern. Also indicated is the direction of convective flow that would produce the type of distortion and associated diffraction patterns.

flow direction the structures and associated diffraction patterns of figure 4.7(e) and 4.7(f) are produced. The arrows in the diffraction patterns indicate the distortion relative to the diffraction pattern from a hexagonal array. The structures in figures 4.7(c) and 4.7(e) are oriented so that lines of spheroids are perpendicular to the flow direction. They have identically shaped unit cells and therefore diffraction patterns with spots in the same positions. The structures in figure 4.7(d) and 4.7(f) are oriented so that lines of spheroids are parallel to the flow direction. The unit cells of these structures are *not* the same and therefore produce differing diffraction patterns. In figure 4.7(d) all of the diffracted spots are produced by an increased periodicity relative to the close-packed hexagonal array, the upper and lower spots closer to the centre than the spots to the left and right. In figure 4.7(f) the upper and lower spots are produced by a reduced periodicity and those to the left and right by an increased periodicity relative to the undistorted array. This distinction provides a means of identifying which distortion is more likely to be present within the arrays. If, for the type of diffraction pattern observed in figure 4.6(b), the periodicity associated with either of the short axes is significantly less than λ_G = 338 nm, calculated from the mean diameter of the stock nanospheres, then it may be surmised that a shape distortion is present. This appears to be the case, measurements yielding an estimated value for the periodicity of $\lambda_G \sim 330$ nm. Measurements from a diffraction pattern of the type in figure 4.6(a) produce a variation in periodicity of approximately 12 nm. Along the short axis the periodicity was estimated to be $\lambda_G \sim 328$ nm and the pitch along the remaining axes to be $\lambda_G \sim 340$ nm. The azimuthal angular separations Φ_1 and Φ_2 are measured to be 59° and 62° respectively.

The elliptical powder diffraction patterns and asymmetrical diffraction patterns from arrays not oriented relative to the flow direction as those of figures 4.7 may be easily explained by the close-packing of ellipsoidal particles. It is not intuitively obvious how a structural separation consistent throughout the crystal can produce these patterns. However, it is possible that defects are induced due to the forced separation of spheres by the ballistic nature of the ordering process. This is shown in figure 4.8 and may be a contributory factor in the formation of extended line and point defects within nanosphere

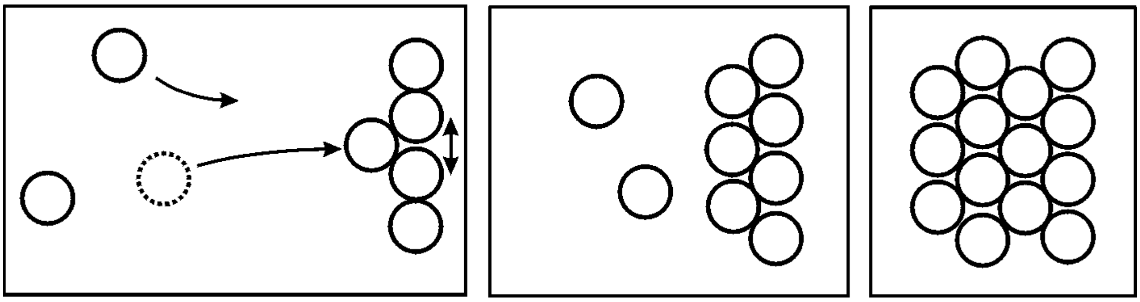

Figure 4.8. Mechanism for defect propagation through ordered array to produce structure in figure 4.7(c).

arrays. The spheres contained in the disordered phase are accelerated by the convective flow of solution generated by the higher rate of evaporation from the ordered region. The impact of the free nanospheres on the ordered spheres would disturb the initial line from their close-packed positions. The initial line is the template by which the spheres in the domain pack together and any disturbance of this line will be propagated across the entire array.

4.5.3 Thermal evaporation of metals

After self-assembly of the nanospheres the next step in the fabrication process is to thermally evaporate a metal across the array using the system shown schematically in figure 4.9. The sample is placed face down in the sample holder above a molybdenum boat connected across two electrodes. The boat holds the silver grains (99.999% purity) in a depressed region at the centre of the boat. Between the sample and the boat there is a removable shutter and attached to the holder close to the sample is a quartz crystal thickness monitor. To evaporate, the chamber is evacuated to a base pressure of $<5 \times 10^{-7}$ mτ after which a current is passed through the molybdenum boat via the electrodes attached to both ends. The boat is heated sufficiently to melt the silver and burn off adsorbed impurities on the surface of the silver grain. Increasing the voltage further results in the evaporation of the metal and upon removal of the intervening shutter the vapour condenses and solidifies on the surface of the sample. The rate of evaporation is controlled by the voltage of the electrical current passed through the boat and monitored by the quartz crystal oscillator.

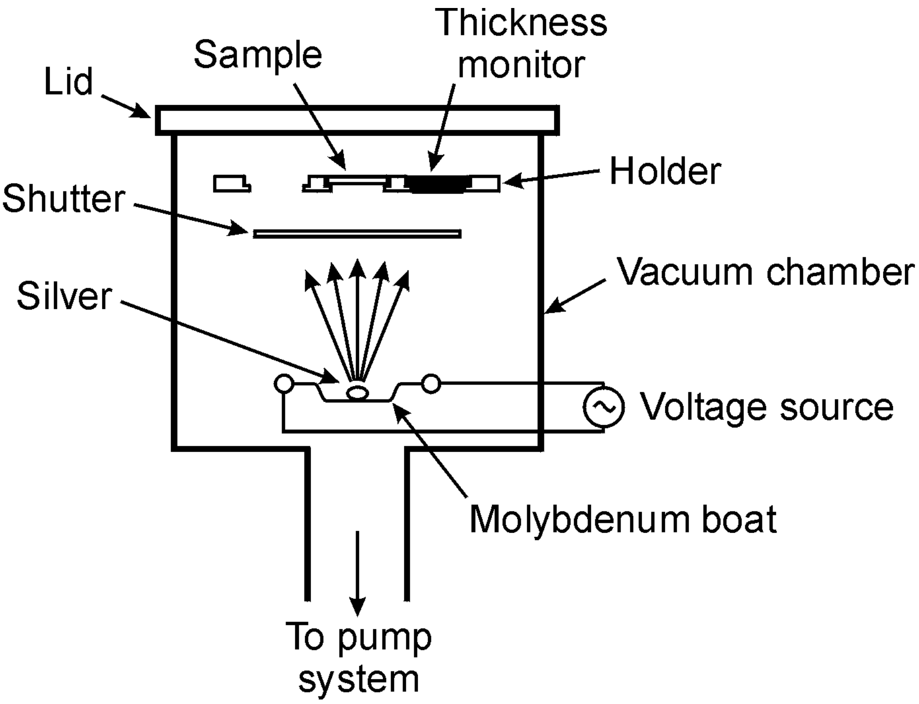

Figure 4.9. Schematic diagram of vacuum thermal evaporation system used to deposit silver.

The diameter of the spheres that make up the lithographic mask defines the maximum thickness of Ag that it is possible to evaporate. To allow the removal of the spheres after silver evaporation a sufficient gap must exist between the silver deposited on the surface and the polystyrene sphere. Therefore the maximum thickness of silver that is evaporated is less than the radius of the spheres. The smallest diameter nanospheres used were ~100nm with a film thickness of 16.0 nm. This is the smallest thickness that it is possible to evaporate as a continuous film; values lower than this result in an islandised film. Figure 4.10 is a scanning electron microscope image of an array of particles formed from a mask consisting of 390 nm diameter nanospheres. The light regions are where silver has deposited onto the silica substrate through the mask and the dark regions are silica. The triangular particles are ~ 90 nm across the perpendicular bisector; size variations and packing defects present in the nanosphere array give rise to line defects. Further details of similar arrays follow in the next chapter.

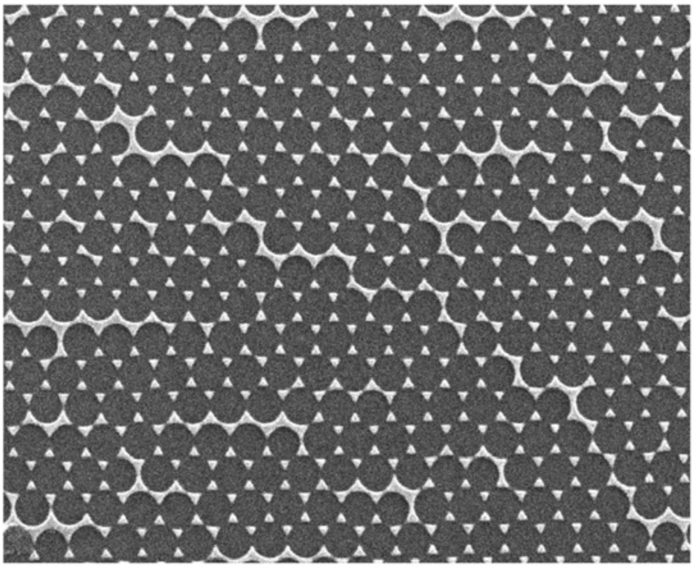

Figure 4.10. Nanoparticle array formed from nanospheres with a mean diameter of 390 nm. Bow-tie and line defects are clearly seen.

4.5.4 Reactive-ion etching

The use of arrays of nanospheres as a means of patterning surfaces is not limited to the fabrication of particle arrays. An additional step whereby a sample is exposed to a reactive gaseous plasma may be used to etch either the nanospheres, substrate or both simultaneously to produce alternative patterns. This is known as a reactive ion etch and a description of the technique follows.

A schematic diagram of the reactive ion etcher is shown in figure 4.11. The system consists of an upper electrode and lower electrode connected across a radio frequency (RF) source capable of delivering a power of up to 300 W. The sample is placed on the lower electrode below the process gas inlet. After introduction of the sample the chamber is evacuated by a two stage rotary pump to a base pressure P_B < 10 mTorr. Upon reaching this pressure a process gas (pure or mixed) enters the chamber through the process gas inlet at a flow rate maintained by a valve located in the process gas line and to a gas pressure P_G maintained by the exhaust valve. When submitted to an intense electric field developed across the electrodes by the RF power source, the gas becomes ionised producing highly reactive species that physically and chemically remove material from a sample. The physical (anisotropic) etch is due to the bombardment of the sample by ions accelerated by the electric field where as the chemical (isotropic) etch is due to chemical reactions of the reactive species with the surface moieties of the sample. The prevalence of the two mechanisms depends on the chemical structure of the sample, the power delivered to the electrodes and the pressure of the reactive plasma within the chamber. These parameters and, additionally, the flow rates of process gases into the chamber all affect the etch rate and need careful adjustment to produce the desired structures.

To etch the nanosphere array a process gas is required that will react with the organic polymer molecules that coil together to form the spherical shape of the particles, but that will not react with the silica substrate. Oxygen is well known as a suitable etchant of organic matter and, since the silica is by its nature highly oxidised, will not chemically etch the silica substrate. However, there will be some physical etching of the substrate that in this instance must be minimised. To do so the gas pressure in the chamber is set at a relatively high value, P_G = 200 mTorr, and the power set to a relatively low value, P = 40 W.

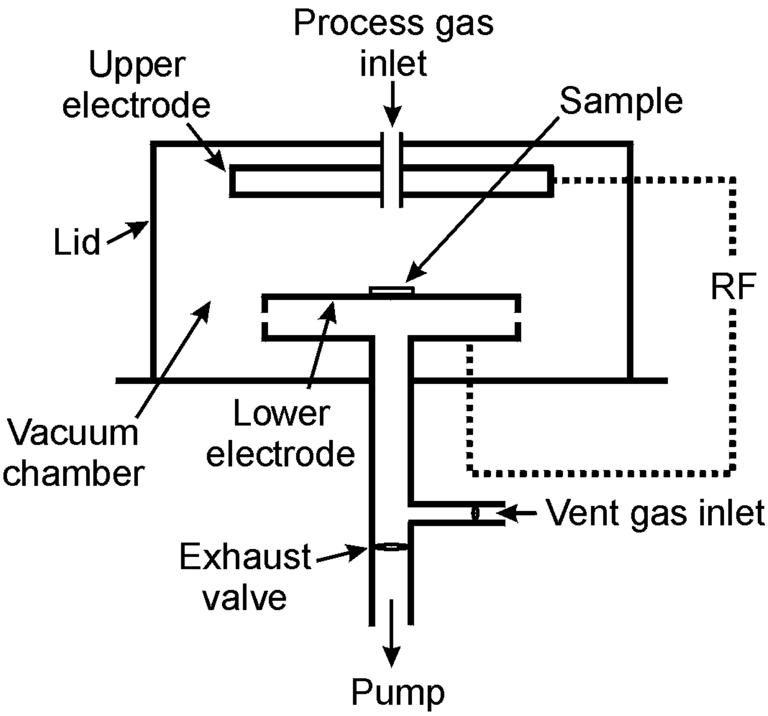

Figure 4.11. Schematic diagram of reactive ion etcher.

To increase the physical etch relative to the chemical etch a high power (P = 200W) and low pressure (P_G < 100 mTorr) is used. With high pressures there are more reactive species produced (ionised and charge neutral monotonic oxygen O^{2-} and ozone O_3) resulting in an increased current between the electrodes relative to a lower gas pressure in which there are less charged particles. For a given power an increased current is accompanied by a decreased accelerating voltage dropped across the electrodes and a reduced physical etch. The flow rate, measured in units of standard cm^3 per second (sccm), is set to 2.0 sccm and the etch time varied to control the amount of polymer material removed from the spheres.

Figure 4.12 is an SEM image of an array of holes fabricated in a 50 nm thick silver film from a mask of 300 nm diameter nanospheres. The diameter of the nanospheres prior to etching was 390 nm. The image illustrates the large area patterning of silver films possible by the technique and the low density of

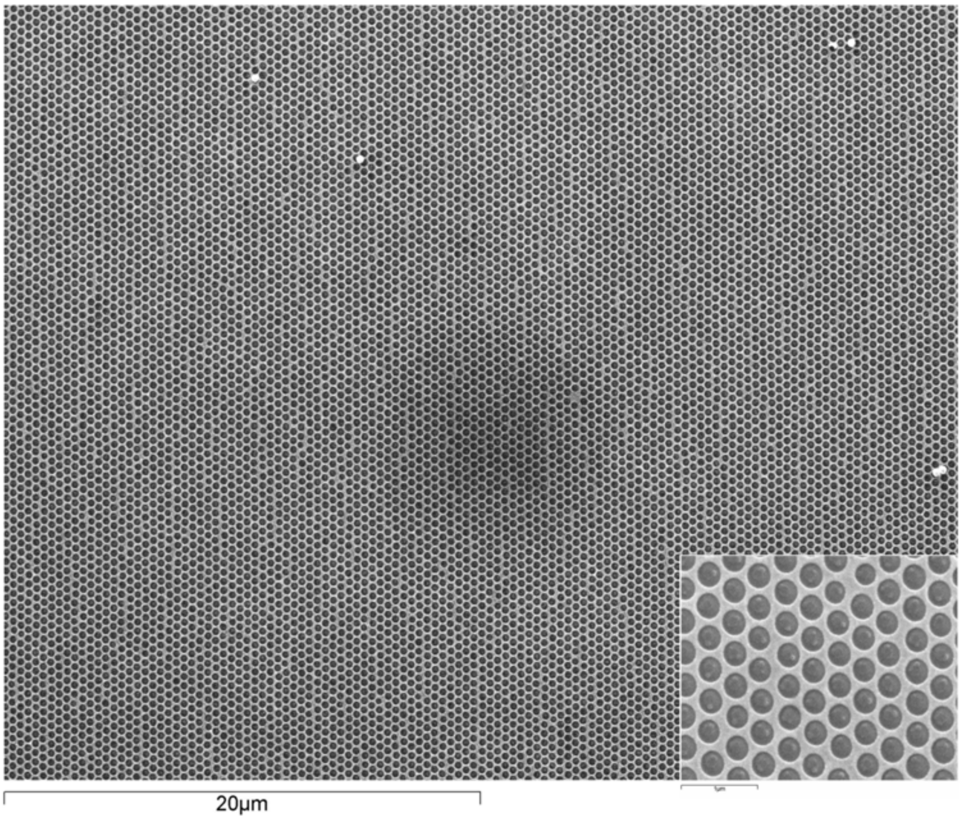

Figure 4.12. SEM image of an array of holes in a 50 nm thick silver film formed by etched nanosphere lithography. Inset shows a magnified region of the sample.

vacancy defects (there is only a single vacancy in the entire image). However, line defects may still be observed running predominantly in a vertical direction as viewed. The dark region at the centre is from carbonisation of the sample due to a previous image capture and is shown in the inset. Further details are given in Chapters 6 and 7.

4.7 Summary

In this chapter the technique of nanosphere lithography has been introduced as a means of fabricating periodic arrays of homogenously sized metallic nanoparticles. A variety of methods to order nanospheres into hexagonal close-packed arrays was discussed with particular attention placed on the realisation of two-dimensional arrays suitable for lithographic applications. A characterisation of nanosphere arrays fabricated at Exeter was shown, followed by a discussion of the possible mechanisms involved in the formation of slightly distorted pseudo-hexagonal structures. Extensions to the basic technique enabled the production of periodic arrays of holes in thin metal films and the patterning of silica substrates. The optical characterisation of the samples fabricated using the techniques described form the bulk of the remainder of this thesis.

Chapter 5

Optical properties of silver nanoparticles formed by nanosphere lithography

5.1 Introduction

The characterisation of metallic nanoparticles is essential in improving our understanding of fundamental material properties and to the development of a diverse range of applications. To enable a systematic study of the many interesting properties of metallic nanoparticles ideally one requires systems that consist of homogeneously shaped particles arranged in a periodic array. A method to achieve this known as nanosphere lithography (NSL) was described in the previous chapter. The optical behaviour of the silver particles produced using NSL have been extensively studied in the past decade with a view to investigating the phenomenon of surface enhanced Raman scattering (SERS) [*Haynes (2003b)*] and their suitability for biological and chemical sensing applications [*Duval-Malinsky (2001)*]. Specifically this has required an understanding of how changing the shape, size and environment of the silver nanoparticles by modifying the lithographic mask, deposition conditions, substrate and embedding medium alters the optical response. *Jensen (2000)* first systematically studied the extinction properties of silver nanoparticle arrays fabricated by nanosphere lithography. Triangular and ellipsoidal nanoparticles were formed with a range of heights and widths and were shown to exhibit a broad range of frequencies throughout the visible spectrum at which the localised surface plasmon resonance (LSPR) was excited. Also, the LSPR was observed to red-shift as layers of silicon oxide (SiO_x) of increasing thickness were evaporated onto a nanoparticle array. In addition to these properties, the effect of altering the refractive index and structure of the external medium by changing the substrate, attaching thiol molecules to the particle surface and immersion in solvents were discussed by *Haynes (2001)*. An understanding of the sensitivity of the LSPR to changes in the local environment is crucial to many of the sensing applications of NSL derived particles. By introducing small amounts of material around the nanoparticle the polarisability of the external medium is altered thus altering the spectral form of the LSPR.

This chapter begins with a brief description of the NSL fabrication technique leading into a description of the Langmuir-Blodgett technique. This technique allows the controlled deposition of dielectric layers with a combined thickness of up to 0.5 μm and with a resolution of only a few nm. The apparatus used in optical measurements to record transmittance spectra is also described in this section. Transmittance measurements are used in the first instance to investigate the effect of the polarisation state of the incident light on the spectral form of the LSPR thus giving further insight into the physical structure of the nanoparticles (*section 5.3*). Chapter 2 introduced many of the optical characteristics of metallic nanoparticles with simple shapes including the effect of changing the size and shape of the particle and embedding the particle in media of differing refractive index. Following on from the studies of the *van Duyne*[1] group referred to above, in section 5.4 results are presented of the transmittance spectra of NSL nanoparticle arrays formed with a variety of widths and heights. Finally the main body of this chapter (section 5.5) is dedicated to a discussion of the sensitivity of the LSPR to thin layers of a dielectric deposited using the Langmuir-Blodgett technique. The LSPR is monitored and the peak extinction and transmittance minimum plotted as a function of thickness of the dielectric layer up to a maximum thickness of 290 nm. The shift is modelled using a classical dipole description of the resonant mode associated with the particle.

5.2 Experiment

5.2.1 Fabrication

The nanoparticle arrays in this study were formed using nanosphere lithography as described in *Chapter 4*. An amount of solution containing polystyrene nanospheres was deposited onto a hydrophilic fused silica substrate and dried

---

[1] North Western University, USA

in an oven at 55°C. As the dispersion medium evaporates the nanospheres self-assemble into a hexagonal close-packed structure suitable for use as a lithographic mask. Silver was evaporated in a direction normal to the substrate and triangular particles are formed where the material is deposited through the gaps between the spheres. In the majority of the experiments described in this chapter the mean diameter of nanospheres used to form the lithographic mask was 390 nm. The exception was in varying the in-plane dimension of the particles when mean diameters of 290 nm and 630 nm were also used (*Section 5.4*). The thickness of silver deposited was measured using a quartz crystal oscillator and it is this value that is quoted in the results that follow. Films were deposited onto the nanosphere arrays with depths ranging from 20 nm to 50 nm.

5.2.2 Langmuir-Blodgett deposition

The primary aim of this chapter is to discuss how layers of dielectric material coating an array of nanoparticles with a thickness of the order of and much smaller than the wavelength of light alter the characteristics of the LSPR. To achieve this in a systematic, quantifiable way the Langmuir-Blodgett technique was employed to controllably deposit layers of known thickness. The basis of the technique is that certain types of molecule will form a monomolecular layer at the surface of a film of water. This insoluble layer may then be compressed to form a crystalline structure of aligned molecules with a thickness determined by the orientation of the molecules with respect to the water surface and their length. If a substrate is passed through the film the compressed molecular monolayer may be transferred to the substrate surface. If this process is repeated then a second layer is deposited onto the first with further film transfers resulting in a multilayer structure. The total thickness is determined simply by multiplying the total number of layers by the thickness of a single layer. The transfer of floating monolayers from a water surface to a solid substrate was first demonstrated by *Katherine Blodgett* in conjunction with *Irving Langmuir* [*Langmuir (1920), Blodgett (1937)*]. Subsequently the films constructed in this way became known as Langmuir-Blodgett films and they have since been applied to many areas of scientific research (see reviews by *Roberts (1990) and Petty (1996)*).

5.2.2.1 Langmuir Monolayers

In earlier work *Langmuir* studied theoretically the adsorption of molecules at a gas-liquid interface [*Langmuir (1915)*]. He identified that the molecules of an insoluble, non-volatile material introduced to the surface of a liquid will reorder themselves so as to minimise the free surface energy. This behaviour is as a consequence of the energy differential between the intermolecular attractions experienced by molecules at the surface of a liquid compared to those in the bulk. If there is little attraction between the insoluble molecules and the liquid molecules then there is a net inward attractive force that acts to minimise the surface area of the liquid. This is the reason why water deposited onto a hydrophobic surface form droplets rather than spreading to form a molecular monolayer. By the same token it is also the reason why long-chain alkanes with the general formula $CH_3(CH_2)_nCH_3$ form droplets when deposited onto a water surface. These are insoluble in water because of the non-polar nature of the aliphatic chain and the relatively strong van der Waals attractive forces between the chains. The mutual attraction between the molecules is greater than the attraction with the water molecules. To form a film on a water surface this effect must be reversed - the attractive forces existing between the deposited molecules and the water molecules must be greater than the mutual attraction. For a similar class of organic compounds this is indeed the case. By substituting one of the methyl end-groups in the alkanes for a carboxylic acid group (alkanoic acids - general formula $CH_3(CH_2)_nCOOH$) the chemistry of the compound changes dramatically. The acidic headgroup is strongly polar and is therefore able to form hydrogen bonds with the water molecules. This attractive force exceeds that of the van der Waals bonds between the aliphatic chains and the molecules spread across the water film so that all of the headgroups become solvated. Importantly, to form a stable film the molecules are only partly soluble. The aliphatic chain remains strongly hydrophobic and prevents the molecules from dissolving in the water sub-phase. Upon compression the molecules are aligned so that the aliphatic tails lift away from the water surface whilst the headgroups remain solvated thus forming an oriented monolayer. A requirement for the formation of these monolayers is that the molecules contain a hydrophilic part to overcome the intermolecular forces between identical species and a hydrophobic part to prevent complete dissolution. Such molecules are known as amphiphiles or surfactants and the floating monolayers they produce are known as *Langmuir* monolayers. The distinction between *Langmuir* films and *Langmuir-Blodgett* films is that the latter have been transferred to a solid substrate.

There are many types of compound suitable for forming Langmuir monolayers, the simplest of which were introduced above. The main influence on the film forming capabilities of the alkanoic acids is the chain length of the hydrophobic tail. The minimum number of carbon atoms required for a stable film is 12, compounds with chain lengths shorter than this becoming completely soluble in water. In this study the molecule used was 22-tricosenoic acid (99.99 % purity, Fluorochem Ltd.) with the molecular structure illustrated in figure 5.1. This material has been extensively characterised and is known to form high quality transparent films for use in optical studies [*Barnes (1986)*]. The structure is very similar to that of the alkanoic acids, the sole difference being a double-bonded carbon atom pair at the end of the aliphatic chain. A monolayer of 22-tricosenoic acid molecules has a thickness of ~ 2.6 nm and a LB multilayer structure therefore has this resolution.

Langmuir monolayers are typically characterised by measuring the change in the surface tension of the sub-phase as the layer is compressed. The repulsive interactions between molecules as the intermolecular separation is reduced cause the surface tension of the film covered surface to be lower than that of pure water. The change in surface tension is defined as the surface

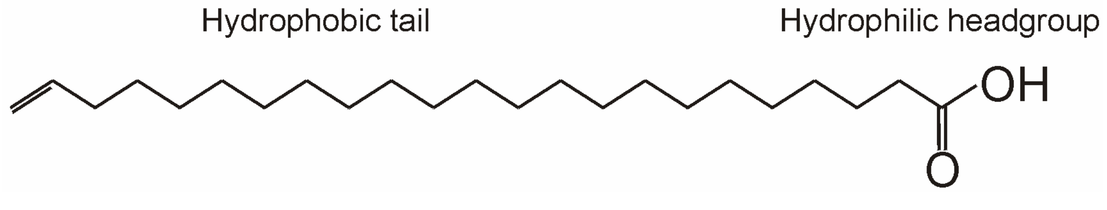

Figure 5.1. The molecular structure of 22-tricosenoic acid.

pressure Π,

$$\Pi = \gamma_0 - \gamma ,$$

where γ_0 is the surface tension of pure water and γ is the surface tension of the film-covered surface. As the separation between neighbouring molecules decreases phase transitions occur. In an uncompressed film the area per molecule is high and the motion of molecules at the surface is essentially unhindered. Rafts of molecules begin to form that only weakly interact resulting in a surface pressure of zero. This indicates that it is unchanged from pure water and is analogous to a gaseous phase, albeit in two dimensions. Further compression results in an increased interaction between the molecules and an increase in the surface pressure as the separation is reduced. At this point the headgroups are not closely packed and there is no order in the molecular orientation; this is analogous to a liquid phase in two dimensions. Eventually a point is reached where only a small reduction in surface area produces a large increase in surface pressure. The molecules are tightly packed and the aliphatic tails are oriented normally to the surface; this is analogous to a solid phase. If compression is continued the monolayer collapses due to buckling or overturning where a bilayer begins to form. A schematic diagram illustrating the three phases is shown in figure 5.2.

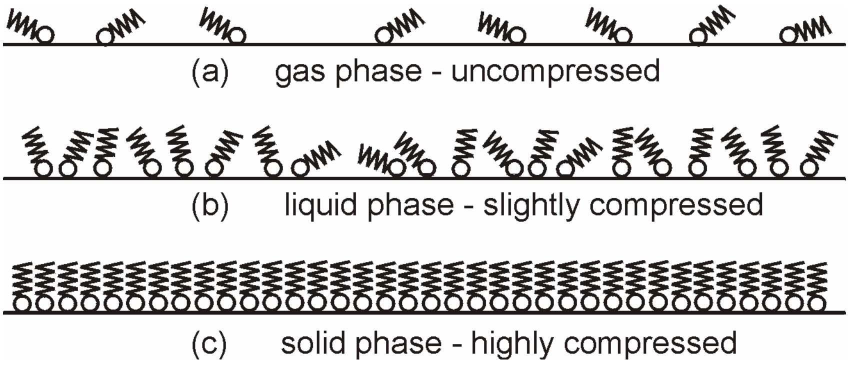

Figure 5.2. Structural phase transitions of a long chain fatty acid Langmuir film on a water surface showing the gas phase (a), liquid phase (b) and solid phase (c). Each molecule comprises of an aliphatic chain represented by a zig-zag line and carboxylic acid headgroup represented by a circle.

5.2.2.2 Film transfer

The film transfer technique developed by *Langmuir (1920)* and *Blodgett (1937)* involves the vertical passage of a substrate through a floating monolayer on a water sub-phase. It is important that the monolayer is well-ordered prior to transferral and consequently must be continuously compressed into one of the higher-pressure condensed phases. For 22-tricosenoic acid a surface pressure is required in the range 25-35 *m*Nm^{-1} and at room temperature results in deposition from the liquid phase.

A typical deposition process is that shown in figure 5.3 where a hydrophobic substrate is passed through a monolayer film from air into the water. The hydrophobic tail bonds to the surface of the substrate and results in a submerged surface terminated with the hydrophilic headgroups of the molecules. Upon completion of this stage the sample is then withdrawn from the sub-phase and a second monolayer of molecules is deposited on top of the first. The hydrophilic heads of each layer are in contact with one another leaving a surface terminated with the hydrophobic tails. Repetition of this process leads to multilayer stacks of bilayers. To achieve a resolution of a monolayer the final emersion process in a dipping sequence can be performed after removing the floating monolayer. The sample is removed from the sub-phase without collecting an additional layer. During all of the above steps the surface pressure must remain constant to ensure uniform and consistent material properties and layer thickness.

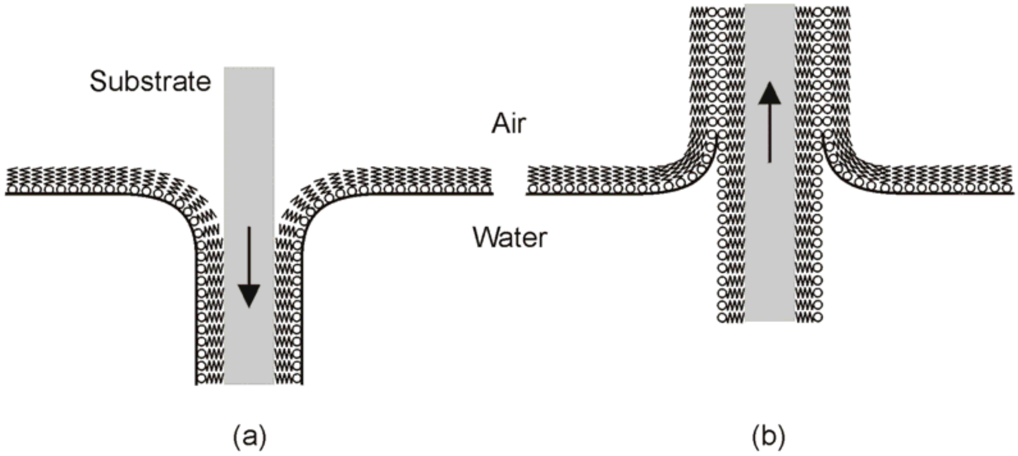

Figure 5.3. Diagram showing Langmuir-Blodgett film transfer on the downstroke (a) and upstroke (b).

5.2.2.3 Langmuir-Blodgett apparatus

The main components of an experimental system for LB deposition include a trough containing the sub-phase, barriers to compress the surface molecules, a dipping mechanism for sample introduction and a surface pressure monitor. A diagram of the apparatus used in Exeter illustrating these components is shown in figure 5.4. The main body of the trough is 10 mm deep with a well to allow the full immersion of the substrate. The total cross-sectional area is 720 cm^2 allowing a maximum of 40 layers to be deposited onto a 25 x 25 mm^2 substrate with a single film. Ultra-pure water is used to fill the trough so that the level of the meniscus formed is between 2 mm and 3 mm above the edge. It is important to ensure there is no spillage of the water across the edge so it is desirable for the trough to be made from a hydrophobic material. Further requirements are that the trough be easily cleaned, that minimal impurities are contained within the material that could leach into the sub-phase and that it is non-reactive. A suitable material that meets these requirements is polytetrafluoroethylene (PTFE) and is used for the sample holder as well as the trough. Also machined from PTFE, the barriers confine the film, one movable so as to achieve and maintain the desired surface pressure, measured using the Wilhelmy plate. The position of the barriers and the sample are computer-controlled allowing full automation of the deposition process.

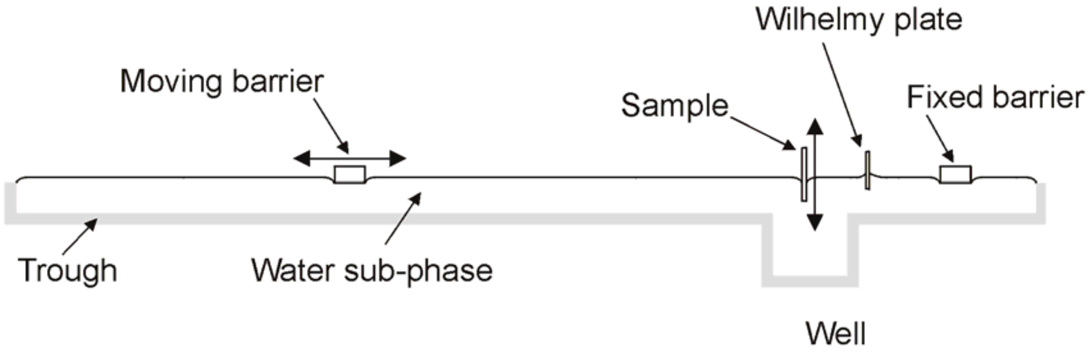

Figure 5.4. Diagram of Langmuir-Blodgett apparatus.

5.2.2.4 Procedure

To prevent particulate contamination of the LB films requires the process to be conducted within a dust-free environment. Samples were used immediately after formation of the metal nanoparticle arrays and at all stages exposure to ambient conditions kept to a minimum. Prior to dipping, samples were cleaned with a jet of filtered air and exposed to 1,1,1,3,3,3-hexamethyldisilazane (HMDS) vapour for a minimum of 4 hours. This treatment has the effect of rendering the substrate hydrophobic through termination of the surface silica molecules with non-polar methyl groups. The silver particles appear to be unaffected by this essential step, transmittance spectra taken before and after exposure exhibiting no significant differences. To ensure a sub-phase free from contaminants the trough was thoroughly cleaned prior to use. It is kept full with water at all times so the first step was to empty the trough and then wipe the exposed surfaces with cleanwipes soaked in *Aristar* grade chloroform. The trough was then refilled with ultra-pure water and the process repeated. Finally the barriers having initially been removed are replaced and swept across the surface to remove any particulate contaminants that may have been introduced to the surface. The movable barrier was positioned at ~ ¾ of the length of the trough prior to introducing the 22-tricosenoic acid to allow expansion of the film if required.

The next stage of the dipping procedure was to prepare the Langmuir film on the water sub-phase. This begins by dissolving the film material in a volatile, water immiscible solvent and then depositing it drop-wise from a syringe onto the surface. The solvent evaporates leaving behind a sub-monolayer of the 22-tricosenoic acid molecules. *Aristar* grade chloroform was used as the solvent to dissolve 22-tricosenoic acid with a solution concentration of 1.0 mg/ml. The syringe was held only a few mm above the water level during the process so as to avoid molecules penetrating the surface. The drops were applied at random points a distance away from the edge of the trough to avoid crystallisation. When a stable surface pressure began to be registered by the Wilhelmy sensor the film was ready to be compressed.

At this point the sample is attached vertically to the dipping mechanism via a PTFE clip and lowered so that the bottom of the substrate just contacts with the surface. The monolayer is then compressed at a rate of 1 cm^2s^{-1} until a surface pressure of 30 $m$$Nm^{-1}$ is reached. At this value the substrate is automatically lowered into the sub-phase at a rate of 0.20 mms^{-1}. Molecules that are attached to the sample are removed from the surface of the sub-phase leading to a decrease in the surface pressure. Consequently the film was continuously compressed at a rate sufficient to maintain the surface pressure at 30 $m$$Nm^{-1}$. When the sample was immersed to the desired depth the film was allowed to settle for 5 seconds before the upstroke commenced. This is conducted at the same rate (0.20 mms^{-1}). Upon reaching the initial start position there was another 5 second delay before further dipping. The bilayer dipping process was repeated until the desired number of layers was deposited.

5.2.3 Optical Measurements

Transmittance data were collected using the apparatus shown in figure 5.5. A collimated beam (divergence ~0.5^o) from a tungsten halogen lamp (*Philips* 240 V, 50 W) was directed onto the samples. These were placed in a bi-translational stage to allow accurate micro-positioning of the incident beam. This was particularly critical in the experiments designed to observe the relative shift of the LSPR with the addition of overlayers of increasing thickness. Transmittance spectra were collected before and after deposition of the overlayers and due to slight variations in the optical response from different regions on the sample it was critical that the beam was repositioned correctly to sample the same area in each case. A *Spectrapro 275* monochromator was used to spectrally filter the incident light (spectral width ~ 2 nm), whilst a mechanical chopper modulated the intensity of the incident light so as to allow phase-sensitive detection of the zero-order transmitted beam. Further, a beam-splitter redirected a small faction of the incident beam onto a second detector to allow source fluctuations to be taken into account. Both outputs from the reference and sample detectors (*Hamamatsu H6780-01* photomultiplier tubes) are fed into *Stanford Research Systems SR810* lock-in amplifiers to filter the signals and extract only the modulated component. The output voltage from the detectors varies as a function of the wavelength with the operational range from 300 nm to 820 nm. The monochromator and light source further limit the

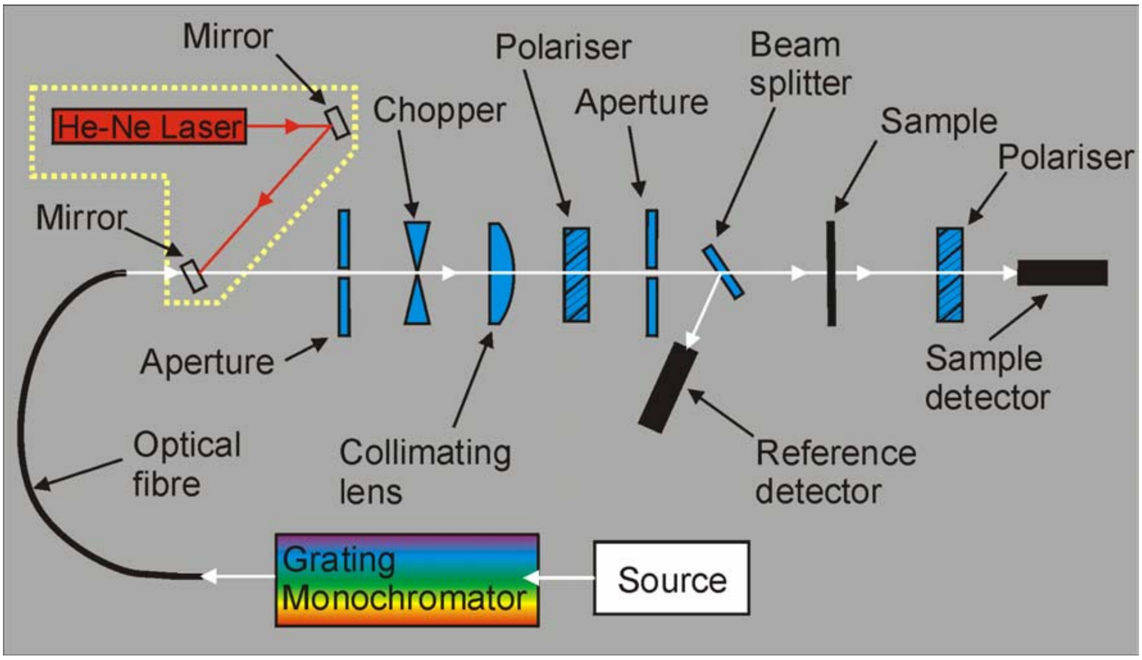

Figure 5.5. Schematic diagram of the experimental setup for obtaining transmittance data as a function of wavelength.

spectral operational window so that data was typically collected for incident wavelengths between 450 nm and 800 nm. A polarizer was placed in the incident beam so that the polarization state of the incident light could be controlled and, on occasion, in front of the sample detector so that the polarisation state of the detected light could be controlled. Apertures located in the path of the beam reduced the diameter of the projected beam spot to ~ 1.0 mm. This was found to generate a satisfactory signal-to-noise ratio whilst reducing the inhomogeneous broadening of spectral features due to domain overlap of the incident beam. Where possible the incident beam was directed onto a single domain.

For each wavelength the signals from the sample and reference detectors are recorded along with the ratio of the two (sample/reference). To obtain absolute transmittance values a normalisation scan is taken by removing the sample and measuring directly the signal from the source. Again the ratio of sample to reference is calculated for each wavelength and this provides the normalisation constant that the sample data is divided by to generate absolute values.

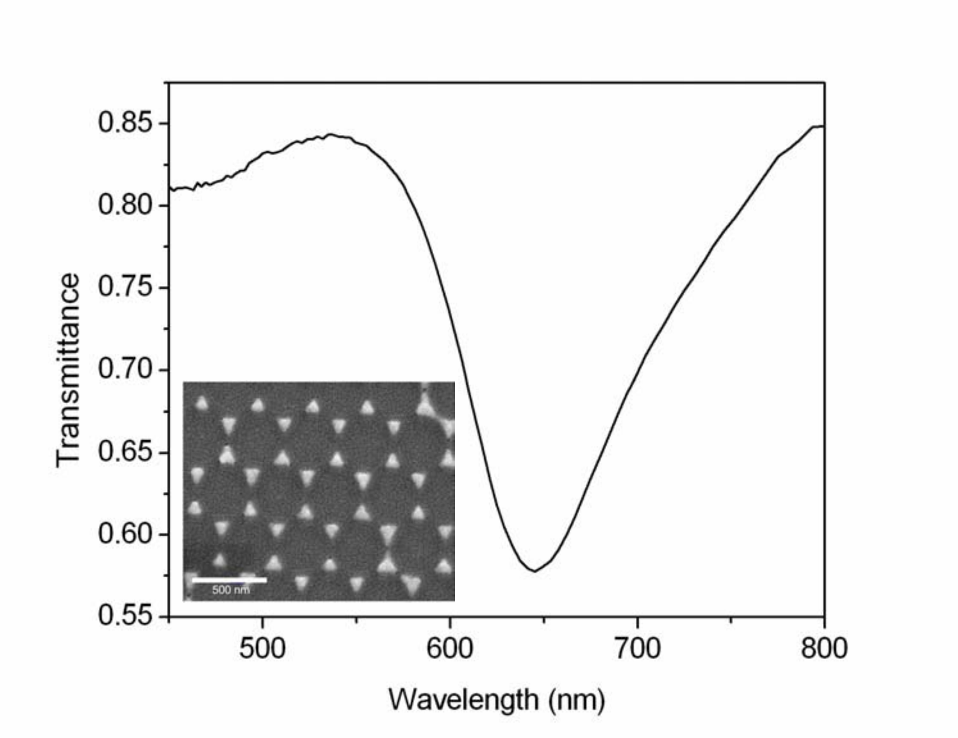

Figure 5.6. A typical example of the spectral transmittance of an array of nanoparticles formed using nanosphere lithography. The diameter of the spheres used to form the lithographic mask was 390 nm and the height of the particles was 50 nm. The scale bar represents a distance of 500 nm.

An example of the spectral response from a silver nanoparticle array formed from nanospheres with a mean diameter of 390 nm and particle height of 50 nm is shown in figure 5.6. An SEM image of a small region of the array is shown in the inset. The dip in transmittance with a minimum at 645 nm is the LSPR associated with the individual nanoparticles. To characterise the optical behaviour of a variety of similar arrays the position of the minimum in transmittance or resonant wavelength λ_{LSP} of the LSPR is monitored in the following sections. A quantitative analysis of the width of the LSPR spectral feature is complicated due to the asymmetry in its form. For a single sample this is mainly due to the frequency dependence of the relative permittivity. Inconsistencies between samples that arise because of inherent variations during sample fabrication cause further difficulties.

5.3 Polarisation dependence

It was seen in Chapter 2, Section 2.6 how the spectral position of the LSPR was dependent on the shape of a particle and the polarisation state of the incident light. For a spheroidal particle there are two resonant frequencies at which a LSPR can be excited associated with the major and minor principal axes. For light polarised along one of the axes, only the particle mode associated with that axis is observed in optical spectra. For light polarised along a line between the axes both modes may be excited, but with a coupling strength determined by the magnitude of the electric field components along each axis. On an ellipsoidal particle three non-degenerate modes associated with the three different principal axes are observed. The important point to note is that the coupling strength to the LSPRs depends on how the incident light is polarised relative to each symmetry axis. Triangular-shaped particles such as those fabricated by nanosphere lithography are more complicated since they should have three lines of mirror symmetry along each perpendicular bisector; therefore one might expect three degenerate plasmon resonances associated with each. Moreover an array fabricated from a perfectly hexagonal structure would be expected to exhibit 60° azimuthal symmetry. However, from Chap. 4, Sect. 4.5.2 the diffraction patterns obtained from nanosphere arrays indicated a distorted hexagonal (base-centred orthorhombic) structure. Therefore the azimuthal dependence of the optical transmittance would be expected to emulate this distortion.

To see if this was the case the polarisation of light incident upon a silver

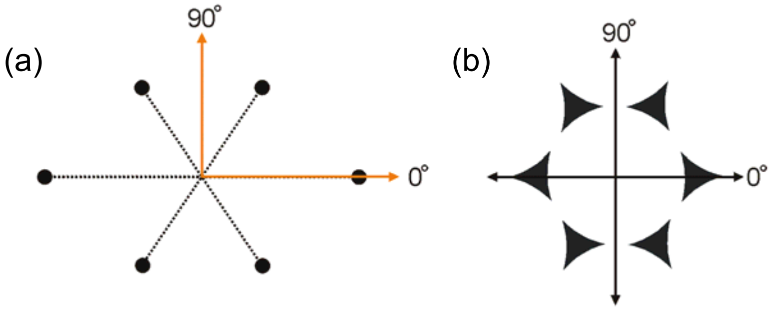

Figure 5.7. Diagram illustrating azimuthal angle φ as defined relative to the distorted–hexagonal diffraction pattern (a) and to a nanoparticle array (b).

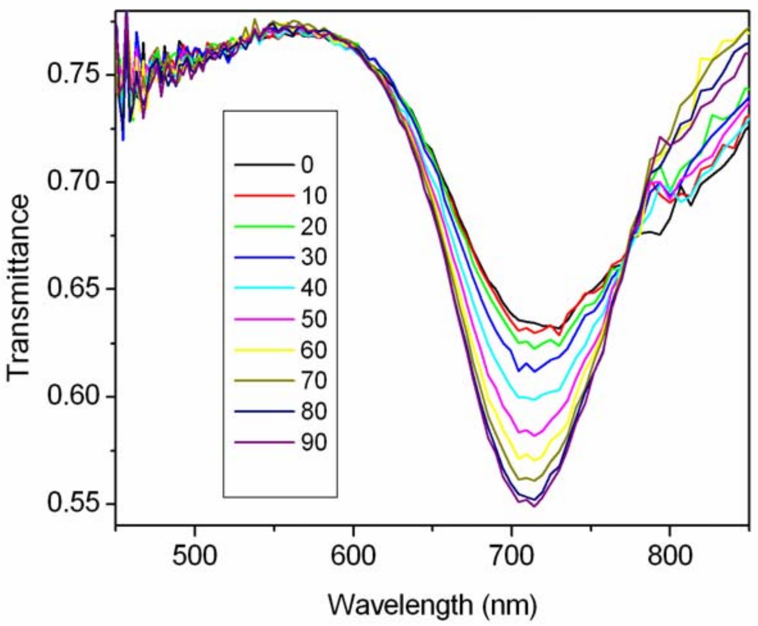

Figure 5.8. Normal incidence transmittance spectra of silver nanoparticles formed from 390 nm diameter spheres as a function of the azimuthal angle. The incident light was linearly polarised with the azimuthal angle defined as the angle between the polarisation direction and the Bragg vector associated with the short pitch of the distorted grating.

nanoparticle array was rotated from 0° to 90° and the spectral transmittance measured at 10° intervals. The light was incident normally onto the sample. The azimuthal angle φ is defined in convention with previous discussions relating to grating-coupling of SPP modes in Chap. 3, Sect. 3.9.2. An angle φ = 0° is parallel to a primitive reciprocal lattice vector associated with the periodic array, this being parallel to a perpendicular bisector of the particles (see figures 5.7(a) and 5.7(b)). At φ = 90° the light is polarised parallel to the side of the triangular particle (figure 5.7(b)).

The results from optical transmittance measurements are shown in figure 5.8. A broad, shallow resonance feature is shown for φ = 0°, increasing in depth, narrowing and appearing to shift towards shorter wavelengths as φ increases. Beyond 30° the form of the spectra would be expected to replicate those leading up to 30° if the array had perfect hexagonal symmetry. It is observed that due to the distortion of the nanosphere mask the spectra continue to narrow and increase in depth up to $\varphi = 90°$. For $\varphi > 90°$ the spectra mirror those for $\varphi < 90°$.

Two possible reasons for the results in figure 5.8 are as follows. Firstly, that there was a distortion to the shape of the particles. Given that the diffraction pattern indicates a distortion of the overall array it can be inferred that the shape of an individual particle will not have 60° symmetry. This being the case, the LSPR would be expected to shift in frequency as the polarisation is rotated. A second explanation is that there was a changing interaction between adjacent particles as the polarisation was rotated. It is well known that changing the separation between particles alters the spectral form of the LSPR (see Chap. 2, Sect. 2.7).

To explain the observations more fully would require a detailed characterisation of the distorted array and the effect this has on the particle shape and the nearest-neighbour particle separations. SEM images from the arrays do not appear to show a significant distortion of the particle shape from triangular or a significant variation in inter-particle separations. This section illustrates that even a subtle structural variation will induce quite a dramatic effect in the optical response.

5.4 Size dependence

The position and width of the LSPR of very small silver particles with a diameter $d \leq 20$ nm are influenced by the size of the particle. So-called *intrinsic* size effects [*Kreibig and Vollmer (1995)*] are accounted for by introducing a size-dependent relative permittivity to describe the macroscopic response of the metal to an incident electromagnetic field. This arises from additional dephasing mechanisms such as surface scattering of the electrons, quantisation of the electronic band-structure and softening of the boundary (electron spill-out). For larger particles the relative permittivity is no longer a function of size and is given by the frequency dependent bulk values. However, the resonant optical properties remain strongly influenced by the size of the particle through *extrinsic* size effects. Retardation of the incident electromagnetic field and increased radiation damping results in significant shifts and broadening of the LSPR as size is increased. These effects were discussed in Chap. 2, Sect. 2.5 where Mie theory was applied to describe the extinction and scattering from spherical particles with radii ranging from 10 nm to 90 nm. The particles studied in this section are all within this range and as such are not influenced by size-dependent intrinsic effects.

The results described in this section are taken from NSL fabricated triangular nanoparticles using nanospheres with diameters of 220 nm, 390 nm and 630 nm. Approximate in-plane widths of the nanoparticles are respectively 50 nm, 90 nm and 150 nm. The height of the particles was 50 nm. The transmittance spectra of unpolarised light incident upon the samples are shown in figure 5.9. The minimum in transmittance associated with the resonant wavelength of the LSPR (λ_{LSP}) red-shifts as the particle size is increased. Other effects are a broadening of the mode and an apparent deepening of the resonance feature with increasing size. In figure 5.10 transmittance spectra from nanoparticle arrays formed from 390 nm diameter spheres with varying height are shown. Evaporated silver films with thickness ranging from 20 nm to 50 nm in 10 nm steps were studied. In contrast to the data in figure 5.9 there is a blue-shift in the position of the resonance as the particle size increases.

To help understand why this occurs it is instructive to consider the aspect ratio of the particles as well as the effects of retardation and radiation damping. Spheroidal particles in the quasi-static limit (no retardation, low radiation damping) were shown in Chap. 2 Sect. 2.6 to have LPSRs excited at two separate frequencies associated with the major and minor principal axes. As the aspect ratio was increased the mode associated with the long axis of the particle was observed to red-shift and the mode associated with the short axis blue-shift. A similar effect may be identified in figures 5.9 and 5.10 where an increasing aspect ratio of the particle in both instances leads to a red-shift of the LSPR. A complication, negligible for small particles, arises through the onset of increased radiation damping as particle width is increased. This undoubtedly contributes to the shift to longer wavelengths and to the increased linewidth of the mode. An increase in the imaginary part of the relative permittivity would also contribute to broadening of the LSPR with increasing wavelength. Furthermore, as the particle height is increased effects due to the retardation of the incident field would become more pronounced. In this case there may be a trade-off between the effects of reducing the aspect ratio of the particle and

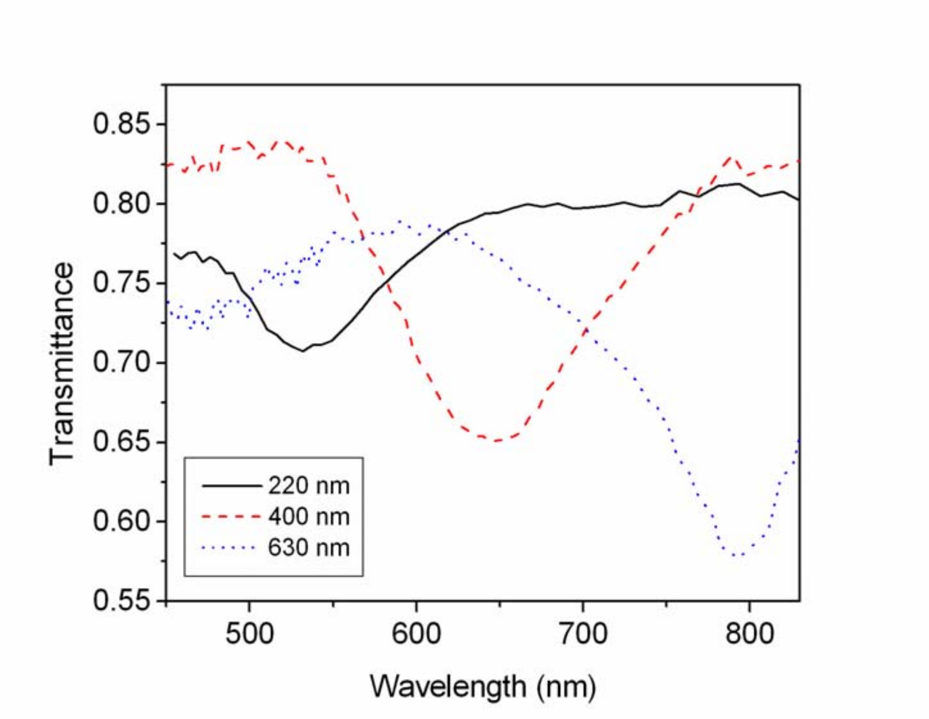

Figure 5.9. Transmittance spectra of silver nanoparticle arrays formed from nanospheres with mean diameters of 220 nm (solid line), 390 nm (dashed line) and 630 nm (dotted line). The height of the particles was 50 nm as measured by a quartz crystal thickness monitor during evaporation.

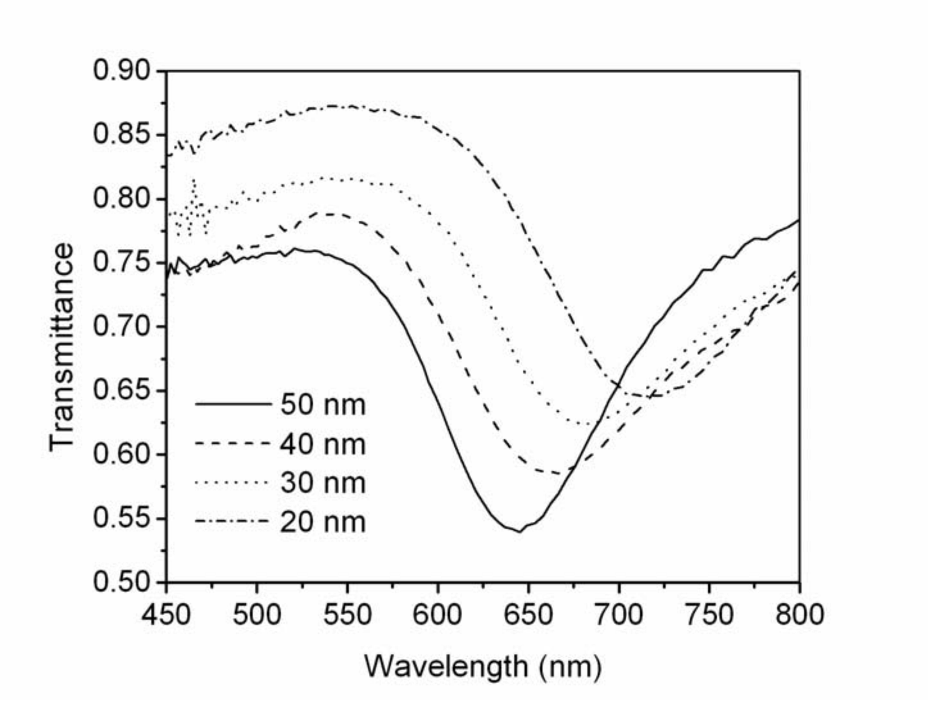

Figure 5.10. Transmittance spectra of silver nanoparticle arrays formed from arrays of 390 nm diameter nanospheres. The height of the particles was varied from 20 nm to 50 nm in 10 nm steps as measured by a quartz crystal thickness monitor during evaporation.

retardation of the incident field. Typically an increased retardation results in a red-shift of the LSPR [*Kreibig and Vollmer (1995)*] in contrast to the blue-shift observed in the experimental data presented. Therefore, in the size regime studied here it is most likely to be the geometry of the particle that dominates the resonance shift. Further increases in height would probably result in a more prominent effect from retardation of the incident field.

In figure 5.9 a deepening of the resonance with increasing particle size is observed. For spherical particles the extinction efficiency Q_{ext} of the dipolar mode is a maximum when the radius is a few tens of nanometres. Also, for an ideal array the surface coverage of the substrate by the particles is independent of particle size. This implies that the depth of the minimum would be expected to be reduced as particle size is increased. However, the density of line defects increases substantially when smaller diameter spheres are used. Furthermore, the standard deviation of the nanosphere diameter increases creating a larger variation in the width of the particles. It is most likely that a combination of these effects results in the reduced transmittance minimum from arrays of smaller particles.

5.5 Dependence on optical environment

If particles supported by a solid substrate are coated with a thin layer of dielectric material the field distribution associated with the LSPR is altered, the most important effect being a change (reduction) in the LSPR resonant frequency. Initially, as the thickness of the layer coating the particles is increased more of the particle's electromagnetic field samples the material and the resonant frequency is reduced still further. For a thickness greater than the decay length of the LSPR the field is contained almost entirely within the coating material and the shift in position of the resonance approaches an asymptotic value. This has been observed by *Haes et al. (2004a)* who monitored the resonance position as successive layers of a self-assembled monolayer (SAM – refractive index n ~ 1.5-1.6) were attached to Ag and Au particles formed by nanosphere lithography. The average thickness of each successive layer in the study by *Haes et al.* was 1.4 nm for the Au particles and 1.6 nm for the Ag particles. Normal incidence extinction spectra were recorded after each layer was added and the position of the dipolar-type extinction peak (λ_{max}) monitored. The maximum thickness was ~30 nm, corresponding to upwards of 20 self-assembled monolayers. The peak position, λ_{max} was observed to red-shift and approach saturation for a relative shift $\Delta\lambda_{max}$ ~ 120 nm. Other investigations have focussed on the LSPR response to the adsorption of single layers of SAM molecules with varying chain length [*Duval-Malinsky (2001)*], how changing particle size, shape and composition alters the near-field sensitivity of the LSPR [*Mock (2003), Haes (2004b)*] and the effect of immersing substrate supported nanoparticles in bulk solvents [*Meriaudeau (1998), Mock (2003)*]. These studies may be separated into two; those relating to layers of material with a thickness much smaller and much thicker than the wavelength of the incident radiation. A third scenario is that relating to particles located on or within layered media with a thickness of the order of the wavelength of the incident radiation. This too can lead to changes in the way light is absorbed and scattered by the particles. *Linden et al. (2001a, 2001b)* demonstrated that the LSPR of gold nanoparticles arranged in a periodic array on the surface of an asymmetric waveguide is significantly altered if the frequency of the resonance coincides with that of a waveguide mode. By changing the periodicity of the nanoparticle array they were able to sweep the frequency of the waveguide modes through the LSPR. They observed a suppression of the extinction associated with the LSPR when the modes overlapped and concluded that this was a consequence of destructive interference between electromagnetic fields associated with the incident light and the waveguide modes. *Holland and Hall (1984)* found that the resonant frequency of the LSPR underwent a shift even in the absence of waveguide modes. A silver island film was thermally deposited onto a lithium fluoride spacer layer coating a continuous silver film. By varying the thickness of the spacer layer they were able to monitor the spectral form of the LSPR as a function of separation from the silver mirror. Initially a red-shift of the resonance was observed compared to the value in the absence of the silver mirror, gradually becoming a blue-shift upon increasing the spacer layer thickness. *Stuart and Hall (1996a,b)* also investigated islandised silver films deposited onto dielectric, semiconducting and metallic layered structures. In particular with the semiconducting structures, they identified resonances in scattering spectra existing at long wavelengths compared to that of the LSPR associated with an isolated islandised film. *Johansson (2001)* attributed this behaviour to the influence of multiply reflected fields from the interfaces in the structure.

Modifying the behaviour of oscillating charge densities has been well documented in particular when molecular dipole emitters are placed within confined geometries [*Drexhage (1974), Amos (1997), Worthing (1999)*]. As with particle resonances the electronic excitations in atomic and molecular entities located near interfaces are different to those located in a bulk, optically isotropic medium. This occurs because the boundary conditions of the electromagnetic field in the vicinity of the moiety are altered, for instance by introducing a planar surface. This well-established concept is the basis underscoring the field of cavity quantum electrodynamics. The experiments by *Drexhage (1974)* on the molecular emission from europium (Eu^{3+}) dye molecules illustrated an oscillatory dependence of the lifetime (inverse decay rate) with separation from a planar metallic-dielectric interface. A similar dependence was found for molecules located near to an interface bounded by dielectrics of differing refractive indices. In both systems the observations could be explained using a model developed by *Chance, Prock and Silbey* (CPS theory) [*Chance et al. (1978)*] that treats the emitters as forced, damped dipole oscillators. This classical approach accounts for the presence of an interface by allowing the driving field to be represented by the retarded dipole field reflected from the interface. The phase relationship between the instantaneous and the retarded fields is the key to understanding the oscillatory dependence of the lifetime. If the fields are in phase the total driving field is enhanced and if the fields are out of phase the total driving field is inhibited. The optical path length, governed by the distance of the oscillator from the interface, is therefore crucial in determining the resonant behaviour.

For particles much smaller in size than the wavelength of the incident radiation the LSPR may be approximated as a dipole resonator [*Bohren and Huffman (1983), Kreibig and Vollmer (1995)*]. By analogy with the optical properties of light-emissive molecules, if a small particle is located within a finite geometry the local photonic density of states may be modified. The field driving the oscillation of the conduction electrons is reduced or enhanced depending on the relative phase of the dipole field and reflected fields. This was identified by

Holland and Hall (1984) as the cause of the frequency variation in their experiments as CPS theory predicts a fluctuation in the resonant frequency as well as the lifetime of the oscillator. When studying molecular emitters it is most convenient and practical to monitor the lifetime of the molecules since only a very small perturbation of the resonant frequency is expected. This changes for resonant particle oscillations and a measurable frequency shift occurs, as is evident from *Holland and Hall (1984)*.

In this section experiments are described that probe the response of nanoparticle arrays when LB layers of varying thickness are deposited onto them. The fabrication process outlined earlier is used to produce samples of the type shown schematically in figure 5.11. By varying the dip length and direction regions with a varying thickness are produced on a single sample. It was found that up to 16 regions arranged in a 4 x 4 array from 0 layers up to 120 layers in 8 layer steps could be deposited on to a single sample, each with an area of ~ 5 x 5 mm^2. This reduces possible inconsistencies from a variation in the relative permittivity of the silver between samples. Ideally a single region would be sampled and spectra taken after each layer was deposited. This was attempted, however surface contamination from the ambient environment resulted in poor film quality as subsequent layers were added thus causing inconsistent results from optical measurements.

Two samples were used, one with 50 nm high particles, the other with 30 nm high particles. Transmittance measurements were taken before and after deposition of the overlayers to account for small variations in the optical

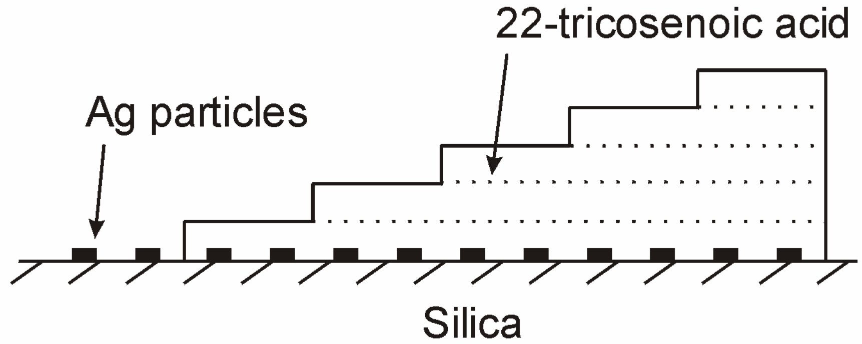

Figure 5.11. Schematic diagram of a coated nanoparticle array. By varying the dip length a stepped overlayer geometry is fabricated allowing a single sample to be used to collect the data.

response across the samples. Selection of suitable samples was based on the initial results and only those with consistent transmittance spectra were used. Polarised light was normally incident on the samples held in a translation stage with a micrometer capability to allow careful positioning of the beam within each region. Section 5.3 illustrated the importance of ensuring that the orientation of the sample relative to the polarisation is the same for each pair of transmittance measurements.

5.5.1 Optical response

The data shown in figure 5.12(a) illustrates the evolution of the LSPR as progressively thicker overlayers are deposited on four regions of sample 1. Normal incidence transmittance spectra of the coated nanoparticle arrays generally showed two main features. Firstly a transmittance minimum is observed at wavelengths between 620 nm and 700 nm, the particular wavelength depending on the overlayer thickness. This is indicative of the dipolar-type LSPR. Without any 22-tricosenoic acid overlayers deposited the LSPR minimum is located at 620 nm. With 32 layers (83 nm) deposited the resonance is seen to red-shift to a value of 690 nm, at the same time it also broadens and becomes shallower. Increasing the total thickness to 64 layers (166 nm) the resonance position blue-shifts to a value of 675 nm and appears

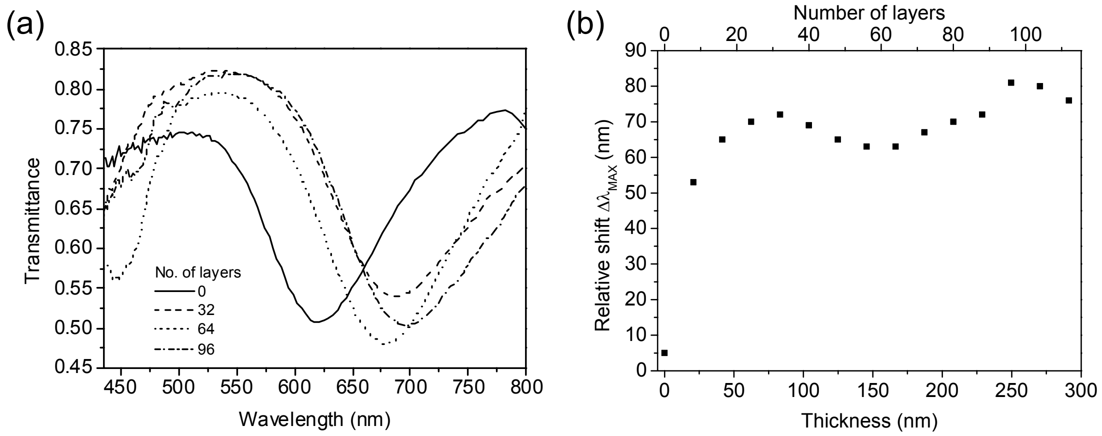

Figure 5.12. (a) Transmittance scattering spectra from Sample 1. (b) Relative shift of the LSPR minimum as a function of overlayer thickness.

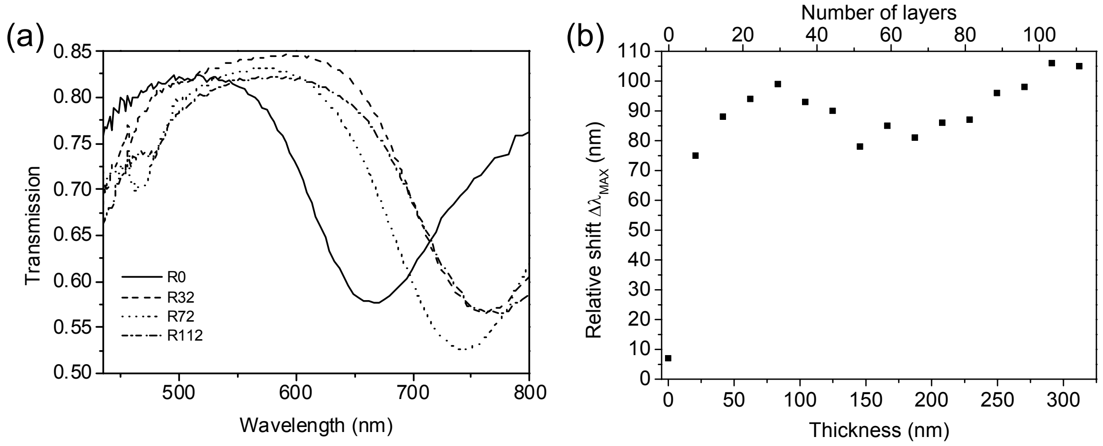

Figure 5.13. (a) Transmittance spectra from Sample 2. (b) Relative shift of the LSPR minimum as a function of overlayer thickness.

to deepen and narrow. With 96 layers (250 nm) deposited the position again red-shifts to a slightly higher value of 698 nm, broadens and shallows. Secondly a drop in transmittance is observed at wavelengths below 470 nm that becomes most pronounced for an overlayer thickness of 64 layers. This may be attributed to a combination of effects, primarily the appearance of a quadrupolar-type resonant mode of the particle [*Kelly (2003)*]. Without any overlayer deposited this quadropolar mode is beyond the spectral range of the experimental setup; however as LB layers are deposited the mode is red-shifted so that the longer wavelength wing of the resonance is observed in the transmittance data. In figure 5.12(b) a plot of the wavelength shift Δλ as a function of overlayer thickness. After an initial steep rise there is a clear oscillation in the data with maxima at ~32 layers and ~96 layers and a minimum between 58 and 62 layers. Further experimental data (not shown) confirms the continuation of the oscillation for >112 layers.

In figure 5.13(a) transmittance spectra are shown from sample 2 (silver now 30 nm thick rather than 50 nm thick) from regions with 0, 32, 72 and 112 layers deposited. With no overlayer deposited the position of the LSPR is at a higher wavelength compared to Sample 1 as has been well documented [*Jensen 1999a*]. An approximately linear red-shift is observed with decreasing particle height in this size regime, as observed in figure 5.10. A similar response to the addition of overlayers is observed in transmittance spectra again in comparison to sample 1, an initial red-shift with the addition of 32 layers followed by a blue-shift with 72 layers deposited and a further red-shift with 112 layers deposited. The relative size of the shift (plotted in figure 5.13(b) as a function of dielectric thickness) is larger than that observed for sample 1, similar to the effect reported by *Haes et al.* from arrays formed using NSL coated with self-assembled monolayers [*Haes 2004b*].

5.5.2 Theory and further discussion

To gain a better understanding of the frequency shifts and behaviour of the dipolar LSPR described above, a model was developed that used the classical dipole approach of CPS theory. This has been extensively applied within the group in Exeter when describing the behaviour of forced, damped dipole emitters embedded in multilayered planar structures [*Amos (1997), Worthing (1999)*]. Since the LSPR monitored in the experimental work detailed above is the dipolar-type resonance, on face value CPS theory should lend itself well to representing the system. However, there are significant differences mainly in the fact that a single point dipole is modelled thus neglecting the influence of neighbouring dipoles. It is well known that particle interactions lead to a modified optical response [*Meier (1985), Lamprecht (2000), Haynes (2003), Enoch (2004)*]. Moreover, CPS theory is designed to be implemented with planar structures. In our samples the particles protrude from the surface meaning that the LB overlayers subsequently deposited onto the particles have a similar profile, particularly when the number of layers *N* < 20. Whilst it is

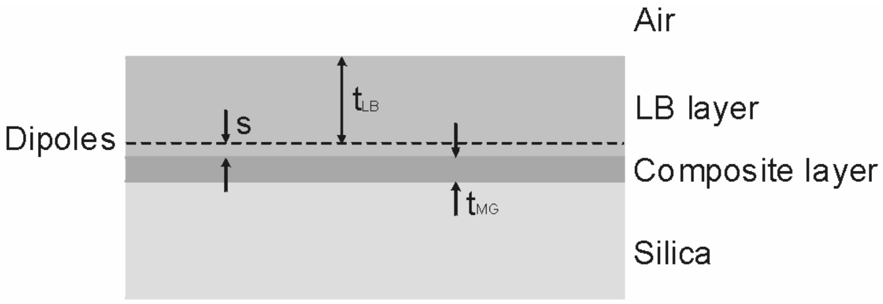

Figure 5.14. Schematic diagram of the system modelled using Maxwell-Garnett theory incorporated into CPS theory. The thickness of the LB and composite layers are denoted by t_{LB} and t_{MG} respectively and the separation of the dipole from the LB/composite interface is denoted by *s*

acknowledged that using CPS theory does not allow an exact representation of the system analysed experimentally, some insight can be obtained by approximating the system as consisting of the four planar layers illustrated in figure 5.14. The top layer and bottom layer are the semi-infinite air and silica regions respectively; the upper-middle layer is the LB layer. In the model the particles are represented by locating point dipoles 10 nm above[2] a fourth layer with relative permittivity determined using Maxwell-Garnett theory [*Maxwell-Garnett (1904), (1906), Bohren and Huffman (1983)*]. This is the lower-middle layer and is a composite LB/particle layer with a thickness of t_{MG} = 50 nm so as to be equal to the height of the particles in Sample 1. By representing the system in this way the general response to an electromagnetic field is governed by the relative permittivities of the layers with the dipoles inserted to act as both source and probe of those fields.

Maxwell-Garnett theory treats a composite layer with particulate inclusions in an otherwise homogeneous embedding medium as having an average relative permittivity $\varepsilon_{\mathrm{av}}$. The average electric field $\mathbf{E}_{\mathrm{av}}$ is given as the superposition of the electric field within the embedding medium $\mathbf{E}_{\mathrm{d}}$ and the electric field within the particles $\mathbf{E}_{\mathrm{k}}$,

$$\mathbf{E}_{\mathrm{av}} = (1-f)\mathbf{E}_{\mathrm{d}} + f\sum_{\mathrm{k}} w_{\mathrm{k}}\mathbf{E}_{\mathrm{k}} \, . \tag{1}$$

Here f is the volume fraction of the particles within the total volume and $w_{\mathrm{k}} = f_{\mathrm{k}}/f$ where f_{k} is the volume fraction of an individual particle. In a similar way the average polarization is given by

$$\mathbf{P}_{\mathrm{av}} = (1-f)\mathbf{P}_{\mathrm{d}} + f\sum_{\mathrm{k}} w_{\mathrm{k}}\mathbf{P}_{\mathrm{k}} \, , \tag{2}$$

where $\mathbf{P}_{\mathrm{d}}$ is the polarization in the embedding medium and $\mathbf{P}_{\mathrm{k}}$ is the polarisation in each individual particle. Assuming that the constitutive relations hold in each case then we can write

$$\mathbf{P}_{\mathrm{av}} = \varepsilon_0 \chi_{\mathrm{av}} \mathbf{E}_{\mathrm{av}} \, , \qquad \chi_{\mathrm{av}} = \varepsilon_{\mathrm{av}} - 1 \tag{3}$$

---

[2] To reduce the complexity of the model the dipoles are located within the non-absorbing LB layer and close to the composite layer. Reducing the separation of the dipole from the composite/LB interface was not found to significantly affect the form of the frequency shift as a function of overlayer thickness.

$$\mathbf{P}_{\mathrm{d}} = \varepsilon_0 \chi_{\mathrm{d}} \mathbf{E}_{\mathrm{d}}, \qquad \chi_{\mathrm{d}} = \varepsilon_{\mathrm{d}} - 1$$

$$\mathbf{P}_{\mathrm{k}} = \varepsilon_0 \chi_{\mathrm{k}} \mathbf{E}_{\mathrm{k}}, \qquad \chi_{\mathrm{k}} = \varepsilon_{\mathrm{k}} - 1$$

where ε_0 is the permittivity of free space, ε_{d} is the relative permittivity of the embedding medium, ε_{k} is the relative permittivity of the particles and $\chi_{\mathrm{av,d,k}}$ are the associated susceptibilities. Substituting equations (3) into equation (2) and combining with equation (1) yields

$$(1-f)(\varepsilon_{\mathrm{av}} - \varepsilon_{\mathrm{d}})\mathbf{E}_{\mathrm{d}} + f\sum_{\mathrm{k}} w_{\mathrm{k}}(\varepsilon_{\mathrm{av}} - \varepsilon_{\mathrm{k}})\mathbf{E}_{\mathrm{k}} = 0, \tag{4}$$

In order to calculate the polarization induced within the particles an expression for $\mathbf{E}_{\mathrm{k}}$ is required. Since analytical expressions for the internal fields of a triangular particle do not exist the particles are represented as oblate ellipsoids (disc-shaped) with the two long axes parallel to the substrate and the short axis perpendicular to the substrate. Moreover it is further assumed that the quasi-static approximation is valid, thus neglecting the effects of retardation, and that the particles do not interact. The field within such a particle is given by [*Bohren and Huffman (1983)*]

$$\mathbf{E}_{\mathrm{m}} = \lambda_{\mathrm{k}} \bullet \mathbf{E}_{\mathrm{d}}, \tag{5}$$

where λ_{k} is a tensor with principal components

$$\lambda_{\mathrm{k}} = \frac{\varepsilon_{\mathrm{d}}}{\varepsilon_{\mathrm{k}} + L_{\mathrm{k}}(\varepsilon_{\mathrm{m}} - \varepsilon_{\mathrm{d}})}, \quad (k = 1,2,3) \tag{6}$$

where L_{k} is one of the three geometrical factors associated with the three principal axes of an oblate spheroid. Since the light is normally incident and is polarised parallel to the substrate (and therefore parallel to the long axis of the particle) only one component of λ_{k} is required. Furthermore all of the ellipsoids are identical resulting in the following expression for the average dielectric function,

$$\varepsilon_{\mathrm{av}} = \frac{(1-f)\varepsilon_{\mathrm{d}} + f\lambda_2 \varepsilon_{\mathrm{m}}}{1 - f + f\lambda_2}. \tag{7}$$

To calculate a value for $\varepsilon_{\mathrm{av}}$ all that remains is to define suitable values for the filling fraction f and geometrical factor L. The geometrical factor L is chosen so as to produce a particle resonance at λ_{max} = 680 nm, the approximate position of the resonance with a thick LB overlayer deposited onto the particle. At this wavelength silver has a bulk relative permittivity of $\varepsilon_{\mathrm{Ag}}$ = 18.0 + 0.8i [*Palik*

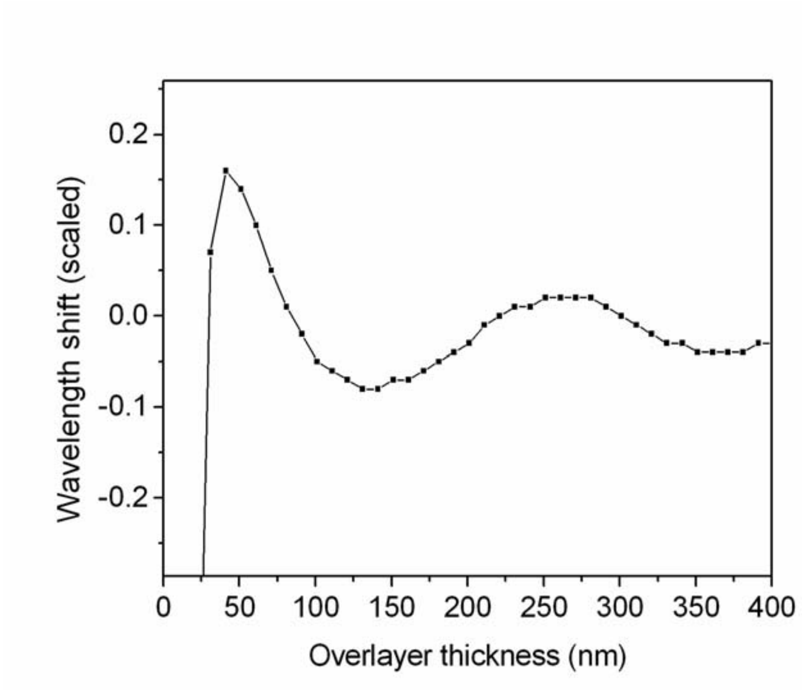

Figure 5.15. Theoretical plot of the wavelength shift (arbitrary units) of a dipole oscillator as a function of overlayer thickness.

(1985)]. The relative permittivity of the 22-tricosenoic acid is known to be anisotropic with a value perpendicular to the molecular axis (parallel to the substrate) of ε_d = 2.39 [*Barnes (1986)*]. A resonance occurs when the denominator of equation (6) is minimized this occurring when L = 0.12 upon insertion of the silver and 22-tricosenoic acid relative permittivities. Substituting these values into equation (7) with f = 0.072, chosen so as to provide an approximate match to that of the nanoparticle array studied in the experiment, results in a complex relative permittivity of the composite layer ε_{av} = -11.7 + 9.9i. Incorporating this into the multilayer CPS theory results in the theoretical plot of the shift in wavelength (for ease of comparison with the experimental data) as a function of overlayer thickness d shown in figure 5.15. Up to a thickness of 20 layers a steep rise is observed in the magnitude of the frequency shift. As thickness increases further the shift begins to level off indicating that the near-field associated with the dipole that extends into the overlayer has decayed sufficiently so as not to extend into the semi-infinite air layer. Thereafter an oscillation is observed in the data with a minimum at 150 nm and a maximum at 250 nm. As referred to in the introduction to Section 5, this is due to the phase relationship between the emitted dipole field and the multiply reflected dipole

field within the LB layer. Comparing the theoretical plot with the experimental data of figure 5.12(b) good agreement is found in the positions of the maxima and minima. It is noted that the amplitude of the oscillation is very much smaller than that observed experimentally. Given that the system modelled is different in many ways to that fabricated for the experiment an exact match with regard to the amplitude would not be expected. However, the overriding parameter in determining the position of the peaks and troughs is the optical path length of the reflected field. This would be consistent in both the theory and experiment. Furthermore, changes to the spectral form of the LSPR could be explained using a related argument. The position and width of the resonance is determined partly by the radiative damping experienced by the collective electron oscillation. If the photonic mode density near to the dipole is reduced then this radiative energy loss route is inhibited, as would occur if the phase of the reflected dipole field does not match that of the dipole itself. A reduction in radiative damping is accompanied by a blue-shift and narrowing of the resonance [*Kreibig and Vollmer (1995)*] as observed in the experimental data.

Work is ongoing to explore more comprehensive and directly applicable methods to model the LSPR shift, for instance by using the discrete dipole approximation or the finite difference time domain technique. These have previously been applied to the problem of modelling particles fabricated by NSL derived particles by the *Schatz Group (North western University, USA)*.

5.6 Summary

This chapter has described experiments that characterise a variety of the optical properties of silver nanoparticles fabricated by nanosphere lithography. It was possible to explore the influence of changing the polarisation state of the incident light, particle size and surrounding environment on the LSPR by monitoring the position of the resonant frequency. Firstly, a structural asymmetry in the particle arrays identified from diffraction measurements was found to result in a 180° azimuthal symmetry in the optical transmittance. Secondly, it was shown that an increase in the aspect ratio (width/height) of the particles resulted in a red-shift of the LSPR. Finally, by depositing thin layers of dielectric onto the particles using the Langmuir-Blodgett technique an oscillation in the frequency of the LSPR was seen to occur. This was explained in part by considering the interference of the dipolar oscillation with the electromagnetic fields reflected from the LB-air interface.

Chapter 6

Transition from localized surface plasmon resonance to extended surface plasmon-polariton as metallic nanoparticles merge to form a periodic hole-array

6.1 Introduction

The optical properties of metal films patterned with features of sub-micron dimensions are dominated by the surface plasmon[1] modes these structures support[2]. In particular two very different regimes are encountered, one applying to isolated noble metal nanoparticles, the other to continuous noble metal nanostructured films. Metallic nanoparticles support localised surface plasmon resonances whilst extended surface plasmon-polariton modes are found on continuous noble metal films. Many studies have separately explored these localised and extended regimes; here the transition from one regime to the other is examined. Given the contrasting nature of the surface plasmon modes involved it is not *a priori* obvious what character this transition will take. The fabrication of a variety of different sample structures is described and results reported of measurements that explore independently both the structural transition from nanoparticle array to nanohole array, and the evolution of the surface plasmon modes they support.

When visible light at an appropriate frequency is incident on a noble metal nanoparticle the spatially confined conduction electrons undergo a coherent oscillation known as the localised surface plasmon resonance (LSPR) [*Kreibig and Vollmer (1995)*]. The spectral position and width of the LSPR is governed by the geometry of the particle, the dielectric functions of both the metal and the surrounding media, inter-particle interactions and the polarisation

---

[1] We note that for convenience we are using the term surface plasmon rather loosely - for a discussion on this point see *Burstein (1974).*

[2] See Special Issue, Appl. Phys. B-Lasers and Optics **73**, 2001

of the incident light [*Kreibig and Vollmer (1995)*, *Haynes (2001)*]. The LSPR leads to a substantial electromagnetic field enhancement relative to the incident field that plays an important role in surface-enhanced Raman scattering (SERS) [*Wokaun (1982)*, *Moskovits (1985)*, *Nie (1997)*, *Schatz (2002)*], near-field microscopy [*Pohl (2001)*] and surface-enhanced fluorescence [*Ditlbacher (2001)*, *Kulakovich (2002)*]. Exploring the properties and underlying physics of individual nanoparticles continues to be an area of keen activity, in part because the underlying physics has still to be fully explored and in part due to the many potential applications. The sensitivity of the LSPR to changes in particle shape and the manner in which adjacent particles interact are particularly important and have been the subject of many recent investigations [*Salerno (2001), Köttmann (2001)*, *Mock (2002)*, *Haynes (2002)*]; nonetheless it is the resonances of individual nanoparticles that usually dominate.

In contrast the electron plasma oscillation at the interface between a continuous metal film and a dielectric, known as the surface plasmon-polariton (SPP), is extended in nature, and for a planar metal-dielectric interface cannot be excited by incident light. This is because for a given frequency the momentum (wave vector) associated with a SPP mode is always greater than that of a photon [*Sambles (1991)*]. The introduction of texture that is periodic on the scale of the wavelength of the incident light onto the surface enables photons to scatter, thus providing them with additional momentum that enables coupling between light and the SPP mode.

Despite a long history, the topic of surface plasmons continues to yield new insight into the interaction between nanostructured metals and light. In addition to allowing light to couple to surface plasmon modes, wavelength scale periodic texture can also be used to construct photonic surfaces for SPPs. This has led to both the demonstration of a full photonic band gap for SPPs [*Kitson (1996)*] and a means to control their propagation [*Bozhevolnyi (2001)*]. SPPs are also involved in the observation of enhanced transmission through otherwise opaque metallic films perforated with a periodic array of sub-wavelength holes [*Ebbesen (1998)*, *Ghaemi (1998)*]. A key aspect of these developments is that not only does the introduction of wavelength scale structure introduce a richness into the resulting surface plasmon modes, it also allows incident light to be coupled in to and out of these modes.

Nanoparticles that form an array of fixed period will have edges that get closer together as the size of the particles increases so that one might expect the surface plasmon modes of the individual particles to interact with each other. Such an interaction might then lead to a soft transition from individual particle to continuous film behaviour; as we will show below this is not what happens. The work presented here explores the transition through an experimental examination of the dispersion of the surface plasmon modes as the nanoparticles of an array increase in size, eventually merging to form a nano-hole array. Dispersion maps were obtained by measuring the optical transmittance as a function of frequency and in-plane wavevector. These data were correlated with images of the arrays obtained using scanning electron microscopy (SEM). In this way we were able to explore the transition in behaviour from the nanoparticle response, dominated by LSPR modes, to the hole-array response, dominated by extended SPP modes.

6.2 Experimental

6.2.1 Sample fabrication

Samples were fabricated using the nanosphere lithography technique as discussed in Chapter 4. In the first step chemical treatment of the substrate (fused silica, 25 mm x 25 mm x 1.5mm) was used to render its surface hydrophilic. This was achieved by soaking in a solution of sulphuric acid/hydrogen peroxide (3:1) for a minimum of 2 hours. The substrates were then rinsed in ultra-pure water followed by immersion and ultra-sonication in a solution of ultra-pure water/ammonium hydroxide/30% hydrogen peroxide (5:1:1) and sonicated for 1 hour. Finally the substrates were thoroughly rinsed in ultra-pure water and stored under ultra-pure water until required. After removal from the water the substrates were dried in air at a temperature of 50 ºC. Next, fresh ultra-pure water was deposited and dispersed across the substrate, the amount of water used depending on the concentration of the colloidal solution and the nanosphere diameter to be used. A colloidal nanosphere solution (390 nm diameter, 4% solids from Duke Scientific Corp) was deposited onto the water film and dispersed by a gentle tipping and rotation of the sample until an even concentration was present across the substrate. Typical volumes used when ordering 390 nm diameter nanospheres were 100 μL of water and 8 μL of solution. Finally, the samples were dried in an oven at 50 °C for ~1 hour.

As the water evaporates the nanospheres self-assemble into a hexagonally close-packed monolayer array suitable for use as a lithographic mask. A typical monolayer region covers an area of ~ 3 cm^2 and consists of randomly oriented monocrystalline domains, the largest single domains being ~ 10 mm^2 in area. The final stage of the process was to thermally evaporate silver through the nanosphere arrays. Subsequent nanosphere removal by ultra-sonication in toluene left an array of triangular silver nanoparticles. In all the samples discussed here 50 nm of silver was deposited.

In order to use the same basic technique to make arrays of larger nanoparticles and nano-hole arrays, the nanospheres were subjected to a reactive ion-etch using an oxygen plasma, prior to evaporating the silver. *Haginoya et al. (1997)* were the first to incorporate this extra step, successfully fabricating hole arrays in silicon by evaporating a Pt-Pd resist across an etched nanosphere array. By incrementing the etch time in 10 second steps from 50 seconds to 120 seconds the diameter of the nanospheres is steadily reduced, resulting in samples with metallic nanoparticles of increasing size until they eventually merge to form hole arrays with a period identical to that of the particle array.

6.2.2 Optical characterisation

Transmittance data were collected using the apparatus shown in figure 6.1. A collimated beam (divergence ~0.5°) from a tungsten halogen lamp (*Philips* 240 V, 50 W) was directed onto the samples. A *Spectrapro 275* monochromator was used to spectrally filter the incident light (spectral width ~ 2 nm) and a mechanical chopper modulated the intensity of the incident light so as to allow phase-sensitive detection of the zero-order transmitted beam. Further, a beam-splitter redirected a small fraction of the incident beam onto a second detector to allow source fluctuations to be taken into account. Both outputs from the reference and sample detectors (*Hamamatsu H6780-01* photomultiplier tubes) were fed into *Stanford Research Systems SR810* lock-in amplifiers to filter the signals and extract only the modulated component. The output voltage from the detectors varies as a function of the wavelength with an optimal operational range between 300 nm to 820 nm. The monochromator further limits the spectral operational window so that normal incidence data was typically collected for incident wavelengths between 450 nm and 800 nm. Outside of this range the light output from the monochromator became polychromatic due to stray light. A polarizer was placed in the incident beam so that the polarization state of the incident light could be controlled and when required in front of the sample detector so that the polarisation state of the detected light could be controlled. Apertures located in the path of the beam reduced the diameter of the projected beam spot to ~ 1.0 mm. This was found to generate a satisfactory signal to noise ratio whilst reducing the inhomogeneous broadening of spectral features due to domain overlap. Where possible the incident beam was

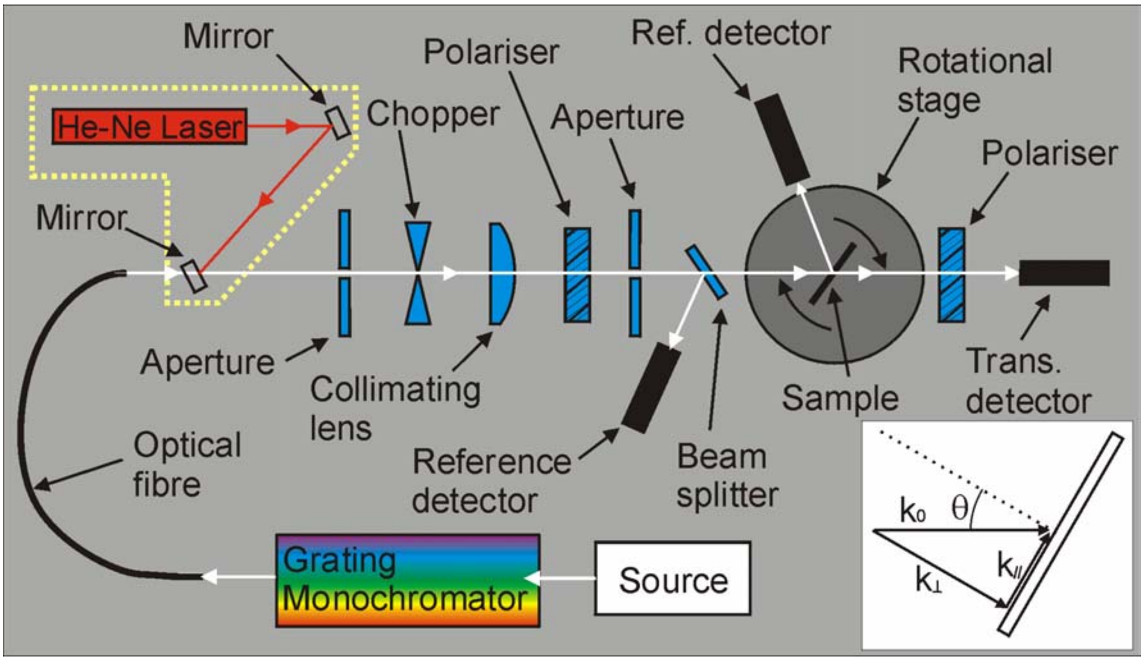

Figure 6.1. Experimental apparatus used to collect transmittance and reflectance as a function of frequency *ω* and in-plane wave vector $k_{//}$. The kit bounded with the dotted line is used in lining up the sample; the mirror in the beam is removed during data acquisition. The inset illustrates the incident, perpendicular component and parallel (in-plane) component of the wave vector and the angle of incidence *θ*.

directed onto a single domain of the sample. For each wavelength the signals from the sample and reference detectors are recorded along with the ratio of the two (sample divided by reference). To obtain absolute transmittance values a normalisation scan is taken by removing the sample and measuring directly the signal from the source. Again the ratio of sample to reference is calculated for each wavelength and this provides the normalisation constant that the sample data is divided by to generate the absolute values.

6.3 Dispersion scans and sample orientation

To understand the optical behaviour of the periodic nanostructures it is necessary to build up dispersion maps from the transmittance data (see Chapter 3). To do this data is collected not only as a function of the frequency, ω, but also as a function of the in-plane wave vector, $\mathbf{k}_{//}$. The in-plane wave vector is the component of the incident wave vector in the plane of the sample with magnitude given by

$$k_{//} = \frac{\omega}{c}\sin\theta\,, \tag{1}$$

where θ is the angle of incidence. Varying the in-plane wave vector was achieved by mounting the sample on a motor driven rotating stage. For a given in-plane wave vector the frequency was scanned and appropriate angles of incidence chosen according to equation (1). The samples were initially oriented so that one of the primitive reciprocal lattice vectors associated with the periodic structure was in the plane of incidence, illustrated in figure 6.1(a). Shown are the coordinate axes, defined relative to the grating, together with the primitive reciprocal lattice vectors $\mathbf{b}_1 = 2\pi/\lambda_G(1,0,0)$ and $\mathbf{b}_2 = 2\pi/\lambda_G(1/2,\sqrt{3}/2,0)$ the incident wave vector $\mathbf{k}_0$, in-plane wave vector and the angle of incidence θ. This is known as the classical mount and corresponds to an azimuthal angle $\varphi = 0^{\circ}$ (the azimuthal angle φ defines rotation about the (0,0,1) axis with $\varphi = 0^{\circ}$ along the (1,0,0) axis). In this orientation the axis of rotation used to vary $k_{//}$ is the (0,1,0) axis. Measurements were made for both *p*- and *s*-polarised incident light. At normal incidence the electric field (E-field) for *p*-polarised light is parallel to the (1,0,0) axis, for *s*-polarised light it is parallel to the (0,1,0) axis.

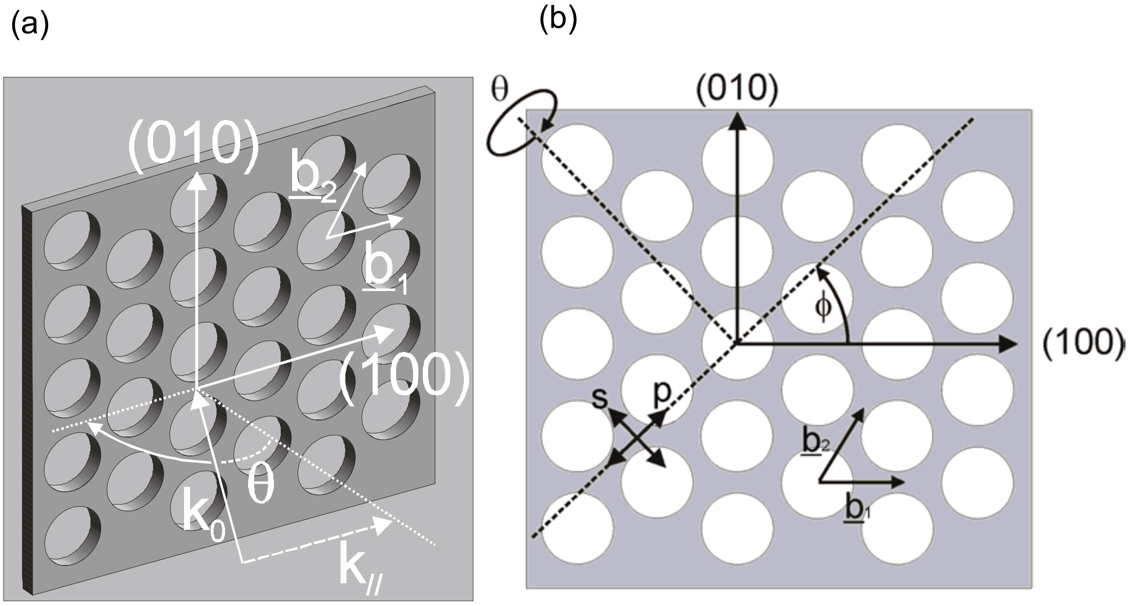

Figure 6.2. Schematic diagrams illustrating orientation of hole array relative to coordinate axes for a sample in the classical mount ($\varphi = 0°$) (a) and in the conical mount ($\varphi \neq 0°$) (b). Shown are the primitive reciprocal lattice vectors $\mathbf{b}_1$ and $\mathbf{b}_2$ where θ is the angle of incidence, incident wave vector $\mathbf{k}_0$ and in-plane wave vector $\mathbf{k}_{//}$. The azimuthal angle φ is defined as the angle the plane of incidence (represented by the long dotted line) makes with the (1,0,0) axis. Shown also is the orientation of the polarisation states – *p*-polarised light is parallel to the plane of incidence and *s*-polarised light is perpendicular to the plane of incidence. The second dotted line in (b) represents the axis of rotation used to vary $\mathbf{k}_{//}$.

Upon rotation of the sample about the (0,1,0) axis, *p*-polarised light has a component of the E-field normal to the interface whereas the E-field for *s*-polarised light remains parallel to the interface for all incident angles.

Upon azimuthal rotation the in-plane wave vector no longer lies parallel to the (1,0,0) axis since this is defined with respect to the primitive reciprocal lattice vectors associated with the periodic structure. Therefore with $\varphi = 90°$ the in-plane wave vector is parallel to the (0,1,0) axis and the axis of rotation of the sample is parallel to the (1,0,0) axis. This is shown in figure 6.1(b) for an arbitrary azimuthal angle where the dotted line at an angle φ to the (1,0,0) axis represents the plane of incidence, parallel to the in-plane wave vector of the incident light, and the second dotted line orthogonal to the plane of incidence represents the polar axis of rotation that varies θ.

6.4 Scattered light-line and SPP schematics for hex array

It is often instructive when interpreting dispersion scans of periodic arrays to generate simple schematic representations of the photonic band structure to compare with the data. By employing the condition for the grating-coupling of light with the SPP modes the dispersion of the scattered modes can be plotted as a function of frequency ω and in-plane wave vector $k_{//}$. Described earlier in Chapter 3, it is recalled that the dispersion relation for the SPP propagating on a planar interface is

$$k_{\mathrm{SPP}} = \frac{\omega}{c}\left(\frac{\varepsilon_{\mathrm{r1}}\varepsilon_{\mathrm{r2}}}{\varepsilon_{\mathrm{r1}}+\varepsilon_{\mathrm{r2}}}\right)^{\frac{1}{2}}, \tag{2}$$

where k_{SPP} is the magnitude of the wave vector of the SPP, ω is the angular frequency, c is the speed of light, ε_1 is the relative permittivity of the silver and ε_2 is the relative permittivity of the bounding dielectric. Comparing equation (2) with the dispersion relation for the light-line (defined as the maximum attainable in-plane wave vector of a propagating photon in the bounding dielectric)

$$k_{\mathrm{L}} = \frac{\omega}{c}(\varepsilon_{\mathrm{r2}})^{\frac{1}{2}}, \tag{3}$$

it is seen that k_{L} always has a value less than k_{SPP} for typical values of ε_2 for silver in the visible emphasising the requirement for enhancement of the incident wave vector to allow light-SPP coupling. In this case it is achieved via grating-coupling, defined by the condition

$$\mathbf{k}_{//} = \mathbf{k}_{\mathrm{SPP}} + \mathbf{G}, \tag{4}$$

where $\mathbf{G}$ is the reciprocal lattice vector that matches the in-plane and SPP wave vectors. When the coupling condition is fulfilled the transmittance and reflectance of light by the structure will be modified, thus allowing observation of the modes of the structure. The diffracted light-lines are found in a similar way, by applying the scattering equation (4) to the light line equation (3), substituting k_{L} for k_{SPP}.

The reciprocal lattice vector $\mathbf{G}$ is the resultant formed from the addition of integer multiples of the primitive reciprocal lattice vectors as defined above,

$$\mathbf{G} = m\mathbf{b}_1 + n\mathbf{b}_2, \tag{5}$$

where m and n can be positive or negative. Equation (5) is used to map the scattering points in two-dimensional reciprocal space, shown in figure 6.3 where the $m = 1$, $n = 0$ (1,0) and $m = 0$, $n = 1$ (0,1) points are indicated. The dotted lines represent the azimuthal orientations $\varphi = 0°$ and $\varphi = 30°$.

By inserting equation (5) into equation (4) it is possible to produce the scattered light-line and SPP schematic diagrams in figure 6.4. Depending on the orientation of the grating the scattered SPP modes and light-lines of a hexagonal structure take on slightly different forms. Figure 6.4(a) shows the dispersion of light-lines and SPP modes from a hexagonal structure with azimuthal orientation $\varphi = 0°$ (equivalent to 60° and 120°) and likewise figure 6.4(b) with $\varphi = 30°$ (equivalent to 90° and 150°). The light-line diagrams are constructed assuming a constant relative permittivity and therefore take the same form regardless of the periodicity of the structure (hence the arbitrary frequency scale). Due to the dispersion of the relative permittivity of the silver, here calculated using the Drude approximation

$$\varepsilon_{r1} = 1 - \frac{\omega_P^2}{\omega^2}, \qquad (6)$$

with the plasma frequency $\omega_P = 7.2$ eV, the schematic SPP diagrams do vary with the periodicity of the structure. To calculate the dispersion of the scattered SPP modes a pitch of $\lambda_G = 335$ nm and permittivity of the bounding dielectric $\varepsilon_1 = 1.46$ (silica) was used.

Considering first the intersecting SPP modes at $k_{//}/b = 0$ with $\varphi = 0°$, the six lowest order scattered modes are those intersecting at the lowest frequency. Two pairs of these six modes are degenerate in this simple representation where mode interactions are neglected. Referring to figure 6.3 the degenerate modes are those identified as being equidistant from a point on the dotted line representing $\varphi = 0°$. This means that the (0,1) and (1,-1) are one degenerate lowest order pair with (0,-1) and (-1,1) the other degenerate pair. The (1,0) and (-1,0) modes are those located on the $\varphi = 0°$ line and in the SPP and light line diagrams of figure 6.4(a) are seen to stem from $\omega = 0$ μm^{-1} at $k_{//}/b = 1$ and $k_{//}/b = -1$ respectively. Increasing in frequency, the next set of modes to intersect at

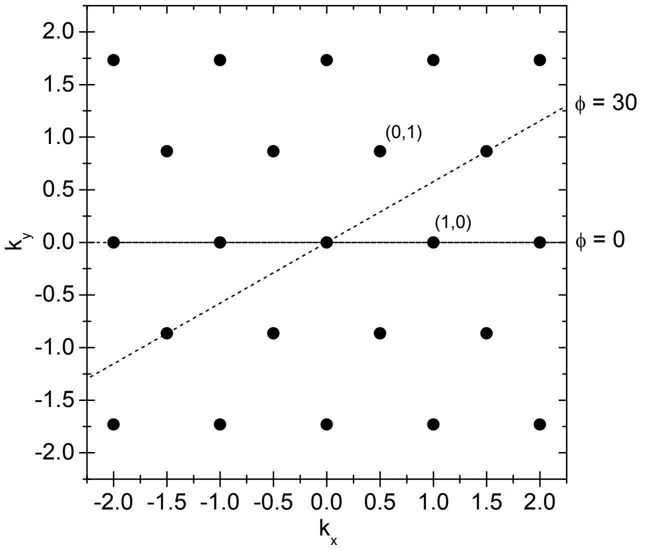

Figure 6.3. A two-dimensional reciprocal space diagram illustrates the orientation of the in-plane wave vector relative to the reciprocal lattice points for the two azimuthal angles.

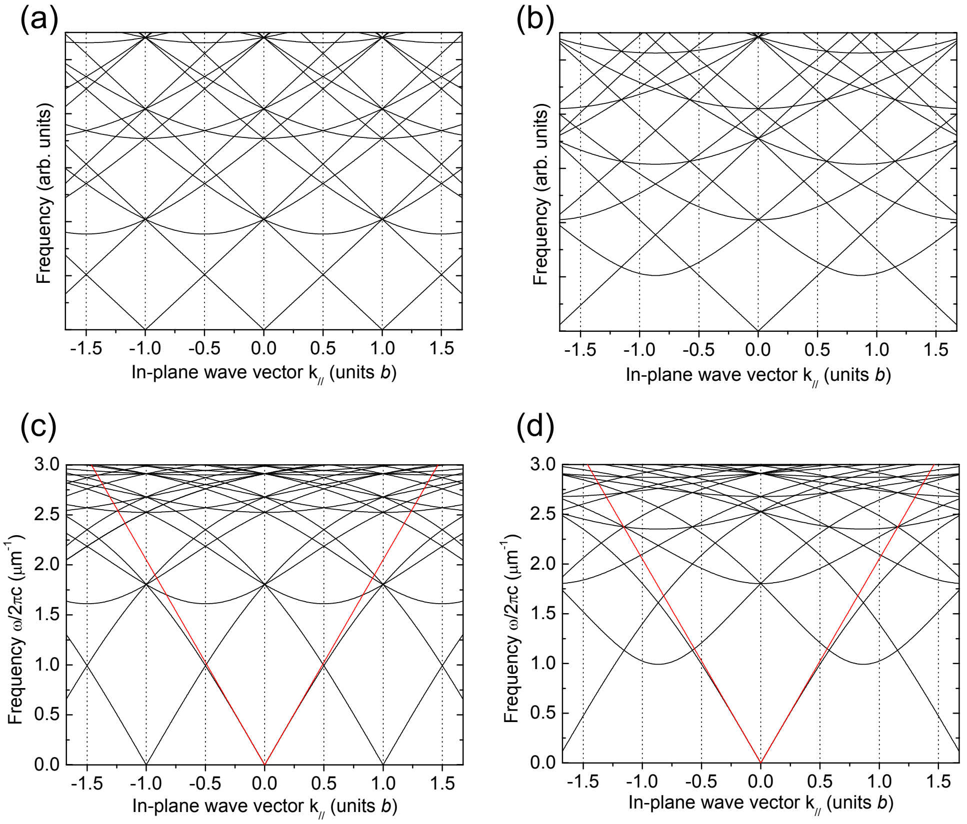

Figure 6.4. Dispersion plots of the scattered light-lines and grating-coupled silica SPP modes for azimuthal angles of φ = 0° (a) and φ = 30° (b). The SPP dispersion is calculated using the Drude approximation for silver and a periodicity of 335 nm. Included are the (0,0) silica light-lines for comparison; no account is taken of mode interactions.

$k_{//}/b = 0$ are those requiring a double-scatter[3] with a resultant magnitude of $G = b\surd 3$, such as the (1,1) and (-1,-1) modes. These are observed as three separate lines in figure 6.4(a) corresponding to three degenerate pairs. Increasing still further in frequency the next set of modes again require a double-scattering event this time with a magnitude of $2b$, for instance the (2,0) and (0,2) modes.

Considering now the modes intersecting at $k_{//}/b = 0$ with $\varphi = 30°$ it is seen from figure 6.4(b) that there are three degenerate pairs of modes associated with the lowest order scatter. In this orientation the (1,0) and (0,1), (-1,1) and (1,-1), and (-1,0) and (0,-1) pairs are degenerate. Since none of the scattering centres lie in the plane of incidence (see figure 6.3) there is a cut-off frequency below which the lowest order modes are not observed for any $k_{//}$. Only when the modes intersect with the plane of incidence are they observed in the dispersion plots, the minimum frequency located at $k_{//}/b = \surd 3/2$. Increasing in frequency, the next set of modes observed to intersect at $k_{//}/b = 0$ are again those requiring a reciprocal lattice vector of magnitude $G = b\surd 3$. However, the (1,1) and (-1,-1) scattering centres now lie in the plane of incidence and are thus seen to approach $\omega = 0$ as $k_{//}/b \rightarrow \pm\surd 3$.

Away from the symmetry axes the degeneracy described above is lifted and the modes associated with each reciprocal lattice vector generated by equation (4) would be observed separately in the plots. This serves to underline the importance of taking care to align the samples correctly when undertaking experimental measurements designed to map the dispersion of SPP modes on structures with two-dimensional periodicity.

6.5 Results and discussion

6.5.1 SEM images

In figure 6.5 we show scanning electron microscopy (SEM) images of (a), a nanoparticle array formed without etching the nanospheres; (b), a

---

[3] Assuming a purely sinusoidal modulation; the higher harmonic components required to describe more complex grating profiles can result in direct coupling to higher order SPP modes.

nanoparticle/nano-hole intermediate structure; and (c), an array of 300 nm diameter holes. The mean diameter of the nanospheres prior to etching was 390 nm that for a hexagonal array without defects would result in a periodicity λ_G = 338 nm. The features caused by the presence of defects in the crystalline structure such as vacancies, slip dislocations and variations in nanosphere diameter, are most apparent in the nanoparticle arrays, figure 6.5(a); nanowires and 'bow-tie' shaped particles are produced. For the nanoparticle arrays these defects seem to have little effect on the overall optical response. However, as the nanospheres are etched the influence of structural defects on the optical response becomes significant. Now even small variations in the nanosphere diameter will lead to a gradual rather than a sudden change as the etch time is increased; some nanoparticles will merge whilst others will remain isolated. This is seen in figure 6.5(b) where there are gaps and channels in the metal film surrounding what would otherwise be holes. The gaps and channels no longer appear after the samples have been etched further, as shown in figure 6.5(c). Here a continuous network of metal perforated with an array of nanoholes approximately 300 nm in diameter has been produced; there are no gaps and no isolated nanoparticles.

Further features to note include the small ring-shaped structures observed at the centre of the holes. These are present due to the deposition of residue contained within the fluid supporting the nanospheres during the drying process. Similar samples fabricated subsequently with less impurities present in the nanosphere solution were observed to have almost identical transmittance spectra; the presence of the residue does not contribute significantly to the optical response. The ellipsoidal shape of the holes, particularly apparent in figure 6.5(c), is mainly due to drifting of either the sample or the electron beam during image capture, though it is noted a slight shape distortion of the spheres also occurs during fabrication (see Chapter 4).

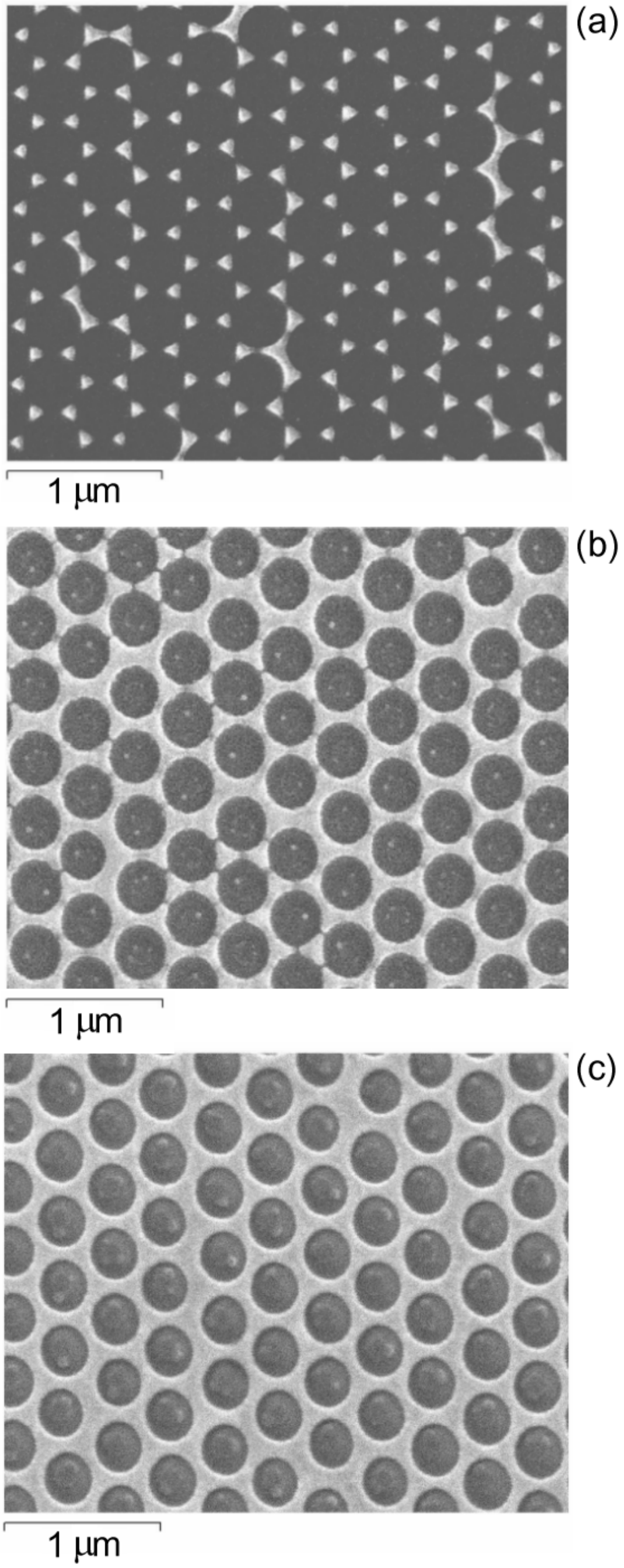

Figure 6.5. SEM images of (a) nanoparticle array formed without etching nanosphere array, (b) intermediate structure formed after etching nanosphere array for 70 s and (c) hole array formed after etching nanosphere array for 120 s.

6.5.2 Optical measurements

Before looking at the acquired dispersion scans it is instructive first to look at some individual transmittance spectra. Figure 6.6 shows the transmittance for normally incident light for samples ranging from arrays of well isolated nanoparticles to nanohole arrays; they were fabricated using etch times of 0 s, 50 s, 70 s, 100 s and 120 s. As the etch time was increased the nanoparticles increased in size so that whilst the centre-to-centre particle distance remained fixed the extremities of neighbouring particles became closer. For the well-isolated nanoparticle array (etch time 0 s), the transmittance shows a clear minimum at 610 nm, attributed to the ensemble averaged LSPR. As the etch time was increased this minimum shifted to longer wavelengths, occurring at 675 nm for a 50 s etch and at ~ 800 nm for a 70 s etch, this behaviour being consistent with data collected from many samples fabricated with a variety of etch times from 0 s to 70 s. This red shift of the LSPR for increasing

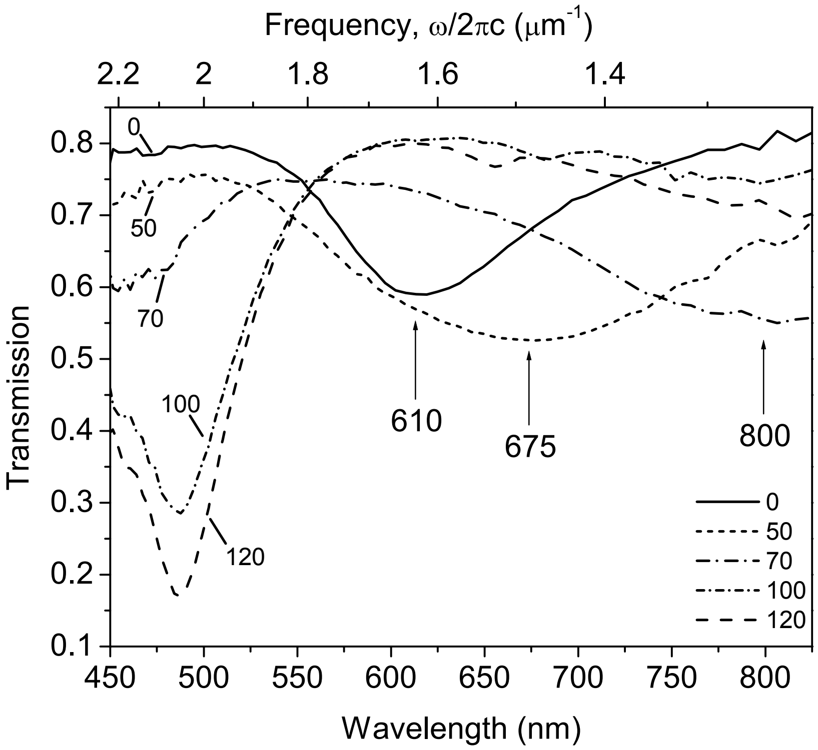

Figure 6.6. Transmittance spectra for *p*-polarised light with $k_{//} = 0$ from samples etched for 0 s, 50 s, 70 s, 100 s and 120 s. Arrows indicate position of the localised surface plasmon resonance.

particle size is well known and is due to the increasing effect of radiation damping as particle size increases [*Kreibig (1995)*].

A shift in the resonant wavelength is also expected to arise from a change in the dipolar coupling between nanoparticles as their separation decreases. For pairs of nanoparticles a red-shift in the position of the LSPR is observed as particle separation decreases when the polarisation of the incident light is parallel to the inter-particle axis whilst a blue-shift occurs for the orthogonal polarisation [*Rechberger (2003)*]. However, the influence of dipolar interactions is more complex with periodic assemblies of nanoparticles. *Haynes (2003)* observed a blue-shift in the LSPR position with a reduction in particle separation when the particles are contained within both square and hexagonal arrays. There are thus likely to be competing processes involved in producing a shift in the position of the LSPR; in our case the dominant effect appears to be the increase in size of the nanoparticles.

As described above, transmittance measurements obtained for a matrix of frequency and in-plane wave vector values allow a dispersion map to be produced. Figure 6.7 shows *p*-polarised transmittance dispersion scans from the nanoparticles (a), intermediate (b) and nano-hole (c) arrays described earlier. The strong, non-dispersive absorption (dark) feature centred at a frequency of 1.63 μm^{-1} (615 nm) in figure 6.7(a) is characteristic of the ensemble averaged LSPR. The dispersion scan for the intermediate structure shows ill-defined features consistent with the random nature of the defect-related discontinuities in the silver film; see figures 6.5(b) and 6.7(b). The dispersion data change dramatically when the etch time is increased such that a perforated thin film structure is produced that does not have any discontinuities. The transition is clearly illustrated in figure 6.7(c) and figure 6.6 with the appearance of a strong extinction feature centred at $\omega/2\pi c$ = 2.05 μm^{-1} for normal incidence, ($k_{//}$ = 0 μm^{-1}) and three modes intersecting at $\omega/2\pi c$ = 1.53 μm^{-1}, also for normal incidence. The frequency at which the modes intersect at the $k_{//}$ = 0 μm^{-1} axis rises as the hole diameter is reduced, evident in figure 6.6 where a slight dip is observed in the transmittance from the samples etched for 100 seconds and 120 seconds at $\omega/2\pi c$ = 1.46 μm^{-1} and $\omega/2\pi c$ = 1.53 μm^{-1}

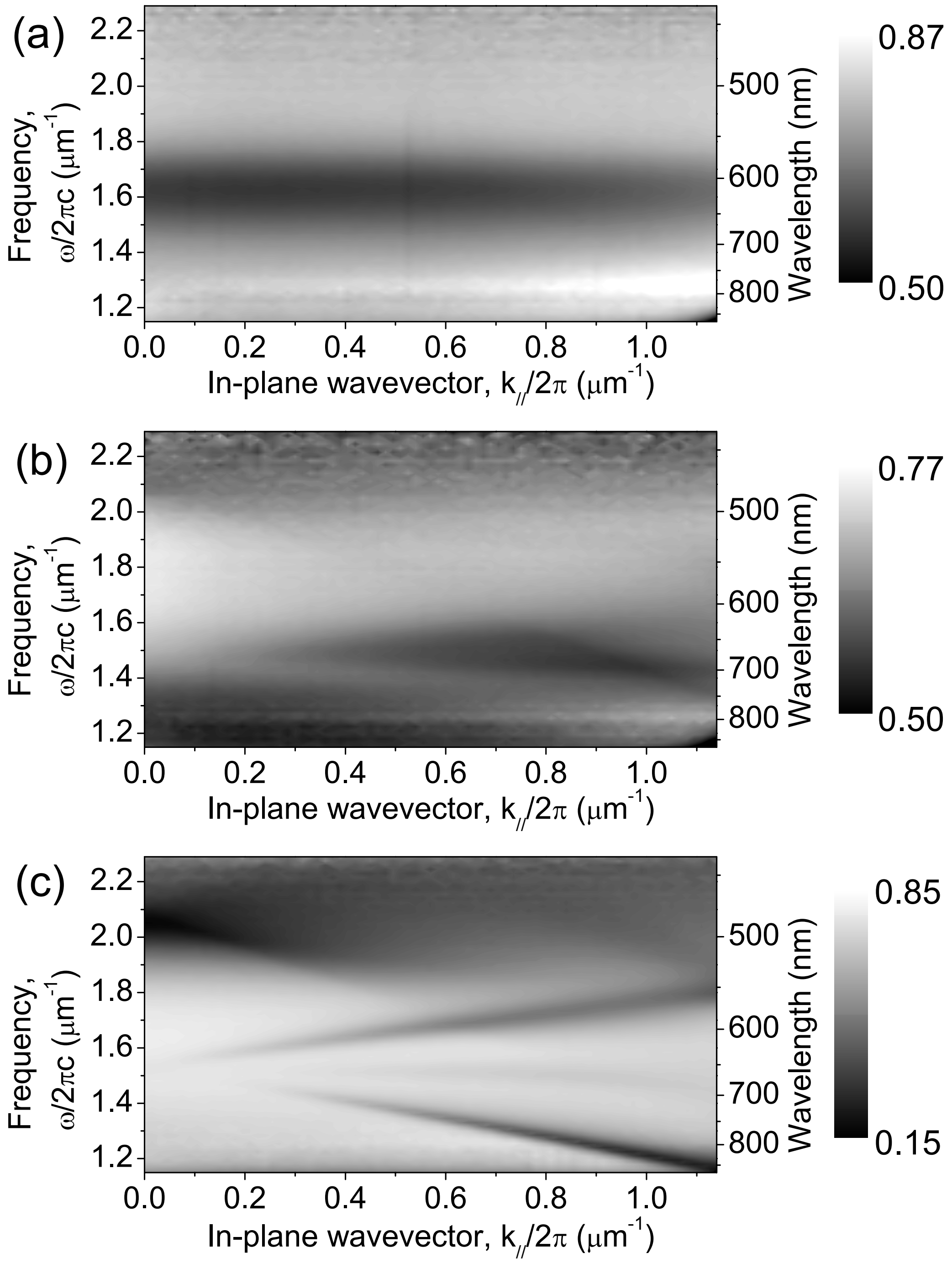

Figure 6.7. Measured transmittance as a function of in-plane wavevector and frequency in the form of a greyscale diagram for p-polarised light incident upon the (a) nanoparticle array, (b) intermediate structure and (c) hole array imaged in figure 3.

respectively. Results obtained from samples etched for as long as 150 seconds confirm this behaviour (see Chapter 7).

The dispersion of the lowest order (m = ±1, n = 0) scattered silica/silver interface SPP modes, calculated by employing a Drude model for the frequency dependent dielectric function of the silver, are shown as the dashed lines in figure 6.8. The offset to higher frequencies of the modelled SPP mode when compared to that obtained experimentally may perhaps be explained by considering how the presence of the holes modifies the effective thickness of the silver layer. In contrast to a uniform metal film, the hole-array is substantially permeated by air. The evanescently decaying electric field associated with the silica/silver interface SPP mode extends into the holes and also directly through the metal into the air bounding the opposite interface; the dispersion of the mode is thus altered. In the absence of an accurate model for the dispersion of SPP modes on perforated metal films we attempted to model this effect simply by using an effective thickness for a planar metal that was thinner than the film used.

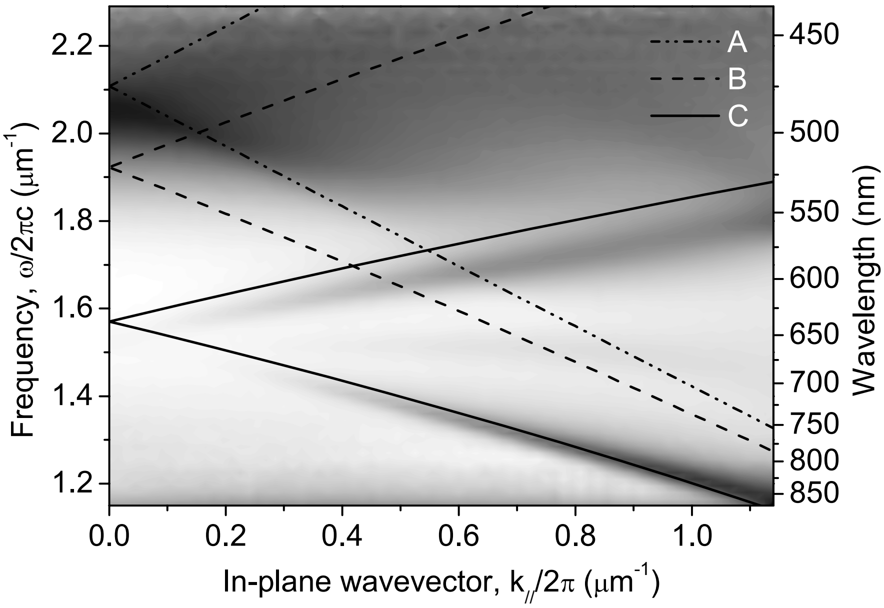

Figure 6.8. Superimposed upon the data from figure 6.7(c), (A) the diffracted (±1,0) silica light lines (dotted lines) and (B, C) modelled dispersion of grating coupled (±1,0) SPP modes associated with a planar silver-silica interface. The dashed lines (B) correspond to the SPP dispersion on a semi-infinite slab whereas the solid lines (C) correspond to the SPP dispersion on a 15 nm thick slab with the second silver interface bounded by air.

To this end the near-field coupling properties of a dipole emitter located close to a dielectric-silver interface are exploited to generate a plot of the SPP dispersion for a thin metal film. The procedure is similar to that used in Chapter 5 where the frequency of a dipole emitter located within a multilayer structure was modelled. The dipole is treated as a forced, damped oscillator, forced since the reflected fields from any interfaces within the structure act to drive the oscillation and damped because power is radiated by the emitter. When the dipole-silver separation is small (< 50 nm for silver) the near-field of the dipole contains higher wave vector components that result in direct coupling to the SPP mode [*Chance (1978)*]. Power is transferred non-radiatively to the SPP and becomes an additional loss channel. Therefore if the power dissipated by the dipole can be calculated as a function of frequency ω and in-plane wave vector $k_{//}$ then a maximum will be observed coinciding with the dispersion of the SPP mode [*Wasey (2000)*]. To achieve this we express the fields of an emitter in free space as a summation of plane waves using the method of *Sommerfeld (1949)*. From this starting point it is then possible to apply the boundary conditions appropriate for an interface located near to the dipole to generate expressions that incorporate the reflected and transmitted fields as extra terms in the expansion. The amplitudes of these additional terms are defined by the Fresnel transmission and reflection coefficients appropriate for each interface and the phase relative to the dipole site by the characteristic dimensions of the structure. Having calculated the fields within each medium it is then possible to evaluate the Poynting vector and from this the power dissipated by the dipole.

A representation of the system is depicted in the inset of figure 6.9; the dipole is located in silica 50 nm from the surface of a thin silver film of thickness d with the opposite interface bounded by air. Using a silver film with d = 15.0 nm produces the dispersion plot shown in figure 6.9. Fitting a polynomial to the silica SPP mode dispersion and applying the grating-coupling condition (equation 6.4) results in the solid lines shown in figure 6.8 for the dispersion of the lowest order scattered silica SPP modes. The periodicity of the array was taken to be λ_G = 330 nm based on estimations from diffraction measurements[4].

---

[4] Note that this is not the 338 nm expected from the sphere size. The difference is probably due to a slight distortion in the structures and possibly the packing was not fully close.

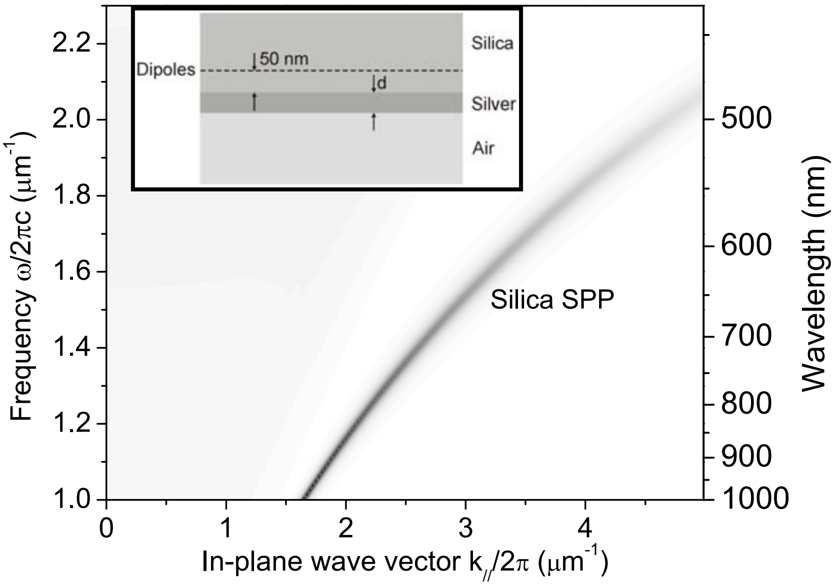

Figure 6.9. Power dissipated by a dipole as a function of frequency and in-plane wave vector. The dipole is embedded in a semi-infinite silica layer located 50 nm from a silver slab of thickness d = 15.0 nm. A semi-infinite air layer bounds the opposite surface of the silver.

The positions of these calculated modes are in fair agreement with the experimentally derived SPP dispersion. The hypothesis is supported by the blue shift of the plasmon modes observed as the hole diameter is decreased, reducing the proportion of air within the layer relative to the amount of silver and therefore increasing the effective thickness (see Chapter 7).

It is also instructive to look at reflectance as well as transmittance since the combination can be used to infer absorption, provided no diffraction is possible. This is useful since when light is coupled to SPPs the enhanced fields associated with such modes leads to an increase in the absorption – absorption is thus another indicator of the presence of SPP modes [*Barnes (2003)*, *Sarrazin (2003)*, *Bonod (2003)*, *Hooper (2003)*]. The first order scattered silica light-lines are plotted as dotted lines in figure 6.8. At frequencies below these lines, the zero-order regime, no diffraction into the far-field is possible. Therefore, to account for a reduction in transmission one need only consider light that is specularly reflected and light that is absorbed by the structure. The absorbance *A* in this zero-order regime is inferred by simply combining the reflectance *R* and transmittance *T* via the relation A = 1 – R – T. Shown in figure 6.10 are reflectance, transmittance and absorbance spectra at an in-plane wave vector of $k_{//} = 0.5\ \mu m^{-1}$, taken with light incident on the air/silver interface of the hole array. From the data we see that reflectance maxima (e.g. at 610 nm) are associated with the transmission minima, and by inference absorbance maxima.

The observation of transmittance minima being associated with reflectance maxima is in marked contrast to the enhanced transmission and associated reduced reflectance seen in hole arrays in much thicker silver films [*Barnes (2003)*]. The hole-arrays studied previously have usually been fabricated in optically thick metal films, typically with a lattice constant somewhat higher than the diameter of the holes. In the present work however the metallic arrays are optically thin, this together with a low surface coverage of silver, results in a far higher probability of direct transmission. This in turn leads to the possibility of interference between light that is directly transmitted

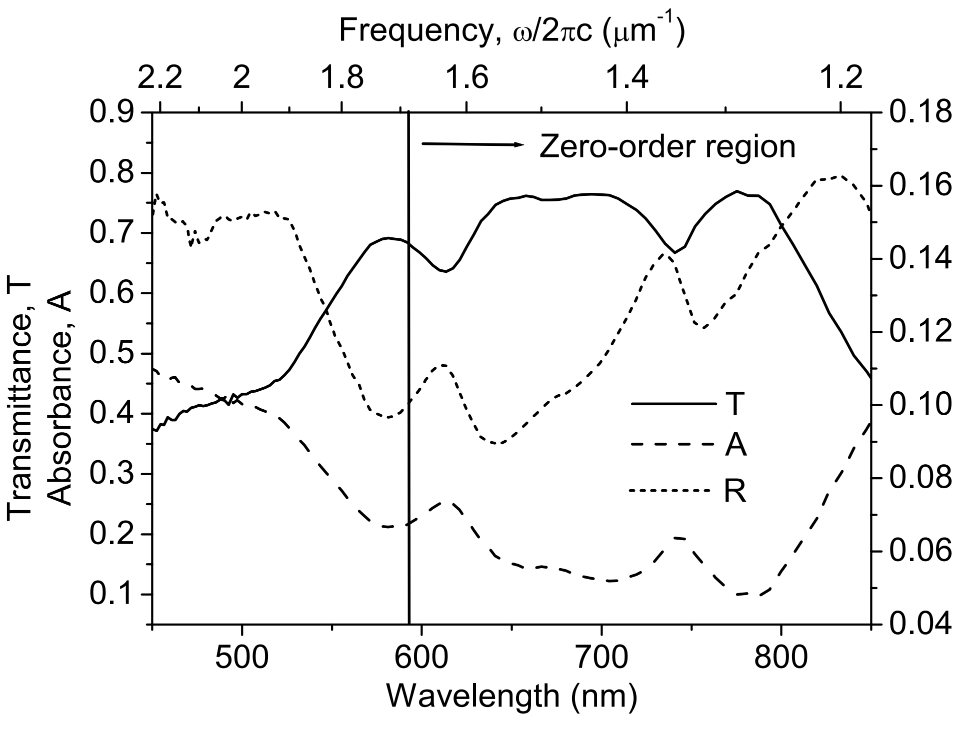

Figure 6.10. Transmittance, reflectance and inferred absorbance spectra at $k_{//} = 0.5\ \mu m^{-1}$ for *p*-polarised light incident upon a hole-array formed with a 120 s etch (detected light was un-polarised).

and light that is first coupled into an SPP mode by scattering and then coupled back out to light, again by scattering. If this SPP mediated light is out of phase with the directly transmitted light then transmittance minima rather than maxima will be observed. One may expect that as the hole diameter is decreased, simply by etching the nanospheres for a time longer than 120 seconds, then transmittance maxima may be observed as the intensity of the directly transmitted light is reduced. From preliminary results this appears to be the case though further investigation is needed.

Similarly, the increase in the (zero-order) reflectance that we observe might be attributed to interference between light that is specularly reflected and that which is first coupled into the SPP and then coupled back out. If the transmitted components are out of phase we would expect the reflected components to be in phase since the specularly reflected component suffers a 180 degree phase change on reflection.

There are three further observations to make concerning the dispersion data, figure 6.7(c) that we cannot fully explain at this stage. Firstly, we note that the SPP modes are only weakly coupled at normal incidence ($k_{//} = 0$). For incident light to generate the surface charge density associated with the SPP the mode there needs to be a component of the incident electric field perpendicular to the interface. Not being able to fulfil this condition for light normally incident on a sinusoidally modulated metal film is responsible for the lack of coupling to one of the band edges associated with an SPP band gap [*Barnes (1996)*]. A similar reason may be behind the lack of coupling we see here for our modes at normal incidence. Secondly, a strong dip in the transmission centred at a frequency of $\omega/2\pi c$ = 2.05 μm^{-1} at normal incidence for the hole arrays, figures 6.6 and 6.7(c). It is located slightly below the frequency at which the diffracted light-lines intersect, $\omega/2\pi c$ = 2.10 μm^{-1}. Lastly, we note from the dispersion data the presence of a third band-like feature centred at $\omega/2\pi c$ ~ 1.5 μm^{-1} that shows only weak dispersion. The origin of this feature is most likely due to SPP modes scattered by the second reciprocal lattice vector, $\mathbf{b}_2$, the one that is not in the plane of incidence. This aspect is considered in more detail in the following chapter.

6.6 Summary

Using an extension of the nanosphere lithography technique in which a two-dimensional array of nanospheres is etched prior to vacuum deposition of a suitable metal, we have been able to fabricate metallic nanoparticle and nano-hole arrays that exhibit very different optical responses due to the different types of plasmon mode they support. We have shown that there is an abrupt transition in the optical response of these structures from localised surface plasmon resonances to delocalised surface plasmon-polariton modes, as nanoparticles increase in size and merge to form a continuous perforated film. In contrast the SEM images show a soft transition from nanoparticles to nano-hole arrays as the etch time is increased arising from the presence of a significant number of defects in the fabricated structures. This contrast between a soft transition in the SEM images and an abrupt transition in the optical response is attributed to the need for connectivity of the metal mesh before extended SPP behaviour can be exhibited.

Chapter 7

Optical properties of hole-arrays formed by nanosphere lithography

7.1 Introduction

Unlike slits of similar dimensions, cylindrical apertures illuminated by radiation of wavelength λ_0 with a diameter $d \lesssim \lambda_0/2$ are unable to support propagating transverse electromagnetic (TEM) modes [*Collin (1991)*]. As a result, in this regime energy may only be transferred through such apertures by an evanescent tunnelling process and the transmittance should be strongly attenuated. Furthermore, an exact analytic expression for the transmittance of electromagnetic radiation through sub-wavelength holes ($d << \lambda_0$), first derived by *Bethe (1944)*, indicated that the transmittance scales as $(d/\lambda_0)^4$. Thus for holes smaller than the wavelength of light one might expect that the transmittance will be very weak. This seems all the more surprising since to generate exact solutions the hole is located in an infinitely thin (though perfectly conducting) material. The work of *Ebbesen et al. (1998)* therefore generated great interest when it showed that the transmittance of light through sub-wavelength hole-arrays in optically thick silver films was several orders of magnitude greater than previously expected. This, and subsequent research spawned by the original paper, has raised a number of issues regarding the transmittance of electromagnetic radiation through sub-wavelength apertures.

To explain the results a mechanism was proposed that ascribed the phenomenon to the excitation of surface plasmon-polariton (SPP) modes via grating coupling with the incident light [*Sambles (1998)*, *Ghaemi (1998)* and *Popov (2000)*]. It was suggested that enhanced evanescent fields associated with the SPP modes formed above and around the apertures and that these fields decayed through the holes into the medium bounding the opposite surface of the metallic film. Power from the SPP was then transferred back into radiative modes by a reverse grating-coupling process. An alternative suggestion prescribed that the transmittance enhancement may be entirely explained using a multiple diffraction argument [*Treacy (2002)*]. Indeed, the arguments regarding the involvement of SPPs in the enhancement mechanism intrinsically contain a multiple diffraction argument as the process of both coupling into and re-radiating from a SPP requires multiple diffraction events. Further it has been proposed that in the case of an array of sub-wavelength slits the SPP may actually play a negative role in transmittance enhancement due to absorption effects on resonance [*Cao (2002)*]. However, as noted above the optical properties of slits and holes are very different – slits that are infinitely long support a transverse electromagnetic mode with a cut-off at zero frequency.

Ghaemi (1998) strengthened the SPP enhancement argument by demonstrating that the spectral variation of enhanced transmittance with incident angle through an array of sub-wavelength circular holes was characteristic of what one expects from the SPP dispersion. Later, *Grupp et al. (2000)* were able to show that the magnitude of the transmittance enhancement was dependent only on the metallic properties of the two in-plane surfaces within a skin depth of the surface and was insensitive to the material of the core and walls of the aperture. ‘Good’ metals with a large negative real part of the relative permittivity and small imaginary part of the relative permittivity showed a marked increase in transmittance over poor metals. They concluded that the dependence of transmittance efficiency on the optical properties of the metal-dielectric interface indicated the involvement of SPPs. A significant step to resolving the issue of how electromagnetic energy is transmitted through the structures was supplied by *Barnes et al. (2003)*. By obtaining data as a function of incident frequency and in-plane wave vector, not only were SPP polarisation characteristics shown to occur in the transmittance through a sub-wavelength hole-array, but also SPP dispersion characteristics in the absorbance, transmittance and reflectance data. It was concluded that although diffraction is central to the transmittance of light through hole-arrays, the effect is dramatically enhanced when coupling conditions allow SPP excitation on one or both of the in-plane surfaces.

Thio (2001) and *Lezec (2002)* used the SPP argument to explain enhanced transmittance through a *single* circular sub-wavelength aperture, surrounded by a concentric arrangement of circular grooves. They attributed the enhancement in transmittance as due to the excitation of SPPs supported on the illuminated surface of the sample since the peak transmission wavelength coincides with the periodicity of the surface profile. However, the theoretical model presented dealt only with a linear aperture (slit) in a semi-infinite perfectly conducting media. In addition there was strong angular confinement of the transmitted signal (approximately ± 3º) through the circular aperture which was attributed to the re-radiation of light back into free space by a SPP supported on the corrugated exit side of the sample. *Martin-Moreno (2001)* later presented a theoretical explanation for this beaming effect in terms of surface resonances using a one-dimensional model. Again using a one-dimensional model, *Garcia-Vidal (2003)* identified three main mechanisms that can enhance optical transmittance: groove-cavity mode excitation, in-phase re-illumination and waveguide mode resonances within the aperture. As previously mentioned, for sub-wavelength holes (rather than one-dimensional slits), this last mechanism cannot operate. Unlike the majority of studies into the enhanced transmittance phenomenon, *Lockyear (2004)* conducted experiments at microwave frequencies. Essentially the work reproduced the structure studied by *Thio (2001)* scaled with some modifications to optimise performance at the long wavelengths and small skin depths associated with microwave radiation. A 17-fold enhancement in transmittance was obtained from the patterned structure over that observed through a ‘bare’ aperture. Finite element modelling of the electromagnetic response of the aperture arrangement indicated that the enhancement was due to *both* a diffracted standing wave set up at the surface and the excitation of a SPP mode. At microwave frequencies the dispersion of a grazing photon and unperturbed SPP mode are nearly degenerate and may be simultaneously excited.

A more complicated analysis is required when alternative hole shapes are investigated. *Klein Koerkamp (2004)* showed that the transmittance through an array of rectangular holes can be increased by an order of magnitude over that from an array of cylindrical holes, this in spite of a reduced hole surface area. Measurements from individual, isolated rectangular holes indicated that resonant transmittance occurred, attributed to the excitation of a localised mode associated with the hole. No such mode was observed from single cylindrical holes. Similar results were obtained by *Degiron (2005)* where the effect of changing the periodicity of rectangular hole-arrays with otherwise constant dimensions was studied. It was found that the localised mode only contributed significantly to the overall transmittance when the resonant frequency coincided with that of an SPP mode.

The majority of research into the transmittance of electromagnetic radiation through sub-wavelength apertures and slits has involved studying opaque (optically thick) films. As the thickness is reduced to such an extent that a significant proportion of the incident light is transmitted through the metal one may expect complications to arise due to interference between light that is re-radiated by the SPP modes and light that is directly transmitted. Furthermore, localised modes within cylindrical holes similar to the resonances associated with metallic nanoparticles may be excited in very thin films even with an asymmetric optical environment[1] [*Prikulis (2003)*]. This chapter describes experiments that map the dispersion of the surface modes excited upon arrays of holes in very thin silver films with a thickness of the order of the skin depth. Using etched nanosphere lithography, silver meshes of varying thickness perforated with a periodic near-hexagonal array of holes with varying diameter were constructed. Transmittance and reflectance data were collated and conclusions drawn as to the origin of the optical modes the structures support.

7.2 Experimental

7.2.1 *Fabrication*

The procedure for producing the samples is an extension of the conventional nanosphere lithography technique described in Chapter 4. Firstly, monodispersed nanospheres suspended in ultrapure water were deposited onto a substrate chemically treated so as to render the surface hydrophilic. The samples were placed in an oven at 50 °C and as the water evaporated spheres

---

[1] The perforated metal layer is bounded by media with differing refractive indices. In a symmetric optical environment the metal is bounded by media with identical refractive indices.

were forced to the meniscus edge by the convective flow of fluid within the droplet. This resulted in the formation of monolayer regions of nanospheres with a near-hexagonal structural symmetry. A small distortion of the structure from perfect hexagonal symmetry is unavoidable using this technique due to the ballistic nature of the ordering process and sphere diameter variations.

To aid in understanding the results of optical measurements it was necessary to measure the transmittance and reflectance from single domains. Furthermore, to observe the relevant modes within the visible region of the electromagnetic spectrum requires the periodicity to be within a specific range. Arrays formed from spheres with a mean diameter of 390 nm were found to best satisfy these criteria and were used in all measurements that follow. By volume the concentration of the colloidal solution deposited onto the substrate was 0.3 % solids (solutions were supplied by Duke Scientific as 4 % solids and further diluted to obtain the correct concentration).

After the samples had dried only those with sufficiently large domains were selected for the next stage. This involved reactive-ion etching the spheres for a period of time in a plasma of oxygen. A reduction in the diameter d of the spheres occurs whilst the periodicity of the overall structure is retained. It was found that the shape of the spheres became irregular when a significant proportion of material is removed. To reduce the shape deformation the parameters that determine the etch rate and mechanism (whether a chemical or physical etch dominates the overall rate) were carefully selected to achieve the best results. An isotropic or chemical etch was desirable requiring a low input power (40 W) and high pressure (200 mTorr). Rather than the individual particles obtained from conventional nanosphere lithography, the subsequent evaporation of silver onto an etched array of spheres resulted in a continuous film deposited onto the surface of the substrate. Removal of the spheres was achieved by immersion and ultrasonication for a few minutes in toluene yielding an array of holes in an otherwise continuous film. SEM images of the arrays are shown later and correlated with the optical data.

Some restrictions are imposed by the nature of the technique, in particular on the thickness t of the silver film that is able to be evaporated. The sphere radius r determines the maximum thickness permitted as lift-off of the spheres after evaporation becomes impractical when $t > r/3$. Also, discontinuous, rough films are produced when t < 15 nm. Therefore, evaporated films that are deposited upon the smallest diameter spheres (d ~ 100 nm) are limited to a very narrow thickness range. Furthermore, full connectivity within the mesh is required to fully develop the SPP modes on the structures. Small etch times lead to arrays of particles being produced of increasing size. As the etch time is increased the particles eventually merge to form a continuous mesh. The structural and optical transition between the discontinuous and continuous films is the subject of Chapter 6; here only fully developed hole arrays are considered.

An alternative method for producing structured metallic films using nanospheres as a template was demonstrated by *Coyle et al. (2001)*. This produced slightly different periodic arrays but was less limited by the thickness of material deposited. In their technique the nanosphere array was immersed in a solution containing gold complex ions. Subsequent electrochemical reduction of the solution resulted in a metallic structure that was the inverse of the nanosphere array.

7.2.2 *Optical measurements*

To obtain optical transmittance data a collimated beam (divergence ~0.5^o) from a tungsten halogen lamp was directed onto the samples. A monochromator was used to spectrally filter the incident light (spectral width ~ 2 nm), whilst a mechanical chopper modulated the intensity of the incident light so as to allow phase-sensitive detection of the zero-order transmitted and reflected beams. Further, a beam-splitter redirected a small fraction of the incident beam onto a second detector to allow source fluctuations to be taken into account. Finally, a polarizer was placed in the incident beam so that the polarization state of the incident light could be controlled.

To understand the optical behaviour of the periodic nanostructures it was desirable to build up dispersion maps from the transmittance data. To do this it is necessary to collect data not only as a function of the frequency ω, but also as a function of the in-plane wave vector $\mathbf{k}_{//}$. The in-plane wave vector is the component of the wave vector in the plane of the sample. Varying the in-plane wave vector was achieved by mounting the sample on a motor driven rotating stage and choosing angles of incidence appropriate for each in-plane wave vector value for which data were to be recorded. Further experimental details regarding the apparatus used and also the orientation of the sample were given in Chapter 6.

7.3 Results and discussion

Normal incidence transmittance spectra and dispersion scans were taken from arrays of holes in silver films. In the first part of this section the effect of grating orientation relative to the plane of incidence is investigated. A single sample is characterised optically with *p*- and *s*- polarised light incident for a number of azimuthal orientations. This provides information regarding the nature of the SPP modes that is essential in developing an understanding of the evolution of the mode dispersion as the structures undergo subtle changes. Having looked at a single sample, the effect on the optical properties of altering the thickness of the evaporated silver film for a given hole diameter is discussed. This is followed by a description of similar experiments that determine the effect of reducing the diameter of the holes for a given film thickness.

7.3.1 *Polarisation and orientation*

To begin, the transmittance through a sample consisting of ~300 nm diameter holes in a silver film with a thickness of 50 nm was investigated by generating transmittance dispersion scans for *p*- and *s*-polarised light incident at azimuthal angles of $\varphi = 0°$ and $\varphi = 90°$. These angles were chosen since the holes form the distorted-hexagonal (base-centred orthorhombic) structure as described in Chapter 4, Section 6.2. Diffraction patterns from the domain were of the form illustrated in figures 4.6(a) and 4.6(b) indicating that the distorted-hexagonal structure results in a shorter pitch (larger Bragg vector) along one axis than would be expected for a perfect hexagonal lattice. It is this axis that is defined as $\varphi = 0°$. Along the two remaining axes associated with first order scattering from a hexagonal structure the pitch is larger (Bragg vector smaller) in the distorted lattice than the perfect lattice. An SEM image of the sample taken from the domain scanned in the optical experiments that follow is shown in

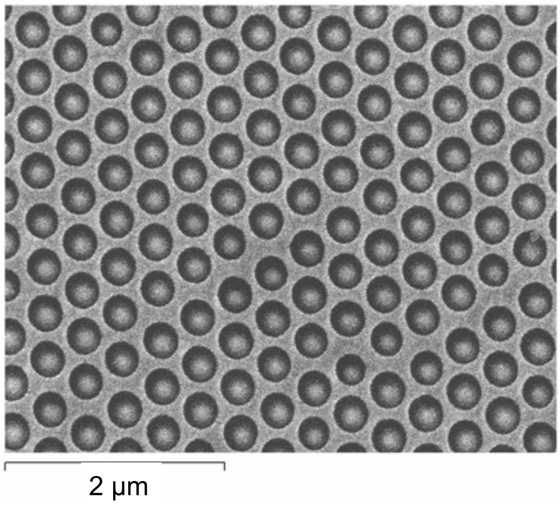

Figure 7.1. SEM image of a hole array in a silver film with a thickness of 50 nm formed from nanospheres with an initial mean diameter of 390 nm. The approximate diameter of the holes is 300 nm. The light regions within the holes are from a charging of the substrate during image capture.

figure 7.1 and is typical of the patterning observed throughout the sample. The familiar line defects associated with structures formed by NSL are seen along with some variation in the diameter of the holes; there are very few vacancy defects. The apparent elliptical shape of the holes is due to drifting of the electron beam during image capture and prevents an accurate analysis of the hole size and shape. High intensity regions observed within the holes are from a charging of the non-conductive silica substrate by the electron beam.

Figures 7.2(a)-(d) are transmittance dispersion scans obtained from the sample with *p*- and *s*-polarised light incident for two azimuthal orientations. Figure 7.2(a) shows the transmittance when *p*-polarised light is incident on a single domain with the grating oriented at an azimuthal angle of $\varphi = 0°$. At $\omega/2\pi c = 2.05\ \mu\text{m}^{-1}$ for normal incidence ($k_{//}/2\pi = 0\ \mu\text{m}^{-1}$) there is a strong extinction feature. Also, there are two distinct modes with a projected intersection at $\omega/2\pi c = 1.53\ \mu\text{m}^{-1}$, also for normal incidence. The upper and lower dispersive modes are more strongly coupled than the middle mode which shows up as a weak feature in this orientation with *p*-polarised light. This changes when the polarisation of the incident light is switched to the orthogonal state (figure 7.2(b)). The middle mode is now strongly coupled with the incident

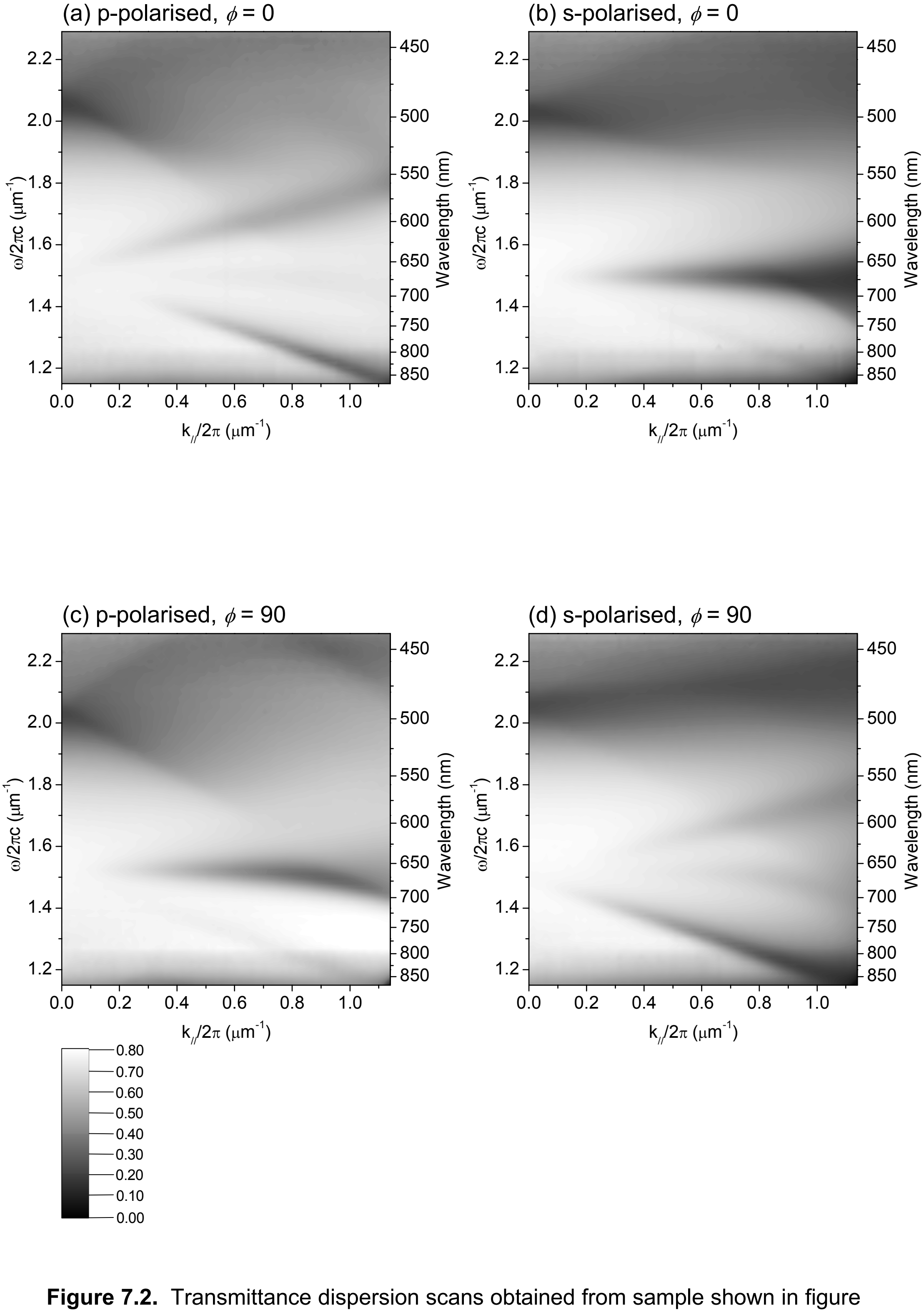

Figure 7.2. Transmittance dispersion scans obtained from sample shown in figure 6.3 with (a) *p*-polarised light and azimuthal angle *φ* = 0°, (b) *s*-polarised light and *φ* = 0°, (c) *p*-polarised light and *φ* = 90°, and (d) *s*-polarised light and *φ* = 90°.

oriented at $\varphi = 90°$. In this orientation the middle mode is strongly coupled with the lower mode observed as a weak feature and the upper mode irresolvable, similarly to *s*-polarised light with the orthogonal orientation. The position of the middle mode appears to be at a slightly higher frequency than in figure 7.2(b) with a projected intersection of 1.53 μm^{-1}, as for *p*-polarised light in the orthogonal orientation. To complete the set figure 7.2(d) shows the transmittance scan for *s*-polarised light incident with $\varphi = 90°$. At normal incidence the polarisation of the light with respect to the grating is identical to *p*-polarised light, $\varphi = 0°$ and the transmittance is identical. As the in-plane wave vector is increased the upper and lower mode are more strongly coupled and the middle mode weakly coupled, as for *p*-polarised light, $\varphi = 0°$. The most obvious difference of figure 7.2(d) compared to figure 7.2(a) is that the region of low transmittance at $k_{//} = 0$, $\omega/2\pi c = 2.05\ \mu m^{-1}$ rises in frequency gradually as the in-plane wave vector increases. Also, the dispersion of the SPP modes occurs at a lower frequency for a given in-plane wave vector when $\varphi = 90°$, intersecting $k_{//} = 0\ \mu m^{-1}$ at $\omega/2\pi c = 1.50\ \mu m^{-1}$.

To explain the physical origin of the features observed in the dispersion scans the same method is used as was employed in the previous chapter. This involved applying the equations that define the scattered light lines and grating-coupled SPP modes to generate a schematic representation that when superimposed upon the original data provides a means of identifying the various modes. It was found that a reasonable fit was obtained when the dispersion of the SPPs was calculated using a double interface solution in conjunction with an effective thickness of 15 nm to account for the extension of the evanescent field of the SPP into the holes. However, only the first-order grating-coupled (1,0) and (-1,0) silica modes were included since the contribution from modes excited by other grating vectors was negligible for *p*-polarised light with $\varphi = 0°$. With alternative grating orientations and using *s*-polarised light a more comprehensive approach is required taking account of the contribution from *all* first order coupling mechanisms.

For clarity, schematic diagrams of the silica-metal interface SPP dispersion (solid) and associated scattered light lines (dotted) for $\varphi = 0°$ and $\varphi = 90°$ are shown separately from the experimental data in figures 7.3(a) and

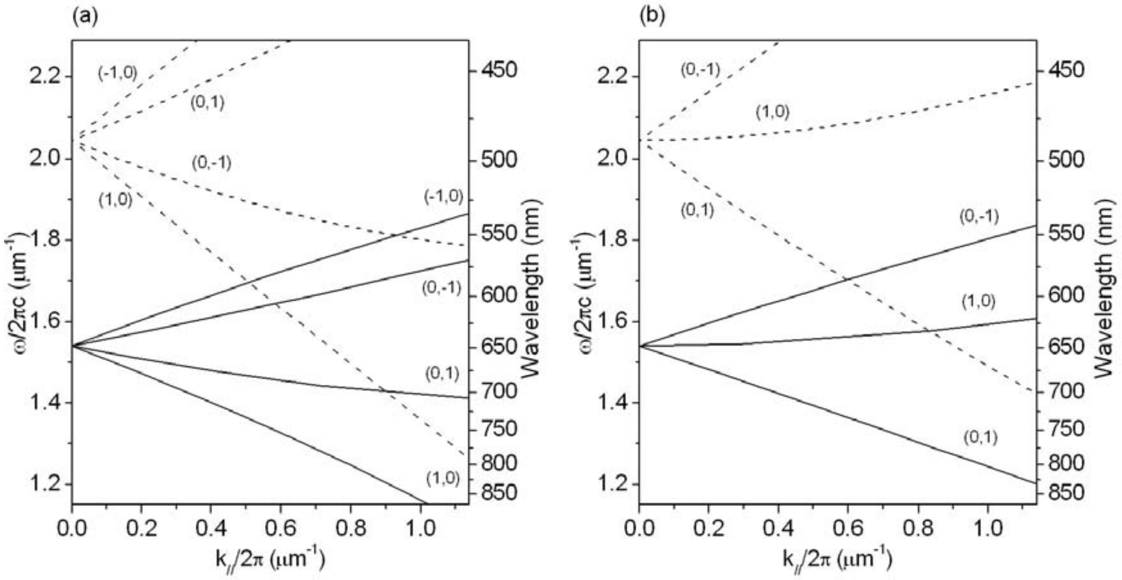

Figure 7.3. Dispersion of silica light lines (dotted) and SPP modes (solid) for grating orientations of φ = 0° (a) and φ = 90° (b). Parameters used in the calculations were pitch λ_G = 335 nm, silica refractive index n = 1.46 and silver thickness t = 14.5 nm.

7.3(b). A perfect hexagonal lattice with a periodicity of λ_G = 335 nm was assumed with the refractive index of the silica taken to be n_3 = 1.46. To generate the SPP dispersion lines in figures 7.3(a) and 7.3(b) a silver thickness of 14.5 nm was used. This was found to yield a good fit to the p-polarised, φ = 0° data, comparing favourably with the results from the similar structure in Chapter 6. Comparing figure 7.3(a) with figure 7.2(a) the light lines align well with the dark features emanating from $\omega/2\pi c$ = 2.05 μm^{-1}. In figure 7.2(b) the (1,0) and (-1,0) light lines do not appear to conform with any feature in the data, however the (0,1) and (0,-1) light lines bound the area of low transmittance seen at high frequencies. Similar associations are observed when comparing the data with the scattered light lines in the orthogonal orientation. The light lines in figure 7.3(b) appear to associate well with the low transmittance features observed at high frequencies in figures 7.2(c) (*p*-polarised) and 7.2(d) (*s*-polarised). However, the effect from (1,0) and (-1,0) diffraction (a degenerate pair in this orientation) is negligible with *p*-polarised light, but strong with *s*-polarised light. Conversely, the effect from (0,1) and (0,-1) diffraction is observed as a strong feature with *p*-polarised light and weak feature with *s*-polarised light. From these observations it is seen how the strength of the diffracted field depends on the polarisation state of the incident wave relative to the grating vectors associated with the periodic structure. Changes in the zero-order transmitted intensity due to the scattering of light by a particular grating vector become less pronounced when the *E*-field is oriented such that it is perpendicular to that grating vector.

The dependence of the diffracted fields on the polarisation state of the incident light is of consequence to the excitation of the SPP modes since the coupling process requires the generation of evanescent diffracted fields; a weak evanescent diffracted field would result in a weakly coupled SPP mode [*Hooper (2003)*]. For instance, with *p*-polarised light and φ = 0° one would expect the coupling due to the (0,1), (1,-1) and (0,-1), (-1,1) diffracted orders to be weak. This indeed seems to be the case as only the (1,0) and (-1,0) SPP modes are observed as strong features. However, when considering *s*-polarised light with the same grating orientation rather than the expected two modes associated with scattering from the (0,1), (1,-1) and (0,-1), (-1,1) grating vectors a non-dispersive single mode is observed. Similarly, with φ = 90° and *p*-polarised light incident a single mode is observed where two would be expected and with *s*-polarised light incident, rather than a single feature, two are observed with a similar dispersion to those in figure 7.2(a). This suggests that when the sample is oriented so that $\mathbf{k}_{//}$ *is not* parallel to a grating vector the dispersion of the SPP modes has a more complex form than can be described by application of the theory used when $\mathbf{k}_{//}$ *is* parallel to a grating vector. This theory relies on expressions that reproduce the dispersion of the SPP mode propagating on a continuous planar interface and is found to match well with the optical data obtained from a number of periodic structures [*Ebbesen (1998), Barnes (2003)*]. These have in common the fact that there is little restriction imposed by the surface on how charge is distributed within the metal. This changes substantially when perforated layers with a low proportion of metal are studied. At microwave frequencies it has recently been shown both theoretically [*Pendry (2004)*] and experimentally [*Hibbins (2005)*] that the dispersion of the SPP modes are significantly modified when they are set up on structures with large (comparable with the pitch) square-shaped holes. *Hibbins (2005)* observed that coupling did not occur at normal incidence and suggested that this was because to do so would require charge to be within the holes. Given that the holes in

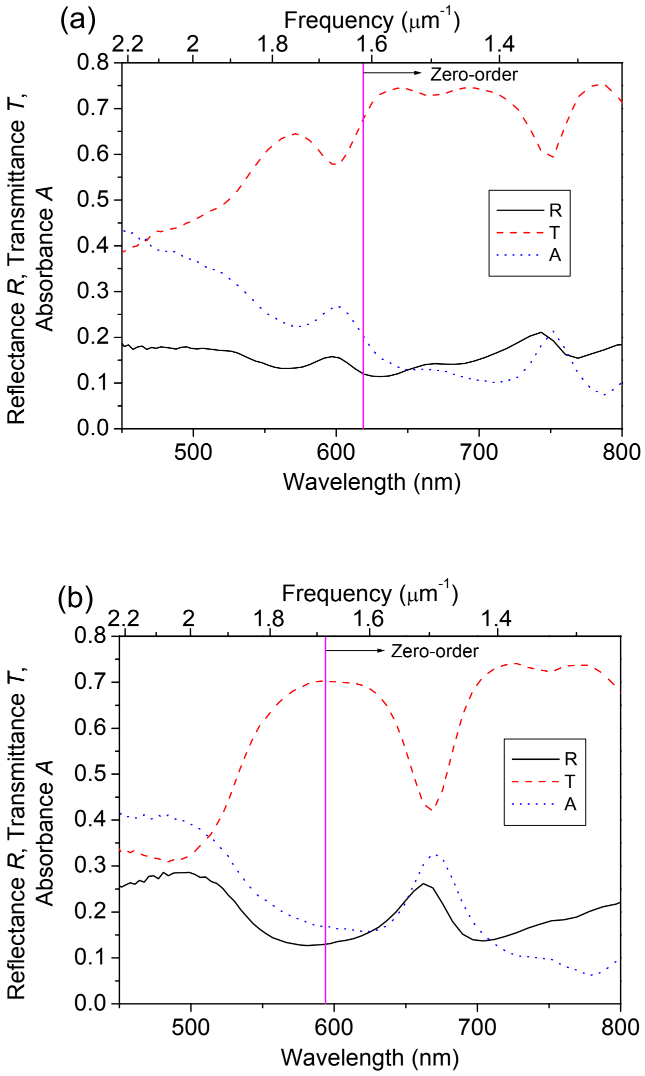

Figure 7.4. Transmittance *T* (dashed), reflectance *R* (solid) and inferred absorbance *A* (dotted) spectra for a constant in-plane wave vector $k_{//} = 0.5$ μm^{-1} and with *p*-polarised light ((a) and *s*-polarised light (b) incident. The vertical line represents the wavelength (frequency) above (below) which the structure is zero-ordered. An absorbance maximum is indicative of a SPP mode in this region.

this study occupy a large proportion of the structure a similar effect may be the cause of the unusual mode dispersion seen in figure 7.2. To generate and sustain the SPP an oscillating field with the correct phase must couple with the electron charge density in the metal. If on a perforated surface there is no metal at the points where the driving field has the correct phase then charge cannot be generated and consequently the SPP cannot be excited.

As shown in Chapter 6, it is instructive when identifying features to infer the absorbance *A* within the zero-order (no diffraction into the far-field) region of the scans by collecting reflectance *R* and transmittance *T* data and applying the equation $A = 1 - R - T$ for a given in-plane wave vector. Figure 7.4 shows *T*, *R* and *A* spectra for $k_{//} = 0.5$ μm^{-1} and with orientation $\varphi = 0°$, figure 7.4(a) with *p*-polarised light and figure 7.4(b) with *s*-polarised light incident. The vertical line represents the wavelength at which the structure becomes zero-ordered (calculated using a pitch λ_G = 335 nm), as indicated by the arrow. Excitation of a SPP mode results in absorption of the incident radiation within the metal through Joule heating. Any peaks in absorption spectra within the zero-order region are therefore indicative of a SPP mode. The minima in transmittance in figure 7.4(a) (upper and lower modes in the corresponding dispersion scan, figure 7.2(a)) are both associated with reflectance maxima and absorbance maxima. With *s*-polarised light incident in this azimuthal orientation the middle mode is excited (see figure 7.2(b)) both in reflectance and transmittance, again giving rise to an associated absorbance maximum. This, in conjunction with the common point of intersection with the $k_{//}$ = 0 μm^{-1} axis, suggests that the middle, non-dispersive mode is indeed a SPP. Similar results, not shown, are obtained for the orthogonal orientation.

Having identified that the modes have the absorptive characteristics of an SPP mode the next step is to understand how they are excited. Out of the six first-order grating vectors available we must identify which couple the incident light with the SPPs. To aid in answering this, *p*-polarised transmittance data was collected as a function of azimuthal angle and frequency for an in-plane wave vector of $k_{//}/2\pi$ = 0.5 μm^{-1} (figure 7.5). A cyclic behaviour of the resonant frequency and coupling strength is apparent as the azimuthal angle is increased from -50° through to 210°. Starting from φ = 0°, as the azimuthal angle is increased the coupling to the upper and lower mode is reduced and coupling to the middle mode is increased peaking at a value of φ = 30°. Further increments up to φ = 60° again results in coupling of the incident light with the upper and lower modes, but at a slightly lower frequency. At φ = 90° coupling to the middle mode is strong as for φ = 30°, but at a higher frequency. A mirroring of this behaviour is observed as φ is increased from 90° to 180°. It is therefore seen from figure 6.5 that the value of the resonant frequency fluctuates with two points of symmetry at φ = 0° and φ = 90° whilst the excitation of the modes occurs with ~ 60° symmetry.

A perfect hexagonal array should only possess 60° symmetry in the photonic mode structure; these results thus emphasise the slight distortion to the periodic lattice described earlier. Far from being a nuisance however, this provides a means of inferring the coupling mechanisms and grating vectors

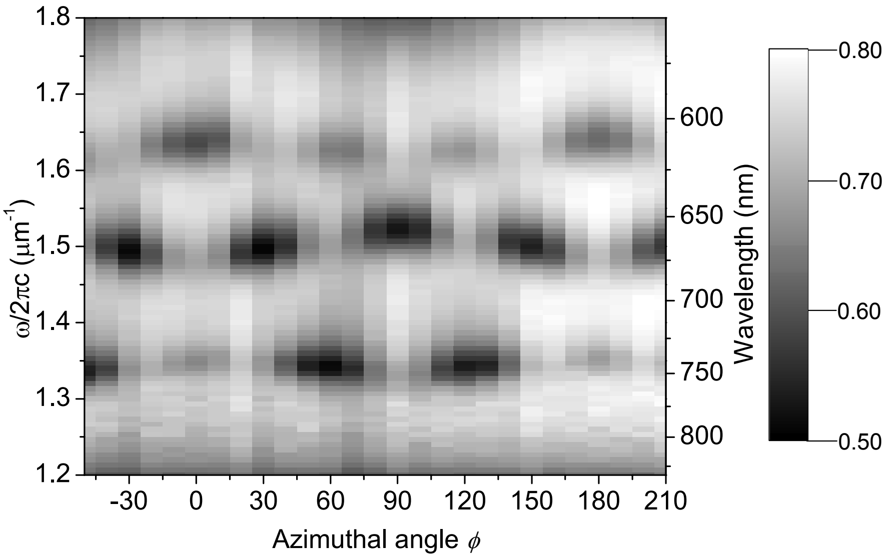

Figure 7.5. Transmittance as a function of frequency and azimuthal angle for an in-plane wave vector of $k_{//}$ = 0.5 μm^{-1}. The dark regions of low transmittance are due to the excitation of the grating-coupled SPP modes.

responsible for exciting the SPP modes observed in figures 7.4. Recalling from Chapter 6, Section 4 how the grating vectors are defined, the (1,0) and (-1,0) grating vectors are slightly larger in magnitude than the other first order grating vectors. Therefore the dispersion of these modes in reciprocal space would occur at a higher frequency for a given in-plane wave vector. This is shown in figure 7.6 where the (1,0) and (-1,0) pair of SPP modes generated using a pitch λ_G = 330 nm are seen to intersect at a higher frequency than the (0,1) and (0,-1) pair generated using λ_G = 340 nm. Returning to figure 7.5 it is therefore initially suggested that the (1,0) and (-1,0) grating vectors provide the means of coupling to the SPP modes with *p*-polarised light when φ = 0° *and* φ = 90° as the position of each mode is at its highest respective frequency value in these orientations. Furthermore, comparing figures 7.2(a) and 7.2(c) the projected intersection of the modes with the $k_{//}$ = 0 μm^{-1} axis occurs at the same frequency suggesting that the magnitude of the grating vector associated with the coupling are equal. Therefore it seems that the middle mode is excited due to evanescent diffraction of the incident light by the grating vector *orthogonal* to the plane of incidence and polarisation. This is surprising given that the effect

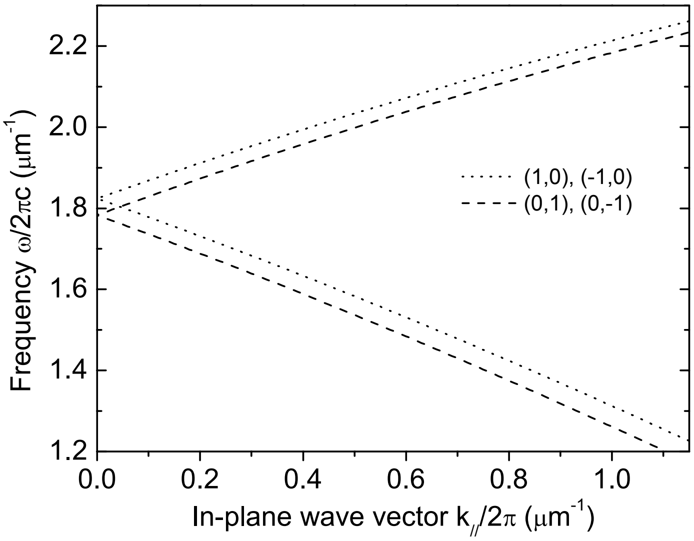

Figure 7.6. Dispersion of single interface SPP modes calculated using a pitch of 330 nm for the (1,0) and (-1,0) modes (dotted) and 340 nm for the (0,1) and (0,-1) modes (dashed).

in the far-field from these grating vectors in this orientation and with this polarisation is weak. It seems that the foremost factor in determining whether the middle mode or upper and lower modes are excited is the polarisation state of the incident light relative to the structure. With *s*-polarised light incident excitation of the modes occurs 90° out of phase azimuthally than with *p*-polarised light incident. When the *E*-field is polarised so that there is a component of the *E*-field parallel to a grating vector the dispersive mode structure is observed. Conversely, when the *E*-field is polarised perpendicularly to a grating vector the non-dispersive flat mode is observed. For other orientations all three modes are excited with the coupling strength determined by the magnitude of the field components parallel and perpendicular to the grating vectors. Furthermore a phase variation across the surface is required since there is no coupling at normal incidence. The direction of the phase variation is parallel to the in-plane wave vector and determines which grating vector couples the incident light and the SPP. To expand on this final point consider figures 7.2(a) and 7.2(d) showing *p*- and *s*-polarised light incident with φ = 0° and φ = 90° respectively. The orientation of the *E*-field relative to the structure is the same in each case; however the dispersion of the modes occurs at a slightly higher frequency for *p*-polarised light than for *s*-polarised light. This suggests that with *p*-polarised light the coupling to the modes is due to the grating vectors associated with the shorter pitch, these being parallel to the in-plane wave vector for $\varphi = 0°$. A variation in phase occurs in this direction allowing coupling to the (1,0) and (-1,0) SPP modes. In the orthogonal orientation there is no variation in phase parallel to the (1,0) and (-1,0) grating vectors and coupling is due to the remaining first order grating vectors, these associated with a longer pitch thus having a smaller magnitude.

7.3.2 *Thickness of silver film*

It has been demonstrated (Chapter 6) that a reasonable fit to the SPP dispersion observed in transmittance data obtained from arrays of holes in a thin film is produced by using an effective thickness for the silver layer. A hole array 50 nm thick is described effectively by applying the grating vectors associated with the periodic array to the dispersion of a SPP mode excited on a planar slab of silver 14.5 nm thick. As the thickness of the planar slab is increased the dispersion of the modes eventually returns to that of a single interface; the overall dispersion of the silica SPP modes occurs at a higher frequency for a given wave vector. Conversely, if the thickness of the layer is reduced then the dispersion of the SPP mode will be further perturbed from the single interface condition. Therefore one would expect that the dispersion of the SPP modes identified in figure 7.4 would behave in a similar way.

To investigate if this was so transmittance dispersion scans of six separate samples were taken, each prepared using identical etch parameters to ensure that the hole diameter is consistent between samples. An example of a similar array with comparable pitch and hole diameter is that shown in figure 7.1. Silver was then deposited, each sample having a different thickness ranging from 15 nm to 70 nm as measured by a quartz crystal thickness monitor during evaporation of the metal. To reduce variations between samples each was fabricated using the same nanosphere solution. Transmittance data was collected from single domains using un-polarised light. Diffraction patterns from the domains were observed prior to scanning so that domains with similar structures were sampled; the type of distortion to the hexagonal structure was consistent.

Figures 7.7(a)-(f) are transmittance dispersion scans of hole arrays with thickness 15 nm, 25 nm, 30 nm, 40 nm, 50 nm and 70 nm with a linear gray-scale from a transmittance minimum of 0.15 (black) to a transmittance maximum of 0.85 (white). Two main features are current throughout the scans; the region of low transmittance associated with the light lines and the SPP modes as identified earlier. The latter are seen to reduce in frequency as the thickness decreases in accordance with the expected behaviour whilst in comparison the position of the former is relatively invariant. To provide further analysis the position of the modes was modelled using the method outlined in the previous chapter. Using code developed to calculate the power flow dissipated by a dipole emitter located close to the surface of a metal slab it is possible to generate theoretical dispersion scans showing the position of the SPP as a function of angular frequency and in-plane wave vector (see Chapter 6, Figure 6.9). An estimate of the effective thickness derived by choosing the best fit for each sample is plotted against the actual thickness in figure 7.8. An inverse exponential function of the form

$$t_{\mathrm{eff}} = t_{\infty}\left(1 - \exp\left(-{}^{t_{\mathrm{Ag}}}\!/_{T}\right)\right)$$

where t_{eff} is the effective thickness, t_{Ag} is the actual thickness and T is a horizontal scaling factor is fitted to the data to yield a value for t_{∞}, the effective thickness associated with an infinitely thick hole array. For the type of structure studied here the dispersion of the SPP modes approaches an asymptotic limit of $t_{\infty} = 16.5 \pm 0.6$ nm emphasising the strong perturbation of the SPP dispersion compared to that of a planar interface. To a lesser extent this effect has been identified by *Degiron (2002)* and *Barnes (2003)* where a reduced dispersion of grating-coupled SPPs excited on optically thick hole arrays was reported. Since in this study the SPP excited on the silica interface is monitored the medium within the holes is the same as that bounding the opposite interface (air). Therefore only the perturbation from the extension of the fields through the metal would contribute significantly to the change in dispersion of the SPP as the thickness of the metal is increased. If the film is free-standing (*i.e.* the

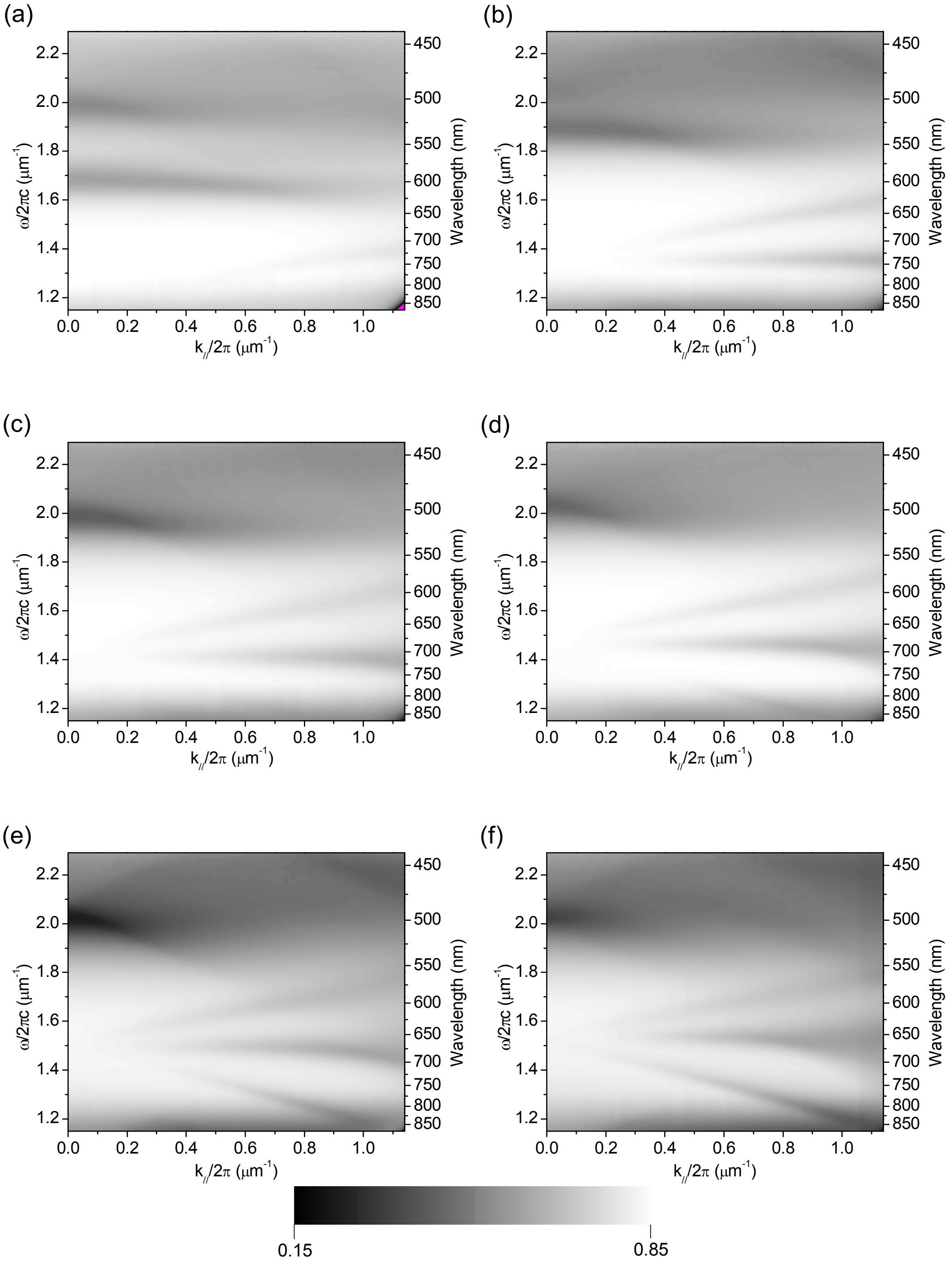

Figure 7.7. Transmittance dispersion scans from hole arrays with Ag thickness 15 nm (a), 25 nm (b), 30 nm (c), 40 nm (d), 50 nm (e) and 70 nm (f).

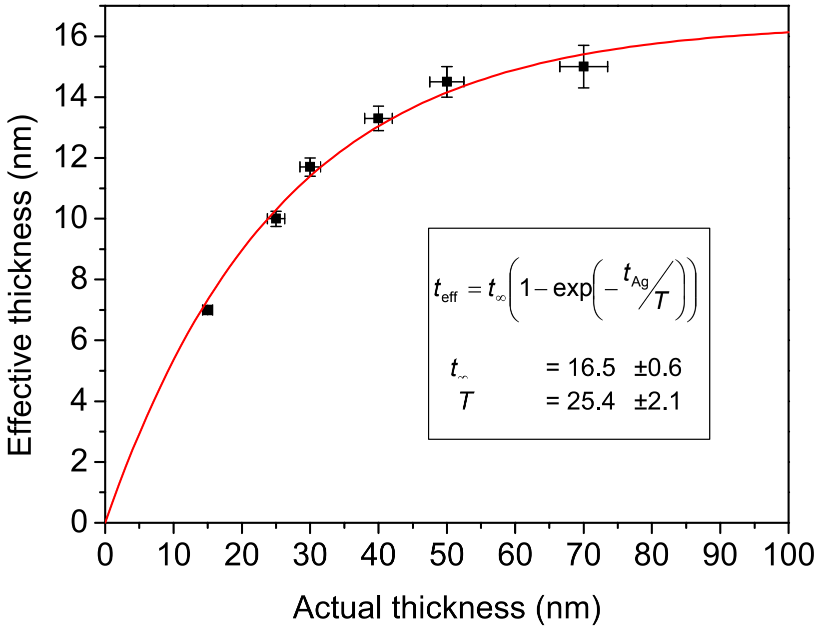

Figure 7.8. Plot of actual thickness of the Ag film evaporated against the effective thickness calculated by modelling the dispersion of an SPP mode on a planar film and fitting to the data in figure 6.7. The solid line is a fit generated by an inverse exponential function.

refractive index of the medium on either side of the hole array is the same) then additional effects may be observed due to coupling of the degenerate SPP modes on each interface [*Martin-Moreno (2001)*, *Degiron (2002)*]. In general two separate contributions to the perturbation of the SPP dispersion should exist. Firstly, due to the extension of the electromagnetic field into and through the holes and secondly, due to the extension of the electromagnetic field through the metal into the medium bounding the opposite interface.

For arrays of holes with a smaller diameter but with the same periodicity and thickness the dispersion of the modes would be less perturbed since the proportion of metal constituting the array increases. Similarly, arrays consisting of holes with an equal diameter but larger periodicity would also be less perturbed. The next section looks at the effect of changing the diameter of the holes on the dispersion of the SPP modes. In particular the transmittance through very thin films is investigated; this motivated by the appearance of a third feature in the dispersion scans of figure 7.7 as the film thickness is reduced below 30 nm. Two possibilities are considered to explain its origin. Firstly, that it is a higher order SPP meaning that a higher-order grating vector (for instance a (1,1) or (2,0) grating vector) provides the light-SPP coupling mechanism. Secondly, that with thin films it is possible for a localised surface plasmon (LSP) mode to exist within the holes.

7.3.3 *Hole diameter*

A perturbation to the dispersion of the SPP mode is apparent when the mode is excited on the surface of perforated thin films. Earlier it was shown how reducing the thickness of the silver layer altered the dispersion of the SPP mode excited on structures with identical hole diameters. In this case the proportion of the structure consisting of metal remains constant and it is the extension of the field through the metal into the opposite medium that results in the reduced frequency of the SPP. Alternatively, a similar effect should be observed if, with the thickness of the silver and periodicity remaining constant, the diameter of the holes is changed.

Figure 7.9 is an SEM image of a 50 nm thick hole array formed from nominally 390 nm diameter spheres etched to a mean diameter of ~ 260 nm. A transmittance dispersion scan taken from the sample with *p*-polarised light

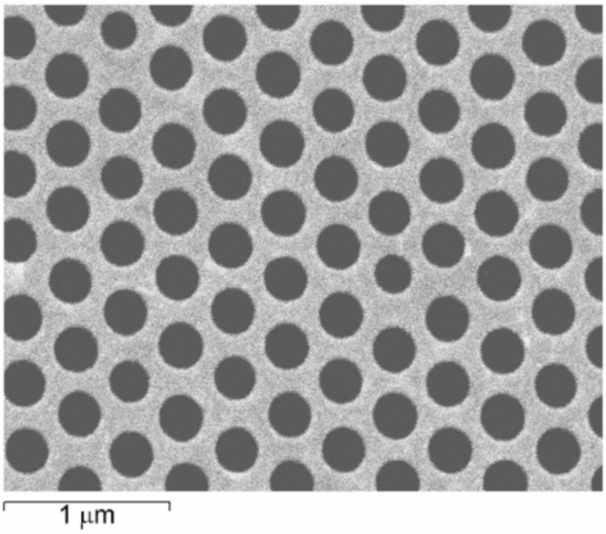

Figure 7.9. SEM image of a hole-array with mean hole diameter *d* ~ 260 nm and silver thickness *t* = 50 nm.

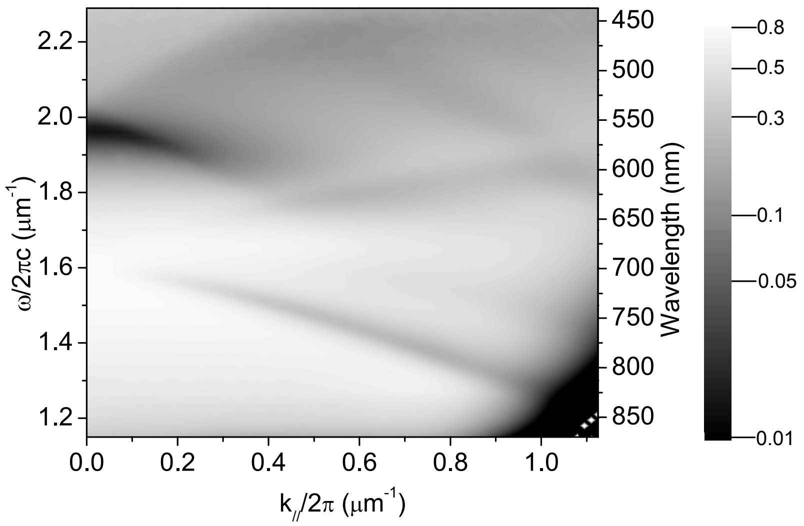

Figure 7.10. Transmittance dispersion scan of the sample in figure 7.9 taken with *p*-polarised light incident at an azimuthal angle *φ* = 0°. The dark region at low frequency, high wave vector is an experimental artefact.

incident at an azimuthal angle *φ* = 0° is shown in figure 6.10. Despite the thickness of the silver being the same as that in figure 7.7(e), the dispersion of the mode is at a higher frequency. This is in accordance with the assertion that an increased proportion of silver reduces the extension of the electromagnetic field associated with the SPP into air; thus the perturbation of the SPP dispersion is reduced.

A more comprehensive analysis is limited by the difficulties associated with fabricating thick films and small holes – the spheres cannot be removed. To realise an array of holes with diameter *d* < 200 nm was not possible when films are evaporated with a thickness *t* > 50 nm. However, smaller diameter hole arrays can be fabricated if thinner films are evaporated, and it was already shown in the previous section that interesting features develop in the scans taken from these films. Therefore arrays were fabricated with hole diameters ranging from ~ 320 nm to ~ 100 nm in silver films with a thickness of 15 nm. As is apparent from the SEM images in figures 7.11(a)-(c) the particles begin to lose their sphericity and become irregularly shaped for small diameters. Nevertheless, a smooth progression is observed in the set of normal incidence transmittance scans in figures 7.12(a)-(c). The diameter of the holes reduces

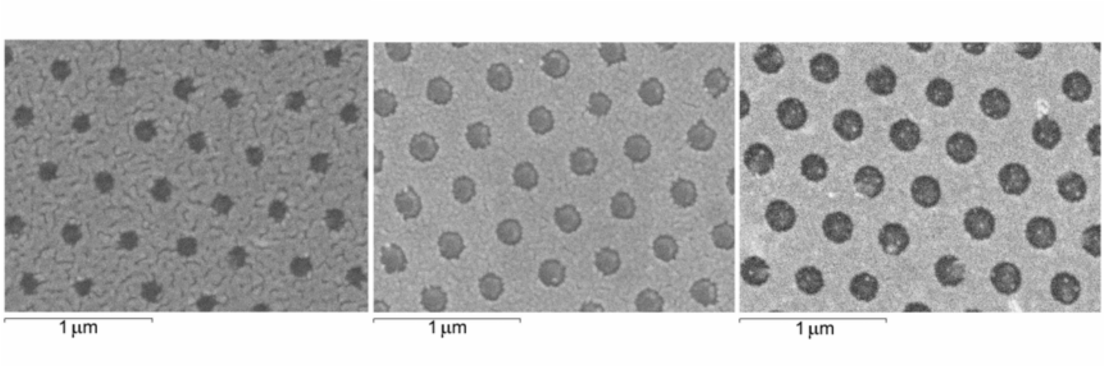

Figure 7.11. SEM images of hole arrays with mean hole diameters of ~ 200 nm (a), 150 nm (b) and 100 nm (c).

as indicated in the graphs with the solid lines in figures 7.12(b) and (c) representing the same data as the short-dashed line in figures 7.12(a) and 7.12(b) respectively. Two distinct transmittance minima are identified in figure 7.12(a) initially as shallow, broad features. These were first seen in figure 7.7(a), an equivalent normal incidence spectra being the dotted line in figure 7.12(a). A blue-shift of the longer wavelength minimum and a red-shift of the shorter wavelength minimum occur as the diameter is further reduced with the former becoming more prominent and the latter weakening. Eventually the shorter wavelength minimum becomes irresolvable in the data in particular

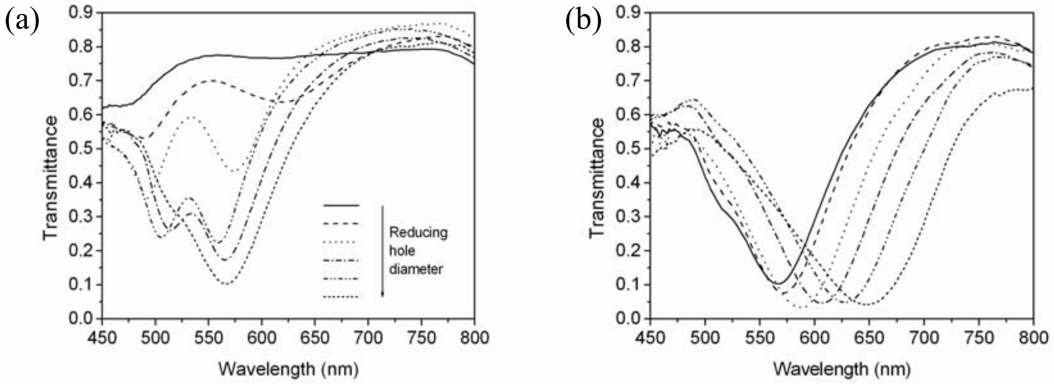

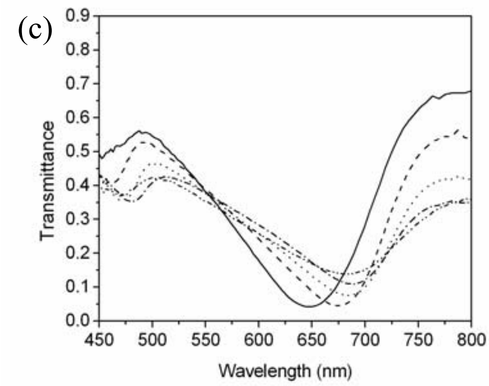

Figure 7.12. Normal incidence transmittance scans of a series of hole arrays formed with decreasing hole diameter (as indicated) in silver films with a thickness of 15 nm. The solid lines in figures (b) and (c) correspond to the short dashed lines shown in figures (a) and (b) respectively.

when compared to the very deep longer wavelength transmittance minimum that, after the initial blue-shift, is seen to red-shift considerably with reducing hole diameter. Further reductions result in a reduced red-shift and an eventual turn-around where the minimum begins to blue-shift again. At this point the array consists of the smallest holes able to be fabricated with d ~ 100 nm, as shown above.

To supplement these observations transmittance dispersion scans were taken from selected samples to aid in identifying the modes supported by the structures. Figures 7.13(a)-(c) are dispersion scans and the corresponding normal incidence transmittance from three arrays with estimated hole diameters of ~ 320 nm, 280 nm and 220 nm. Again it is observed that with an increase in the proportion of metal the familiar (1,0) and (-1,0) grating-coupled SPPs shift towards higher frequencies for a given in-plane wave vector. From figure 7.13(a) we see that for large diameter holes (meaning a low proportion of metal in the structure) these SPPs intersect at a frequency of < 1.2 μm^{-1}. Similarly the dispersion of the (2,0) and (-2,0) SPPs would also be at a reduced frequency, intersecting with the $k_{//}$ axis at a frequency within the zero-order region of the scan. From figure 7.13(a) it therefore appears that the minima developing from $k_{//}$ = 0 μm^{-1}, $\omega/2\pi c$ = 1.72 μm^{-1} are the SPPs excited with grating vectors of magnitude 2G, these originating from the (±2,0) points in reciprocal space. In figure 7.13(b) where the hole diameter has been reduced the modes have shifted to a higher frequency seeming to confirm this. However, from the normal incidence scans in figures 7.12 and figure 7.13(c) it is seen that the higher frequency (shorter wavelength) minimum moves towards lower frequencies (higher wavelengths) contradicting the assignment of SPP excitation as the cause of these minima in spectra taken from samples with small hole diameters. To account for this discrepancy it is suggested that the amount of light directly transmitted through the sample is reduced as the hole diameter decreases at frequencies coinciding with the excitation of the SPP modes. The effect this has is to change the SPP from a transmittance minimum to a transmittance maximum; there is no longer a process of destructive interference between light re-radiated by the SPP and light that is directly transmitted. This is seen in figure 7.13(c) where the SPP mode crosses the low transmittance band at 0.5 < $k_{//}$ < 0.7 μm^{-1}, $\omega/2\pi c$ = 1.6 μm^{-1}. At first glance it

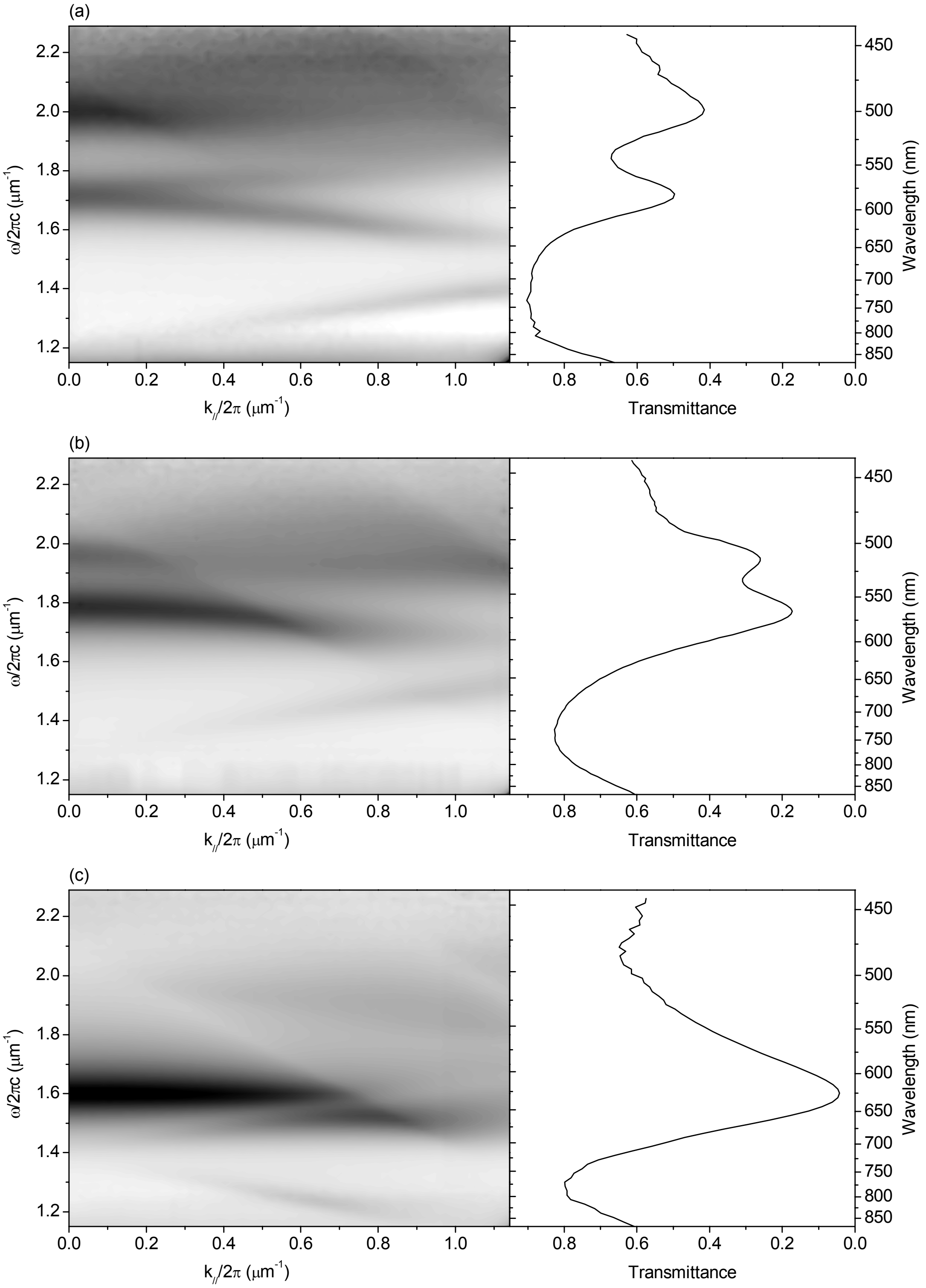

Figure 7.13. Transmittance dispersion scans and associated normal incidence line-scans from three samples with *d* ~ 320 nm (a), 280 nm (b) and 220 nm (c). Incident light was *p*-polarised and the sample was oriented with *φ* = 0°.

seems that the transmittance minimum is simply due to the *absence* of both directly transmitted light and an SPP mode that would otherwise result in enhanced transmittance. However, still required is an explanation of the blue-shift of the transmittance minimum when the holes have a diameter d ~ 100 nm. Also, the value of the minimum transmittance is much lower ($T < 5$ %) than that expected from simple calculations. The thickness of the metal is less than the skin depth so even regarding the metal layer as a planar slab of equivalent thickness a transmittance $T > 1/e$ would be expected. Thus it is suggested that a third process may be involved, namely the excitation of a mode localised within the hole. *Prikulis (2003)* observed localised modes excited within circular holes with d = 110 nm in gold films with a thickness of 20 nm. The response to changes in the local refractive index of the bounding medium and size of the hole is similar to the response of the localised surface plasmon resonance (LSPR) associated with a metal nanoparticle. A decrease in hole diameter leads to a lower resonant wavelength of the hole mode. One would therefore expect that the position of the transmittance minimum would blue-shift if it was a hole mode with decreasing diameter. However, this neglects the possible influence of interactions between modes set up in adjacent holes on the position of the resonance. It is well known that particle interactions dramatically affect the position of the LSPR [*Tamaru (2002)*, *Gunnarsson (2003)*, *Rechberger (2003)*] leading to both red-shifts and blue-shifts depending on the structure and separation of the particles. As the hole diameter is reduced the interactions between particles would be reduced and size effects would become more dominant in determining the position of the mode.

7.4 Summary

In this chapter arrays of sub-wavelength holes perforating thin silver films have been optically characterised. Using the technique of etched nanosphere lithography the diameter of the holes in silver films was varied ranging in thickness from 15 nm to 70 nm. Prior to etching the mean diameter of nanospheres used to form the arrays was 390 nm with a periodicity λ_G = 338 nm calculated by assuming a perfect hexagonal lattice. Transmittance data were collected typically as a function of frequency and in-plane wave vector thus allowing dispersion plots to be constructed. Initially transmittance through a sample fabricated with a hole diameter *d* ~ 310 nm and thickness of 50 nm was obtained for a number of grating orientations (azimuthal angles) for both p- and *s*-polarised light. Depending on the polarisation and orientation either propagating or standing SPP modes are excited via grating-coupling. With *p*-polarised (*s*-polarised) light and φ = 0° (φ = 90°) propagating modes with a familiar dispersion modelled by adopting an effective thickness to describe the perforated silver film are observed. With *p*-polarised (*s*-polarised) light and φ = 90° (φ = 0°) non-dispersive standing wave modes are excited. As the thickness of the film is changed the dispersion of the SPP mode is less perturbed due to the reduced extension of the field associated with SPP silica mode across opposite air-silver interface. For very thin films an additional feature develops in the zero-order region of the dispersion scans moving towards lower frequencies as the thickness is reduced. By observing the effect of reducing the diameter of the holes in arrays with a constant thickness of 15 nm it was suggested that the feature was a higher-order scattered SPP mode. As the hole diameter was reduced towards the minimum achievable value of ~ 100 nm a second type of mode may be excited. It was proposed that this was a localised mode associated with individual holes.

Publications

'Surface plasmon polaritons and their role in the enhanced transmission of light through periodic arrays of subwavelength holes in a metal film', W. L. Barnes, W. A. Murray, J. Dintinger, E. Devaux, and T. W. Ebbesen, Phys. Rev. Lett. **92**, 107401 (2003).

'Transition from localized surface plasmon resonance to extended surface plasmon-polariton as metallic nanoparticles merge to form a periodic hole array', W. A. Murray, S. A. Astilean and W. L. Barnes, Phys. Rev. B **69**, 165407 (2003).

'Fabrication of large-area ferromagnetic arrays using etched nanosphere lithography', S. M. Weekes, F. Y. Ogrin and W. A. Murray**,** Langmuir **20,** 11208 (2004).

'Optical Response of Thin Silver Film Periodic Arrays Fabricated Using Etched Nanosphere Lithography', CLEO Europe Conference on Lasers and Electro-Optics, Munich, Germany (June 2003). Oral presentation.

'Optical characterisation of nanoscale particle and hole arrays formed by nanosphere lithography', Euro Conference on Nano-Optics: Surface Plasmon Photonics, Granada, Spain (September 2003). Poster presentation.

References

Amos RM and Barnes WL	1997	Phys. Rev. B **55**, 7249
Amos RM, Rarity JG, Tapster PR Shepherd TJ and Kitson SC	2000	Phys. Rev. E **61**, 2929
Barnes WL and Sambles JR	1986	Surf. Sci. **177**, 399
Barnes WL, Preist TW, Kitson SC, Sambles JR, Cotter NPK and Nash DJ	1995	Phys. Rev. B **51**, 11164
Barnes WL, Preist TW, Kitson SC and Sambles JR,	1996	Physical Review B **54**, 6227
Barnes WL, Murray WA, Dintinger J, Devaux E, Lezec HJ and Ebbesen TW	2003	Phys. Rev. Lett. **92**, 107401
Berreman D	1972	J. Opt. Soc. Am. **62**, 502
Berreman D	1973	J. Opt. Soc. Am. **63**, 1374
Bethe H. A.	1944	Phys. Rev **66**, 163
Bohren CF and Huffman DR	1983	*'Absorption and scattering of light by small particles'* Wiley, New York
Blodgett K and Langmuir I	1937	Phys. Rev. **51**, 964
Bloemer MJ, Buncick MC, Warmack RJ and Ferrell TL	1988	J. Opt. Soc. Am. **5**, 2552
Bonod N, Enoch S, Li L, Popov E and Neviere M	2003	Optics Express **11**, 482
Bozhevolnyi SI, Erland J, Leosson K, Skovgaard PMW and Hvam JM	2001	Phys. Rev. Lett. **86**, 3008
Bryan-Brown GP and Sambles JR	1990	J. Mod. Opt. **37**, 1227
Bullen HA and Garrett SJ	2002	Nano Lett. **2**, 739
Burstein E and De Martini F	1974	*'Polaritons'*, Pergamon Press Inc., New York, 1
Cao Q and Lalanne P	2002	Phys. Rev. Lett. **88**, 057403

References

Chance RR, Prock A and Silbey R	1978	Adv. Chem. Phys. **37**, 1
Chandezon J, Dupuis MT, Cornet G and Maystre D	1982	J. Opt. Soc. Am. **72**, 839
Choi DG, Yu HK, Jang SG, Yang SM	2004	J. Am. Chem. Soc. **126**, 7019
Collin RE	1991	*'Field theory of guided waves 2nd ed.'*, IEEE (New York)
Cowley JM	1984	*'Diffraction Physics 2nd ed.'*, Elsevier Science (Amsterdam)
Coyle S, Netti MC, Baumberg JJ, Ghanem MA, Birkin PR, Bartlett PN and Whittaker DM	2001	Phys. Rev. Lett. **87**, 176801
Craighead HG and Niklasson GA	1984	Appl. Phys. Lett. **44**, 1134
Deckman HW and Dunsmuir JH	1982	Appl. Phys. Lett. **41**, 377
Degiron A, Lezec HJ, Barnes WL and Ebbesen TW	2002	Appl. Phys. Lett. **81**, 4327
Degiron A and Ebbesen TW	2005	J. Opt. A: Pure Appl. Opt. **7**, S90-S96.
Denkov ND, Velev OD, Kralchevsky, Ivanov IB, Yoshimura H and Nagayama K	1992	Langmuir **8**, 3183
Denkov ND, Velev OD, Kralchevsky, Ivanov IB, Yoshimura H and Nagayama K	1993	Nature **361**, 26
Dinsmore AD, Crocker JC and Yodh AG	1998	J. Curr. Opi. Colloid Interface Sci. **3**, 5
Ditlbacher H, Felidj N, Krenn JR, Lamprecht B, Leitner A and Aussenegg FR	2001	Appl. Phys. B-Lasers O **73**, 373
Dragila R, Luther-Davies B and Vukovic S	1985	Phys. Rev. Lett. **55**, 1117
Drexhage KH	1974	*Progress in Optics XII*, edited by E. Wolf, North-Holland

		(Amsterdam), p.165
Duval-Malinsky M, Kelly KL, Schatz GC and Van Duyne RP	2001	J. Am. Chem. Soc. **123**, 1471
Eagen CF	1981	Appl. Opt. **20**, 3035
Ebbesen TW, Lezec HJ, Ghaemi HF, Thio T, Wolff PA	1998	Nature **391**, 667
Elston SJ, Bryan-Brown GP, Priest TW and Sambles JR	1991a	Phys. Rev. B **44**, 3483
Elston SJ, Bryan-Brown GP and Sambles JR	1991b	Phys. Rev. B **44**, 6393
Enoch S, Quidant R and Badenes G	2004	Opt. Exp. **12**, 3422
Fano U	1941	J. Opt. Soc. Am. **31**, 213
Faraday M	1857	Philos. Trans. **147**, 145
Felidj N, Aubard J, Levi G, Krenn JR, Salerno M, Schider G, Lamprecht B, Leitner A and Aussenegg FR	2002	Phys. Rev. B **65**, 075419
Fischer UC and Zingsheim HP	1981	J. Vac. Sci. Technol. **19**, 881
Fulda KU, and Tieke E	1994	Adv. Mater. **6**, 288
Garcia-Vidal FJ, Lezec HJ, Ebbesen TW and Martin-Moreno L	2003	Phys. Rev. Lett. **90**, 213901
Gifford DK and Hall DG	2002	Appl. Phys. Lett. **81**, 4315
Ghaemi HF, Thio T, Grupp DE, Ebbesen TW and Lezec HJ	1998	Phys. Rev B **58**, 6779
Glass AM, Wokaun A, Heritage JG, Bergmann JG, Liao PF and Olson DH	1981	Phys. Rev. B **24**, 4906
Gotschy W, Vonmetz K, Leitner A and Aussenegg FR	1996	Appl. Phys. B **63**, 381
Granet G	1995	Pure Appl. Opt. **4**, 777
Grupp DE, Lezec HJ, Ebbesen TW, Pellerin KM and Thio T	2000	Appl. Phys. Lett. **77**, 1569
Gunnarsson L	2003	PhD thesis, Chalmers University of Technology
Haes AJ and van Duyne RP	2002	J. Am. Chem. Soc. **124**, 10596

Haes AJ, Zou S, Schatz GC and van Duyne RP	2004a	J. Phys. Chem. B **108**, 109
Haes AJ, Zou S, Schatz GC and Van Duyne RP	2004b	J. Phys. Chem. B **108**, 6961
Haginoya C, Ishibashi M and Koike K	1997	Appl. Phys. Lett. **71**, 2934
Hanarp P, Käll M, Sutherland DS	2003	J. Phys. Chem. B **107**, 5768
Harris JB, Priest TW, Sambles JR, Thorpe RN and Watts RA	1996	J. Opt. Soc. Am. A **13**, 2041
Hayashi S, Kumamoto Y, Suzuki T and Hirai T	1991	J. Colloid Interface Sci. **144**, 538
Haynes CL and van Duyne RP	2001	J. Phys. Chem B **105**, 5599
Haynes CL, McFarland AD, Smith MT, Hulteen JC and van Duyne RP	2002	J. Phys. Chem. B **106**, 1898
Haynes CL and van Duyne RP	2003a	Nano Lett. **3**, 939
Haynes CL, McFarland AD, Zhao L, van Duyne RP, Gunnarsson L, Prikulis J, Kasemo B and Käll M	2003b	J. Phys. Chem. B **107**, 7337
Hecht B, Bielefeldt H, Novotny L, Inouye Y and Pohl DW	1996	Phys. Rev. Lett. **77**, 1889
Heilwell EJ and Hochstrasser RM	1985	J. Chem. Phys. **82**, 4762
Hibbins AP, Evans BR and Sambles JR	2005	Science **308**, 670
Holland WR and Hall DG	1984	Phys. Rev. Lett. **52**, 1041
Hooper IR and Sambles JR	2003	Physical Review B **67**, 235404
Hooper IR and Sambles JR	2004	Phys. Rev. B **70**, 045421
Huang ZP, Carnahan DL, Rybczynski J, Giersig M, Sennett M, Wang DZ, Wen JG, Kempa K and Ren ZF	2003	Appl. Phys. Lett. **82**, 460
Hulteen JC and van Duyne RP.	1995	J. Vac. Sci. Technol. A **13**, 1553
Hurd AJ and Schaefer DW	1985	Phys. Rev. Lett. **54**, 1043
Jensen TR, Schatz GC and van Duyne RP	1999a	J. Phys. Chem. B **103**, 2394

Jensen TR, Duval Malinsky M, Kelly KL, Lazarides AA, Schatz GC, and van Duyne RP	1999b	J. Phys. Chem. B **103**, 9846
Jensen TR, Duval Malinsky M, Haynes CL and van Duyne RP	2000	J. Phys. Chem. B **104**, 10549
Jin RC, Cao YW, Mirkin CA, Kelly KL, Schatz GC and Zheng JG	2001	Science **294**, 1901
Johansson P	2001	Phys. Rev. B **64**, 165405
Kelly KL, Coronado E, Zhao LL and Schatz GC	2003	J. Phys. Chem. B **107**, 668
Kempa K, Kimball B, Rybczynski J, Huang ZP, Wu PF, Steeves D, Sennett M, Giersig M, Rao DVGLN, Carnahan DL, Wang DZ, Lao JY, Li WZ, Ren ZF	2003	Nano Lett. **3**, 13
Kikuchi S	1928	Jpn. J. Phys. **5**, 83
Kitson SC, Barnes WL and Sambles JR	1996	Phys. Rev. Lett. **77**, 2670
Klein Koerkamp KJ, Enoch S, Segerink FB, van Hulst NF and Kuipers L	2004	Phys. Rev. Lett. **92**, 183901
Kneipp K, Wang Y, Kneipp H, Perelman LT, Itzkan I, Dasari RR and Feld MS	1997	Phy. Rev. Lett. **78**, 1667
Kosiorek A, Kandulski W, Chudzinski P, Kempa K and Giersig M	2004	Nano Lett. **4**, 1359
Kottmann JP and Martin OJF	2001	Opt. Lett. **26**, 1096
Kreibig U	1974	J. Phys. F **4**, 999
Kreibig U and Völlmer M	1995	*‘Optical properties of metallic particles’* (Springer, Berlin)
Krenn JR, Dereux A, Weeber JC, Bourillot E, Lacroute Y, Goudonnet JP, Schider G, Gotschy W, Leitner A,	1999	Phys. Rev. Lett. **82**, 2590

Aussenegg FR and Girard C		
Krenn JR , Schider G, Rechberger W, Lamprecht B, Leitner A, Aussenegg FR and Weeber JC	2000	Appl. Phys. Lett. **77**, 3379
Kretschmann E and Raether H		Z. Natur. **23a**, 2135 (1968).
Kuai S-L, Hu X-F, Hache A, and Truong V-V	2004	J. Crystal Growth **267**, 317
Kume T, Hayashi S and Yamamoto K	1997	Phys. Rev. B **55**, 4774
Kuo CW, Shiu JY, Chen PL, Somorjai GA	2003	J. Phys. Chem. B **107**, 9950
Kottmann JP and Martin OJF	2001	Opt. Lett. **26**, 1096
Kulakovich O, Strekal N, Yaroshevich A, Maskevich S, Gaponenko S, Nabiev I, Woggon U and Artemyev M	2002	Nano Lett. **2**, 1449
Lakowicz JR	2001	Anal. Biochem. **298**, 1
Lamprecht B, Schider G, Lechner RT, Ditlbacher H, Krenn JR, Leitner A and Aussenegg FR	2000	Phys. Rev. Lett. **84**, 4721
Langmuir IV	1915	J. Am. Chem. Soc. **37**, 1139
Langmuir IV	1920	Trans. Faraday Soc. **15**, 62
Lenzmann F, Li K, Kitai AH, Stover HDH	1994	Chem. Mater. **6**, 156
Lezec HJ, Degiron A, Devaux E, Linke RA, Martin-Moreno L, Garcia-Vidal FJ and Ebbesen TW	2002	Science **297**, 820
Lin K-H, Crocker JC, Prasad V, Schofield A, Weitz DA Lubensky TC and Yodh AG	2000	Phys. Rev. Lett. **85**, 1770
Linden S, Kuhl J and Giessen H	2001a	Phys. Rev. Lett. **86**, 4688
Linden S, Christ A, Kuhl J and Giessen H	2001b	Appl. Phys. B: Lasers Opt. **73**, 311
Link S and El-Sayed MA	1999	J. Phys. Chem. B **103**, 8416

Lockyear MJ, Hibbins AP, Sambles JR and Lawrence CR	2004	Appl. Phys. Lett. **84**, 2040
Lu Y, Yin Y, Gates B and Xia Y	2001	Langmuir **17**, 6344
McClelland JJ, Scholten RE, Palm EC and Celotta RJ	1993	Science **262**, 877
Maier SA, Brongersma ML, Kik PG, Meltzer S, Requicha AAG and Atwater HA	2001	Adv. Mater. **13**, 1501
Maier SA, Brongersma ML, Kik PG, and Atwater HA	2002	Phys. Rev. B **65**, 193408
Martin-Moreno L, Garcia-Vidal FJ and Lezec HJ	2001	Opt. Commun **200**, 1
Maxwell-Garnett JC	1904	Philos. Trans. R. Soc. **203**, 385
Maxwell-Garnett JC	1906	Philos. Trans. R. Soc. **205**, 237
Meier M and Wokaun A	1983	Opt. Lett. **8**, 581
Meier M, Wokaun A and Liao PF	1985	J. Opt. Soc. Am. B **2**, 931
Meriaudeau F, Downey TR, Passian A, Wig A and Ferrell TL	1998	Appl. Opt. **37**, 8030
Micheletto R, Fukada H and Ohtsu M	1995	Langmuir **11**, 3333
Mie G	1908	Ann. Phys **25**, 377
Mock JJ, Barbic M, Smith DR, Schultz DA and Schultz S	2002	J. Chem. Phys. **116**, 6755
Mock JJ, Smith DR and Schultz S	2003	Nanolett. **3**, 485
Moskovits M	1985	Rev. Mod. Phys. **57**, 783
Murray C	1998	MRS Bull. **23**, 33
Nash DJ and Sambles JR	1996	J. Mod. Opt. **43**, 81
Nie S and Emory SR	1997	Science **275**, 1102
Otto A	1968	Z. Phys. 216, 398
Palik E	1985	*'Handbook of optical constants of solids'*, Academic Press, Inc. (London)
Park SH, Qin D and Xia Y	1998	Adv. Mater. **10**, 1028
Pendry JB	1999	Science **285**, 1687

Pendry JB, Martin-Moreno L and Garcia-Vidal FJ	1999	Science **305**, 847
Petty MC	1996	*‘Langmuir Blodgett films’*, Cambridge University Press (Cambridge)
Pieranski P	1980	Phys. Rev. Lett. **45**, 569
Pipino ACR and Schatz GC	1994	J. Opt. Soc. Am. B **11**, 2036
Pockrand I	1975	Opt. Commun. **13**, 311
Pockrand I	1978	Surf. Sci **72**, 577
Pockrand I, Brillante A and Mobius D	1980	Chem. Phys. Lett. **69**, 499
Pohl DW	2001	*‘Near-field optics and surface plasmon polaritons’*, edited by S. Kawata, Springer-Verlag, Heidelberg, **81**, 1.
Popov E, Neviere M, Enoch S and Reinisch, R	2000	Phys. Rev B **62**, 16100
Powell CJ and Swan JB	1959	Phys. Rev. **115**, 869
Powell CJ and Swan JB	1960	Phys. Rev. **118**, 640
Prikulis J, Hanarp P, Olofsson L, Sutherland D and Käll M	2003	Nano Lett. **4**, 1003
Purcell EM and Pennypacker C	1973	Astrophys. Journ. **186**, 705
Raether H	1988	*‘Surface plasmons on smooth and rough surfaces and on gratings’* (Springer, Berlin)
Rakers S, Chi LF and Fuchs H	1997	Langmuir **19**, 7121
Rayleigh JWS	1871	Phil. Mag. **41**, 107, 274
Rayleigh JWS	1907	Phil. Mag. **13**, 214
Rechberger W, Hohenau A, Leitner A, Krenn JR, Lamprecht B and Aussenegg FR	2003	Opt. Comm. **220**, 137
Ritchie RH	1957	Phys. Rev. **106**, 874
Ritchie RH, Arakawa ET and Hamm RH	1968	Phys. Rev. Lett. **21**, 1530

Roberts G	1990	*‘Langmuir-Blodgett films’*, Plenum Press (New York)
Roder H, Hahn E, Brune H, Butcher J-P and Kern K	1993	Nature **366**, 141
Russell BK, Mantovani JG, Anderson VE, Warmack RJ and Ferrell TL	1987	Phys. Rev. B **35**, 2151
Rybczynski J, Ebels U and Giersi M	2003	Colloids and Surfaces A **219**, 1
Salerno M, Felidj N, Krenn JR, Leitner A, Aussenegg FR and Weeber JC	2001	Physical Review B **63**, 165422
Sambles JR, Bradbery GW and Yang FZ	1991	Contemporary Physics **32**, 173
Sambles JR	1998	Nature **391,** 641
Sarrazin M, Vigneron JP, and Vigoureux JM	2003	Physical Review B **67**, 085415
Schatz GC and Van Duyne RP	2002	*‘Handbook of vibrational spectroscopy’*, edited by J. M. Chalmers and P. R. Griffiths (Wiley, Chichester), 1
Schröter U and Heitmann D	1999	Phys. Rev. B **60**, 4992
Schultz DA	2003	Curr. Opin. Biotech. **14** 13
Sommerfeld A	1949	*‘Partial Differential Equations’* (Academic Press, New York)
Special Issue	2001	Appl. Phys. B-Lasers and Optics **73**, all articles therein
Stratton JA	1941	*‘Electromagnetic theory’*, McGraw-Hill (New York)
Stuart HR and Hall DG	1996a	Phys. Rev. Lett. **80**, 5663
Stuart HR and Hall DG	1996b	Appl. Phys. Lett. **73**, 3815
Taflove A and Hagness SC	2000	*‘Computational electrodynamics – the finite difference time domain method’*

		2nd ed., Artech House
Tamaru H, Kuwata H, Miyazaki HT and Miyano K	2002	Appl. Phys. Lett. **80**, 1826
Thio T, Pellerin KM, Linke RA, Lezec HJ and Ebbesen TW	2001	Opt. Lett. **26**, 1972
Treacy MMJ	2002	Phys. Rev. B **66**, 195105
Wang JJ, Zhu MY, Zhao X, Outlaw RA, Manos DM, Holloway BC, Park C, Anderson T and Mammana VP	2004	J. Vac. Sci. Technol. B **22**, 1269
Warmack RJ and Humphrey SJ	1986	Phys. Rev. B **34**, 2246
Wasey JAE and Barnes WL	2000	J. Mod. Opt. **47**, 725
Watts RA, Preist TW and Sambles JR	1997	Phys. Rev. Lett. **79**, 3978
Watts RA, Hibbins AP and Sambles JR	1999	J. Mod. Opt. **46**, 2157
Weast RC	1972	*'Handbook of chemistry and physics – 53rd edition'*, (CRC, Cleveland)
Wedge S, Hooper IR, Sage I and Barnes WL	2004	Phys. Rev. B **69**, 245418
Weekes SM, Ogrin FY and Murray WA	2004	Langmuir *in press*
Weber WH and Eagen CF	1979	Opt. Lett. **4**, 236
Wellner A, Preece PR, Fowler JC, Palmer RE	2001	Microelectron. Eng. **57**, 919
Whitney AV, Myers BD and van Duyne RP	2004	Nano Lett. **4**, 1507
Wiesendanger R, Bode M, Kleiber M, Lohndorf M, Pascal R, Wadas A and Weiss D	1997	J. Vac. Sci. Technol. B **15**, 330
Wokaun A, Gordon JP, and Liao PF	1982	Phys. Rev. Lett. **48**, 957
Wood EL, Sambles JR, Cotter NJK, and Kitson SC	1995	J. Mod. Opt. **42**, 1343

Wood RW	1902	Phil. Mag. **4**, 396
Worthing PT, Amos RM and Barnes WL	1999	Phys. Rev. A **59**, 865
Xia Y, Yin Y, Lu Y and McLennan J	2003	Adv. Func. Mater. **13**, 907
Xu H, Bjerneld EJ, Käll M and Börjesson L	1999	Phys. Rev. Lett. **83**, 4357
Yablonovitch E	1987	Phys. Rev. Lett. **58**, 2059
Yablonovitch E	1993	J. Opt. Soc. Am. **10**, 283
Ye Y-H, LeBlanc F, Hache A and Truong V-V	2001a	Appl. Phys. Lett. **78**, 52
Ye Y-H, Badilescu S, Truong V-V, Rochon P and Natansohn A	2001b	Appl. Phys. Lett. **79**, 872
Zhang X, Hicks EM, Zhao J, Schatz GC and Van Duyne RP	2005	Nano Lett., **5**, 1503
Zhao L, Kelly KL and Schatz GC	2003	J. Phys. Chem. B **91**, 7343